



Temperature and Strain Sensing using Rare Earth Fluorescence and Bragg Gratings in Optical Fibres

by

Steven Trpkovski

BSc.(Hons) Victoria University

Submitted for the degree of

Doctor of Philosophy

Optical Technology Research Laboratory

School of Electrical Engineering

Victoria University of Technology

Australia

2005

FTS THESIS
621.3692 TRP
30001008595631
Trpkovski, Steven
Temperature and strain
sensing using rare earth
fluorescence and Bragg

To my much loved family

ABSTRACT

Temperature and Strain Sensing using Rare Earth Fluorescence and Bragg Gratings in Optical Fibres

by Steven Trpkovski

BSc.(Hons) Victoria University

Principal Supervisor:

Dr. Stephen Collins

This thesis describes the study of the temperature and strain effects on rare earth fluorescence and Bragg gratings in optical fibres. The development and performance of simultaneous temperature and strain measurement systems utilising a combined technique of the fluorescence intensity ratio and the Bragg wavelength shift are investigated.

The fluorescence intensity ratio technique uses the thermal coupling of two closely spaced energy levels in a rare earth ion. The ratio of the intensities generated from these levels has a temperature dependence that is insensitive to strain. The other technique investigated is the Bragg wavelength shift to temperature and strain. Fibre Bragg gratings have been widely used as temperature or strain sensors. The problem associated with the fibre Bragg grating cross-sensitivity to temperature and strain is addressed by using the strain insensitive fluorescence intensity ratio to measure the temperature directly.

The fluorescence intensity ratio and Bragg wavelength shift was studied using five different erbium doped fibre sensors. These sensors were fabricated with varying erbium concentrations and core compositions and the fibre Bragg gratings were inscribed either within the doped fibre or in close proximity. Sensors with the fibre Bragg gratings inscribed within the doped fibre demonstrated superior performance compared to those FBGs in close proximity to the doped fibre. The temperature

and strain ranges measured by these sensors were 20 - 200 °C and 350 - 2534 $\mu\epsilon$, respectively. The sensors achieved root-mean-square errors as small as 0.3 °C and 4.8 $\mu\epsilon$. These results are, to the best of the author's knowledge, amongst the best achieved for fibre-optic simultaneous temperature and strain sensors.

Tin doped optical fibre has been shown to increase the thermal stability of fibre Bragg gratings at elevated temperatures. An erbium:tin doped fibre with a fibre Bragg grating inscribed within was successfully used as a simultaneous and co-located temperature and strain sensor over an extended temperature range of 20 - 600 °C. The strain range used was 350 - 1988 $\mu\epsilon$. It demonstrated reasonable root-mean-square errors of 1.7 °C and 27.0 $\mu\epsilon$ over the specified measurement ranges.

The fluorescence intensity ratio and Bragg wavelength shift were also studied using five different erbium:ytterbium doped fibre sensors. These sensors were fabricated with varying erbium:ytterbium concentration, core compositions and the fibre Bragg gratings were inscribed within the doped fibre. With these fibres, the fluorescence intensity ratio was investigated from the ytterbium ion, while the erbium fluorescence was used to illuminate the Bragg wavelength. The temperature and strain ranges measured by these sensors were 20 - 150 °C and 350 - 2534 $\mu\epsilon$, respectively. The sensors achieved root-mean-square errors as small as 0.3 °C and 3.6 $\mu\epsilon$. The sensors based on erbium:ytterbium doped fibre demonstrated comparable performance to the erbium doped fibre sensors described above. These sensors did provide some advantages to those based on erbium doped fibre. Due to the wavelengths of interest and the fibre-optic couplers available, these sensors were configured so that they could be utilised as 'sensor probes'. Also, the majority of erbium:ytterbium based sensors were calibrated as complete commercially feasible fibre systems using fibre couplers and a fibre pigtailed laser diode.

The problems of high temperature stability and sustainability of fibre Bragg gratings have been highlighted in this thesis. Fibre Bragg gratings that are highly stable at elevated temperatures, commonly referred to as chemical composition gratings,

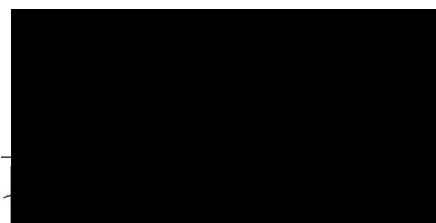
have been fabricated. Chemical composition gratings having reflectivities of up to 37%, have been fabricated in various erbium doped optical fibres for the first time. Erbium:tin doped fibre produced chemical composition gratings with the highest reflectivities, while erbium doped fibre that did not contain tin or phosphorus did not produce chemical composition gratings. The chemical composition gratings fabricated demonstrated excellent thermal stability and repeatability to temperatures up to 800°C, with no evidence of hysteresis.

“I, Steven Trpkovski, declare that the PhD thesis entitled

Temperature and Strain Sensing using Rare Earth Fluorescence and Bragg Gratings in Optical Fibres

is no more than 100,000 words in length, exclusive of tables, figures, appendices, references and footnotes. This thesis contains no material that has been submitted previously, in whole or in part, for the award of any other academic degree or diploma. Except where otherwise indicated, this thesis is my own work”.

Signature _____



Date 12/8/05

ACKNOWLEDGMENTS

I am grateful to many individuals who have provided assistance and support throughout the course of my studies. I would firstly like to thank Dr. Stephen Collins and Dr. Greg Baxter for providing me with the opportunity to undertake this research.

A special thank you to Dr. Scott Wade for his helpful discussions regarding some of this research. I would like to thank Dr. Thinh Nguyen for his help, providing motivation and good humor throughout the course of my research. Also, I would like to thank all the postgraduate students and technical staff for all the interesting conversations and company provided in the local gym.

I gratefully acknowledge Victoria University, for the financial support through the provision of the Victoria University Research Scholarship. Also, I would like to thank the Australian Research Council for their financial support in the project through the provision of the ARC Large Grant.

I would also like to acknowledge members at the Laboratoire de Physique de la Matière Condensée at the University of Nice, France, for providing the rare earth doped optical fibre used during my studies. A thankyou to Claire Davis from the Defence Science and Technology Organisation and Swinburne University for providing the use of their fibre Bragg grating manufacturing facilities.

I am deeply appreciative of my family, whose unquestioned patience, support and encouragement formed essential ingredients in the completion of this research. Finally, to my Petal, thankyou for your understanding, encouragement and unconditional love and support throughout the duration of this thesis.

CONTENTS

Abstract	ii
Declaration	v
Acknowledgements	vi
Table of Contents	vii
List of Figures	xi
List of Tables	xiv
1 Introduction	1
1.1 Historical view - Harnessing the power of light	1
1.2 Fibre-Optic Sensors	3
1.3 Scope of Thesis	8
2 Fibre-Optic Temperature and Strain Sensors	12
2.1 Fluorescence Lifetime Based Temperature Sensors	13
2.2 Fluorescence Intensity Ratio Based Temperature Sensors	14
2.2.1 FIR Detection Methods	17
2.3 Fibre Bragg Grating Sensors	18
2.3.1 High Temperature FBG Sensing	21
2.3.2 Bragg Wavelength Interrogation Schemes	21
2.4 Simultaneous Temperature and Strain Measurement	26
2.4.1 Fully Distributed Sensing	26
2.4.2 Point Sensing	28
2.5 Temperature and Strain Sensor Applications	34
2.5.1 Aerospace and Marine	34

2.5.2	Civil Engineering and Mining	36
3	Fibre-Optic Sensing Elements	38
3.1	Rare Earth Doped Optical Fibres	38
3.1.1	Fabrication of Rare Earth Doped Optical Fibres	40
3.1.2	The Erbium Ion	43
3.1.3	Ytterbium-sensitised Erbium	45
3.1.4	FIR Theory	45
3.2	Fibre Bragg Grating Characteristics	48
3.2.1	Photosensitivity in Optical Fibres	51
3.2.1.1	Colour-centre Model	52
3.2.1.2	Stress Relaxation Model	52
3.2.1.3	Densification-compaction Model	53
3.2.1.4	Increased Photosensitivity by Hydrogen Treatment	53
3.2.2	Core Composition Effects	54
3.2.2.1	Bragg Gratings in Rare Earth Doped Fibres	55
3.2.2.2	Effects Of Various Dopants	55
3.2.3	FBG Decay Models	58
3.2.3.1	Power-Law Model	58
3.2.3.2	Accelerated Aging Model	59
3.2.3.3	Hydrogen-loading Effects and the Log-time Model	60
3.2.4	Fabrication Techniques for Fibre Bragg Gratings	60
3.2.4.1	Victoria University FBG Facility	61
3.2.4.2	Swinburne University FBG Facility	62
3.2.4.3	FBG Sensor Fabrication	63
3.2.4.4	Annealing of FBGs	66
3.3	Conclusion	67
4	Temperature and Strain Discrimination	69
4.1	Matrix Analysis (Method A)	69
4.1.1	Limitations and Assumptions	71
4.2	Non-Linear Analysis of FIR (Method B)	73

4.2.1	FIR Temperature and Strain Dependence	73
4.2.2	Non-Linear Temperature Dependence of Bragg Wavelength (Method C)	75
4.3	Analysis of FBG Spectra	76
4.3.1	Minima Method	76
4.3.2	Half-Maximum Method	77
4.3.3	Weighted Average Method	78
4.4	Conclusions	79
5	Erbium Based Sensors	80
5.1	FIR Wavelength Ranges	80
5.2	Pump Power and Wavelength Effects	81
5.3	Doped Fibre Length	84
5.4	Erbium Doped Sensor Configurations	85
5.5	Experimental Arrangement	88
5.5.1	Temperature and Strain Environment	90
5.6	Er1 Sensor Calibrations	92
5.6.1	Sensor 1 Results	92
5.6.2	Sensor 2 Results	99
5.7	Er3 Sensor Calibrations	104
5.7.1	Sensors 3 and 4 Results	104
5.8	Er4 Sensor High Temperature Calibration	110
5.8.1	Sensor 5 Results	110
5.9	Conclusions	114
6	Erbium:Ytterbium Based Sensors	118
6.1	FIR Wavelength Ranges	118
6.2	Pump Power and Wavelength Effects	119
6.3	Doped Fibre Length	122
6.4	ErYb Sensor Configurations	124
6.5	Experimental Arrangement	125
6.6	ErYb1 and ErYb2 Sensor Calibrations	127

6.7	Sensors 6 and 7 Results	127
6.8	ErYb ₃ Sensor Calibrations	132
6.9	Sensors 8, 9 and 10 Results	132
6.10	Conclusions	137
7	FBG Characteristics at Elevated Temperatures	141
7.1	Thermal Stability of FBGs	141
7.2	Experimental Arrangement	141
7.3	Type I FBGs in Erbium Doped Fibre	142
7.4	Chemical Composition Gratings	143
7.4.1	Fabrication of CCGs	144
7.4.1.1	CCGs in Er ₁ Fibre	144
7.4.1.2	CCGs in Other Erbium Doped Fibres	147
7.4.2	Temperature Dependence of CCGs	151
7.4.3	Strain Dependence of CCGs	153
7.5	Conclusions	154
8	Conclusions	155
8.1	Summary of Key Outcomes	155
8.2	Future Work	161
	Bibliography	163
	Appendices	182
A	List of Publications	182
A.1	Journal Articles	182
A.2	International Conference Proceedings	183
A.3	National Conference Proceedings	184

LIST OF FIGURES

1.1	Sensing system based on conventional electrical transducer.	4
2.1	Previously used FIR detection schemes.	18
2.2	Sensing system based on fibre Bragg gratings.	20
2.3	Michelson interferometry based FBG interrogator.	22
2.4	Tunable laser based FBG interrogator.	23
3.1	Periodic table of the elements.	39
3.2	Optical fibre cross-section.	40
3.3	Fabrication of rare earth doped optical fibre using the MCVD technique.	41
3.4	Energy level diagram for Er^{3+} in silica glass	43
3.5	Fluorescence spectra from the ${}^2\text{H}_{11/2}$, ${}^4\text{S}_{3/2}$ and ${}^4\text{I}_{13/2}$ levels in Er^{3+}	44
3.6	Energy level diagram for Yb^{3+} sensitised Er^{3+} in silica glass.	46
3.7	Fluorescence spectrum from the ${}^2\text{F}_{5/2}$ level in Yb^{3+}	47
3.8	Simplified energy level for FIR scheme.	48
3.9	Growth rate of Type I Bragg grating written in Er1 fibre.	49
3.10	FBG fabrication arrangement at Victoria University.	61
3.11	FBG fabrication arrangement at Swinburne University.	62
3.12	Growth of Type I FBGs in Er1, ErYb1, ErYb2 and ErYb3 fibre.	66
3.13	Spectra of fabricated FBGs.	67
3.14	Bragg wavelength versus time for an FBG inscribed in Er1 fibre.	68
4.1	FBG spectrum modelled with a Gaussian function for use with the Half-Maximum method.	78
4.2	FBG spectrum modelled with a Gaussian function for use with the Weighted Average method.	79
5.1	FIR versus pump wavelength for Er1 fibre.	82

5.2	Fluorescence intensity versus pump wavelength for Er1 fibre.	83
5.3	FIR versus pump power for Er1 fibre.	84
5.4	Fluorescence intensity versus doped fibre length for Er1 and Er4.	85
5.5	Erbium doped fibre sensor configurations.	86
5.6	Fluorescence spectrum from the $^4I_{13/2}$ level in Er1 fibre.	87
5.7	Experimental arrangement using bulk, free-space optics.	89
5.8	Experimental arrangement using complete fibre system.	90
5.9	Temperature versus position within the Carbolite tube oven.	91
5.10	Counter-propagating fluorescence spectra from Sensor 1.	93
5.11	Bragg wavelength vs temperature and strain for Sensor 1.	94
5.12	Calibration maps of <i>FIR1</i> and <i>FIR2</i> for Sensor 1.	94
5.13	Temperature and strain deviations for Sensor 1.	96
5.14	Temperature and strain deviations for Sensor 1 using the non-linear temperature dependence of the FIR.	98
5.15	Counter-propagating fluorescence spectra from Sensor 3.	105
5.16	FBG reflection spectra from Sensor 5.	111
5.17	Bragg wavelength calibration map and Bragg wavelength sensitivity vs temperature.	112
5.18	FIR Calibration map and FIR sensitivity vs temperature.	113
5.19	Summary of linear temperature and strain FIR coefficients evaluated for Sensors 1-4.	115
5.20	Summary of some of the best RMS strain and temperature errors for Sensors 1-5.	115
6.1	Normalised FIR versus pump power for ytterbium.	120
6.2	Erbium $^4I_{13/2}$ fluorescence intensity versus pump power.	121
6.3	$^4I_{13/2}$ and $^2F_{5/2}$ fluorescence intensity versus pump wavelength.	121
6.4	Normalised fluorescence intensity versus ErYb doped fibre length.	123
6.5	Erbium:ytterbium doped fibre sensor configurations.	124
6.6	Experimental arrangement for ErYb doped fibre sensors.	125
6.7	Counter-propagating fluorescence spectra from Sensor 7.	128

6.8	Temperature and strain deviations for Sensors 6 and 7.	130
6.9	Reflected and transmitted FBG spectra from ErYb fibre.	133
6.10	Temperature and strain deviations for Sensors 8, 9 and 10.	136
6.11	Summary of some of the RMS strain and temperature errors for Sensors 6-10.	138
7.1	Experimental arrangement for the fabrication of CCGs.	141
7.2	Normalised reflectance vs time for Type I FBGs.	143
7.3	Reflectance versus time during fabrication of CCGs in Er1 fibre (Victoria University Type I FBGs).	146
7.4	Reflectance versus time during fabrication of CCGs in Er1 fibre (Swinburne University Type I FBGs).	147
7.5	Normalised CCG reflectance versus wavelength.	148
7.6	Reflectance versus time during annealing process of Type I FBGs. . .	148
7.7	CCG reflectance versus time during fabrication in Er2 and Er4 fibre. . .	149
7.8	CCG Bragg wavelength versus temperature.	152
7.9	CCG reflectance versus temperature.	152
7.10	CCG Bragg wavelength versus strain.	153
8.1	RMS temperature and strain error comparison of the results from this work to that of other authors.	159

LIST OF TABLES

1.1	Fibre-optic measurement techniques for various measurands.	5
2.1	FIR temperature calibration details of various rare earth ions.	15
2.2	Tunable laser sources for FBG interrogation.	24
2.3	Summary of fibre-optic simultaneous temperature and strain distributed sensors.	27
2.4	Summary of fibre-optic simultaneous temperature and strain point sensors.	32
3.1	Physical characteristics of the fibres used as sensing elements.	42
3.2	Absorption bands for common defects related to photosensitivity.	52
3.3	FBG sensor fabrication details in Er^{3+} doped fibre.	64
3.4	FBG sensor fabrication details in $\text{Er}^{3+}:\text{Yb}^{3+}$ doped fibre.	65
5.1	Summary of erbium based sensors.	87
5.2	Summary of important parameters for Er1 sensors.	92
5.3	Linear coefficients with associated errors for Sensor 1.	95
5.4	Polynomial coefficients with associated errors for Sensor 1.	97
5.5	Summary of RMS strain errors for Sensor 1.	97
5.6	Summary of RMS temperature errors for Sensor 1.	99
5.7	r^2 values for function fits to FIR for Sensor 1.	100
5.8	Linear coefficients with associated errors for Sensor 2.	101
5.9	RMS strain errors for Sensor 2 using a pump power of 765 mW.	102
5.10	RMS strain errors for Sensor 2 using a pump power of 140 mW.	103
5.11	RMS temperature errors for Sensor 2.	103
5.12	Summary of important parameters for Er3 sensors.	104
5.13	Linear coefficients with associated errors for Sensors 3 and 4.	106
5.14	RMS strain errors Sensor 3.	107

5.15	RMS strain errors for Sensor 4.	108
5.16	RMS temperature errors for Sensors 3 and 4.	109
5.17	RMS temperature and strain errors for Sensor 5.	112
5.18	Summary of important parameters for Sensors 1-5.	114
5.19	Summary of the best RMS temperature and strain errors for Sensors 1-5.	116
6.1	Summary of erbium:ytterbium based sensors.	124
6.2	Linear coefficients with associated errors for Sensors 6 and 7.	129
6.3	RMS temperature errors for Sensors 6 and 7.	131
6.4	RMS strain errors for Sensors 6 and 7.	131
6.5	Linear coefficients with associated errors for Sensors 8, 9 and 10.	133
6.6	RMS temperature errors for Sensors 8, 9 and 10.	134
6.7	RMS strain errors for Sensors 8, 9 and 10.	135
6.8	Summary of important parameters for Sensors 1-5.	137
6.9	Summary of RMS temperature and strain errors for Sensors 6-10.	139
7.1	Annealing procedure of Type I FBGs for the formation of CCGs.	145
7.2	Characteristics summary of all CCGs formed in Er^{3+} doped fibre.	150
7.3	Linear temperature coefficients of CCGs.	151
7.4	RMS temperature errors and r^2 values for CCGs.	153
8.1	Summary of most promising sensors investigated in this work.	158

Chapter 1

INTRODUCTION

1.1 Historical view - Harnessing the power of light

The role of light for communications dates back to antiquity if we interpret optical communication in a broad sense. A significant breakthrough into the area known today as photonics came after the Second World War, initially with the invention of the transistor and the development of the semi-conductor industry. The modern photonics industry began in earnest in 1960, with the invention of the laser, closely followed by the optimisation of optical fibres as an effective means of transmitting information using these intense laser beams. It was the potential application of these technologies to the telecommunications field that would become the foundation and driving force behind the photonics industry.

The development of the first low-loss optical fibre in 1970 by industry giant Corning, was the catalyst to ignite the communications revolution. Compared to copper cables, (twisted pair and coaxial) optical fibres have many unique properties. The key advantage is the seemingly unlimited bandwidth of optical fibre; for example, the useful bandwidth per single fibre strand at optical telecommunication wavelengths at the present day is in excess of one thousand times the total radio bandwidth worldwide (i.e., 45 Tb/s vs. 25 Gb/s).

As the fibre-optic communication networks matured and became the transporting medium of choice for voice, video, and data, particularly for high speed communication, the need for improved photonics products continued to grow (e.g. laser

sources, optical amplifiers, detectors, and myriads of other optical/optoelectronic components). This demand resulted in an exponential growth of the industry, and as a result, scientists and engineers around the world realised other potential applications of this technology. Therefore, new fields of photonics emerged. Some examples of photonic equipment, instrumentation, subsystems or systems at the present day are:

- Sensors (temperature, strain, distance, pressure, etc.)
- Imaging systems (video and digital cameras)
- Optically-based information storage systems (CD, DVD, etc.)
- Laser and LED printers
- Ground-based and space-based telescopes
- Microscopy
- Photolithography equipment
- Fibre-optics
- Laser communication systems
- Digital and barcode scanners
- Laser-based cutters, welders and markers
- Medical diagnostics and surgical equipment
- Remote sensing and surveillance instruments and systems

Considering photonics is still a relatively new emerging industry, all these photonic applications continue to attract considerable interest. One of the promising fields that continues to develop rapidly, particularly over the past decade, is that of optical fibre sensor technology.

1.2 Fibre-Optic Sensors

The fibre-optic sensors industry has spawned by taking advantage of the components developed for communications and optoelectronic markets [1]. For the last two decades, an increasing amount of resources has been expended on research and development worldwide on the application of novel fibre-optic sensor systems. The main reasons for this are a combination of two factors. Firstly, the advantages that fibre-optic sensors offer over conventional electrical sensors in particular environments, and secondly, the demand from industry, which is continually seeking the benefits of improved measurement accuracy and reliability of physical/chemical/biological parameters.

Fibre-optic sensors have developed into a powerful class of sensors. They bring to measurement systems many of the advantages that optical-fibre technology have brought to communication systems. Many of these benefits stem from the fact that the fibres are made from non-conducting glass, and photons, not electrons, are used to carry the signal. The glass' dielectric properties provides many advantages over conventional electrical sensors. Some of these are:

- High sensitivity (i.e. interferometry)
- High spatial resolution
- Wide bandwidth
- Immunity to electromagnetic interference
- Resistance to corrosion and nuclear radiation
- Small size and low weight
- Intrinsic sensing of multiple measurands
- Wide operating temperature range
- Fast response time

- Long-term stability and repeatability
- High tensile strength

Transducers (eg. piezoelectric crystals or thermocouples) from traditional, electrical based sensor technologies generally emit relatively weak signals. Therefore, this signal must be immediately amplified and converted electronically into a signal that can be transmitted over long distances. The electronics must typically be located close to the transducer to limit noise pickup prior to amplification and digitisation, as shown in Figure 1.1. This is a tremendous disadvantage compared to fibre-optic sensors, for which the associated electronic read-out instrumentation can remain in a benign environment, possibly many kilometres from the sensor location.

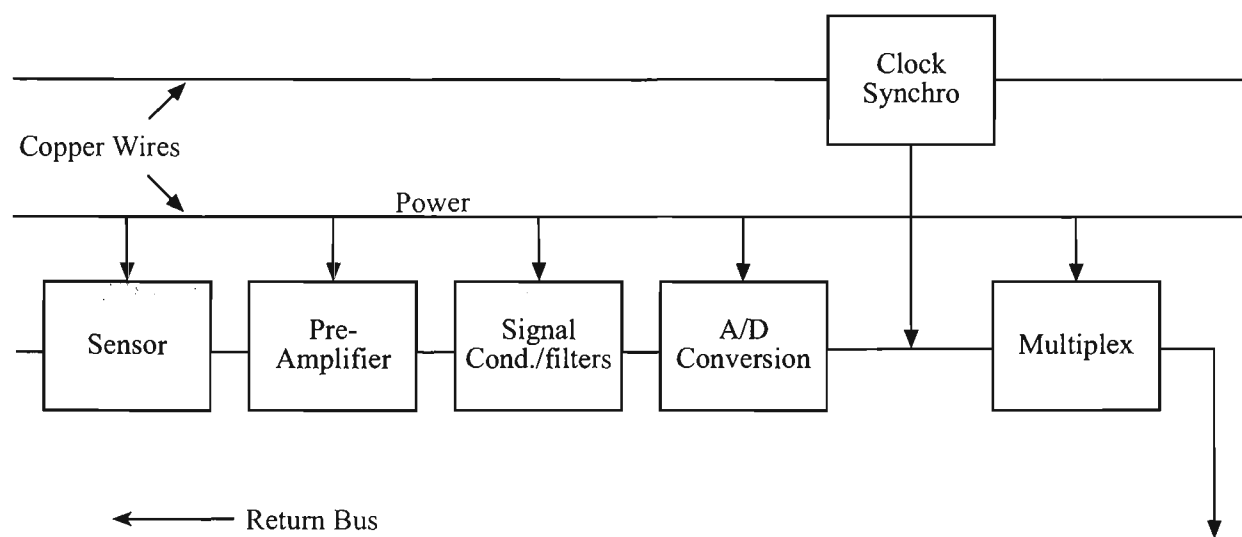


Figure 1.1: Sensing system based on conventional electrical transducer.

The very high bandwidth and multiplexing ability of optical fibres allows them to convey a large amount of measurand information through a single fibre (e.g. one fibre-optic strand can carry the information equivalent of 1000 copper wires). Fibre-optic sensors can function under adverse conditions of temperature and pressure. Toxic and corrosive atmospheres, that can erode metals, (i.e. normally used for conventional electrical based sensors) have little effect on optical fibres. In addition, fibre-optic sensors are intrinsically safe in explosive environments (i.e. produce no electrical sparks).

At this point in the evolution of optical sensing technology, one can measure nearly all of the physical measurands of interest. Examples of some of these are listed in Table 1.1. As a result of this diverse range of fibre-optic sensing schemes, some type of classification is required.

Table 1.1: Fibre-optic measurement techniques for various measurands. Note: Parameters and measurement techniques of interest in this work are shown in italics.

Parameter	Measurement Technique	Reference
<i>Temperature</i>	<i>Fluorescence</i>	[2–6]
	<i>Fibre Bragg Gratings</i>	[7–9]
	Interferometry	[10]
	Brillouin	[11]
Flow	Doppler	[12]
Humidity	Intensity	[13]
Pressure	Interferometry	[14, 15]
<i>Strain</i>	Brillouin	[16]
	Interferometry	[17]
	Intensity	[18]
	<i>Fibre Bragg Gratings</i>	[7, 8, 19]
	Polarisation	[20]
Vibration	Interferometry	[21]
Acoustic Emission	Fibre Bragg Gratings	[22]
Displacement	Interferometry	[23]

Optical sensors are generally based on either measuring an intensity change in one or more light beams or looking at phase changes in the light beams by causing them to interact or interfere with one another. Thus, these two types of sensors are termed either intensimetric sensors or interferometric sensors. Interferometric sensors present extremely high resolution and are insensitive to any fluctuations in the

illuminating source intensity because information is obtained by detecting the phase shift induced by the measurand. However, they require relatively complicated and expensive signal processing techniques to recover the phase information. Intensity-based sensors, on the other hand, are generally much simpler in construction, but can suffer from noise caused by random fluctuations on the optical power levels in the system. Also, intensimetric sensors generally exhibit lower levels of sensitivity and accuracy than interferometric sensors.

Recently, due to their versatility to being applied to a myriad of sensing applications, the fibre Bragg grating has been defined as the third category of fibre-optic sensing and is explained in a number of review articles [7, 8]. The fibre Bragg grating has become one of the most attractive types of fibre-optic sensors, particularly for embedded sensing of temperature and strain. The fibre Bragg grating will be discussed in greater detail in sections 2.3 and 3.2.

Further distinction is often made in the case of fibre sensors as to whether measurands act externally or internally to the fibre [1]. External or extrinsic sensors, are normally defined as those in which the light wave is guided by the fibre, but the interaction between the light and the measurement quantity takes place outside the fibre itself [24]. Internal or intrinsic sensors, are those where the optical fibre is the sensing medium itself [24].

Fibre optic sensors can also be designated as ‘point’ sensors when the sensing gauge is localised to discrete regions. If the sensor is capable of sensing a measurand field continuously over its entire length, it is known as a “distributed” sensor; with the most popular of these utilising Raman [25] and Brillouin scattering [11, 26–28]. ‘Quasi-distributed’ sensors adopt point sensors at various locations along the fibre length. Recently, fibre Bragg gratings have been used in this type of scheme for temperature sensing for clinical hyperthermia [29].

Optical fibre, by nature, is very resilient, a trait that enables it to perform reliably

under extreme conditions, such as very high temperatures. Optical fibre is limited to temperatures $<1200^{\circ}\text{C}$, where the glass matrix is altered, affecting parameters such as mechanical strength and guiding properties. To date, no fibre Bragg grating based optical fibre system exists on the market that is capable of measuring temperature over a wide operating range (e.g. from room temperature to $>300^{\circ}\text{C}$).

Although it appears that optical fibre sensors have numerous advantages over traditional sensing methods, in general, they have yet to achieve wide industrial acceptance for various reasons including high cost, complexity or measurand cross-sensitivity [8,24,30–32] and lack of market education of the technology. An example of this is the current problems associated with temperature cross-sensitivity in FBG strain sensors. The majority of commercial manufacturers of these sensors limit the operating temperature range to minimise this effect with some completely failing to address the problem.

Currently, one of the fields of interest is that of simultaneous temperature and strain measurement using fibre-optic sensors. Over the past decade, fibre optic temperature and strain sensors have been combined to try and address the problems associated with measurand cross-sensitivity. Numerous techniques have been successfully proven (described in greater detail in Section 2.4) but have not been commercially developed, possibly due to many factors, such as, financial feasibility, sensor complexity and integration into existing systems, to name a few. Fluorescence based temperature sensors, such as the fluorescence lifetime technique have shown potential in being integrated with FBGs [33,34] as a ‘low cost’ alternative for simultaneous temperature and strain sensing. The fluorescence lifetime temperature sensor will be described in Section 2.1. An alternative technique that shows more promise to the fluorescence lifetime, to some extent, is the fluorescence intensity ratio [35], and is described in greater detail in section 2.2. The integration of the fluorescence intensity ratio technique with fibre Bragg gratings is investigated as a simultaneous temperature and strain sensor and forms the basis of this work.

1.3 Scope of Thesis

The ability to accurately determine temperature and strain simultaneously continues to be an area of great interest. Many fibre-optic schemes have been developed and proven but at the expense of sensor complexity, complicated fabrication techniques and costly interrogation methods. There is clearly a requirement to simplify a simultaneous temperature and strain sensing scheme, which would ultimately lead to a sensor system that is reduced in size, weight, cost and fully utilise the advantages of fibre-optic based temperature and strain sensor systems. Also, many of these fibre-optic sensor schemes, particularly those incorporating fibre Bragg gratings, are limited in application due to their failure to operate at elevated temperatures for prolonged periods of time. Thus a simplified sensing scheme that can make co-located measurements of temperature and strain simultaneously over a wide dynamic temperature range is sought.

Previous techniques have used mainly two independent sensors, that are not co-located, to determine temperature and strain simultaneously. This is undesirable, particularly if there are large measurand fluctuations between the two sensors. Also, some of these techniques use a combination of two fibre Bragg gratings with slightly varying temperature and strain coefficients [36–38]. Such sensor characteristics could degrade the accuracy during the de-convolution process of the measured parameters. Therefore, in addressing such a criteria, a sensing system that comprises two co-located temperature and strain sensors, with different dependencies upon these parameters, is sought. To further this, a simplified scheme is pursued in this work by utilising the intrinsic properties of rare earth doped fibre fluorescence together with fibre Bragg gratings.

With the increasing popularity of fibre Bragg grating sensors over the past decade, and predictions of increased use in future years [39], a sensing system that incorporates fibre Bragg gratings is desired. The advantages provided by fibre Bragg gratings and the fluorescence intensity ratio for sensing provides the motivation for

developing a simultaneous temperature and strain sensor based on these techniques. In this thesis, the temperature and strain characteristics of the fluorescence intensity ratio in erbium and erbium:ytterbium rare earth doped optical fibres and Bragg gratings inscribed within them are studied to assess the possibility of developing a co-located, simultaneous temperature and strain sensor.

This research is not concerned with novel methods of optoelectronic interrogation of a combined fluorescence intensity ratio and fibre Bragg grating simultaneous temperature and strain sensing scheme. Interrogation techniques for the fluorescence intensity ratio and Bragg wavelength have been previously reported and are detailed in Chapter 2. Rather, this research is concerned with fluorescence intensity ratio and fibre Bragg grating properties in rare-earth doped optical fibre and whether the combination of these two sensing techniques could be integrated successfully for simultaneous temperature and strain sensing.

This thesis is divided into 8 chapters. Chapter 2 provides a review of fibre-optic sensing technologies and their applications to temperature and strain sensing. It examines the present state of the technology and current problems, in particular those associated with temperature and strain cross-sensitivity, which is of major concern with the ever increasing popularity of the fibre Bragg grating as a sensing element.

Chapter 3 investigates the characteristics of the fluorescence from erbium and erbium:ytterbium doped fibre, particularly the fluorescence transitions used for the fluorescence intensity ratio and amplified spontaneous emission for fibre Bragg grating interrogation. The different types of fibre Bragg gratings are reviewed together with the different effects fibre composition has on the characteristics of the fibre Bragg grating (e.g. photosensitivity and high temperature sustainability). This is performed in order to try and determine the optimum fibre composition for fibre Bragg grating fabrication and consequently, temperature and strain sensing. The techniques used to fabricate various rare earth doped fibres and fibre Bragg gratings for this work are discussed.

Chapter 4 investigates three mathematical methods for the simultaneous deconvolution of temperature and strain. The conventional matrix inversion method used for a pair of sensors which assume linear dependencies on a pair of measurands, such as temperature and strain, is examined. Another mathematical technique, that utilises the strain independence of the fluorescence intensity ratio, is also described. Finally, a mathematical method that is an extension of the previous technique, which examines the non-linear temperature dependence of the Bragg wavelength is proposed. Also included in this chapter is a detailed examination of three analysis techniques that have been developed by the author and used in this thesis to determine the Bragg wavelength from a fibre Bragg grating spectrum. These are denoted as the Minima, Half-Maximum and Weighted Average methods.

Chapter 5 characterises erbium doped fibre combined with fibre Bragg gratings for simultaneous temperature and strain measurement. Initially, investigations are made into the effects of pump power and wavelength, and doped fibre length on the fluorescence properties of the fibres used. Calibrations to temperature and strain are performed on five sensors fabricated in various configurations using three types of erbium doped fibres. Also, investigations of an erbium:tin doped fibre combined with a fibre Bragg grating for simultaneous temperature and strain sensing at high temperatures are presented. Their performance is analysed and compared using the mathematical analysis techniques documented in Chapter 4.

Chapter 6 characterises erbium:ytterbium doped fibre combined with fibre Bragg gratings for simultaneous temperature and strain sensing. Initially, investigations are made into the effect of pump power and wavelength, and doped fibre length on the fluorescence properties of the fibres used. Calibrations of temperature and strain are performed on five sensors fabricated in two different configurations using three types of erbium:ytterbium doped fibres. Their performance is analysed and compared using the mathematical analysis techniques documented in Chapter 4.

Chapter 7 describes the high temperature characteristics of fibre Bragg gratings. A new type of grating, commonly referred to as a chemical composition grating, is developed in erbium doped fibre for the first time. The annealing and fabrication processes for these gratings are investigated. Also, their temperature dependence and sustainability up to temperatures of 800 °C are examined.

Chapter 8 provides a summary of the key outcomes of this thesis. Suggestions are detailed for further work on simultaneous temperature and strain measurement using the fluorescence intensity ratio combined with fibre Bragg gratings. Also, comments on further research is required to improve the understanding of the formation of chemical composition gratings are provided.

Chapter 2

FIBRE-OPTIC TEMPERATURE AND STRAIN SENSORS

This chapter summarises fibre-optic sensors that can measure temperature and strain either separately or simultaneously. In particular, it details FBG and rare earth fluorescence based temperature and strain sensors along with their corresponding interrogation techniques. Finally, it provides an overview of applications for these sensors.

Spectrally based fibre-optic sensors depend on a light beam being modulated in wavelength by an environmental effect. Examples of these types of fibre sensors include those based on blackbody radiation, absorption, fluorescence, etalons and fibre Bragg gratings.

One of the simplest of these types of sensors is the blackbody sensor [40, 41]. A blackbody cavity is placed at the end of an optical fibre. When the cavity rises in temperature it starts to glow and act as a light source. Detectors in combination with narrow band filters are then used to determine the profile of the blackbody curve and in turn the temperature. This type of sensor has been commercialised successfully and has been used to measure temperature to within a few degrees Celsius under intense RF fields. However, a problem with this sensor scheme is that its performance and accuracy falls off at temperatures of the order of 200 °C and below because of a low signal to noise ratio. Also, care must be taken to ensure the hottest spot is the blackbody cavity and not on the optical fibre as this can corrupt the integrity of the signal.

Another type of spectrally based temperature sensor is based on absorption [42]. For example a gallium arsenide (GaAs) sensor probe may be used in combination with a broadband light source and input/output optical fibres. The absorption profile of the probe is temperature dependent and may be used to determine temperature.

Fluorescent-based fibre sensors are being used widely for medical applications and chemical sensing, and have also been used to measure such physical parameter measurements as temperature, viscosity and humidity. A number of configurations have been developed for these sensors. Fluorescence intensity ratio and fluorescence lifetime based temperature sensors are possibly two of the most extensively studied techniques due to the relatively simple construction of the sensor gauge. Generally during fabrication, an optical fibre is doped with a specific rare earth, which fluoresces when excited with the appropriate energy/photon. The fabrication of these fibres and measurement principles of these techniques are explained in detail in Chapter 3.

2.1 Fluorescence Lifetime Based Temperature Sensors

The fluorescence lifetime (FL) of an energy level from an element, such as a rare earth, is a measure of the rate of reduction in the intensity of fluorescence after the source of excitation has been removed. This decay rate has been shown to depend strongly upon temperature for energy levels of many materials and therefore, can be used to measure temperature.

Ytterbium FL temperature sensors have shown satisfactorily stable performance from room temperature up to 700 °C [43]. Accuracies of ± 5 °C over that temperature range have been demonstrated. It was also shown that pre-annealing at 700 °C is necessary to stabilize the FL temperature dependence, thus, minimizing any hys-

teresis in the sensing scheme to about 1.1 °C deviation [43].

FL based temperature sensors have also been demonstrated using erbium and thulium over wide temperature ranges. Erbium doped sensors have shown accuracies in the order of ± 5 °C over a temperature range of 1100 °C [44]. Thulium doped crystal fibre temperature sensors have shown comparable accuracy (± 6 °C) and at extended temperature ranges up to 1350 °C [3]. This extended temperature range is achievable due to the higher melting point of a single crystal fibre as opposed to silica based fibres. Again, pre-annealing appears necessary to stabilize the FL to minimize any hysteresis.

It has been shown that the FL technique does exhibit a strain dependence in a range of rare earth materials [45]. Neodymium doped fibre has shown to exhibit the smallest amount of cross-sensitivity (1.8 °C $\equiv 1000$ $\mu\epsilon$), while erbium and ytterbium doped fibres have a larger cross-sensitivity (4.0 °C $\equiv 1000$ $\mu\epsilon$) and (6.1 °C $\equiv 1000$ $\mu\epsilon$), respectively [45]. Recently, tests in praseodymium doped silica fibre found a cross-sensitivity comparable to those described above (2.2 °C $\equiv 1000$ $\mu\epsilon$) [46]. The FL technique has still been applied to dual temperature and strain sensing on the assumption that the FL temperature and strain dependencies are linear [33, 34].

2.2 Fluorescence Intensity Ratio Based Temperature Sensors

The idea of measuring a ratio of intensities from two wavelength bands of fluorescence to determine temperature dates back to 1976 [47]. The temperature dependent material investigated was $Y_2O_2S:Eu$ and the measurement technique resulted in an uncertainty of 1 °C over a temperature range of -15 to 75 °C. Although problems such as poor sensitivity were encountered, the measuring technique showed potential for future improvements.

The first fluorescence intensity ratio (FIR) measurement from a rare earth originating from the ${}^2H_{11/2}$ and ${}^4S_{3/2}$ energy levels of erbium (Er^{3+}) doped in a fluoride glass [48]. The sensor demonstrated an accuracy of 2°C over a temperature range of 20 to 200°C . The main limitation of the sensor reported was a maximum operating temperature of approximately 250°C , due to the use of fluoride glass.

The FIR technique has been investigated using the energy levels from many rare earth ions doped into a wide variety of glass or crystal host materials [6]. Table 2.1 shows a detailed summary of various rare earths and hosts used for FIR temperature sensing. The contributing energy levels are also indicated. The temperature sensi-

Table 2.1: Temperature calibration details of rare earth ions used for FIR sensing [6].

Rare Earth (Host)	Energy Level Transition	Temperature Range ($^\circ\text{C}$)	Standard Deviation ($^\circ\text{C}$)
Pr^{3+} (ZBLANP)	${}^3P_0, {}^3P_1 + {}^1I_6 \rightarrow {}^3H_5$	20 \rightarrow 145	3.7
Pr^{3+} (ZBLANP)	${}^3P_0, {}^3P_1 + {}^1I_6 \rightarrow {}^1G_4$	20 \rightarrow 145	0.6
Pr^{3+} (silica)	${}^3P_0, {}^3P_1 + {}^1I_6 \rightarrow {}^1G_4$	22 \rightarrow 250	4.9
Pr^{3+} (aluminosilica)	${}^3P_0, {}^3P_1 + {}^1I_6 \rightarrow {}^1G_4$	$-140 \rightarrow 257$	14.5
Nd^{3+} (YAG)	${}^4F_{3/2}, {}^4F_{5/2} \rightarrow {}^4I_{9/2}$	26 \rightarrow 250	1.1
Nd^{3+} (YVO_4)	${}^4F_{3/2}, {}^4F_{5/2} \rightarrow {}^4I_{9/2}$	23 \rightarrow 260	2.9
Nd^{3+} (ZBLANP)	${}^4F_{3/2}, {}^4F_{5/2} \rightarrow {}^4I_{9/2}$	23 \rightarrow 200	4.4
Nd^{3+} (silica)	${}^4F_{3/2}, {}^4F_{5/2} \rightarrow {}^4I_{9/2}$	18 \rightarrow 500	2.2
Sm^{3+} (silica)	${}^4F_{3/2}, {}^4G_{5/2} \rightarrow {}^6H_{5/2}$	22 \rightarrow 475	3.8
Eu^{3+} (silica)	${}^5D_0, {}^5D_1 \rightarrow {}^7F_1$	220 \rightarrow 400	5.7
Dy^{3+} (silica)	${}^4F_{9/2}, {}^4I_{15/2} \rightarrow {}^6H_{13/2}$	22 \rightarrow 250	1.2
Er^{3+} (silica)	${}^4S_{3/2}, {}^2H_{11/2} \rightarrow {}^4I_{15/2}$	25 \rightarrow 560	4.4
Yb^{3+} (silica, a)	${}^2F_{5/2} \rightarrow {}^2F_{7/2}$	22 \rightarrow 500	3.1
Yb^{3+} (silica, b)	${}^2F_{5/2} \rightarrow {}^2F_{7/2}$	24 \rightarrow 160	1.5

tivity of the FIR has been shown to be dependent on numerous intrinsic properties of the rare earth dopant used, such as dopant type and concentration, intensity

level and host composition [6], and is partially summarised in Table 2.1. There are other reports of the FIR scheme, in specific samples, as potential temperature sensors [4, 49–52].

Upconversion green fluorescence from erbium has been used by numerous groups for temperature sensing. Accuracies of $0.3\text{ }^{\circ}\text{C}$ over a temperature range of $20\text{--}200\text{ }^{\circ}\text{C}$ have been demonstrated using fluorescence generated in Er^{3+} and $\text{Er}^{3+}\text{-Yb}^{3+}$ doped chalcogenide glass [50]. Although this scheme used bulk glass samples, this sensor operated on an excitation source power as low as 2 mW . Another similar scheme using Er^{3+} -doped bulk fluoride glass was examined over a temperature range of $23\text{--}175\text{ }^{\circ}\text{C}$ [53]. Maciel *et al.* believes this scheme is capable of achieving accuracies of $< \pm 1\text{ }^{\circ}\text{C}$ with an appropriate detection scheme. These schemes have significant disadvantages due to the use of bulk samples of glass other than silica making them difficult to integrate into existing fibre optic sensing systems and networks.

Recently, the upconversion green fluorescence scheme from erbium has been developed into a point sensor in an Er^{3+} doped silica-on-silicon waveguide [54]. The sensor was tested over a temperature range of $20\text{--}140\text{ }^{\circ}\text{C}$ and demonstrated an accuracy of $< \pm 2\text{ }^{\circ}\text{C}$. The sensor system showed reasonable sensitivities with pump powers as low as 7 mW . Although this system showed promising results, like other systems, it wouldn't be suited to many applications due to its extrinsic nature (e.g. not a complete optical fibre sensing system).

Er^{3+} doped silica fibres show more promise than fluoride fibres for integrated temperature sensors [6, 55]. A silica host allows a relatively wide temperature range to be measured with temperatures up to $640\text{ }^{\circ}\text{C}$ being reported [55]. The main drawback of this host, however, is a relatively low fluorescence intensity. Therefore, this needs to be considered during the investigation of this sensing scheme.

Although there has been extensive work in characterising the FIR scheme for temperature sensing, there still appear to be deficiencies in achieving optimum efficiencies.

Further work is required on the strain effects if this scheme is to be integrated as a simultaneous temperature and strain sensor. It has been suggested that the FIR technique in Nd^{3+} and Yb^{3+} is virtually independent of applied strain [6] but further work is required to verify this in other rare earths and host materials. Also, minimal analysis has been performed of the annealing effects on the FIR. To date, only one publication has shown annealing effects on the FIR [56]. It has been shown that annealing the sensor sample at temperatures of 750°C improves the standard deviation of the FIR, but has only a small effect ($\sim 0.6\%$) on the hysteresis of the technique [56]. This is roughly an order of magnitude less than that measured using the FL technique. It must also be noted that the temperature sensitivity of the FL has been shown to be low at low temperatures, whereas the FIR maintains reasonable sensitivity [35]. The FIR technique is investigated in greater detail in Section 3.1.4. The work in this thesis builds upon existing knowledge of Er^{3+} and Yb^{3+} FIR temperature schemes [57] and applies this to simultaneous temperature and strain sensing.

2.2.1 FIR Detection Methods

Numerous techniques have been previously adopted for the measurement of the FIR [4, 54, 58]. The most common laboratory based method involves the use of an optical spectrum analyser (OSA) to record the fluorescence spectra which is then analysed using a PC. This method was adopted here and is explained in more detail in both Chapters 5 and 6. In a commercially feasible situation, a simpler detection scheme needs to be developed that doesn't involve the use of complicated and expensive equipment, such as an OSA. Such methods have been successfully demonstrated [4, 58] and are shown in Figure 2.1. Key components that comprise these detection methods are appropriate optical filters, dichroic mirrors and photo-detectors. In the future, other FIR detection techniques may become feasible, such as MEMS technology and the use of diffraction gratings in conjunction with CCD arrays that are capable of resolving fluorescence from rare earth ions.

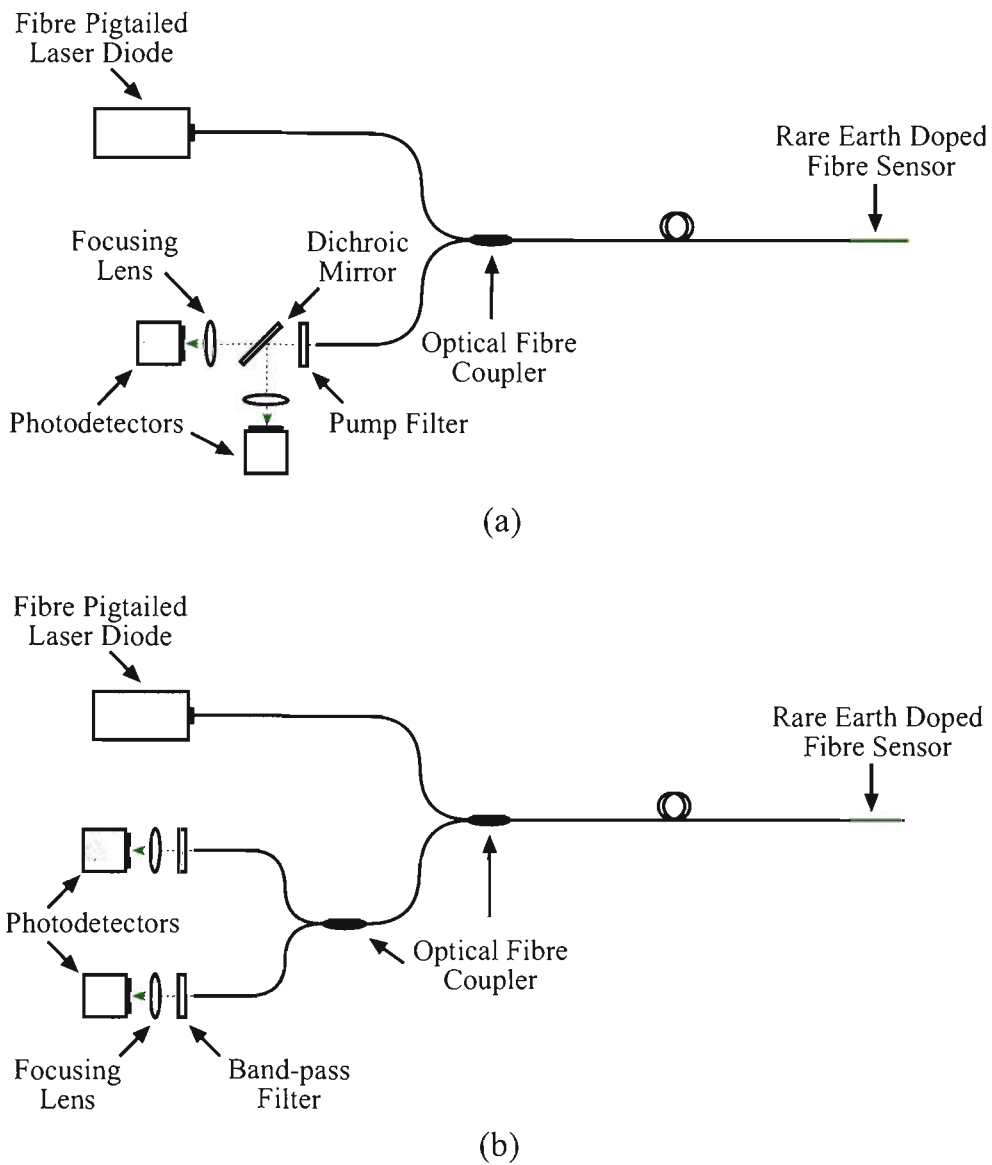


Figure 2.1: (a) and (b) FIR detection schemes previously used [59].

2.3 Fibre Bragg Grating Sensors

A major development occurred in 1989 when a simple technique for producing fibre Bragg gratings within optical fibres was invented [60]. Their potential was realised in the communications industry as dense-wavelength-division-multiplexing (DWDM) components, but soon interest was generated in the sensing field. They became attractive fibre-optic components for sensing mainly because of their compact, intrinsic properties and wavelength-encoding capabilities.

Fibre Bragg gratings (FBGs) are spectral filters fabricated within segments of optical fibre. They typically reflect light over a narrow wavelength range and transmit

all other wavelengths, but they can also be designed to have more complex spectral responses [61]. FBGs are based on the principle of Bragg reflection. When light propagates through periodically alternating regions of higher and lower refractive index, it is partially reflected at each interface between those regions. If the spacing between those regions is such that all the partial reflections add up in phase, when the round trip of the light between two reflections is an integral number of wavelengths, the total reflection can grow to nearly 100%, even if the individual reflections are very small. This condition will only hold for specific wavelengths. For all other wavelengths, the out-of-phase reflections end up cancelling each other, resulting in high transmission. The wavelength at which this occurs is known as the Bragg wavelength and is given by the following equation:

$$\lambda_B = 2n\Lambda, \quad (2.1)$$

where n is the effective refractive index of the fibre core and Λ is the periodicity of the refractive index variations. The FBG requirements as sensing gauges are different compared to those of telecommunications, such as add-drop filters. The main difference is that a large Δn (translating to a Bragg reflection >99%) isn't required for sensing FBGs.

Another type of fibre grating is a long period fibre grating (LPFG) [8, 61]. In single mode fibres, a LPFG couples the fundamental HE_{11} core mode and multiple forward-propagating HE_{1m} cladding modes. Therefore, they have a higher sensitivity to external perturbations compared to FBGs. One drawback of LPFGs, is the relatively large rejection bandwidth, which may reduce the resolution of measurement.

When the FBGs are applied as sensors, the measurands can be temperature, strain, pressure, magnetic fields, and others [7, 8, 62, 63]. Of these measurands, FBGs are being most extensively developed as strain and temperature sensors [7, 8]. The wavelength encoding offers high accuracies and multiplexing capabilities, and makes the

sensor immune to optical power fluctuations. The multiplexing ability of FBGs has allowed the development of quasi-distributed sensor systems. These systems have the advantage of superior spatial resolution compared to fully distributed Raman or Brillouin sensor systems. A simplified example of a quasi-distributed FBG sensing system is shown in Figure 2.2. Commercially available systems from Smartec, Micron Optics and Burleigh are capable of simultaneously monitoring up to 512 FBG sensors (Micron Optics) [64]. These sensor arrays are limited by the bandwidth of the illuminating source, resolving power of the interrogation system and the dynamic ranges of each individual FBG sensor. An intrinsic measurement problem

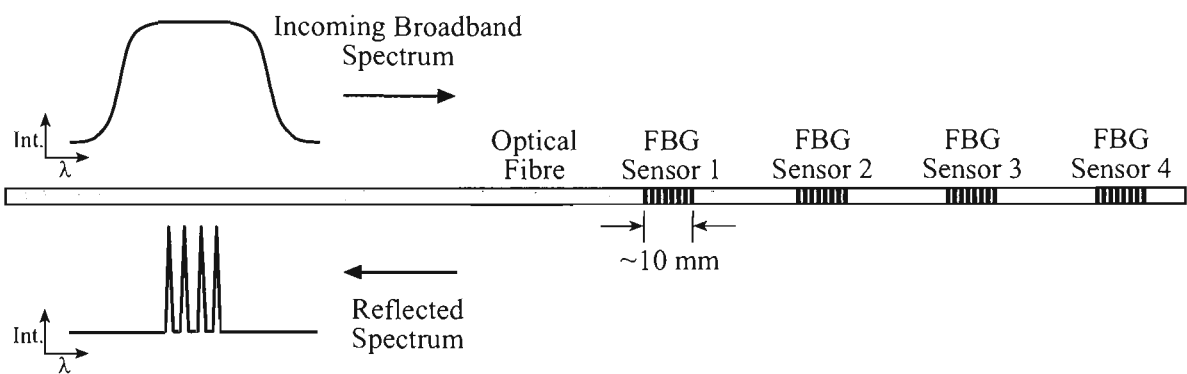


Figure 2.2: Quasi-distributed sensing system based on fibre Bragg gratings.

with FBGs is that the Bragg wavelength is affected by strain and temperature. The elimination or compensation of this strain-temperature cross sensitivity is of great importance.

One method of measuring temperature and strain accurately is to put two fibre Bragg gratings in close proximity to one another [65]. The FBG attached to the material on which strain is to be measured will be influenced by both temperature and strain, while the other, nearby but not attached to the material, is subject to temperature only. Another method is to use fibre Bragg gratings in combination with another fibre sensor that measures only temperature [66]. The main issue associated with both of these approaches is that the temperature at the position of the strain sensor may be substantially different to that at the position of the tempera-

ture sensor. This would result in an inaccurate interpretation of the actual strain being applied on the strain sensor.

2.3.1 High Temperature FBG Sensing

One of the current limitations of FBGs used as temperature sensors or, to some extent, strain sensors, is their relatively short operational life when exposed for prolonged periods of time at elevated temperatures (generally above $>300^{\circ}\text{C}$). FBGs tend to become erased above these temperatures. Recently, a range of specialty optical fibres has been fabricated along with various FBG writing techniques to overcome this problem, with some showing reasonable performance up to 800°C [67–72]. To date, no commercially available FBG based temperature sensor exists for high temperature applications above 400°C . This could pose a limitation in applications where FBG sensing networks were utilised. The problem of high temperature sustainability of FBGs will be discussed in Chapter 7.

2.3.2 Bragg Wavelength Interrogation Schemes

Due to the increasing popularity and diverse range of applications of FBGs, numerous interrogation techniques have been developed [73–78]. There are two fundamental approaches to monitoring the change in Bragg wavelength. In the first technique, the fibre Bragg grating is illuminated with a broadband light source, and the reflected or transmitted wavelength is monitored with an optical spectrum analyser (OSA). In the second technique, a narrowband tunable laser is swept across the appropriate spectral region, and a reflected signal is observed with a broadband detector only when the laser is tuned precisely to the sensor's Bragg wavelength.

The first technique of determining the precise Bragg wavelength is to use a broadband source with a Michelson interferometer based OSA. This method does provide accurate measurements of the reflected wavelengths. This technique is most important in monitoring applications where reliable sensor measurements must be made over a long period under varying environmental conditions without re-calibrating the

instrument. Michelson interferometry has been used for many years in wavelength meters to determine accurately the wavelength of laser sources. It has also been applied and commercialised by Micron Optics and Exfo Burleigh Products Group Inc. as an OSA for Bragg wavelength interrogation [79]. Advantages of this type of OSA over other types of wavelength discrimination is its absolute wavelength accuracy and reliable repeatability under all conditions. The main limitation of this, and other comparable OSAs (e.g. diffraction grating and Fabry-Perot based) is their limited wavelength resolution and tuning range.

Figure 2.3 shows an OSA based on Michelson interferometry. An incident beam is

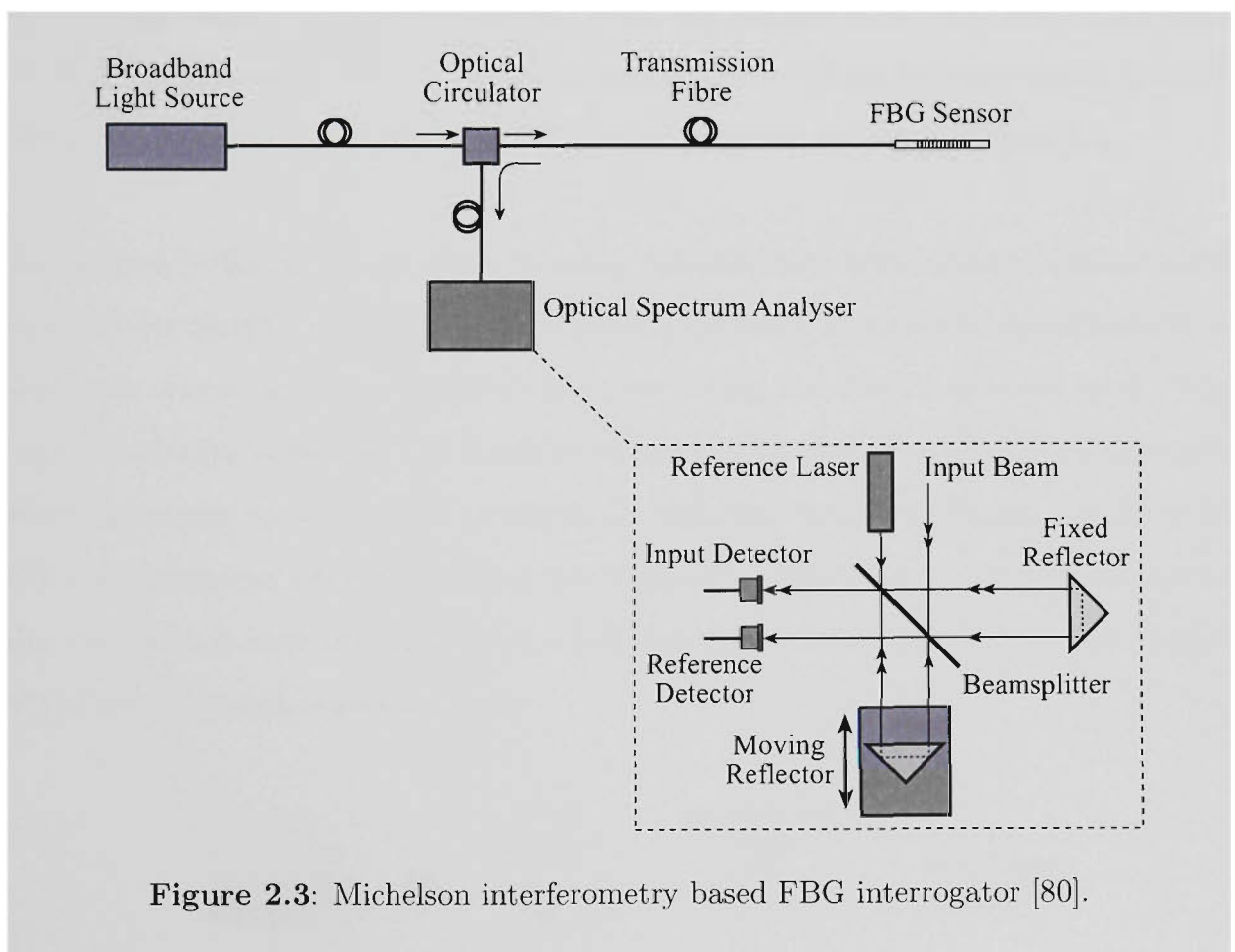


Figure 2.3: Michelson interferometry based FBG interrogator [80].

split between a fixed path and a path that can be changed by a moving end reflector. The end reflectors in both paths are corner-cube retroreflectors that displace the returned beams. Beams of a single wavelength recombined at the beamsplitter produce a sinusoidal intensity variation at the detector as the moving reflector changes the optical path difference.

The advantage of the displaced paths in this Michelson interferometer is that a second beam from a reference laser with a known wavelength can be introduced along exactly the same path in the opposite direction, so that its fringe signal is picked up by a separate detector. This reference signal is used to calibrate accurately the scan of the interferometer and to determine the absolute wavelengths in the spectrum of input light.

This system requires a broadband light source to illuminate the FBG sensor. A commonly preferred choice is an ASE source that has high output power and that can provide sufficient reflected signal, even for sensors with very low reflectivity (<10%). ASE sources can have a broad spectrum (>100 nm in some cases) to allow illumination of many sensors in one fibre optic line, as shown in Figure 2.2.

The second technique is achieved by using tunable laser technology combined with absolute wavelength referencing. The method works by sweeping a narrowband tunable laser source over the spectral range, including the FBG's spectral peak. The laser wavelength measurement module records the wavelength of the scanning laser, while the power meter records a peak in the reflected intensity. Figure 2.4 shows an FBG interrogation system based on the tunable laser technique. One advantage to this approach is that the laser choices are abundant as a result of the rapid growth of the telecommunications industry.

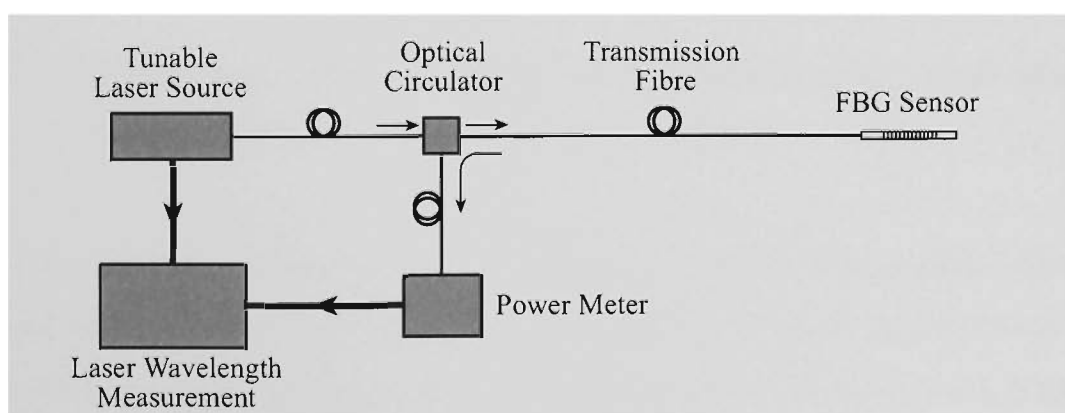


Figure 2.4: Tunable laser based FBG interrogator [81].

Fast-sweeping test-and-measurement lasers have been developed, and widely tunable telecom transmission lasers are commercially available. Any of these devices are adequate, although to satisfy the stability requirements, control architectures must be considered for each configuration. Tuning speed and characteristics, the maturity and ruggedness of the technology, the supply chain and output power all factor into a design choice. Some of the most popular tunable laser sources available are DFB lasers, multisection distributed Bragg reflector (DBR) lasers, external cavity (EC) lasers and optically pumped vertical cavity surface emitting lasers (VCSELs) with MEMS structures for tuning. Table 2.2 summarises the important parameters that need to be considered when adopting the swept laser scheme for FBG interrogation.

Temperature-tuned DFB lasers are readily available devices (Mitsubishi, Agere) [82]. Their lasing wavelength changes continuously with temperature at a rate of 0.1 nm/°C. So to tune over only 4 nm, the operating temperature should be changed by

Table 2.2: Tunable laser sources for FBG interrogation.

Laser Source	Power (mW)	Tuning Range (nm)	Tuning Speed
DFB	10	4	1 s
DBR	1	40	20 ns
EC	10	>40	0.1 s
VCSEL	0.5	20	100 μ s

40°C. Despite their high power, simplicity, and manufacturability, their slow tunability and narrow tunable range limit their applications.

Multisection DBR lasers are fibre pigtailed lasers (available from Agility) that provide broad tuning [82]. Rather than being continuously tunable, they are switchable devices. They were developed for dense-wavelength-division multiplexed (DWDM) telecommunications systems. Despite having the fastest tuning speed, very complicated processing technology makes their manufacture difficult and elaborate controls

complicate their electronics.

External cavity lasers are commercially available from such vendors as Iolon and NewFocus [82]. The output of the semiconductor laser chip is coupled optically to an external diffractive grating and tuned by rotating an external mirror. They have high power (1-10 mW) and continuous tuning over a >40 nm range, but have a fairly slow tuning speed (~ 0.1 s). They are quite complicated to manufacture because of their complex optical scheme and hybrid packaging.

MEMS-based continuously tunable electrically pumped VCSELs are commercially available from Bandwidth9 [82]. Tunable MEMS VCSELs, emitting in the $1.55 \mu\text{m}$ wavelength region, are very appealing laser sources for low-cost sensor systems because of their capacity to be tested at the wafer level, low threshold currents and low power consumption, and high manufacturability. For MEMS-based tunable VCSELs, wavelength tuning is continuous and controlled simply by a voltage applied to the MEMS structure. In contrast to other tunable lasers such as multisection DBR lasers, emission wavelength control over time implies only a closed loop on the voltage to compensate for any aging effects. This simplicity of tuning lends itself to very good operability in a real sensor configuration.

In summary, it can be seen that a range of techniques have been proven in the interrogation of FBGs for sensing applications. Many of these have reached a maturity level in which they have been implemented into commercial systems. Ultimately, the end users final decision as to which technique they wish to adopt depends on the targeted application for the sensor system. Two simple examples are highlighted below:

- Impact stress analysis requires high sampling speed ($>$ a few kHz) over short periods of time.
- Long-term health monitoring of a civil structure generally requires slow sampling speed ($<$ 100 Hz) but may require higher optical power and bandwidth

for interrogation of a large array of FBG sensors (e.g. 128) over long fibre lengths (e.g. a few km).

Despite all this commercial interest in FBGs and their interrogation systems, the temperature and strain cross-sensitivity must still be considered.

2.4 Simultaneous Temperature and Strain Measurement

The accurate and reliable simultaneous measurement of both temperature and strain is of much interest for numerous applications where large fluctuations of both measurands are present, such as civil infrastructure, aerospace, power and process control, to name a few. Improved measurement of these parameters is important so that these and related industries will benefit, in terms of improved safety and reliability. Furthermore, a multi-functional sensor that can measure multiple parameters offers significant economic advantages, compactness and end user appeal. Numerous simultaneous temperature and strain measurement techniques have been developed for both distributed and point sensing.

2.4.1 Fully Distributed Sensing

Simultaneous distributed measurement of temperature and strain is a development of the distributed temperature sensors that are currently based on the Brillouin technique. Distributed temperature sensors have been applied to numerous applications with the most popular being in the monitoring of high voltage transmission lines and in oil or gas wells. In some cases strain information is required. Therefore, numerous groups have developed simultaneous measurement systems, mainly based on spontaneous Brillouin backscatter [27, 28, 83]. A brief summary of some of these sensors is provided in Table 2.3.

A distributed simultaneous temperature and strain sensor has been demonstrated using the Landau-Placzek ratio and Mach-Zehnder interferometry to measure Brillouin

Table 2.3: Summary of fibre-optic distributed temperature and strain sensors, listed in chronological order (most recent first).

RMS Errors		Range	Technique	Reference
Temp ($^{\circ}\text{C}$)	Strain ($\mu\epsilon$)			
5	60	30-50 $^{\circ}\text{C}$ 107-960 $\mu\epsilon$	Brillouin Frequency Shift	[16]
4	100	22-60 $^{\circ}\text{C}$ 730-4240 $\mu\epsilon$	Spontaneous Brillouin Backscatter	[28]
4	290	23-53 $^{\circ}\text{C}$ 0-6500 $\mu\epsilon$	Spontaneous Brillouin Backscatter	[27]
1.6	32	10-60 $^{\circ}\text{C}$ 178-1245 $\mu\epsilon$	Spontaneous Brillouin Scattering	[83]
1.5	20	10-60 $^{\circ}\text{C}$ 500-4000 $\mu\epsilon$	Stimulated Brillouin Scattering and FBGs	[84]
4	100	3-70 $^{\circ}\text{C}$ 0-5350 $\mu\epsilon$	Noise-initiated Brillouin Scattering	[85]

loun backscattered signal [27]. The system was capable of measuring temperature and strain over a length of 15 km with a spatial resolution of 20 m. Later work by another group [28] showed improvement on this technique by increasing the sensing length to 30 km and improving the strain accuracy (see Table 2.3). When comparing the accuracies of the sensors shown in Table 2.3 to those of point type (see Table 2.4) it is evident that their performance in terms of RMS error is inferior.

For specific sensing applications that require sensing over large areas without a requirement for high spatial resolution, this type of sensor would be advantageous over other methods. It must be noted that these sensing systems are highly complex and costly compared to most point and FBG based quasi-distributed sensing systems. This is due mainly to the sophisticated interrogation equipment that these sensor systems require.

2.4.2 Point Sensing

For applications where localised temperature and strain information (of the order of ~ 10 cm) is required, distributed sensing doesn't provide sufficient spatial resolution. FBG-based point sensors are in widespread use but the temperature/strain cross-sensitivity is still an issue. In many instances the temperature/strain cross-sensitivity is addressed by the use of a pair of FBGs located in close proximity, one of which is engineered to be unaffected by strain [65]. However, in this arrangement the two sensors are not co-located. To address this issue, alternative techniques have been investigated and are summarised in Table 2.4. In general, these techniques have involved the combination of two different sensing methods with the most popular being a combination of:

- Rare earth doped fibre (REDF) fluorescence lifetime or intensity with a single FBG.
- Fabry-Perot interferometric sensor in close proximity to a FBG.
- Combination of two different types of FBGs (e.g. Type I and II) in close proximity.
- Amplified spontaneous emission from a rare earth doped fibre with a single FBG.

A fibre-optic sensor scheme utilising a single FBG written in Er:Yb doped fibre has shown reasonable performance (as shown in Table 2.4) as a 'low-cost' scheme where high resolution isn't required [86]. The sensor comprised of a 8 mm-long FBG written into a 25 cm length of Er:Yb doped fibre. The scheme used the temperature dependence of amplified spontaneous emission (ASE) from the doped fibre to measure strain and temperature. The ASE was also used to interrogate the FBG, therefore, making use of a single pump source to 'illuminate' two sensors. This scheme, however, is susceptible to pump power and wavelength fluctuations and it requires sensor lengths that are too long for the scheme to be considered a point sensor.

Another technique able to measure temperature and strain simultaneously with reasonable accuracies is by utilising a pair of LPFGs [87]. Two LPFGs were fabricated with one having suppressed and the other enhanced temperature sensitivities. This was achieved by modifying particular host composition elements (B_2O_3 and GeO_2) in the core and cladding of the optical fibre. By suppressing the temperature sensitivity of one LPFG, strain information can be deduced and used to de-convolve the temperature information from the other LPFG. This technique has limitations, such as the requirement of specialty fibre and measurements that aren't co-located.

Fabry-Perot interferometric (FPI) sensors have also been combined with FBGs for successful measurement of temperature and strain [62]. An FBG, used as a temperature sensor, was arranged in close proximity to an extrinsic FPI sensor, which was mounted onto a composite surface that required strain monitoring. Although the sensor scheme showed reasonable accuracies (as shown in Table 2.4) and fabrication was simple, some limitations still exist, such as the intrinsic/extrinsic nature of the two sensors which were not co-located.

The fluorescence lifetime from the $^4I_{13/2}$ level in erbium has been used in conjunction with an FBG to measure temperature and strain [33]. A significant advantage of this sensor scheme compared to others previously reported is that by inscribing the FBG into the rare earth doped fibre, two independent sensors effectively become co-located. The technique produced comparable accuracies to previously reported sensor schemes while using sensor lengths (~ 12 cm). Limitations that may inhibit this scheme in a practical application is the integration of the two very different sensing techniques. The FBG requires an interrogating technique, like those mentioned previously in Section 2.3.2 while the FL technique requires a pulsed pump source together with a fast response photodetector. This could potentially increase the cost significantly of the the sensor system.

Another promising technique utilises the different temperature sensitivities of type IA and type IIA FBGs for simultaneous temperature and strain sensing [36,38]. The

sensor comprised of a pair of type IA and IIA FBGs fabricated in close-proximity (within a few centimetres) along a single optical fibre. The authors claim this scheme is simplified since the strain coefficients of the type IA and type IIA FBGs were virtually identical, therefore, reducing the signal processing required for de-convolving the temperature and strain information.

Most of the FBG-based simultaneous temperature and strain sensing techniques reported to date require the fabrication of two different types of FBGs written at slightly different wavelengths. These approaches have the drawback of an expensive waste of bandwidth and increased transducer size. Transducer size has been reduced by superimposing two gratings for temperature and strain sensing but a two step writing process is required [88]. A single FBG has been used for simultaneous temperature and strain sensing by utilising the first- and second-order diffraction wavelengths of a FBG [89]. The scheme is capable of measuring strain and temperature simultaneously due to the different sensitivities at the two very different wavelengths. Inherent problems that could limit the development of this scheme in a practical situation is the requirement for two separate FBG illumination sources at wavelengths corresponding to the first- and second-order diffraction wavelengths (e.g. 1536 and 768 nm).

Interferometric interrogation of an FBG written in highly birefringent fibre has enabled the simultaneous measurement of temperature and strain [90]. This is achieved by independent measurement of the shift in the wavelengths of the reflected light from the grating components along the fast and slow axes of the highly birefringent fibre. The scheme showed good results and a relatively simple sensor construction, though, limitations may exist in the sampling speeds the system would be capable of measuring. Also, highly birefringent fibres are very sensitive to transverse strain, which could induce large errors in the deconvolution of temperature and strain.

Multi-axis FBG-based sensors have been utilised for simultaneous measurement of transverse strain in multiple directions, axial strain and temperature [19]. Dis-

tinguishing the transverse strain from two directions is achieved by independent measurement of the shift in the wavelengths of the reflected light from the grating components along the fast and slow axes of birefringent fibre.

It can be seen from the above discussion that numerous techniques have been developed for simultaneous temperature and strain sensing, each with its own unique advantages and limitations. Other techniques have also been demonstrated successfully and their RMS temperature and strain errors over specific ranges have been summarised in Table 2.4. It is evident from the majority of previous work that there is an upper limit on the temperature range at which these schemes can operate, particularly those utilising FBGs. This would limit the schemes to being applied to low temperature (<200 °C) applications.

In general, not one sensing scheme is suitable for all applications. Therefore, the end user needs to have clearly defined specifications so that they are able to make a professional decision as to which sensor type would be best suited for their application.

Table 2.4: Chronological summary (most recent first) of fibre-optic simultaneous temperature and strain point sensors and their performance.

RMS Error		Range	Technique	Reference
Temp. ($^{\circ}\text{C}$)	Strain ($\mu\epsilon$)			
0.3	4.9	20-150 $^{\circ}\text{C}$ 350-1460 $\mu\epsilon$	FBG and FIR from REDF	[91]
0.7	15.6	35-90 $^{\circ}\text{C}$ 0-1200 $\mu\epsilon$	Long Period FBG	[92]
2.8	36	20-600 $^{\circ}\text{C}$ 0-2000 $\mu\epsilon$	FBG and REDF Fluorescence	[93]
5.6	50	25-300 $^{\circ}\text{C}$ 0-500 $\mu\epsilon$	Two FBGs (Type IA and Type IIA)	[36]
2	14	-50-80 $^{\circ}\text{C}$ 0-1400 $\mu\epsilon$	Two FBGs in High- Birefringent Fibre	[94]
1	22.9	18-150 $^{\circ}\text{C}$ 350-2534 $\mu\epsilon$	FBG and FIR from REDF	[95]
1	30	20-220 $^{\circ}\text{C}$ -520-0 $\mu\epsilon$	FBG and Extrinsic FP Interferometry	[66]
6	36	22-500 $^{\circ}\text{C}$ 0-1150 $\mu\epsilon$	FBG and REDF Fluorescence	[96]
0.7	8.3	22-140 $^{\circ}\text{C}$ 0-8300 $\mu\epsilon$	Two Long-Period FBGs	[97]
1.5	8.49	20-500 $^{\circ}\text{C}$ 0-1200 $\mu\epsilon$	Two FBGs (Type IA and Type IIA)	[37]
1	20	40-70 $^{\circ}\text{C}$ 200-1500 $\mu\epsilon$	FBG and Extrinsic FP Interferometry	[62]
0.8	7	30-120 $^{\circ}\text{C}$ 220-1330 $\mu\epsilon$	FBG and FL from REDF	[33]
0.54/pm	4.4/pm	0-80 $^{\circ}\text{C}$ 0-2000 $\mu\epsilon$	Two FBGs (Type IA and Type IIA)	[38]

continued on next page

continued on from previous page

RMS Error		Range	Technique	Reference
Temp. (°C)	Strain ($\mu\epsilon$)			
0.3	N/A	20-80 °C	Thermochromic	[98]
		0-6600 $\mu\epsilon$	Material and FBG	
1.56/pm	14.27/pm	0-100 °C	FBG First- and	[89]
		0-1800 $\mu\epsilon$	Second-Order Diffraction	
1.1	35.9	20-100 °C	FBG and Extrinsic FP	[99]
		0-2000 $\mu\epsilon$	Interferometry	
0.2	15	16-36 °C	Distributed-Feedback	[100]
		0-513 $\mu\epsilon$	FBG Laser	
1.3	23	-30-80 °C	Long Period FBGs	[87]
		0-3000 $\mu\epsilon$		
0.9	32	20-90 °C	REDF Fluorescence and	[101]
		0-1800 $\mu\epsilon$	FP Interferometry	
2.5	26	20-140 °C	Two FBGs in High-	[90]
		0-1000 $\mu\epsilon$	Birefringent Fibre	
3	55.8	50-180 °C	Amplified	[86]
		0-1100 $\mu\epsilon$	Spontaneous Emission	
1.2	20	20-120 °C	Superstructure FBG	[102]
		0-1200 $\mu\epsilon$		
0.4	30	20-60 °C	In-Line FBG-FP Cavity-	[103]
		0-3000 $\mu\epsilon$	FBG	
0.7	18.2	45-150 °C	Amplified	[104]
		0-1200 $\mu\epsilon$	Spontaneous Emission	
2.2	18.4	30-130 °C	FBGs in Ge and Boron-	[105]
		0-1000 $\mu\epsilon$	Codoped Ge Fibres	
0.04	3	15-45 °C	Dual Polarization DFB	[106]
		0-1299 $\mu\epsilon$	Fibre Laser	
0.7	40	20-60 °C	Low-Coherence	[107]

continued on next page

continued on from previous page

RMS Error		Range	Technique	Reference
Temp. (°C)	Strain ($\mu\epsilon$)			
		0-1600 $\mu\epsilon$	Interferometry	
1.72/pm	17.4/pm	35-56 °C	FBG First- and	[108]
		0-1800 $\mu\epsilon$	Second-Order Diffraction	
1	58	25-150 °C	Long Period FBG	[109]
		0-2100 $\mu\epsilon$		
1	17	20-140 °C	Two FBGs in Different	[110]
		0-2500 $\mu\epsilon$	Diameter Fibre	

2.5 Temperature and Strain Sensor Applications

Fibre-optic strain sensors have been embedded into equipment, structures and composite materials for real-time monitoring of their health [19, 111]. The following sections provide a brief overview of typical applications for these sensors and how they could potentially be improved by incorporating a simultaneous temperature and strain measurement system.

2.5.1 Aerospace and Marine

The benefits of high strength, low weight and high resistance to fatigue have meant that composites are already widely used in range of air- and space-craft [112]. Fibre-optic temperature and strain sensors are ideal for use with composite technology due to their ease of being embedded, to form an intelligent, self sensing structure. This enables the continuous monitoring of strains and temperatures within the composite structure, throughout its service life as well as test and manufacture.

Fibre-optic temperature and strain sensors allow for comprehensive in-service temperature and strain data to be collected. This is a prerequisite for the implementation of condition based maintenance in which, service and inspection activities are

optimised, based on actual operational history of the aero or marine structure. This could potentially produce major savings in terms of reduced maintenance costs and downtime as well as significantly improved safety.

De-bonding at key structural joints can be detected using this technology [113]. Also, damage could be indicated by a change in structural response to a given load. Accurate databases can be created for history and service use of specific components. This can quantify the extent of structural deterioration for implementing systematic maintenance schedules. These extensive databases establish specific in-use criteria for developing techniques which can reduce fatigue.

The detailed strain and temperature data provided by the embedded fibre-optic sensors can be used as a powerful tool for aeronautical engineers in speeding up the design and development process. It can also determine aerodynamic loads and provide important insight into deformation of the structure during actual flight.

Measurement of dimensional stability and temperature is of particular importance for spacecraft structures, due to the extreme temperature variation and stresses that these structures experience. Fibre-optic temperature and strain sensors can be mounted on satellites and satellite antenna systems to maintain correct functionality by monitoring their dimensional stability.

Today's marine vessels require the health of various components to be monitored. FBG based strain sensors have been utilised in the design of a system for health monitoring of a naval surface ship, with the system being used for long-term load monitoring of the vessel [114]. Fibre-optic strain sensors have also been applied for accurate dockside set-up of yacht rigs [115]. They can achieve results more quickly and efficiently, ensuring that correct tensions are applied through each rigging element by actual measurement. The rig's performance could also be assessed more accurately during sea trials. Common set-ups can be replicated quickly and precisely for a fleet of boats if needed, through the fine tuning capabilities of fibre-optic strain

sensors. This ensures accurate correlation for soil analysis and development.

2.5.2 Civil Engineering and Mining

Fibre-optic temperature and strain sensing technology is not only ideally suited to composite structure applications (e.g. aerospace), but also offers significant advantages when applied to steel, concrete and other structures [116].

They provide inherent long-term accuracy which allows for true comparison of data over long periods of time, and avoiding the need for re-calibration. With the multiplexing ability of fibre-optics, many sensors can be configured on a single optical fibre, dramatically reducing the cabling and installation costs. Coupled with long transmission lengths of several kilometres, intrinsically safe fibre-optic sensors enable safe installation and operation in mines and other explosion hazard areas.

To date, fibre-optic temperature and strain sensing has been applied in the following areas:

Composite Bridge Decks. Monitoring of in-service loads, such as transient loads imposed by vehicles [117].

Concrete Structures. Fibre-optic sensors can be surface bonded in the form of a composite patch or embedded in the concrete during construction [118]. For embedment the sensor is normally in the form of a rugged steel dumbbell.

Steel Structures. Sensors are usually surface bonded to steel structures, although weldable sensors are an alternative [119].

Tendons. Monitoring of pre-stressing tendons with fibre-optic sensors has been performed to enable accurate compensation for in-service relaxation [120].

In-well fibre-optic sensing systems offer the potential for continuous, highly accurate, highly reliable, real-time data measurements [121, 122]. Recently, permanent down-hole fibre-optic pressure and temperature transducers have become an accepted new technology in the oil and gas industry due to their reliability at high temperatures

and their ability to survive the severe shock and vibration conditions associated with post-installation perforating operations. Real-time downhole pressure data are critical to managing the miscible-gas injection enhanced-recovery process. The real-time data can provide valuable information to the asset team in monitoring the perforating program, determining initial reservoir pressure, managing well draw-down, diagnosing completion problems, building well-bore-hydraulics and inflow-performance models, and providing pressure-buildup data, all without the need for well interventions and the resulting loss in production volume.

Another example of FBG use is in the electrical power industry where electromagnetic interference prevents the use of on-line measurement systems for transformers and turbines. Regular, possibly unnecessary, downtime for inspection and routine maintenance costs many millions of dollars a year. This industry clearly has interest in temperature, voltage and current sensors [123]. For example, voltage transformers require temperature measurement in the 'hotspots' of transformer windings. Transformer lifetime depends critically on 'hotspot' temperature; the lifetime is halved for every 6 °C of increased temperature. Designs could be improved if actual temperatures were known; any reduction of the over-engineering that occurs at present would result in material savings. Alternatively, if an existing transformer had its rating upgraded because of over-design a greater sale price could result. Commercial temperature sensors are unsuitable for the required point measurements and are also very expensive. In general, no one sensor is suitable for all situations given the wide-range of possible applications.

Chapter 3

FIBRE-OPTIC SENSING ELEMENTS

3.1 Rare Earth Doped Optical Fibres

Due to their unique characteristics, rare earth ions have a long history in optical applications, particularly in lasers and optical amplifiers. Important characteristics that distinguish rare earths from other optically active ions are: they fluoresce and absorb over relatively narrow wavelength ranges, the wavelengths of the emission and absorption transitions are relatively insensitive to the host material, the intensities of these transitions are weak, the lifetimes of metastable states are long, and the quantum efficiencies are high. These properties all result from the nature of the states involved in these processes and lead to excellent performance of rare earth ions in many optical applications.

The rare earths are divided into two groups of fifteen elements each, as shown in Figure 3.1. The lanthanide series is characterised by the gradual filling of the $4f^N 5s^2 5p^6 6s^2$ electronic shells and begin with lanthanum (La), which has an atomic number, Z , of 57 and end with lutetium (Lu, $Z = 71$). The actinide series lies below the lanthanide series in the periodic table, filling the $5f$ shell from actinium (Ac, $Z = 89$) to lawrencium (Lr, $Z = 103$). Many actinides do not have isotopes stable enough to be useful for applications such as lasers and amplifiers. Therefore, only the lanthanides are considered of importance for optical applications. In the lanthanide series, the screening by the $4f$ electrons leads to an increase in effective nuclear charge as the atomic number increases. As a result, the $4f$ electrons become increasingly more tightly bound with increasing atomic number [124]. It is the number of electrons occupying the $4f$ shell that determines the optical characteristics of the particular rare earth.

Group Ia	IIa		Transition metals								IIIb	IVb	Vb	VIb	VIIb	VIII	
1 H																	2 He
3 Li	4 Be									5 B	6 C	7 N	8 O	9 F	10 Ne		
11 Na	12 Mg									13 Al	14 Si	15 P	16 S	17 Cl	18 Ar		
19 K	20 Ca	21 Sc	22 Ti	23 V	24 Cr	25 Mn	26 Fe	27 Co	28 Ni	29 Cu	30 Zn	31 Ga	32 Ge	33 As	34 Se	35 Br	36 Kr
37 Rb	38 Sr	39 Y	40 Zr	41 Nb	42 Mo	43 Tc	44 Ru	45 Rh	46 Pd	47 Ag	48 Cd	49 In	50 Sn	51 Sb	52 Te	53 I	54 Xe
55 Cs	56 Ba	57 La	72 Hf	73 Ta	74 W	75 Re	76 Os	77 Ir	78 Pt	79 Au	80 Hg	81 Tl	82 Pb	83 Bi	84 Po	85 At	86 Rn
87 Fr	88 Ra	89 Ac	104 Unq	105 Unp	106 Unh												
Rare earths: Lanthanide series																	
58 Ce	59 Pr	60 Nd	61 Pm	62 Sm	63 Eu	64 Gd	65 Tb	66 Dy	67 Ho	68 Er	69 Tm	70 Yb	71 Lu				
Rare earths: Actinide series																	
90 Th	91 Pa	92 U	93 Np	94 Pu	95 Am	96 Cm	97 Bk	98 Cf	99 Es	100 Fm	101 Md	102 No	103 Lr				

Figure 3.1: Periodic table of the elements.

The lanthanide ions are most stable when they are in the trivalent ($3+$) level of ionisation. Ionisation preferentially removes the $6s$ electrons, and the electronic configuration for these ions is that of the xenon structure plus a certain number (1-14) of $4f$ electrons. The outer $5s$ and $5p$ remain filled, which has the effect of shielding the remaining electrons in the $4f$ shell from perturbation due to external fields [125]. Consequently, electronic transitions within the $4f$ shell are relatively insensitive to the host material and only weak perturbation occurs. The observed, relatively sharp infrared and visible optical spectra of triply ionised rare earth ions is a consequence of the shielding of transitions between $4f$ states.

Over the past number of decades these rare earth ions have been incorporated into the core region of optical fibres. They have been referred as 'rare earth doped optical fibres'. In this work, the rare earth doped optical fibres studied were from the lanthanide series.

3.1.1 Fabrication of Rare Earth Doped Optical Fibres

In this work, erbium doped and erbium:ytterbium doped silica fibres were investigated as the sensing gauge. The physical characteristics of a rare earth doped optical fibre are very similar to that of conventional telecommunications optical fibre (e.g. Corning SMF28). The main variation is the composition of the core and the cladding. Figure 3.2 shows a cross-section of a typical rare earth doped fibre together with the occurrence of specific elements used in this work.

The rare earth doped fibres were fabricated using the modified chemical vapor deposition (MCVD) technique incorporating solution doping [126] at the Laboratoire de Physique de la Matière Condensée (LPMC), University of Nice (Nice, France). The MCVD method is a derivative from the chemical vapor deposition (CVD) technique, which is a popular method used for manufacturing standard telecommunications fibre [127]. In the MCVD technique, the glass forming materials, such as SiCl_4 , GeCl_4

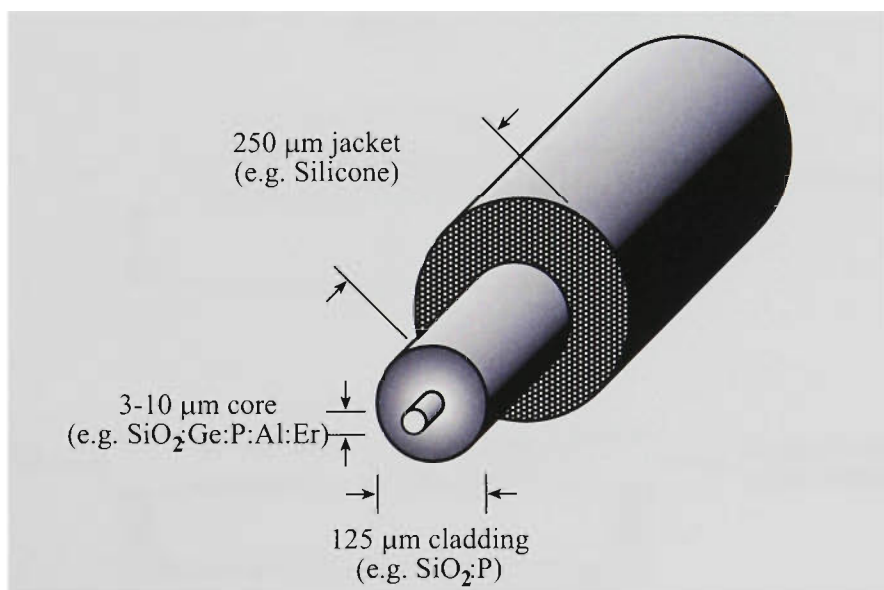


Figure 3.2: Optical fibre cross-section detailing physical dimensions and common compositions of various layers.

and POCl_3 are heated to produce a vapour. This vapour is passed through a glass tube which is rotating on a lathe. As the gas travels through the tube, a high temperature burner traverses along the length of the tube. The heat produced causes the chlorides and oxygen to react by thermal oxidation. Fine particles of oxides are

produced and deposited on the inside walls. After several layers of material have been deposited to form the cladding of the fibre, the gas mixture is altered to produce the core region with a slightly varied refractive index. The core layers are deposited in the same manner but at a lower temperature which does not allow the core layers to be fully sintered. This results in the core layers being porous, therefore, allowing all elements smaller than the pore, such as rare earths, to be absorbed during the solution doping stage.

In the solution doping method, as illustrated in Figure 3.3, the porous core layers are soaked in an aqueous chloride solution containing the required dopants (e.g. erbium and aluminium). This solution is allowed to soak for some hours allowing

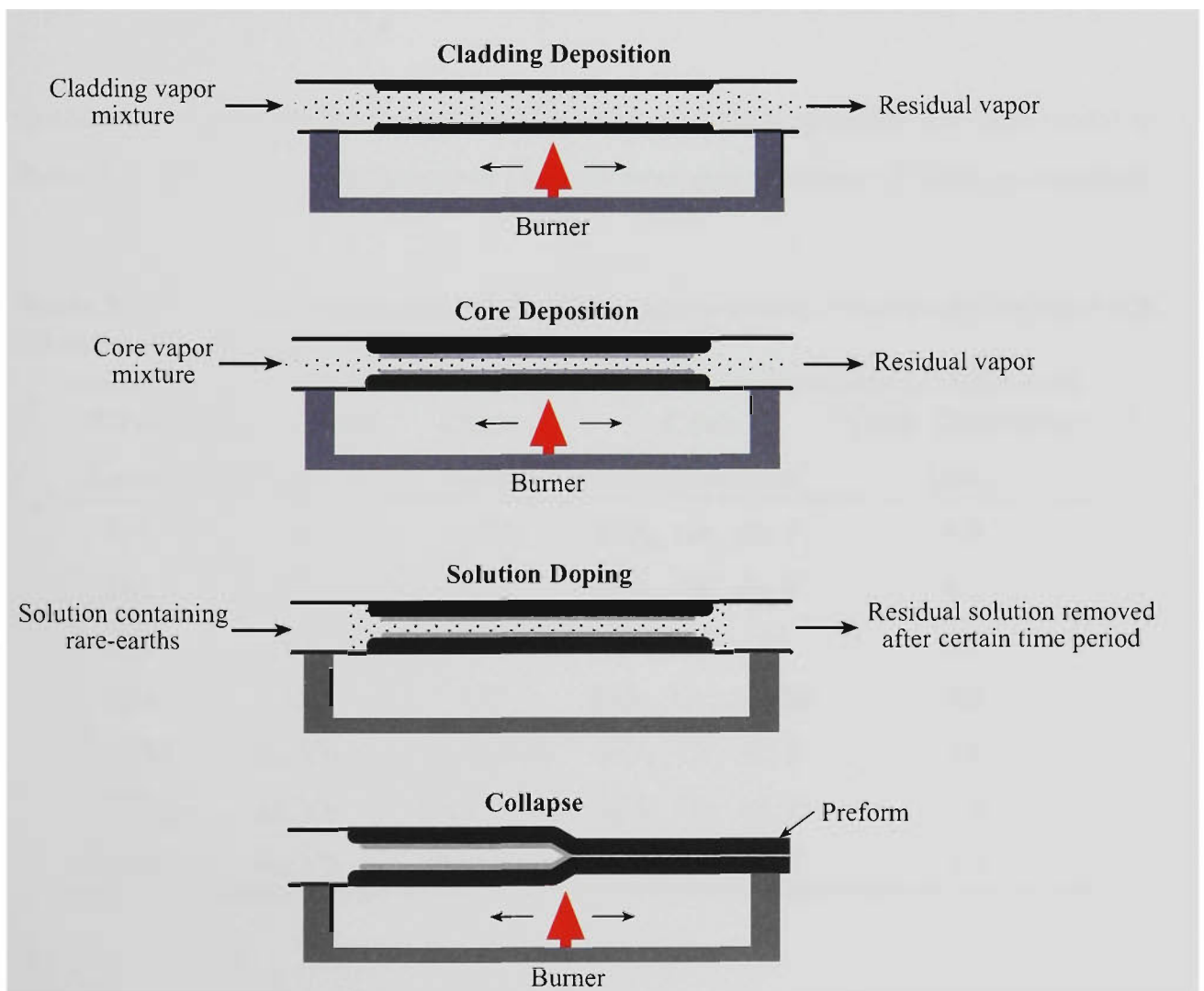


Figure 3.3: Main stages during fabrication of rare earth doped optical fibre using the MCVD technique, incorporating solution doping.

rare earths and other elements to impregnate into the pores. The solution is then drained and the impregnated layer is dried at high temperatures in the presence of a flowing chlorine/oxygen mixture. Once dried, the cylindrical preform is collapsed at a fusing temperature of 1400 °C to fuse the core layers, it is collapsed and drawn into a rare earth doped fibre.

After the preform has been manufactured, optical fibre is fabricated using a drawing tower [128]. This process comprises of heating one end of the preform to a melting temperature in a high temperature furnace. The resulting melted section is drawn down at a specific rate to produce optical fibre with the required dimensions. A protective coating material (e.g. silicone) is usually applied to the solidified fibre as it passes through a curing oven, to improve the strength of the completed fibre.

Numerous fibres were fabricated for this work and their specifications are shown in Table 3.1. The main constituents of the core were combinations of silica, germanium,

Table 3.1: Physical characteristics of the fibres used as sensing elements during this work. All fibres were fabricated at the LPMC.

Fibre Label	Rare Earth Dopant	Conc. (ppm)	Core Composition	Core Diameter (μm)
Er1	Er	1430	SiO ₂ , Ge, Al, P	8.0
Er2	Er	490	SiO ₂ , Ge, Al, P	8.8
Er3	Er	2680	SiO ₂ , Ge, Al	3.9
Er4	Er	90	SiO ₂ , Ge, Al, Sn	4.9
ErYb1	Er:Yb	1500:1500	SiO ₂ , Ge, Al, P	3.8
ErYb2	Er:Yb	2000:2000	SiO ₂ , Ge, Al, P	5.5
ErYb3	Er:Yb	3000:3000	SiO ₂ , Ge, Al, P	4.4

phosphorus, aluminium and tin. Apart from the rare earth dopant concentration, fibres Er1, Er2, ErYb1, ErYb2 and ErYb3 had the same core composition. Er3 and Er4 did not include phosphorus, while only Er4 had the addition of tin. These ele-

ments were chosen due to a number of factors which are explained in greater detail in Section 3.2.2.

3.1.2 The Erbium Ion

The erbium ion would undoubtedly be the most studied of all the rare earth ions. This is mainly due to its fluorescence at 1550 nm corresponding to the third telecommunications window. Figure 3.4 shows the energy level diagram for Er^{3+} , indicating the absorption and emission transitions of interest in this work. There are two

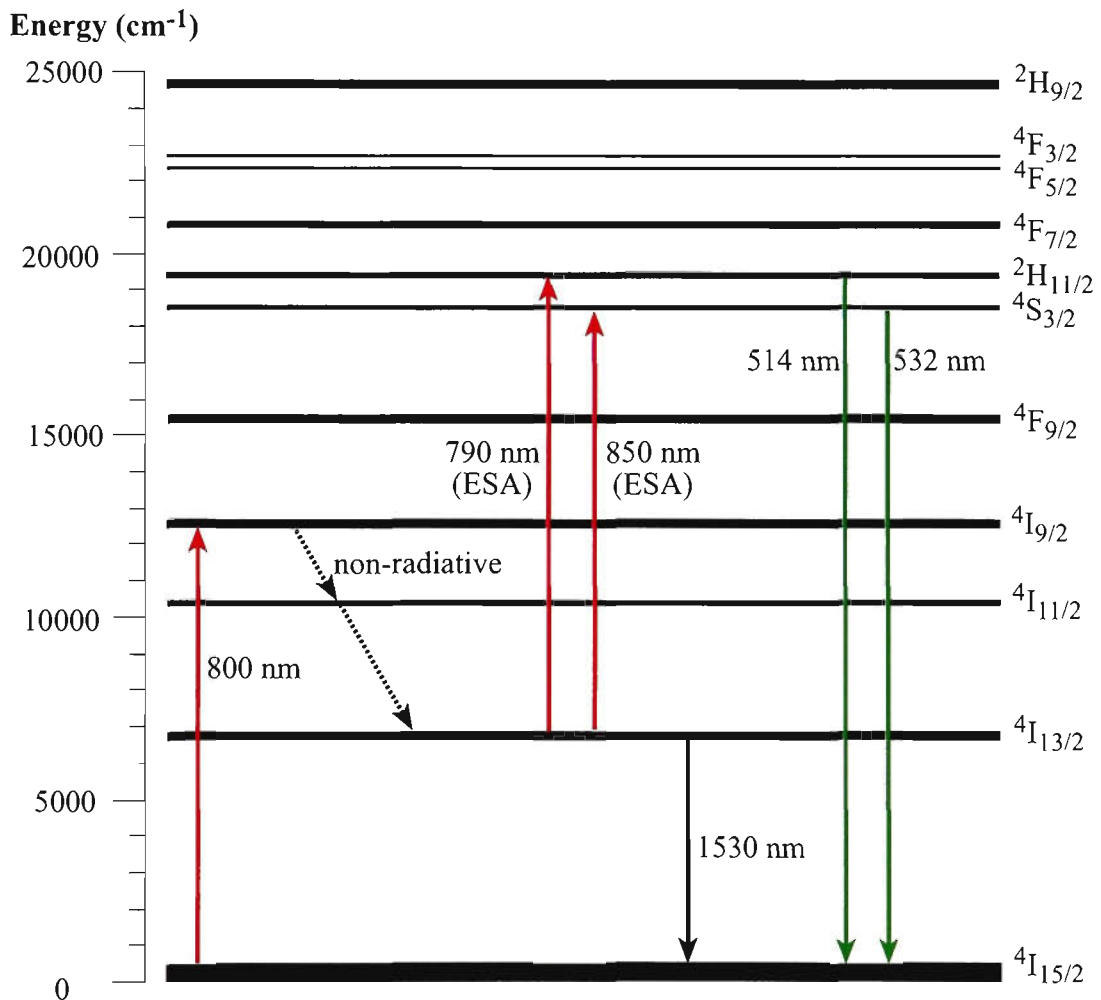


Figure 3.4: Energy level diagram for the triply ionised erbium ion in silica glass [129]. Note: Only transitions of interest in this work are shown. Wavelengths shown are peak values only.

closely spaced energy levels in Er^{3+} for which their relative populations are thermally coupled and thus of interest for FIR measurements. These are the ${}^2\text{H}_{11/2}$ and

$^4S_{3/2}$ levels, which emit fluorescence between 500-570 nm.

A practical method of populating these states is by populating initially the $^4I_{9/2}$ state with 800 nm radiation. When the $^4I_{9/2}$ level of the Er^{3+} ion is excited, the $^4I_{13/2}$ metastable level is quasi-instantaneously populated through fast non-radiative transitions. The $^2H_{11/2}$ and $^4S_{3/2}$ levels are then populated by the process of excited state absorption. Er^{3+} exhibits excited state absorption (ESA) for many levels. ESA occurs when an ion that is already in an excited state absorbs a photon and is promoted to a higher energy level.

The most important and extensively studied transition in Er^{3+} is undoubtedly the $^4I_{13/2} \rightarrow ^4I_{15/2}$ that fluoresces a broad-band centered at 1530 nm. This transition is possible via 800 nm excitation, as shown in Figure 3.4. It is used in this work as a broadband illuminating source for interrogating FBGs with Bragg wavelengths inscribed within this wavelength band. Figure 3.5 shows fluorescence from the energy levels in fibre sample Er1. Fluorescence from the $^2H_{11/2}$ and $^4S_{3/2}$ levels was

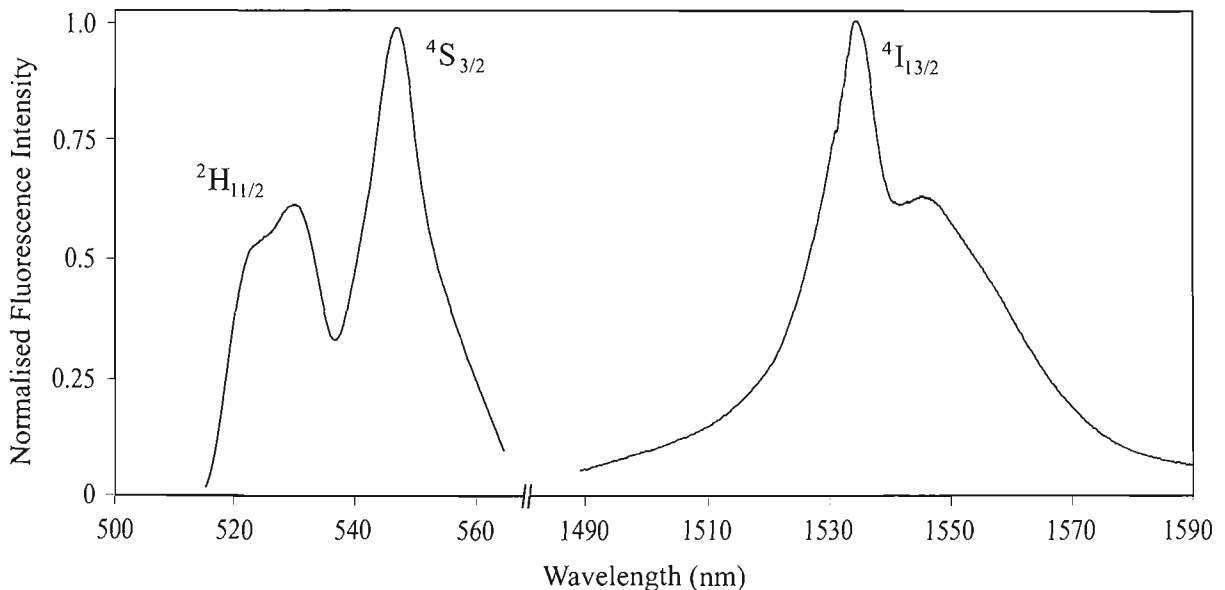


Figure 3.5: Fluorescence spectra from the $^2H_{11/2}$, $^4S_{3/2}$ and $^4I_{13/2}$ levels in Er^{3+} from sample Er1 when pumped at 800 nm. Note: The two fluorescence bands shown have been independently normalised.

recorded through a Oriel 550 nm bandpass filter and captured on an OSA with a

resolution of 5 nm, while fluorescence from the ${}^4I_{13/2}$ was captured via a 980/1550 nm WDM coupler on an OSA with a resolution of 0.1 nm. The pump source used was a Ti:Sapphire laser emitting 500 mW of 800 nm radiation.

3.1.3 Ytterbium-sensitised Erbium

The sensitisation of Er^{3+} doped silica fibres by Yb^{3+} presents several advantages [127]. First, it allows for $\text{Er}^{3+}:\text{Yb}^{3+}$ doped fibre to absorb the pump power strongly. Also, ytterbium is added as a sensitiser because of clustering effects when erbium concentration is too high. This is significant in terms of increasing the efficiency of the sensor scheme investigated in this work. It increases fluorescence intensity from the ${}^4I_{13/2}$ level in erbium by means of energy transfer, as illustrated in Figure 3.6. The Yb^{3+} ion can absorb a photon to the ${}^2F_{5/2}$ excited energy level and then transfer efficiently its energy to the ${}^4I_{11/2}$ state of an Er^{3+} ion. The erbium ion then undertakes ESA, and non-radiative decay to the ${}^4I_{13/2}$ state and produce fluorescence as it decays back to the ground state.

A second advantage is that the significant inhomogeneous broadening of the ${}^2F_{5/2}$ level of the Yb^{3+} ions (Stark splitting) results in a broad absorption band, as illustrated in Figure 3.6. This permits a wider range of pump wavelengths to be used, typically about ± 140 nm around 930 nm. This large Stark splitting of levels has also been used for temperature measurement using the FIR technique [6]. The large spacing between the Stark levels make the emission peaks easy to resolve, as illustrated by the broad fluorescence spectrum in Figure 3.7. This fluorescence is investigated in this work for application in simultaneous temperature and strain measurement.

3.1.4 FIR Theory

The theory behind the fluorescence intensity ratio is based on the two energy levels of interest being spaced closely enough that their relative ion populations, which are in a quasi-equilibrium state, are governed by a Boltzmann distribution. The general

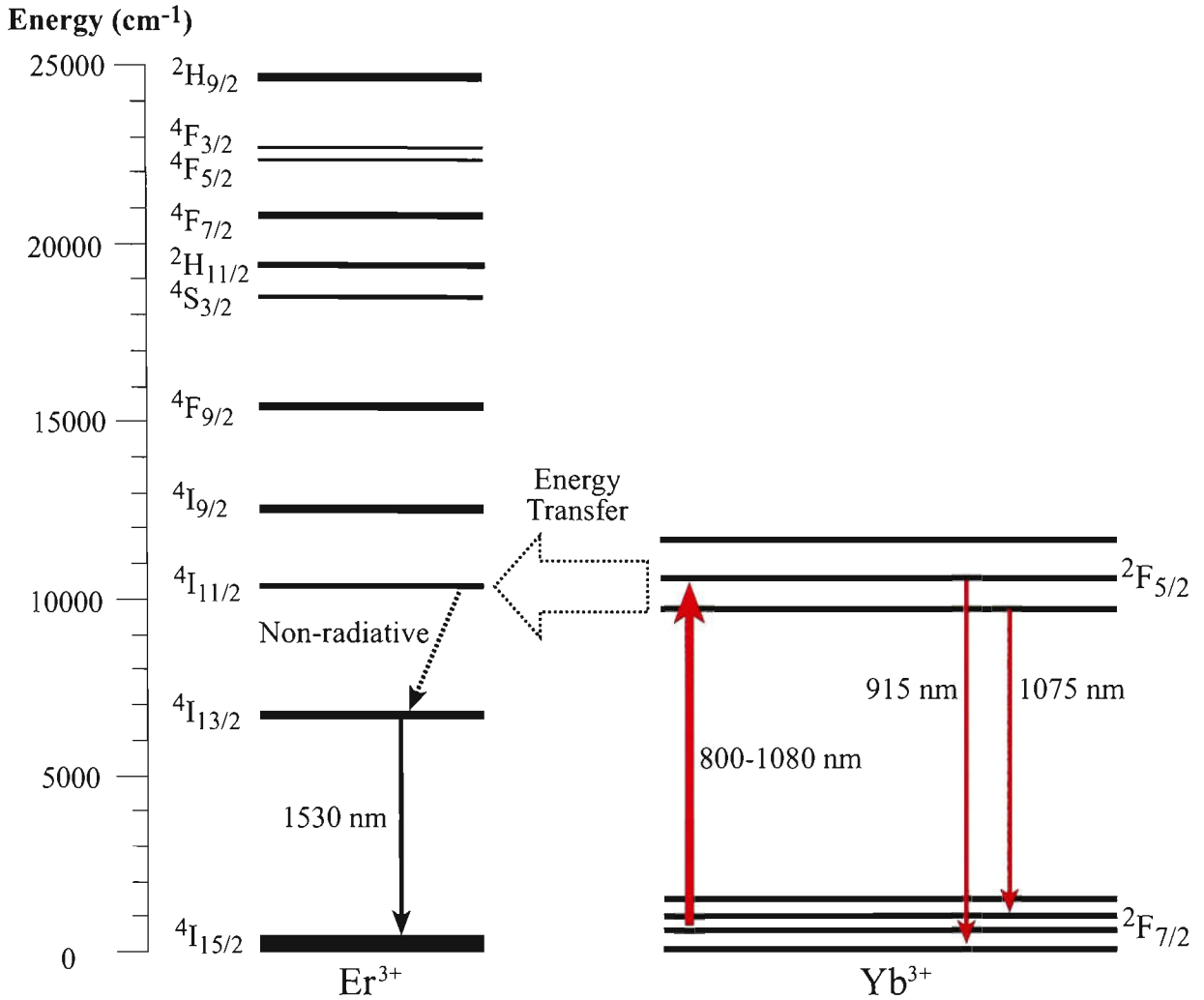


Figure 3.6: Energy level diagram for ytterbium sensitised erbium in silica glass. Note: Only transitions of interest in this work are shown.

form of the Boltzmann distribution for a given system comprising of two energy levels, labelled 1 and 2 where $E_2 > E_1$ is given by

$$\frac{N_2}{N_1} = \exp \frac{-(E_2 - E_1)}{kT}, \quad (3.1)$$

where N_1 and N_2 are the relative populations of the levels with energies E_1 and E_2 , respectively, k is the Boltzmann constant (1.38041×10^{-23} J/K) and T is the absolute temperature. It can be seen from Equation 3.1 that as the temperature of the system is increased, the number of ions in energy level E_2 will increase relative to the number in E_1 . Since the emitted intensities are proportional to the population of each energy level, Equation 3.1 can be expressed in terms of the fluorescence

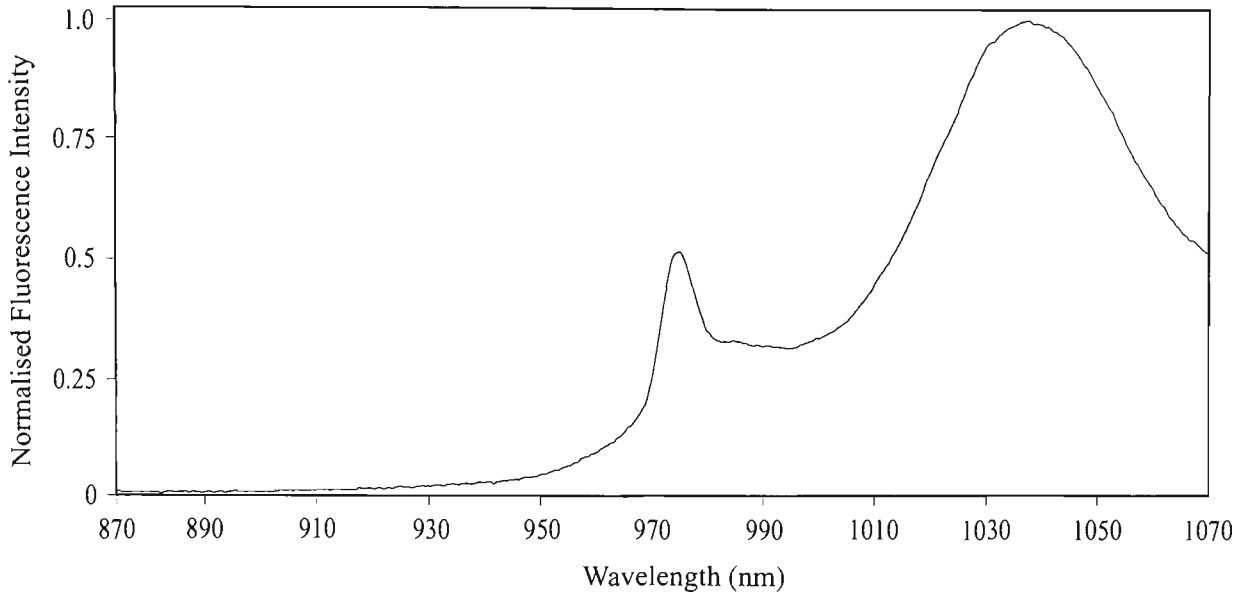


Figure 3.7: Fluorescence spectrum from the ${}^2F_{5/2}$ level in Yb^{3+} . Note: Fluorescence taken from fibre sample ErYb3 used in this work.

intensity ratio, R , and is given by

$$R = \frac{N_2}{N_1} = \frac{I_{2j}}{I_{1j}} = \frac{g_2 \sigma_{2j} \omega_{2j}}{g_1 \sigma_{1j} \omega_{1j}} \exp \frac{-\Delta E}{kT} = B \exp \frac{-\Delta E}{kT}, \quad (3.2)$$

where

$$B = \frac{g_2 \sigma_{2j} \omega_{2j}}{g_1 \sigma_{1j} \omega_{1j}}, \quad (3.3)$$

and I_{ij} , g_i , σ_{ij} , ω_{ij} are the fluorescence intensity, the degeneracy, the emission cross-section, and the angular frequency of fluorescence transitions, respectively, from the upper and lower thermalising energy levels to a terminating level j . ΔE is the difference in energy between levels E_1 and E_2 . Figure 3.8 shows the dynamics of the FIR measurement technique in a simplified energy level diagram of a rare earth ion. The dashed lines represent non-radiative decay and the solid arrows labelled, I_{2j} and I_{1j} , representing the fluorescence transitions used to measure the FIR.

The general form of the FIR sensitivity S , is defined as the fractional rate of change in the FIR with temperature [6]. An expression is derived from Equation 3.2 and is given by:

$$S = \frac{1}{R} \frac{\delta R}{\delta T} = \frac{\Delta E}{kT^2}. \quad (3.4)$$

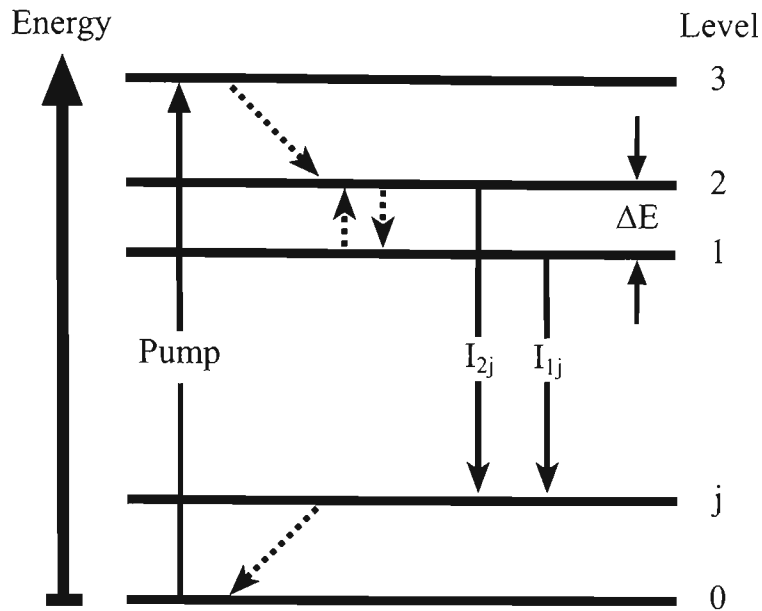


Figure 3.8: Simplified energy level diagram and corresponding transitions related to the FIR technique.

Previous work has summarised the theoretical FIR sensitivities of two thermally coupled energy levels from various types of rare earths [6]. Equation 3.4 suggests that using pairs of energy levels with large energy differences increases the FIR sensitivity. The drawback is that if the levels are too far apart, thermalisation will no longer be observed. Additionally, as the energy difference increases, the population and hence the fluorescence intensity from the upper thermalising level will decrease.

3.2 Fibre Bragg Grating Characteristics

Various FBG fabrication techniques have resulted in FBGs with various characteristics in response to physical effects, such as high temperature. These various types of FBGs have been classified below.

Type 0 gratings are also referred to as *Hill gratings* [60]. They are self-organised gratings, formed by launching light in the fibre from which a partial reflection from the cleaved fibre end-face creates the periodic interference pattern. As the grating is formed more light will be reflected within the fibre and hence increase the growth rate of the grating. These gratings have limited use, as the writing wavelength is

also the Bragg wavelength of the grating. To date, they have not been reported for applications in temperature or strain sensing.

Type I gratings are the most common and can be found in applications such as telecommunications DWDM systems and strain sensors. These gratings are characterised by a monotonic increase in the amplitude of the refractive index modulation growth and are generally formed at low intensities. Figure 3.9 illustrates the growth dynamics of a Type I Bragg grating written in erbium doped fibre (fibre composition shown in Table 3.1) by the author. Type I gratings are formed by side illumination

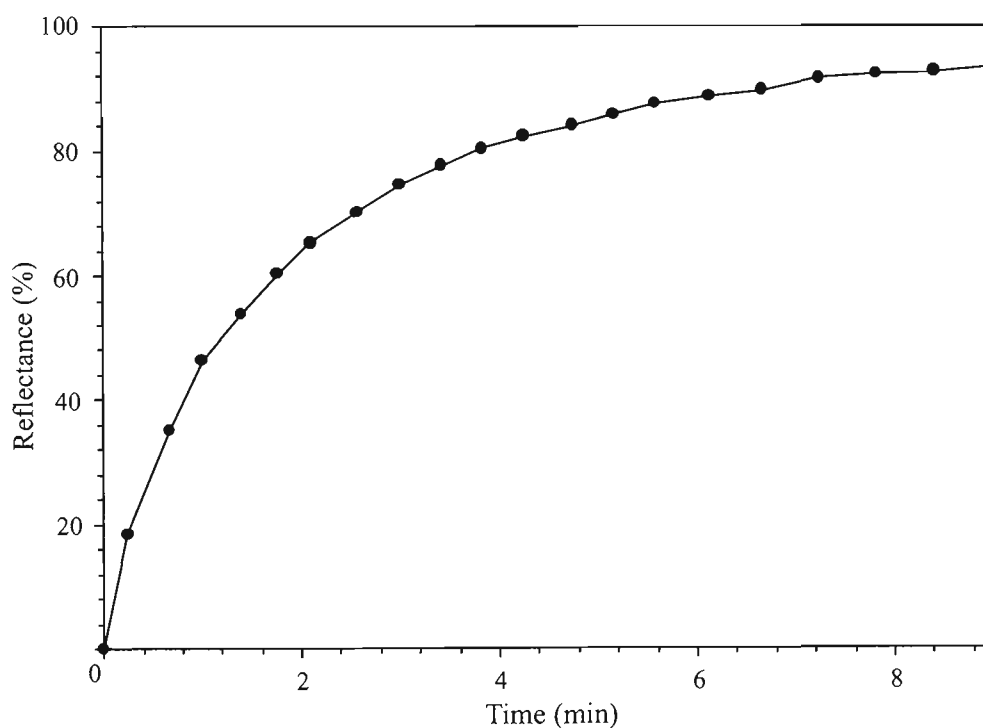


Figure 3.9: Growth rate of Type I Bragg grating written in hydrogenated Er1 fibre.

of a bare optical fibre using UV radiation. These gratings were fabricated by the author for the majority of the work presented here and the technique is explained in detail in Section 3.2.4.

These gratings exhibit least resistance to erasure from exposure to prolonged periods of high temperature relative to the other grating types mentioned below. Most commercially available Type I FBG sensors have operating temperature ranges below

~120°C as they become erased above these temperatures.

Type IA gratings are characterised by an initial growth profile consistent with that of a Type I, followed by complete or partial erasure and followed again by another growth of the grating [38]. Type IA gratings experience a Bragg wavelength red-shift of approximately 15 nm with respect to the initial Type I grating. Type IA gratings can be formed in hydrogenated fibre of all types.

A Type II grating is a damaged grating formed when the fibre is exposed to a high energy, single pulse writing beam above 30 mJ [61]. Physical damage is caused in the fibre core on the side of the writing beams accompanied by a large change in refractive index modulation. The sudden growth of the refractive index is accompanied by a large short-wavelength loss due to the coupling of the guided mode to the radiation field. The gratings generally tend to have an irregular reflection spectrum due to 'hotspots' in the laser beam profile. These gratings decay at much higher temperatures than Type I, being stable up to ~700°C [72]. A similar damaged grating can be formed with a Ge-doped telecommunications fibre exposed to 800 nm femtosecond radiation for a few minutes [130]. These gratings have thermal sustainability to temperatures up to 300 C.

Type IIA gratings are characterised by an initial growth profile consistent with that of a Type I, followed by complete or partial erasure and followed again by another growth of the grating in hydrogen-free B-Ge and high Ge fibres. The final grating is stronger than the original and is able to withstand higher temperature [69]. These gratings have been formed at low power densities and with pulsed lasers after long exposure [61]. These FBGs require longer exposure times, thereby possibly resulting in an overall increase in the cost of the sensor. Also, these gratings have been combined with Type I gratings for strain independent measurement by taking advantage of their different temperature sensitivities [36,37], achieving a temperature accuracy of 6.6°C over a range of 25-300°C [36].

Chemical Composition Gratings (CCGs) do not fit into any of the grating types defined above [131–133]. The optical characteristics do not differ from any of the grating types described, but, the manufacturing procedure, growth of refractive index and, most importantly for this work, thermal properties differ significantly.

The main principle of CCG formation is to periodically change the diffusion properties of different dopants. By thermal processing of such a structure, differential diffusion results in a periodic variation in dopant concentration, which results in a periodic refractive-index structure [134]. By fringed UV exposure of hydrogen loaded fibres, periodic concentration of hydroxyl groups are formed and subsequent thermal processing results in a periodic variation of either the fluorine [131] or oxygen [133, 134] concentrations.

CCGs can be formed with the same periodicity as conventional gratings by side exposure of fringed UV radiation. The thermal stability properties of CCGs are dependent on the diffusion properties of the modulated dopant and so, CCGs should exhibit stable performance at higher temperatures compared to Type I FBGs. CCGs have been formed at temperatures ranging from 830-1000 °C [132, 133] and have demonstrated slow decay above 1000 °C [132, 134].

In this thesis the formation of oxygen-modulated CCGs in fibre doped with Er^{3+} , Si, Ge, Sn, P_2O_5 and Al is presented [135]. This is the first time that such gratings have been observed in erbium doped fibre to the best of the author's knowledge.

3.2.1 Photosensitivity in Optical Fibres

Although numerous models of the photosensitivity of optical fibres have been developed recently, which are discussed in this Chapter, it still appears that this phenomena is not completely understood. One area that requires an increased amount of research is the effects of photosensitivity of optical fibres on chemical composition gratings.

3.2.1.1 Colour-centre Model

The phenomena of photosensitivity in germanium-doped fibre is associated with an absorption band at approximately 240 nm, which is attributed to a germanium-oxygen deficiency [136]. Irradiating the fibre core using an ultra-violet source within this absorption band, results in bleaching of the 240 nm band and growth of absorption bands located near 190 nm. Numerous authors have used the Kramers-Krönig relation to link these absorption changes in the UV region to the change in refractive index [137]. A number of different defects have been observed [61, 138], of which the most common are summarised in Table 3.2 with their associated absorption bands. Generally, oxygen deficient centres (GODC) are precursors and GeE' , $\text{Ge}(1)$ and $\text{Ge}(2)$ are products of the photochemical pathways, which have been presented to explain transformation of defects and the glass structure.

Table 3.2: Associated absorption bands for common defects related to photosensitivity.

Defect	Absorption Peak	Reference
GODC - wrong bond	240 nm/5 eV	[138]
GeE'	195 nm/6.4 eV	[138]
$\text{Ge}(1)$	281 nm/4.4 eV	[138]
$\text{Ge}(2)$	213 nm/5.8 eV	[138]

3.2.1.2 Stress Relaxation Model

As the stress-optic effect changes the refractive index in silica glass, relaxation of stress will consequently also change the refractive index [139]. Due to material properties and manufacturing procedures, optical fibres may have highly stressed regions. The residual stress arises from the difference in thermal expansion between core and cladding regions (thermo-elastic stress) and due to difference in transition temperature in combination with the applied tension during fibre drawing (mechanical stress).

With an optical fibre core having a higher thermal expansion coefficient than the cladding, the contraction of the core as the fibre cools down will be restricted by the cladding glass and vice-versa if the core has a lower thermal expansion than the cladding. This will result in residual areas of stress in different regions of the fibre. The mechanical stress is due to the tension used to extract the fibre from the drawing furnace. The drawing tension will essentially be applied to the region that solidifies first while the remaining glass with the lower transition temperature will solidify once the temperature has decreased sufficiently. When the drawing tension is released, the fibre will contract resulting in a compressive stress in regions with a lower transition temperature. Estimated refractive index change due to stress relaxation in highly stressed fibre is in the order of $\Delta n \sim 10^{-3}$ [140]. However, there is some debate on whether UV induced stress relaxation is a mechanism involved in photosensitivity.

3.2.1.3 Densification-compaction Model

There is evidence that densification and stress increase in optical fibres contributes to the change in refractive index [61, 141, 142]. Surface atomic force microscope scans of un-etched samples have shown that the surface densifies in the UV illuminated regions [61]. Also, stress measurements made optically have shown that the tensile stress increases in the core, reducing the induced refractive index change by as much as 30% [61].

3.2.1.4 Increased Photosensitivity by Hydrogen Treatment

A well known effect is the reaction of hydrogen with the germanium ion to form GeH. This reaction considerably changes the band structure in the UV band. These changes, in turn, influence the local refractive index, as described by Kramers-Krönig model. The reaction rates have been shown to be strongly temperature dependent [143] and therefore many different techniques have been adopted to hydrogenate particular optical fibres to increase their photosensitivity for FBG writing.

High temperature hydrogen treatment of the fibre preform is one technique that has

shown increased levels of photosensitivity [144]. The absorption at 5 eV, corresponding to oxygen-deficient defect absorption, was shown to increase by heating a highly germanium doped preform in a hydrogen atmosphere. The preform was heated in a hydrogen atmosphere at 610°C for 75 hours. Fibres drawn from this preform showed significantly higher photosensitivity compared to untreated preforms.

Another hydrogen treatment is to simply place the fibre in a high-pressure hydrogen atmosphere at room temperature. Hydrogen molecules will diffuse inertly into the glass matrix. Loading the fibre prior to UV exposure significantly increases the photosensitivity [145]. Refractive index changes as high as $\Delta n \sim 6 \times 10^{-3}$ have been reported for standard hydrogen loaded telecommunications fibre. The diffusion of hydrogen is not only dependent on pressure but also temperature. The diffusion coefficient of hydrogen is [61]:

$$D = 2.83 \times 10^{-4} e^{-40.19/RT}, \text{ cm}^2/\text{s}, \quad (3.5)$$

where $R = 8.311 \text{ J}/(\text{K}\cdot\text{mol})$ and T is the temperature in kelvin. It can be seen clearly from Equation 3.5 that the diffusion coefficient of hydrogen increases with increasing temperature. Therefore, to further accelerate the hydrogen loading of the fibre, a fibre is placed in an elevated temperature and high-pressure hydrogen atmosphere. This is the most common method used for increasing photosensitivity and was used by the author on all fibres where hydrogen loading was preferred.

3.2.2 Core Composition Effects

The chemical composition of the optical fibre has been shown to have an influence on numerous parameters of FBGs (e.g. high temperature stability and photosensitivity). With the integration of rare earth doped fibres with FBGs in this work it is important to understand the effects that variations in fibre composition have on the FBGs, which could ultimately affect the performance of the sensor.

3.2.2.1 Bragg Gratings in Rare Earth Doped Fibres

One of the earliest uses of FBGs in rare earth doped fibres was as high reflectors to define the laser cavity in fibre lasers [146]. Recently, FBGs have been written in rare earth doped fibres for simultaneous temperature and strain sensing [33]. The sensor exhibited reasonable performance over a relatively low temperature range ($< 120^{\circ}\text{C}$). Although these results showed FBGs written successfully in rare earth doped optical fibres, there is still a considerable amount of research required to optimise the fibre composition and FBG writing procedure in these fibres.

Generally, it is more difficult to write Bragg gratings in rare earth doped fibres than in standard fibres due to the photo-insensitive nature of these fibres. Germanium is often replaced or partially replaced by aluminium (Al_2O_3) to reduce the effect of quenching and lifetime shortening [129]. The lack of germanium reduces the photosensitivity of optical fibres, even with hydrogen loading. Gratings can still be formed in most fibres, but the refractive index changes remain weak ($< 10^{-4}$) in most cases with 240 nm irradiation. The direct writing of gratings in rare earth doped fibres is limited to long lengths, which could have implications in the spatial resolution of quasi-distributed FBG sensor systems. To date, gratings of CCG type have not been reported in rare earth doped optical fibre. Gratings resembling CCGs have been fabricated in rare earth doped optical fibre for the first time by the author, which is discussed in detail in Chapter 7.

The rare earth doped fibres investigated by the author had varying core compositions, allowing the FBG fabrication parameters and thermal stability to be investigated. The role of the chemical elements of interest in this work and some of those used previously by other authors follows.

3.2.2.2 Effects Of Various Dopants

Boron

Boron co-doped germanosilicate optical fibres result in highly photosensitive fi-

bres [147]. The addition of boron to germanium doped silica does not alter the 240 nm absorption band characteristic for germanium fibres. The disadvantage of boron co-doping is a lower thermal stability compared to germanium doping alone [148]. Large changes in refractive index due to fibre drawing conditions also impose a problem on the thermal stability of these gratings, especially concerning wavelength stability.

Aluminium

Absorption measurements in MCVD preforms show that Al_2O_3 does not cause any significant absorption at 240 nm. However, an addition of Al_2O_3 to GeO_2 doped silica reduces the 240 nm absorption band. Aluminium is often combined with rare earth dopants for reasons previously mentioned.

Phosphorous

Although the majority of research on the photosensitivity of glass has been directed towards forms of germanium doping, many applications, such as the one investigated by the author, demand co-doping with rare-earth ions. Germanosilicate glass is not an ideal host because the solubility of rare earth ions is low. A better host is achieved by doping silica with phosphorous and small amounts of aluminium, rare earth ions, and/or with tin, boron, or germanium [138]. It is well known, however, that the presence of phosphorous bleaches the absorption band centered around 240 nm and thus reduces the photoinduced refractive index change.

Photosensitivity in phosphorous doped silica has been observed in hydrogen or deuterium loaded fibres after long exposure times [149]. Increase in photosensitivity is achieved by different hydrogen treatment techniques including UV pre-exposure followed by hydrogen out diffusion and thermal treatment ($\sim 80^\circ\text{C}$) of hydrogen loaded fibres [150].

Tin

Tin doping in combination with many other dopants has been reported, with Dong

et al. being the first to demonstrate a photosensitive tin-germanosilicate co-doped fibre [151]. The main advantages of using tin as a dopant are lower losses at 1500 nm and higher thermal stability compared to boron-germanosilicate co-doped fibres. Highly photosensitive tin-phosphorous doped silica fibre fabricated using the MCVD technique has been reported for both Type I and Type II gratings [152]. A refractive index change ($\Delta n \sim 1.2 \times 10^{-3}$) was observed and the fibre had an intrinsic loss of 40 dB/km at 1500 nm.

Pal *et al.* have investigated photosensitivity and thermal stability of Sn-Er-Ge doped silica fibre [96]. Results have shown that this fibre exhibits higher temperature stability than B-Ge doped fibre and would be suitable for temperature sensing up to 500 °C.

Germanium

The first gratings were written in GeO₂ doped silica fibres, and GeO₂ appears still to be the most suitable dopant for highly photosensitive fibres. Under similar manufacturing conditions, the photosensitivity grows linearly with GeO₂ concentration. It is well known that the photosensitivity in GeO₂ doped fibres and preforms is associated with the absorption band near 240 nm. Co-doping with B₂O₃ or SnO₂ increases the photosensitivity significantly, as described previously.

Fluorine

Fluorine is generally not used as a co-dopant for enhancing photosensitivity, possibly because of the decrease of the GODC absorption band at 240 nm. Fluorine has been used as a refractive index decreasing dopant to manufacture fibres with a photosensitive core and cladding. Fluorine has been added to germanium-silicate fibre for the fabrication of CCG gratings [131]. These gratings have shown superior high temperature performance relative to conventional gratings such as Type I, II and IIA [69]. The MCVD process used at the Laboratoire de Physique de la Matière Condensée to manufacture the fibres used by the author in this work did not include any fluorine.

Antimony

Photosensitive antimony (Sb) doped fibres have been reported addressing problems such as photosensitivity and thermal stability [153]. Sb-doped fibres have been deuterium loaded and an index change of $\Delta n \sim 4 \times 10^{-4}$ has been achieved. Photosensitivity was comparable to that of germanium doped fibres fabricated under reduced atmosphere, but improvement in FBG thermal stability below 850 °C has been observed [68, 153].

Nitrogen

It has been shown that nitrogen doped germanosilicate optical fibres have increased levels of photosensitivity [154]. Refractive index changes of $\Delta n = 2.8 \times 10^{-3}$ were achieved using fibres without hydrogen loading. When hydrogen loaded the result was as high as $\Delta n = 1 \times 10^{-2}$. A large amount of hydrogen in nitrogen doped fibres could pose a problem, as the H-N bond absorbs in the third telecommunications window. Grating formation has also been reported in germanium free, nitrogen doped fibres [155]. The grating formation dynamics follow Type IIA behaviour and the results have shown high thermal stability (> 1000 °C).

3.2.3 FBG Decay Models

For FBGs to be widely accepted as temperature sensors, they need to prove their long-term stability. The thermal stability of FBGs is dependent on factors such as the type of fibre used, use of hydrogen loading, and the type of grating written. Two models have been developed to predict the refractive index modulation of fibre Bragg gratings after being annealed [156]. The two models are referred to as the power-law model and the accelerated aging model. The models are described below.

3.2.3.1 Power-Law Model

Instead of using the Bragg gratings peak reflectivity as a measure of the grating strength, the integrating coupling constant (ICC) is chosen. The ICC is a preferred

measurement quantity since it is proportional to the UV-induced refractive-index change, even in the case of non-uniform gratings [156]. The peak reflectivity of a Bragg grating can be calculated from its spectral profile by using

$$R = (1 - T_{min}), \quad (3.6)$$

where T_{min} is the minimum transmission at the Bragg wavelength. The ICC is defined by

$$ICC = \tanh^{-1}(\sqrt{R}). \quad (3.7)$$

For convenience, a normalised ICC, η , is defined and is given by

$$\eta = \frac{\tanh^{-1}(\sqrt{R_{t,T}})}{\tanh^{-1}(\sqrt{R_{0,T}})}. \quad (3.8)$$

where $R_{t,T}$ and $R_{0,T}$ are the peak reflectivities after an annealing time t at a temperature T and the initial reflectivity at a temperature T , respectively.

The decay phenomena of a grating generally follows a decay curve indicative of a ‘power-law’ dependence with time [156]. The power-law model can be described as

$$\eta = \frac{1}{1 + A(t/t_1)^\alpha}, \quad (3.9)$$

where t is the decay time in minutes, A is the power-law factor and α is the power-law decay coefficient. To keep the dimensions constant, a time $t_1 = 1$ minute was introduced. In this form A and α are dimensionless but both depend on temperature.

3.2.3.2 Accelerated Aging Model

In the accelerated aging approach the decay in refractive index is characterised for a given time and temperature combination using an aging parameter referred to as the demarcation energy. The demarcation energy, E_d , is given by

$$E_d = kT \ln(\nu t), \quad (3.10)$$

where k is Boltzmann's constant, T is absolute temperature, t is time and ν is a fitting parameter which is determined from a series of decay measurements.

3.2.3.3 Hydrogen-loading Effects and the Log-time Model

It has been stated that FBGs fabricated in hydrogen-loaded fibres exhibit less thermal stability and accelerated self-erasure compared to FBGs fabricated in unhydrogenated fibre [148, 157]. The power law model does not explain the thermal decay of FBGs inscribed in hydrogen loaded fibre, therefore an alternative model has been developed to better explain this effect [148, 157]. This model is referred to as the 'log-time' model, where the normalised ICC, η , can be expressed as

$$\begin{aligned}\eta &= 1 - K \log\left(\frac{t}{\tau}\right) & \text{for } t > \tau \\ &= 1 & \text{for } t \leq \tau,\end{aligned}\tag{3.11}$$

and K is an empirical constant and τ is temperature dependent. The Arrhenius type relationship for τ is similar to that observed in aging glass and τ can be expressed as

$$\tau = A e^{E_a/RT},\tag{3.12}$$

where $E_a = 105$ kJ/mol and $A = 9 \times 10^{-15}$ min [148].

3.2.4 Fabrication Techniques for Fibre Bragg Gratings

Fibre Bragg gratings were fabricated using two arrangements, one at Victoria University and the other at Swinburne University. Both arrangements used Coherent Inc. frequency doubled (FreD) argon ion lasers which produced 244 nm continuous-wave outputs. The output beam of the FreD has very good uniformity, power, emission direction stability and is horizontally polarised (extinction ratio of 100:1). The spatial coherence properties of the FreD laser resulted in negligible grating bandwidth reduction, which is normally caused by coherence-related decrease in the visibility of replicated interference pattern. Both arrangements used the phase-mask technique with particular variations as explained below.

3.2.4.1 Victoria University FBG Facility

The majority of FBGs used for this work were fabricated using the FBG writing facility at Victoria University. A Coherent Innova FreD laser emitting a power of around 100 mW was utilised, as is illustrated in Figure 3.10. An optical telescope was used to expand the beam to produce a beam spot size of ~ 10 mm. A pinhole

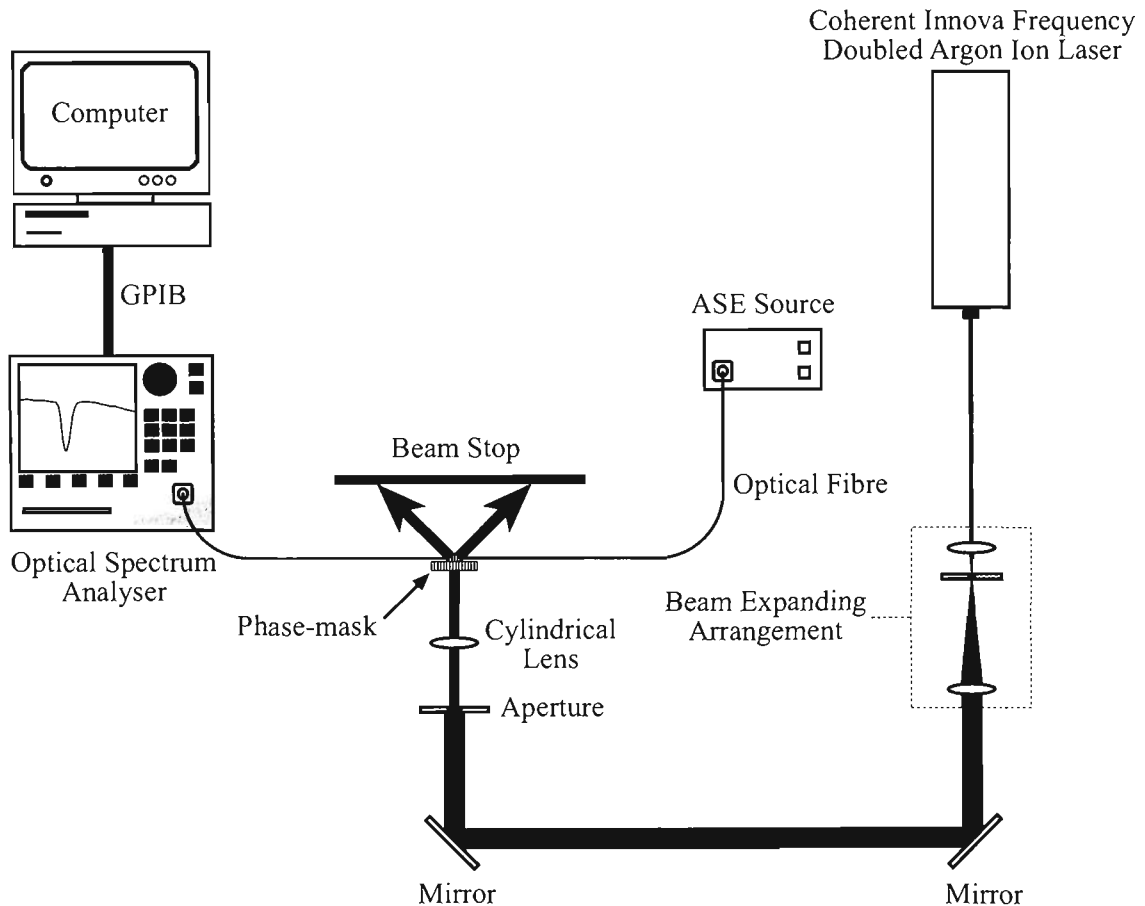


Figure 3.10: Interrogation equipment and optical arrangement used for the fabrication of fibre Bragg gratings using the phase mask technique at Victoria University.

was used within the optical telescope to spatially filter the beam. Steering mirrors were used to re-direct the beam through a known, pre-set aperture. This aperture determined the length of the FBG to be inscribed in the fibre. The laser beam was then focused on to a short length of fibre via a cylindrical lens. The growth of the grating could be monitored in real-time using an OSA and a broad-band light source, as shown in Figure 3.10.

3.2.4.2 Swinburne University FBG Facility

The Swinburne University FBG fabrication facility used by the author utilises a Coherent Saber frequency doubled laser, emitting a power of around 250 mW, and is shown in Figure 3.11. Beam steering mirrors are computer controlled with active

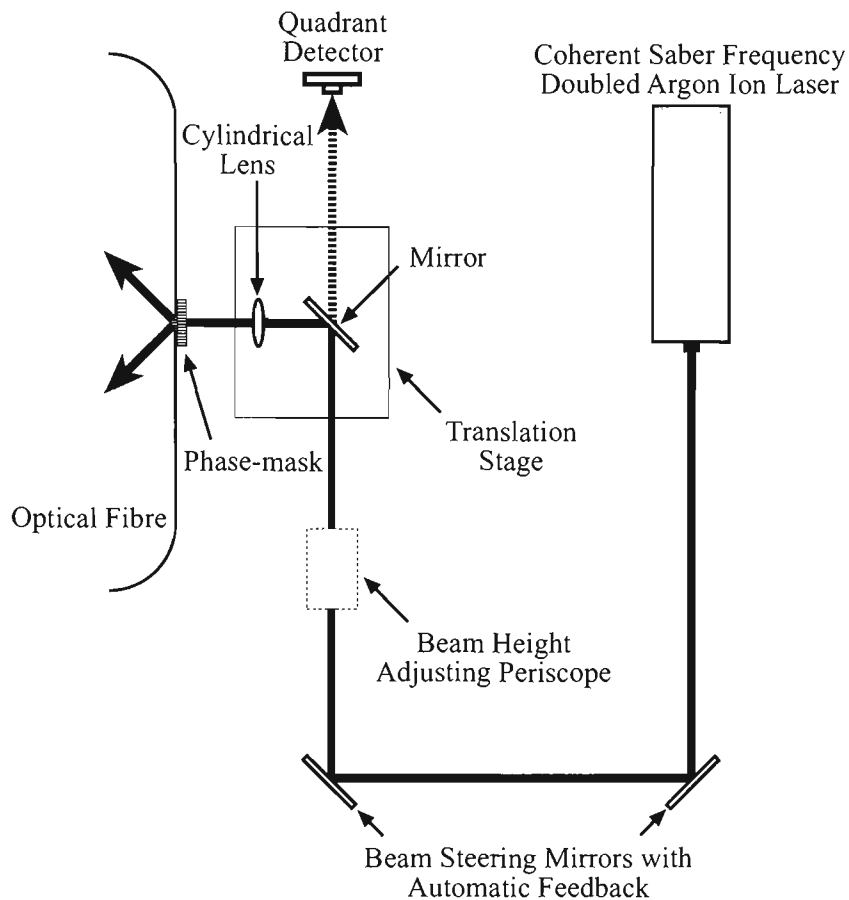


Figure 3.11: Optical arrangement used for the fabrication of fibre Bragg gratings using the phase mask technique at Swinburne University.

feedback provided by a quadrant detector. A periscope was used to adjust the beam height. This was utilised to obtain optimum beam location and stability during the FBG writing process. A steering mirror and cylindrical lens are mounted on a computer controlled Aerotech high precision translation stage which was used to re-direct and focus the laser beam along a short length of the optical fibre. The fibre was pneumatically clamped and its position computer controlled to locate the fibre in a precise position immediately behind the phase-mask. This equipment was mounted on a granite block to further reduce any vibrations that could effect the

grating writing process. User defined parameters, such as apodisation profile, grating length and scanning speed are pre-defined. A tensioning system was used to allow fine control of the final Bragg wavelength. Increased tension would result in a shorter Bragg wavelength when the fibre was removed from the system.

FBGs were written by scanning the laser beam across the phase mask at a rate determined by the user (e.g. a slower scan rate will give a stronger FBG reflectance and larger full-width-half-maximum). The apodised profile was created by dithering the beam; this helps suppress side lobes. This FBG writing system was fully automated and was originally developed by JDS-Uniphase (Australia) to manufacture FBGs for the telecommunications industry. Due to space and access restrictions, the real-time monitoring of FBG growth dynamics is only possible when using long lengths of optical fibre.

The process involved in the fabrication of CCG type gratings was quite different from that of conventional grating writing. It can be classified as a two step process. The first process involves the fabrication of a Type I FBG in optical fibre with particular dopants using the conventional technique as described above. The second stage involves a high temperature treatment of the fibre, as discussed in Chapter 7.

3.2.4.3 FBG Sensor Fabrication

FBG sensor samples were inscribed in all of the fibres fabricated for this work. Table 3.3 shows the FBG fabrication details in the Er^{3+} doped fibres, while Table 3.4 shows the details for FBGs fabricated in the $\text{Er}^{3+}:\text{Yb}^{3+}$ doped fibre samples.

It has been shown that an effective approach to achieving very high UV photosensitivity is by soaking the fibre in hydrogen gas at temperatures ranging from 20-75°C and pressures from ~20 atm to more than 750 atm. This results in diffusion of hydrogen molecules into the fibre core [138]. Therefore, all fibres were hydrogen loaded at elevated pressures and temperatures for prolonged time periods, as indicated in Tables 3.3 and 3.4.

Table 3.3: FBG sensor fabrication details in Er³⁺ doped fibre. Note: λ_B was recorded at room temperature.

Fibre Type	Er1	Er1	Er2	Er3	Er4	Er4
H ₂ Loading Info.						
<i>Time</i> (hrs)	168	72	161	168	72	168
<i>Pressure</i> (atm)	80	123	75	123	67	123
<i>Temperature</i> (°C)	80	55	50	55	95	55
UV Power (W/cm ²) ^a	4	25	7	25	6	25
System Used	Vic.	Swin.	Vic.	Swin.	Vic.	Swin.
Writing Time (min)	9	1	45	0.5	1.5	1
λ_B (nm)	1536.0	1529.5	1532.5	1574.0	1549.0	1565.0
Reflectivity (%)	90	90	50	95	95	95
$\Lambda_{phase-mask}$ (μm)	1.0668	1.0554	1.0668	1.0768	1.0668	1.0768

^a UV power density on optical fibre.

FBGs were inscribed in Er1, Er4, ErYb2 and ErYb3 using both systems described in Section 3.2.4. FBGs in ErYb1 and Er2 were written using only the Victoria University system and FBGs in Er3 were inscribed using the Swinburne University system only. Due to the higher UV power and scanning beam technique adopted by the Swinburne University system, the desired grating strength was achieved in a shorter time period compared to those written with the Victoria University facility. This is evident when comparing writing times for FBGs written in Er1, Er4 and ErYb3 fibre samples in Tables 3.3 and 3.4.

The core composition of Er1, ErYb1 and ErYb3 was the same, apart from the rare earth dopant concentration, and so the FBG growth characteristics of these fibre samples was expected to be comparable. As shown in Figure 3.12, grating growth characteristics in ErYb1 and ErYb3 are similar. The small variation may possibly be attributed to the reproducibility limitation of the Victoria University system, due to the high reliance on manual adjustment. For Er1, a longer time

Table 3.4: FBG sensor fabrication details in $\text{Er}^{3+}:\text{Yb}^{3+}$ doped fibre. Note: λ_B was recorded at room temperature.

Fibre Type	ErYb1	ErYb2	ErYb2	ErYb3	ErYb3
H ₂ Loading Info.					
<i>Time</i> (hrs)	161	161	168	161	168
<i>Pressure</i> (atm)	75	75	123	75	123
<i>Temperature</i> (°C)	50	50	55	50	55
UV Power (W/cm ²) ^a	7	7	25	7	25
System Used	Vic.	Vic.	Swin.	Vic.	Swin.
Writing Time (min)	2.5	9	1.5	3.5	1
λ_B (nm)	1540.0	1535.5	1561.5	1538.0	1565.5
Reflectivity (%)	95	90	90	90	90
$\Lambda_{\text{phase-mask}}$ (μm)	1.0668	1.0668	1.0768	1.0668	1.0768

^a UV power density on optical fibre.

period was required to achieve a reflectance value similar to ErYb3 and ErYb1, as shown in Figure 3.12. This was due to the lower UV power density on the fibre (4 W/cm²) as compared to that used for the FBG fabrication in the ErYb3 and ErYb1 samples (7 W/cm²). Grating growth in Er2 fibre was stopped at approximately 50% reflectance, due to the very long exposure time (45 min). This was a result of the low germanium concentration causing low UV photosensitivity relative to the other rare earth doped fibres used in this work. In a practical situation, this is undesirable as it would increase the fabrication cost of the sensor significantly.

The particular Bragg wavelengths of each FBG sensor sample fabricated were chosen so that fluorescence from the $^4\text{I}_{13/2}$ level of Er^{3+} (as shown in Figure 3.5) could be used as an illumination source. Figure 3.13 illustrates spectra from FBGs inscribed in the rare earth doped fibres using the Victoria University and Swinburne University facilities. The spectra shown are of FBGs prior to any annealing treatment. A reflectivity of $\geq 90\%$ was chosen for the majority of the FBGs fabricated, to allow for sufficient grating strength to remain after annealing treatment, along

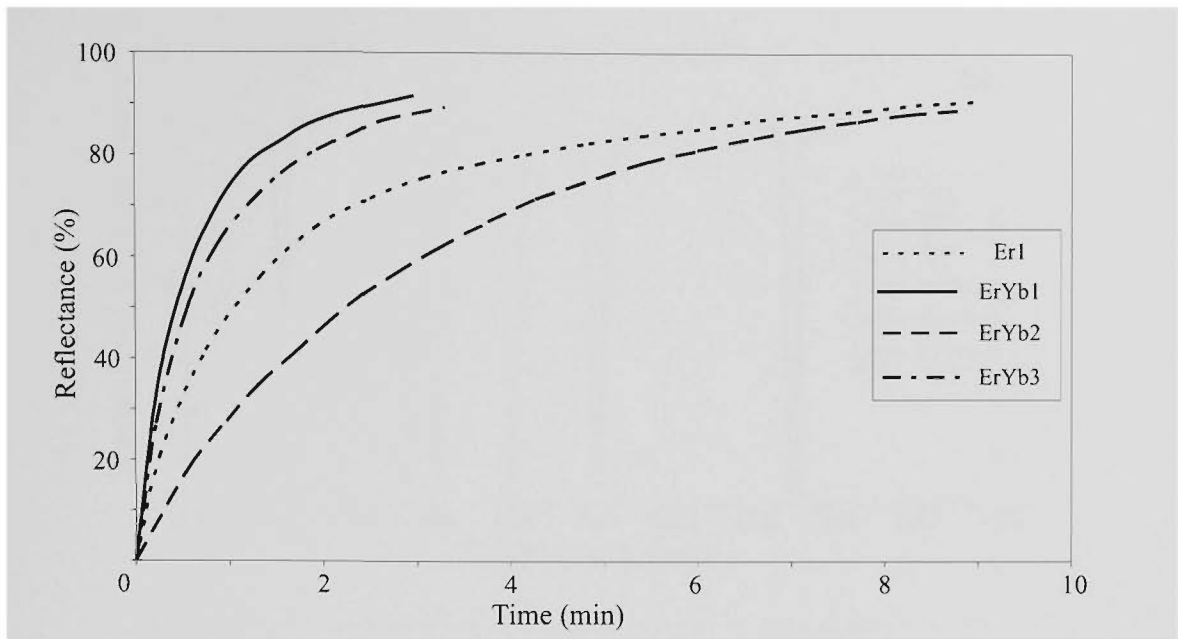


Figure 3.12: Growth rate of Type I Bragg gratings written in hydrogenated Er1, ErYb2, ErYb3 and ErYb1 fibre using the Victoria University system.

with attempting to keep the grating characteristics comparable to those FBG sensors available commercially. The reflectivities of the FBGs shown in Tables 3.3 and 3.4 were recorded prior to annealing using an optical spectrum analyser with a resolution of 0.05 nm. It must be noted that the FBGs fabricated at the Swinburne University facility were 2 mm in length compared to those at Victoria University for which the length was 10 mm.

3.2.4.4 Annealing of FBGs

An initial annealing procedure was necessary for all the FBGs that required temperature and strain calibration. This was performed to remove any residual hydrogen in the fibre. Generally, during this process the FBG suffers an irreversible shift towards the violet end of the spectrum. This would be undesirable during the temperature and strain calibration of the Bragg wavelength. Figure 3.14 shows a typical characteristic of the Bragg wavelength shift during an annealing procedure performed on an FBG inscribed in Er1 doped fibre. The annealing process consisted of heat treatment at 100 °C for a 24 hour period.

It can be clearly seen from Figure 3.14 that the Bragg wavelength experiences an initial rapid shortening of the wavelength which gradually decreases until the Bragg

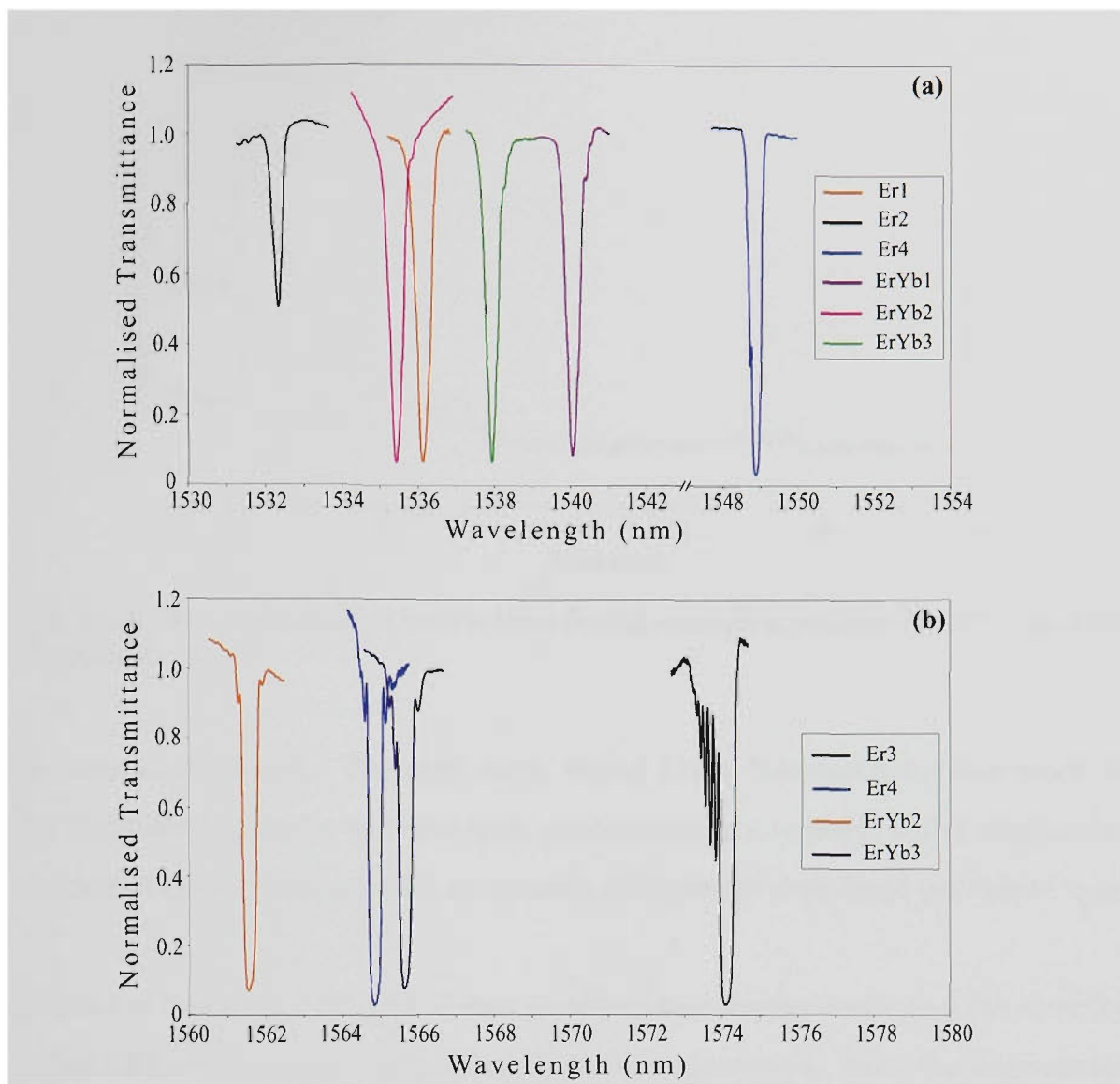


Figure 3.13: Independently normalised spectra of FBGs written in rare earth doped fibre samples using the (a) Victoria University and (b) Swinburne University facilities. Note: Spectra shown in (a) and (b) were recorded using 0.1 nm and 0.05 nm resolution on the OSA, respectively.

wavelength has stabilised after approximately 10 hrs. At this temperature, a small decrease in the strength of the FBG (e.g. reflectance) was observed. This was considered to be insignificant in terms of its effect on the requirement of an FBG based temperature or strain sensor.

3.3 Conclusion

The techniques for the fabrication of the rare earth doped fibres and the Bragg gratings inscribed within them have been presented. The effects that specific dopants have on phenomena such as photosensitivity and high temperature sustainability of

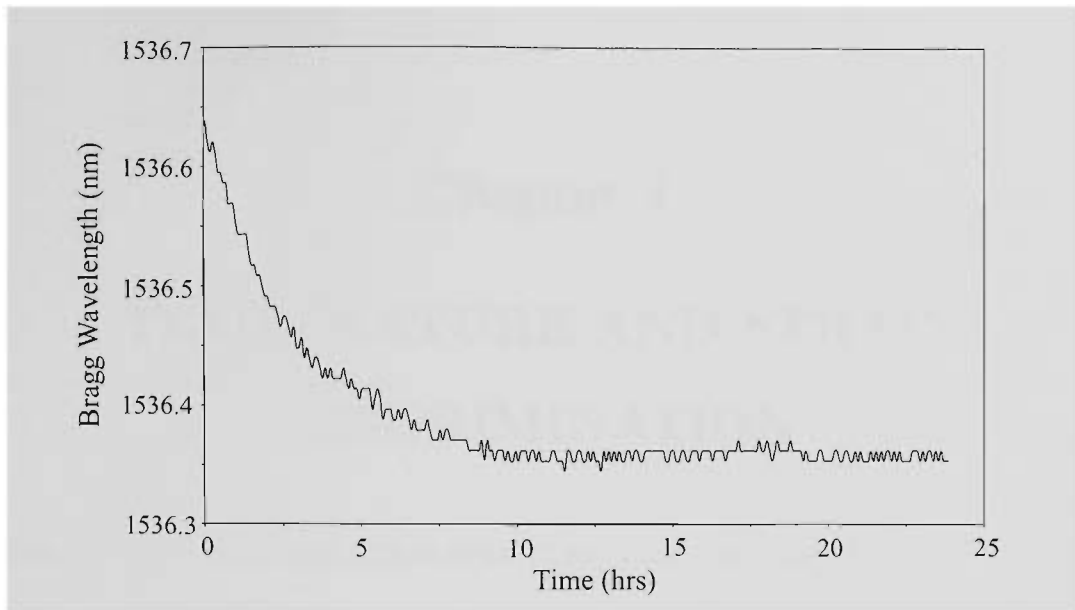


Figure 3.14: Bragg wavelength versus time during annealing process at 100 °C for FBG inscribed in Er1 fibre.

FBGs were summarised. The rare earth doped fibres fabricated for this work required hydrogen loading to increase their photosensitivity to levels which enabled the fabrication of Bragg gratings with acceptable reflectances over short periods of time.

The formulae describing the FIR of two closely spaced energy levels and the sensitivity of the FIR to changes in temperature have been presented. Also, the fluorescence scheme for producing the broad 1550 nm fluorescence from erbium and the appropriate fluorescing levels from erbium and ytterbium for FIR measurements have been discussed.

Chapter 4

TEMPERATURE AND STRAIN DISCRIMINATION

Fibre-optic temperature and strain sensors are important for simultaneously detecting strain and temperature in a range of applications. However, strain measurement is often affected by temperature variations and vice-versa. In general, if two parameters are approximately linear functions of both temperature and strain they can be calculated using a matrix inversion, as explained in Section 4.1. However, if the sensor possess a relatively large cross-sensitivity and non-linear response functions to temperature and strain (e.g. non-linear thermo-optic effect of FBGs), large errors are introduced. The sensor scheme presented here takes advantage of a strain independent temperature measurement (e.g. FIR technique) which should reduce these errors in the matrix inversion.

This Chapter also presents various techniques for de-convolving temperature and strain for the particular sensing scheme investigated here, for example, the non-linear dependencies of the FIR and FBG on temperature are taken into account. Various FBG spectral analysis techniques are investigated and their individual characteristics compared.

4.1 Matrix Analysis (Method A)

The temperature and strain de-convolution process can be described using a matrix that maps the temperature and strain ranges to the outputs of the observable measurands. For the matrix technique to be applicable, these outputs should have linear dependencies upon temperature and strain. To recover temperature and strain vari-

ations from a single sensing fibre, measurements are made on two parameters at the same time. Provided that both measurement schemes are not influenced equally by the two measurands of interest, a set of simultaneous equations can be developed to describe the measurement process and recover the required information.

The parameters that can be measured, ϕ_1 and ϕ_2 , are usually assumed to be related to the desired measurands (eg. temperature and strain) through a linear transform represented in matrix format [158] as;

$$\Phi = K\Omega, \quad (4.1)$$

where

$$\Phi = \begin{bmatrix} \phi_1 \\ \phi_2 \end{bmatrix}, \quad (4.2)$$

and

$$\Omega = \begin{bmatrix} T \\ \epsilon \end{bmatrix}, \quad (4.3)$$

and

$$K = \begin{bmatrix} K_{1T} & K_{1\epsilon} \\ K_{2T} & K_{2\epsilon} \end{bmatrix}. \quad (4.4)$$

K is usually referred to as the transfer matrix from Ω to Φ or the characteristic matrix of the sensor. Provided that the determinant of K , $\Delta = K_{1T}K_{2\epsilon} - K_{2T}K_{1\epsilon}$ is not equal to zero, the above equation can be inverted and T and ϵ changes can be calculated as

$$\Omega = K^{-1}\Phi. \quad (4.5)$$

In the above equation K^{-1} represents the inverse of matrix K and can be written as

$$K^{-1} = \frac{K'}{\Delta}, \quad (4.6)$$

with K' equal to

$$K' = \begin{bmatrix} K_{2\epsilon} & -K_{1\epsilon} \\ -K_{2T} & K_{1T} \end{bmatrix}, \quad (4.7)$$

with the general solution for T and ϵ given by

$$T = \frac{K_{2\epsilon}\phi_1 - K_{1\epsilon}\phi_2}{\Delta} \quad (4.8)$$

and

$$\epsilon = \frac{K_{1T}\phi_2 - K_{2T}\phi_1}{\Delta}. \quad (4.9)$$

When applied to the sensor scheme investigated here, where the parameters ϕ_1 and ϕ_2 represent the FIR and Bragg wavelength, respectively, the solutions for absolute temperature and strain measurement can be given by

$$T = \frac{K_{2\epsilon}(\phi_1 - \phi_{R_0}) - K_{1\epsilon}(\phi_2 - \phi_{\lambda_0})}{\Delta} \quad (4.10)$$

and

$$\epsilon = \frac{K_{1T}(\phi_2 - \phi_{\lambda_0}) - K_{2T}(\phi_1 - \phi_{R_0})}{\Delta}, \quad (4.11)$$

where ϕ_{R_0} and ϕ_{λ_0} are defined as the FIR and Bragg wavelength, respectively, at 0°C and $0\ \mu\epsilon$. In this work, these constants were extrapolated from the matrix elements.

The recovery of temperature and strain values is influenced by a range of errors that include the precision with which ϕ_1 and ϕ_2 can be determined, and any errors present in the estimation of the elements in the matrix K , which are usually determined from calibration experiments.

4.1.1 Limitations and Assumptions

The resolution of a sensor can be limited by the errors in the transfer matrix elements K and the measurand matrix Φ . This has been previously described and is given by the following matrix equation [158]:

$$\delta\Omega = \frac{K'_0\delta\Phi\Delta_0 + \delta K'\Phi_0\Delta_0 + \delta K'\delta\Phi\Delta_0 - K'_0\Phi_0\Delta^*}{\Delta_0(\Delta_0 + \Delta^*)}, \quad (4.12)$$

where

$$\delta K' = K' - K'_0 = \begin{bmatrix} K_{2\epsilon}\delta_{2\epsilon} & -K_{1\epsilon}\delta_{1\epsilon} \\ -K_{2T}\delta_{2T} & K_{1T}\delta_{1T} \end{bmatrix}, \quad (4.13)$$

and

$$\Delta^* = \Delta - \Delta_0 = K_{1T}K_{2\epsilon}(\delta_{1T} + \delta_{2\epsilon} + \delta_{1T}\delta_{2\epsilon}) - K_{1\epsilon}K_{2T}(\delta_{1\epsilon} + \delta_{2T} + \delta_{1\epsilon}\delta_{2T}). \quad (4.14)$$

For the known error conditions δ_{ij} and $\delta\phi_i$ ($i = 1, 2; j = T, \epsilon$), which are determined from the error estimations from the experimental data fits, the errors in T and ϵ can be evaluated directly by using Equation 4.12 [158]. The resultant error information would indicate the resolution limitation of the sensor being evaluated.

When applying the calibration results for the sensors investigated in Chapters 5 and 6 to Equation 4.13, it was found that the errors in the transfer matrix elements, δK_{ij} , were less than 1%, and so for simplicity, it was assumed that the sensor resolution would only be limited by the errors in ϕ_1 and ϕ_2 ($\delta\phi_1$ and $\delta\phi_2$). All sensor performance analyses were performed using negligible transfer matrix element errors, as described below.

Using the expressions described above, the associated errors can be examined. The most obvious form of error is where the errors within the transfer matrix can be neglected and all the errors can be attributed to the inaccuracies in determining ϕ_1 and ϕ_2 . The measurement error in this case can be described using a modified version of Equation 4.12 [158];

$$\delta\Omega = \frac{K'\delta\Phi}{\Delta}. \quad (4.15)$$

Writing Equation 4.15 in terms of δT and $\delta\epsilon$, the maximum error in T may be expressed as:

$$|\delta T| \leq \frac{|K_{2\epsilon}||\delta\phi_1| + |K_{1\epsilon}||\delta\phi_2|}{|\Delta|} \quad (4.16)$$

and for ϵ it is given by:

$$|\delta\epsilon| \leq \frac{|K_{2T}||\delta\phi_1| + |K_{1T}||\delta\phi_2|}{|\Delta|}. \quad (4.17)$$

It is evident from these expressions that if a zero exists in the matrix then the maximum error in T and ϵ would reduce. In the case of the work presented in this thesis, the FIR exhibits a strain dependence that is consistent with zero (e.g. $K_{1\epsilon} = 0$). Therefore, the maximum error in T may now be expressed as:

$$|\delta T| \leq \frac{|K_{2\epsilon}||\delta\phi_1|}{|\Delta|}. \quad (4.18)$$

4.2 Non-Linear Analysis of FIR (Method B)

The matrix analysis method is most commonly adopted to de-convolve the required temperature and strain information from two independent sensing elements that have linear dependencies on both temperature and strain. In this work, a linear approximation for the dependence of the FIR to temperature has been used with reasonable errors over relatively narrow temperature ranges (as shown in Chapters 5 and 6). If an extended temperature range is required by the sensor scheme, the temperature and strain errors of the sensor system increase significantly when using a linear assumption. The inherent strain independence of the FIR technique allows for alternative analysis methods to be used in an attempt to reduce the errors of the sensing scheme through the use of more realistic non-linear equations.

4.2.1 FIR Temperature and Strain Dependence

A unique characteristic of the FIR technique for the measurement of temperature is that it exhibits a strain dependence that is consistent with zero. The assumption of a zero strain dependence allows for various methods of de-convolving temperature and strain without increasing the number of fitting parameters significantly and, therefore, with no increase in associated errors. With this assumption, no cross-sensitivity consideration is required to determine the temperature from the

FIR. This information could then be used to correct the temperature and strain cross-sensitivity of the Bragg wavelength, which would enable the required strain information to be deduced.

Since the FIR has a dependence upon temperature that is non-linear, as described by Equation 3.2, and a strain dependence that is consistent with zero, we may write

$$\phi_R = A_R T^2 + B_R T + \phi_{R_0} + K_{1\epsilon} \epsilon, \quad (4.19)$$

where ϕ_R represents the FIR and A_R , B_R and ϕ_{R_0} are appropriate constants obtained from empirical fits to the data. If we assume the strain dependent constant, $K_{1\epsilon}$, is equal to zero, the absolute temperature, T , is given by the following quadratic solution

$$T = \frac{-B_R + \sqrt{B_R^2 - 4A_R(\phi_{R_0} - \phi_R)}}{2A_R}. \quad (4.20)$$

The negative solution of the quadratic was disallowed on physical grounds. In this form, the coefficient ϕ_{R_0} is defined as the absolute FIR at a temperature of 0°C. For simplicity, only a second order polynomial is used, which is expected to give a reasonable approximation of the improved temperature precisions compared to the matrix analysis. Higher order polynomial fits should result in slight improvements in precision, particularly at extended temperature ranges, but were not investigated in this work, due to the increased complexity of the expressions.

Using the temperature information acquired from the FIR technique, the strain information could be deduced from the FBG sensing component by correcting its temperature dependence. Assuming linear dependencies of the Bragg wavelength upon temperature and strain, the absolute strain can be deduced by

$$\epsilon = \frac{\phi_\lambda - \phi_{\lambda_0} - TK_{2T}}{K_{2\epsilon}} \quad (4.21)$$

where ϵ is the absolute strain, ϕ_λ is the measured data in terms of the Bragg wavelength, and K_{2T} and $K_{2\epsilon}$ are the coefficients deduced from the matrix analysis. The

constant ϕ_{λ_0} was extrapolated from the matrix elements K_{2T} and $K_{2\epsilon}$.

4.2.2 Non-Linear Temperature Dependence of Bragg Wavelength (Method C)

The techniques described in Sections 4.1 and 4.2.1 assume the Bragg wavelength has a linear dependence upon both temperature and strain. A fibre Bragg grating has been shown to have a periodic variation of the refractive index along the fibre core, as described by Equation 2.1. Usually, over narrow temperature ranges the dependence of the Bragg wavelength to temperature has been approximated to be linear. Recently, it has been shown that the temperature dependence of the Bragg wavelength is better described by a combination of thermal expansion and the non-linear thermo-optic effect [159–161]. Since the thermo-optic effect creates a change in effective refractive index of the fibre core, the shift of the Bragg wavelength, ϕ_λ , can be expressed as

$$\frac{\Delta\phi_\lambda}{\phi_\lambda} = (1 - p_e) \frac{\Delta L}{L} + \frac{\Delta n}{n}, \quad (4.22)$$

where p_e is the thermo-elastic coefficient of the fibre (≈ 0.22 for fused silica glass), $\Delta L/L$ is the strain induced in the fibre arising from the thermal expansion and $\Delta n/n$ is the fractional refractive index change due to the thermo-optic effect [159]. Alternatively, the Bragg wavelength dependence upon both temperature and strain may be written, more generally as,

$$\phi_\lambda = A_\lambda T^2 + B_\lambda T + \phi_{\lambda_0} + K_{2\epsilon} \epsilon, \quad (4.23)$$

where A_λ , B_λ and ϕ_{λ_0} are appropriate constants obtained from fits to FBG calibration data. The linear strain coefficient $K_{2\epsilon}$ is obtained from the matrix analysis. Using Equation 4.20 to determine the temperature, the strain information could be retrieved from a modified version of Equation 4.21, which is given by,

$$\epsilon = \frac{\phi_\lambda - \phi_{\lambda_0} - (A_\lambda T^2 + B_\lambda T)}{K_{2\epsilon}}. \quad (4.24)$$

This technique requires five fitting parameters to de-convolve the temperature and strain values, compared to the previous two techniques described which require only four.

4.3 Analysis of FBG Spectra

Numerous techniques have been proposed and developed for the interrogation of the Bragg wavelength, as described in Chapter 1. Spectrally based techniques require the interpretation of a captured FBG spectrum into a known quantity of strain or temperature. Three methods of FBG spectral profile interpretation are investigated in this work to determine which technique shows superior temperature and strain accuracy. Their advantages and disadvantages are also highlighted.

4.3.1 Minima Method

The simplest form of analysing the Bragg wavelength is denoted as the “Minima” method. This technique, depending on sensor design, analyses a transmitted or reflected FBG spectrum by determining the minimum or maximum intensity, respectively. The corresponding wavelength to this intensity is then referred to as the Bragg wavelength. Computationally, this method requires the least processing relative to the other techniques proposed in this thesis, but is very susceptible to signal noise and resolution limitations. This degradation in resolution is due to the small dependence of wavelength on intensity in the region of the Bragg wavelength, compared to the Half-Maximum intensity region of the FBG spectrum. There will be a greater influence of this problem with FBGs that have a relatively broad full-width-half-maximum or with chirped profiles. Also, the inherent characteristics of this method involve extracting a single intensity with its corresponding wavelength. The technique does not take into consideration any noise that could be embedded within the FBG spectra. This is most critical in the interrogation of a transmitted spectrum from a strong FBG (transmittance $< 10\%$), where its Bragg intensity could be encroaching the noise floor.

4.3.2 Half-Maximum Method

The second technique used was denoted as the ‘‘Half-Maximum’’ method. Initially, this technique normalizes an FBG spectrum before identifying the maximum reflected intensity. The two half-maximum intensities (50% of the normalised FBG reflected intensity), together with their corresponding wavelengths, are recorded. The mid-point of these two wavelengths is defined as the Bragg wavelength. This technique is explained in greater detail below.

As shown in Figure 4.1, an FBG spectrum can be modelled with a simple Gaussian function, which is given by

$$f(x) = e^{-ax^2}, \quad (4.25)$$

where $f(x)$ and x may represent the reflected intensity profile of an FBG and wavelength, respectively. Assuming that $f(x) = 0.5$, a pair of solutions can be determined for the half-maximum intensities of the FBG, which is given by

$$x = \pm \sqrt{\frac{-\ln(0.5)}{a}}. \quad (4.26)$$

Therefore, the Bragg wavelength, which in this case is denoted as x_0 , can be determined with the expression

$$x_0 = \frac{x_1 + x_2}{2}, \quad (4.27)$$

where x_1 and x_2 represent wavelengths at the half-maximum points.

This method results in increased sensitivity due to the high dependence of wavelength to intensity in the half-maximum regions of the FBG spectra. Compared to the Minima method, the Half-Maximum method requires additional computational processing to determine the Bragg wavelength due to the increased complexity of the spectral interrogation and mathematical processing.

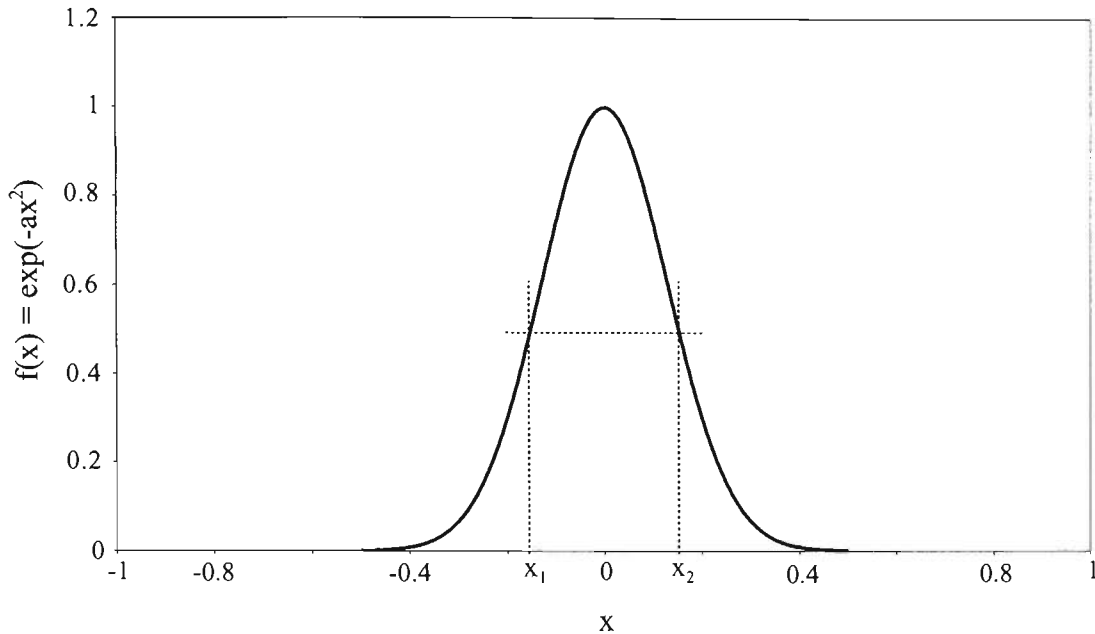


Figure 4.1: Reflected FBG spectrum modelled with a Gaussian function, which also includes regions used for determining the Bragg wavelength by the Half-Maximum method.

4.3.3 Weighted Average Method

The final technique in determining the Bragg wavelength is referred to as the “Weighted Average” method. As shown previously, an FBG spectrum can be modelled using a simple Gaussian, which is shown in Figure 4.2. Therefore, the Weighted Average method is given by

$$x_0 = \frac{\sum_{x_1}^{x_2} e^{-ax^2} x}{\sum_{x_1}^{x_2} e^{-ax^2}}, \quad (4.28)$$

where x_0 may represent the Bragg wavelength. The Gaussian function may represent the Bragg reflectance at a particular wavelength, x , and the limits, x_1 and x_2 , are defined in the regions where the reflectance of the Bragg grating approaches zero. The marked region within the limits shown in Figure 4.2 defines the region used for the calculation of the weighted average to determine the Bragg wavelength. In cases where the FBG spectral profile exhibits relatively low sensitivity in the half-maximum intensity region and where high levels of noise exist throughout the FBG spectrum, the Weighted Average method has advantages relative to the techniques discussed in Sections 4.3.1 and 4.3.2. However, this technique requires the most computational processing, relative to the other techniques proposed in this work.

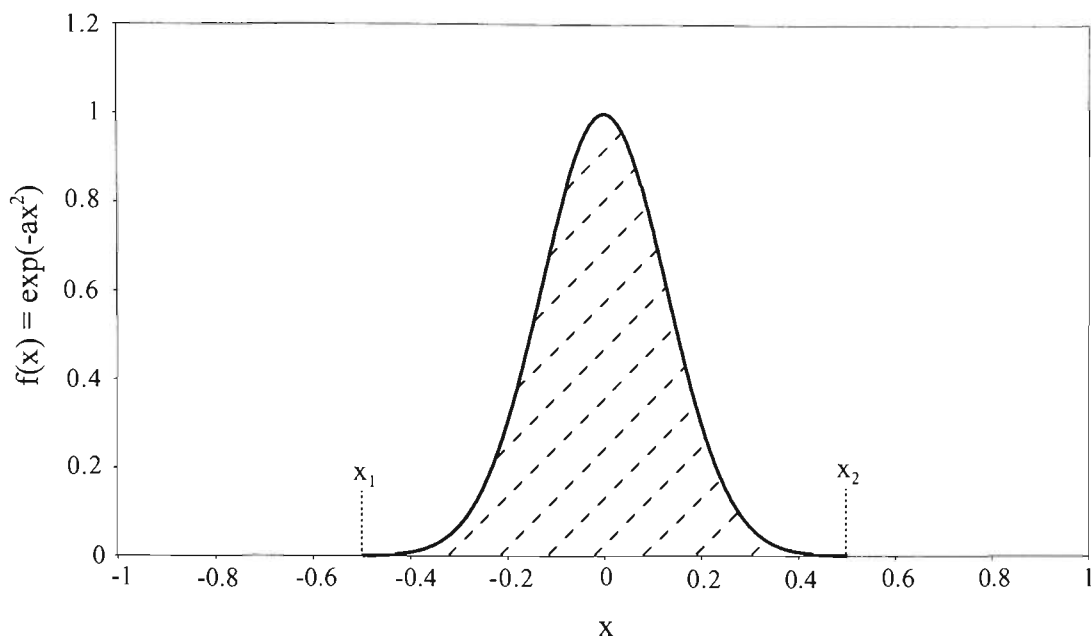


Figure 4.2: Reflected FBG spectrum modelled with a Gaussian function, which also includes regions used for determining the Bragg wavelength by the Weighted Average method.

4.4 Conclusions

Various techniques for the de-convolution of temperature and strain using a combination of the FIR and Bragg wavelength shift have been presented. The general matrix inversion is discussed for sensing elements that have linear dependencies upon both temperature and strain. De-convolution techniques unique to the sensing scheme investigated in this thesis are presented. These include taking into consideration the strain independence and non-linear temperature dependence of the FIR, and the non-linear temperature dependence of the Bragg wavelength shift.

Three different techniques for FBG spectral analysis were presented. Each technique has its distinct advantages and disadvantages, either in terms of accuracy and resolution, or processing speed. It is anticipated that the Half Maximum and Weighted Average methods produce the best temperature and strain precisions, although requiring the most complex computational processing.

Chapter 5

ERBIUM BASED SENSORS

This chapter, details investigations of erbium doped fibre combined with FBGs for potential use for simultaneous temperature and strain measurement. Combinations of various excitation power and wavelengths, and rare earth doped fibre lengths are investigated. Changes in these parameters will result in an error in the FIR temperature measurement, which would also contribute to a strain error deduced from the Bragg wavelength shift. Calibrations were performed on sensor samples fabricated from fibres Er1, Er3 and Er4. Performance comparisons in terms of root-mean-square temperature and strain errors were made between sensor configurations (e.g. FBG inscribed in doped fibre vs FBG spliced in close proximity to doped fibre), variations in erbium concentration of the doped fibre and fibre length.

5.1 FIR Wavelength Ranges

The wavelength ranges over which the fluorescence intensities were integrated were chosen to select fluorescence from the thermalising levels of interest, while avoiding the region of overlap between the two peaks. In the region of fluorescence peak overlap, the temperature sensitivity tends to diminish. In addition, the extent of linearity of the ratio with temperature needs to be considered when choosing the appropriate wavelength bands. Equation 5.1 shows one of the sets of wavelength ranges chosen to calculate the FIR, which is denoted as *FIR1*. It is given by

$$FIR1 = \frac{\sum_{515}^{533} I}{\sum_{543}^{561} I}, \quad (5.1)$$

where I represents the intensity at each wavelength with the wavelength limits of the summation given in nanometres. Extensive analysis has been performed on optimising the FIR wavelength ranges from the ${}^2\text{H}_{11/2}$ and ${}^4\text{S}_{3/2}$ levels in erbium [51, 162]. The responsivity, power ratio and sensitivity for a number of possible wavelength bands that correspond to commercially available filters were compared. An alternative set of wavelength bands that have been found to exhibit a maximum sensitivity to temperature using a specific erbium doped silica fibre were also chosen for this work [162]. This ratio, denoted here as $FIR2$ is given as

$$FIR2 = \frac{\sum_{515}^{525} I}{\sum_{555}^{565} I}, \quad (5.2)$$

The two fluorescence intensity ratios proposed for this work will be compared in terms of their performance when applied to simultaneous temperature and strain measurement using the FIR and Bragg wavelength shift.

5.2 Pump Power and Wavelength Effects

The dependence of the pump power and wavelength on the fluorescence properties of erbium were investigated to quantify the effects that these parameters have on the measurement of temperature.

Measurements of green fluorescence spectra from Er1 were recorded for excitation wavelengths between 792 nm and 815 nm using a 10 cm length of doped fibre. The pump power during the tests was 670 ± 10 mW from a Ti:Sapphire laser. For the analysis of the FIR, counter-propagating green fluorescence was captured via an OSA using the arrangement discussed in Section 5.5.

The normalised FIR versus pump wavelength is shown in Figure 5.1 (the wavelength bands denoted by $FIR1$ were used for this analysis). This figure illustrates the region at which the FIR exhibits the smallest dependence to a variation in wave-

length is at ≈ 803 nm. A shift of one nanometre in this region will induce a 0.1% error in the FIR measurement, as opposed to an error of 3.2% if a shift of the same

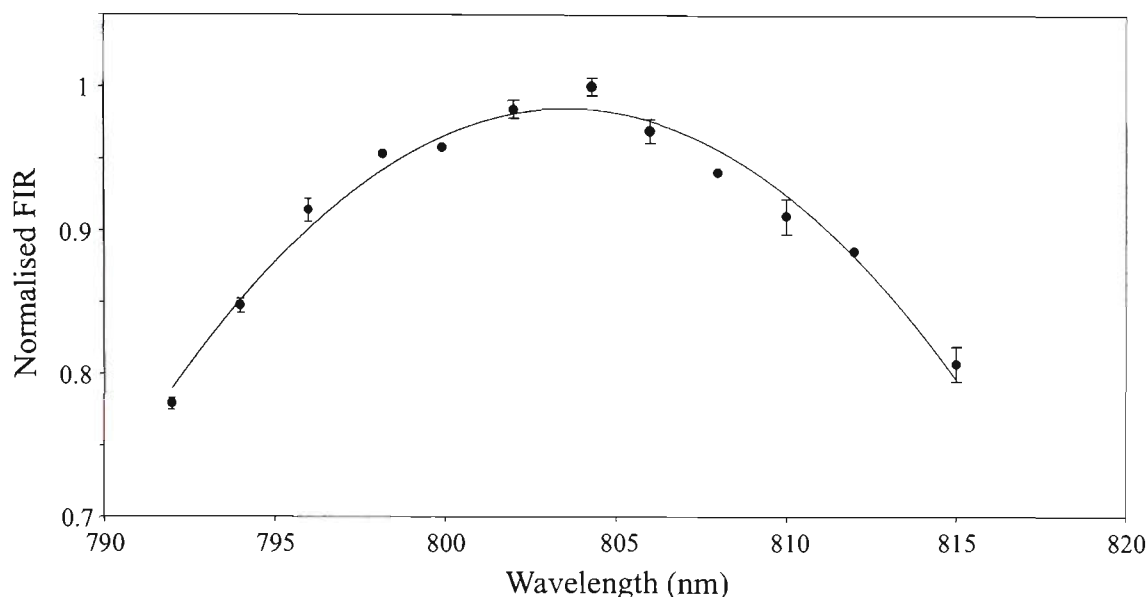


Figure 5.1: Normalised FIR versus pump wavelength for Er1 fibre. Note: The solid line is a guide only.

magnitude occurred with a pump wavelength of ≈ 793 nm. The data presented here for Er1 are comparable to results obtained for the other Er fibres. Also, these results are consistent with other work for Er^{3+} doped fibre [163].

The sensing scheme investigated here also utilises the fluorescence from the ${}^4\text{I}_{13/2}$ level in Er^{3+} as a broadband light source for the interrogation of FBGs. Figure 5.2 shows the fluorescence intensities from the energy levels of interest versus pump wavelength. The fluorescence intensities are calculated by summing the intensities over the wavelength bands, 515-565 nm (${}^2\text{H}_{11/2}$ and ${}^4\text{S}_{3/2}$ fluorescence) and 1500-1600 nm (${}^4\text{I}_{13/2}$ fluorescence). The pump power used for this test was 670 mW. It can be seen that at the wavelength at which the FIR is most stable (≈ 803 nm), sufficient fluorescence is generated from both fluorescence bands.

Pump power effects of the FIR of Er1 fibre were measured for launched pump powers between 30 and 600 mW, using a pump wavelength of 800 nm from a Ti:Sapphire

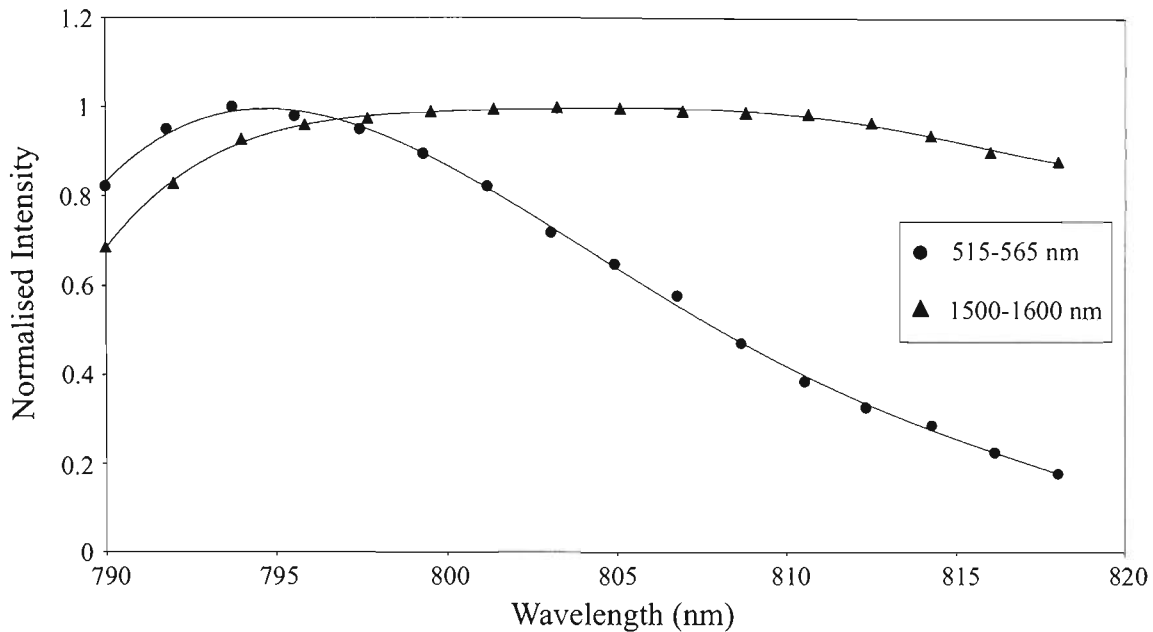


Figure 5.2: Fluorescence intensity versus pump wavelength for Er1 fibre. The fluorescence intensity from both bands has been independently normalised. Note: The solid lines are a guide only.

laser. Pump power was measured using a Coherent Fieldmaster power meter prior to the pump light being launched into communications fibre via a microscope objective. The doped fibre was spliced to this communications fibre.

Figure 5.3 shows the FIR rate of change versus pump power, calculated from the fluorescence spectra using the wavelength ranges shown in Equation 5.1. It can be seen that the FIR sensitivity increases linearly as the pump power is reduced. Assuming a linear temperature dependence of $FIR1$, a 1% power fluctuation would induce temperature errors of 0.06 and 0.09 °C for pump powers of 50 and 500 mW, respectively.

It should be noted that the high pump powers used in this experiment would be impractical for a sensor prototype due to the cost of such high powered laser sources. A sensor prototype would comprise a fibre pigtailed laser diode coupled with specific optical fibre couplers. This would reduce pump power losses in the system. This would enable practical pump powers of the order of tens of milliwatts to be used.

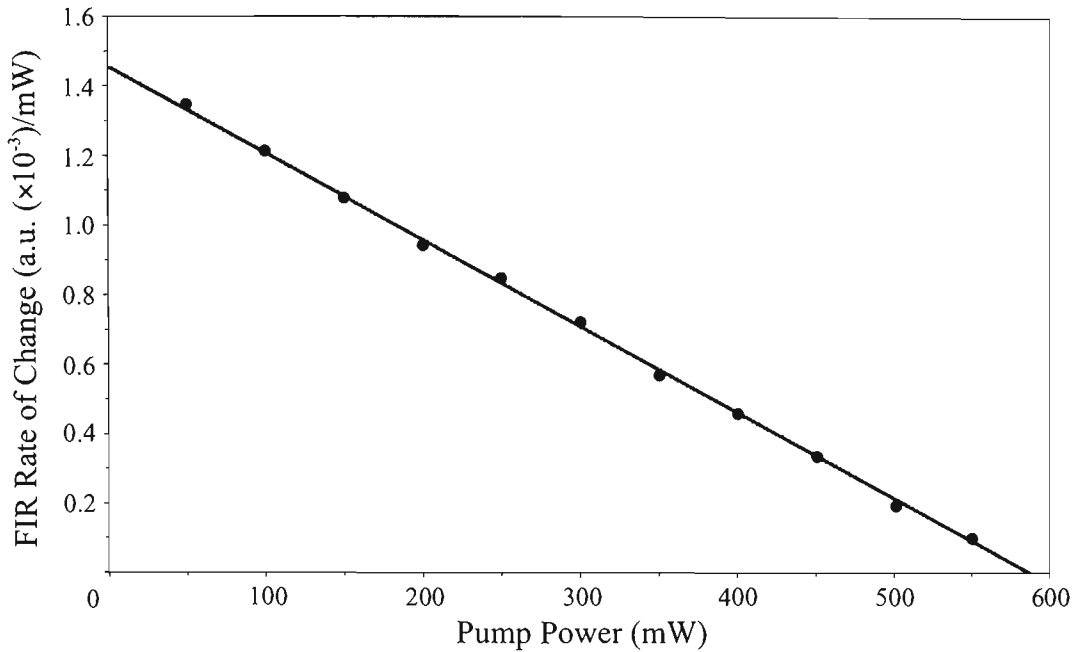


Figure 5.3: FIR rate of change versus pump power for Er1 fibre (note: solid line represents a linear fit).

5.3 Doped Fibre Length

The effect of doped fibre length on the green fluorescence from erbium was also investigated. Fluorescence intensity measurements were made for doped fibre lengths up to 0.5 m. Fluorescence spectra were recorded from Er1 (high doping concentration) and Er4 (low doping concentration) fibre, for which the pump power was 670 mW. As before, the pump power was measured prior to being coupled into the fibre via a microscope objective. The pump wavelength used for both fibre types was 800 nm. Co-propagating fluorescence was captured by an OSA with 5 nm resolution. The fluorescence intensity versus doped fibre length and fluorescence spectra for various lengths of Er1 and Er4 are illustrated in Figure 5.4 for the green fluorescence from Er^{3+} . Figure 5.4(a) shows that the green fluorescence from the fibre with the higher Er^{3+} concentration (Er1) begins to saturate at lengths greater than 30 cm. This thesis is aimed at developing a point sensor; therefore the region of interest is in lengths < 20 cm. It can be seen that neither doped fibre suffers from a decrease in green fluorescence due to excited state absorption. Also, as expected, the fibre with the higher Er^{3+} concentration demonstrated higher levels of fluorescence for short lengths of fibre.

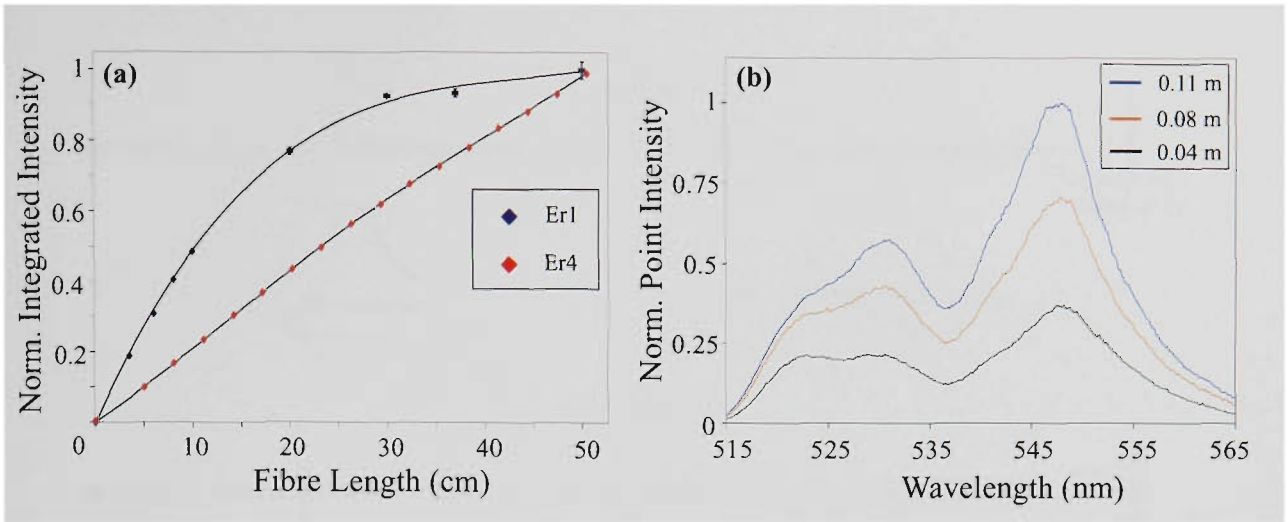
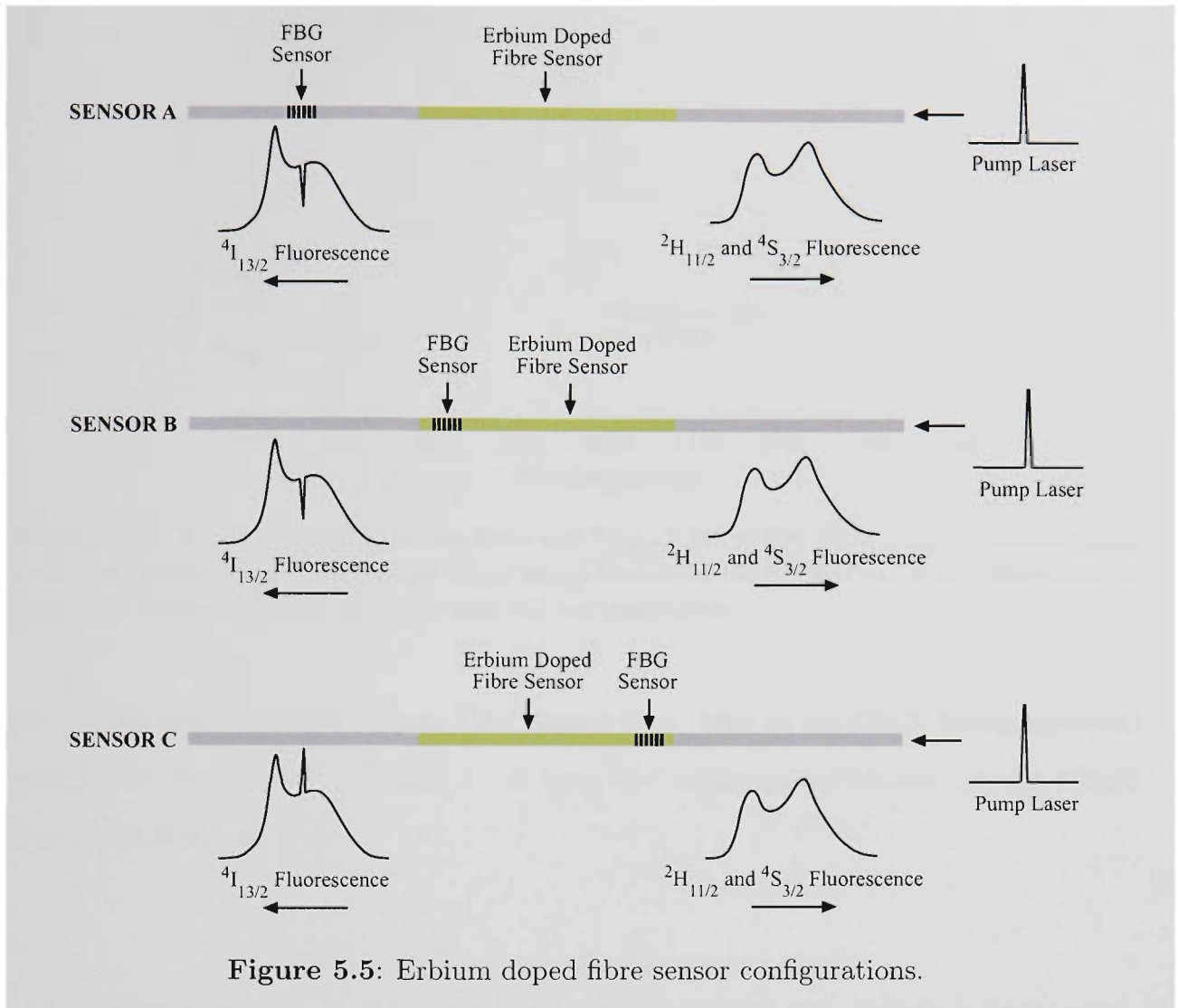


Figure 5.4: (a) Independently normalised fluorescence intensity (integrated over 515 - 565 nm) versus doped fibre length for Er1 and Er4 (note: solid lines are a guide only) and (b) normalised fluorescence spectra at various Er1 fibre lengths.

The dependence of the FIR upon doped fibre length, of around 10 cm, for both the Er1 and Er4 samples was investigated. A 2.5% variation of the doped fibre length would result in a 0.8 °C and 0.6 °C error for Er1 and Er4 doped samples, respectively. This was calculated using the FIR dependence upon doped fibre length and the linear temperature sensitivity, which was deduced for each of the sensors calibrated in Section 5.6. This parameter would only be an important consideration in the case of commercialisation of the sensor. Commercially available sensors would require appropriate tolerances of doped fibre length during production so that each individual sensor would not require individual calibration.

5.4 Erbium Doped Sensor Configurations

A number of erbium doped sensor samples were prepared. These sensors were fabricated in three different configurations as shown in Figure 5.5. All sensors were configured so that counter-propagating green fluorescence and co-propagating $^4I_{13/2}$ fluorescence were detected by an OSA. An important consideration when designing the sensors was the location of the FBG relative to the doped fibre. For sensors adopting Sensor A configuration, the FBG was inscribed in Corning SMF28 communications fibre and spliced in close proximity to the Er^{3+} doped fibre. This



configuration resulted in a transmitted FBG spectrum being observed by the detection system (in this case an OSA), as illustrated in Figure 5.6. For sensors adopting Sensor B configuration, FBGs in the Er^{3+} doped fibres were inscribed 10 mm from one particular end. This was done to minimise the Bragg grating spectral profile being ‘washed out’, due to the $^4I_{13/2}$ fluorescence being emitted from the doped fibre between the FBG and the detector. Sensor C configuration was similar to that of Sensor B configuration. The difference was that the FBG was inscribed in a region of the doped fibre furthest from the detection system. This resulted in a reflected FBG spectrum being observed, which is in contrast to the Sensor B configuration, where the detection system captured a transmitted FBG spectrum.

Table 5.1 shows the physical dimensions and configurations of all the sensor samples calibrated in this work. For Sensor 1, an FBG was inscribed in SMF28 fibre

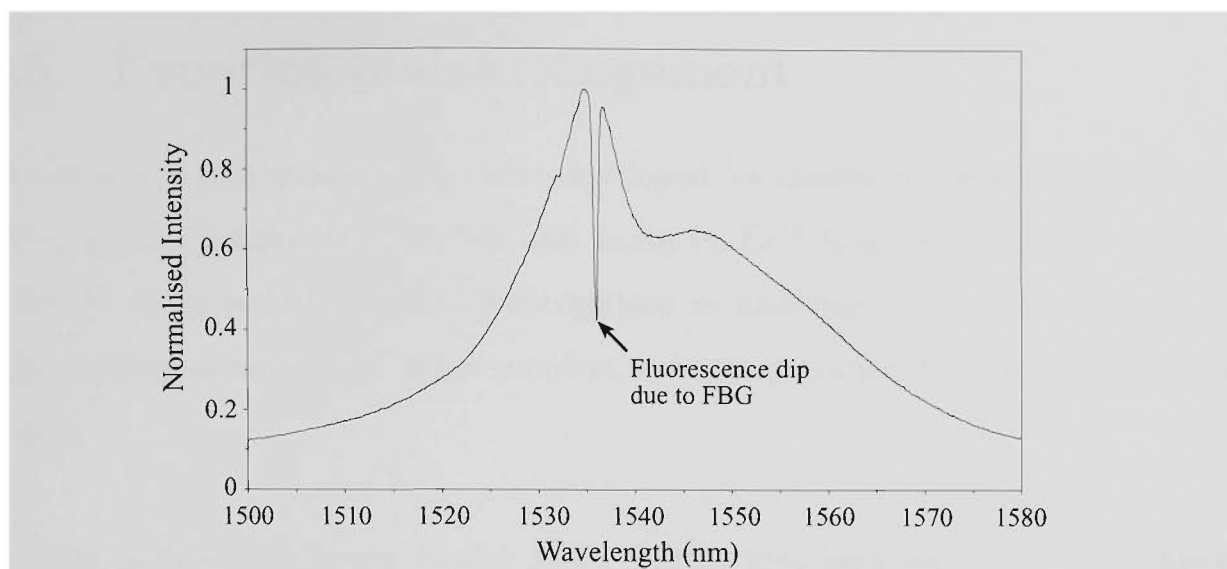


Figure 5.6: Fluorescence spectrum from the $^4I_{13/2}$ level in Er1 fibre with a Bragg grating inscribed within this fluorescence band using Sensor A configuration. Note: fluorescence spectrum recorded using an OSA with 0.5 nm resolution.

which was spliced 5 cm from the Er^{3+} doped fibre. Due to the FBGs being inscribed within the doped fibre, Sensors 2 - 5 have the advantage of shorter sensor length and co-located sensing.

Table 5.1: Summary of erbium based sensors.

Sensor	Sensor Configuration	Er^{3+} doped fibre	Er^{3+} doped fibre length (cm)	Total Sensor length (cm)
1	A	Er1	6	12
2	B	Er1	10	10
3	B	Er3	6	6
4	B	Er3	9	9
5	C	Er4	16	16

5.5 Experimental Arrangement

Two experimental arrangements were developed for measuring the FIR and Bragg wavelength shift upon temperature and strain for Er^{3+} based sensors. The components for these techniques can be categorised as involving an excitation source, a light guiding network (e.g. fibre couplers, microscope objectives) and a detection system.

Initially, a Spectra Physics Model 3900S Ti:Sapphire laser was used. This laser provided wavelength tunability in the region of interest for the excitation of appropriate energy levels in Er^{3+} (≈ 800 nm) and relatively high powers (up to 600 mW). The second source used was a fibre-pigtailed laser diode. This laser diode provided a wavelength of 808 nm with a power of 50 mW in 4 μm core single-mode fibre.

A diverse range of detection systems for Bragg wavelength and FIR measurement already exist, as summarised in Chapter 2. During this work, an ANDO AQ-6310B optical spectrum analyser was used to capture fluorescence spectra for FIR and Bragg wavelength measurements. Fluorescence spectra were transferred in real-time to a computer via a GPIB for analysis. A LabView based program controlled the entire data acquisition process.

Figure 5.7 shows the first experimental arrangement used to measure the FIR and Bragg wavelength shift due to temperature and strain. This arrangement used a Ti:Sapphire laser and free-space bulk optics to guide and filter out the pump source and specific fluorescence. The pump was directed through a dichroic beamsplitter and coupled into Corning SMF28TM fibre via a microscope objective with a numerical aperture (NA) of 0.2. The dichroic beamsplitter was positioned at 45° to the pump source to enable counter-propagating fluorescence to be collected. The beamsplitter was chosen for transmission at 800 nm and reflection at 540 nm at 45° incident light. Counter-propagating green fluorescence was directed through a green band-pass filter (centre wavelength 550 nm, bandwidth 100 nm) to remove any

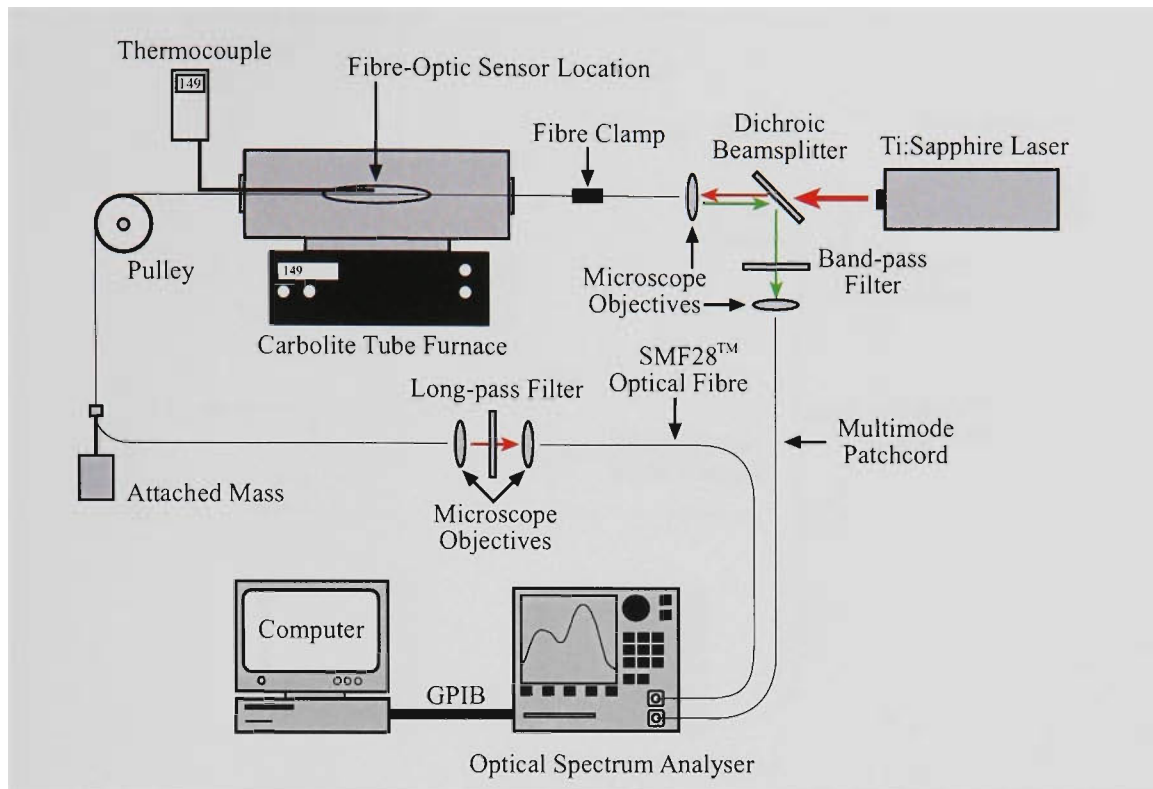


Figure 5.7: Experimental arrangement for dual temperature and strain calibration of Er^{3+} doped fibre sensors using a Ti:Sapphire laser and bulk free-space optics.

residual pump. This fluorescence was then collected by a multimode fibre patchcord via a microscope objective with a NA of 0.2 and detected by the OSA set on 5 nm resolution.

Co-propagating fluorescence from the $^4\text{I}_{13/2}$ level was guided through Corning SMF28 fibre, which was then collimated via a microscope objective with a NA of 0.2. The fluorescence passed through a long-pass filter (wavelength pass > 830 nm), which removed the residual pump. The fluorescence was then coupled back into SMF28 fibre via a microscope objective with the same NA and captured by the OSA.

Figure 5.8 shows the second experimental arrangement designed to be a complete fibre system, which utilised a fibre-pigtailed laser diode and fibre-optic couplers. The pigtail was of FlexcoreTM fibre with a cut-off wavelength of 780 nm and a core diameter of $4 \mu\text{m}$ and was spliced to one of the ports of a 825 nm fibre-optic coupler. This coupler exhibited a 50/50 split ratio at 825 nm. Counter-propagating $^2\text{H}_{11/2}$ and $^4\text{S}_{3/2}$ fluorescence was directed through the 825 nm coupler and was detected

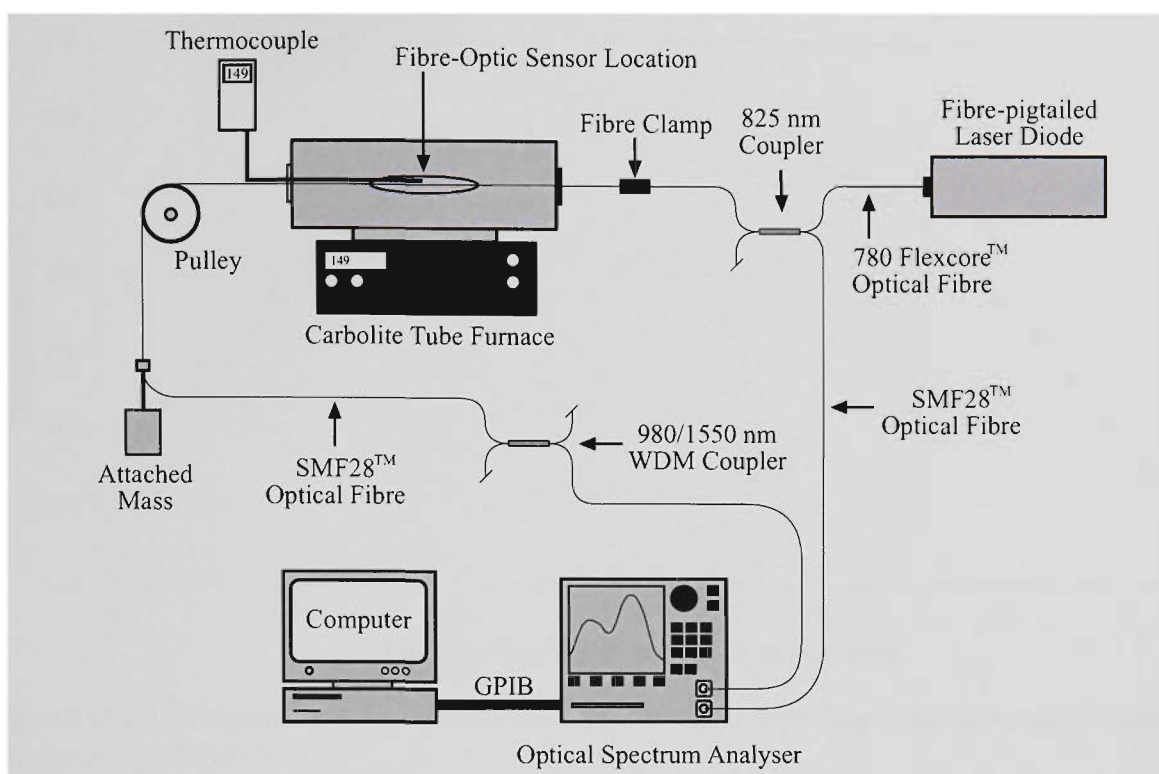


Figure 5.8: Experimental arrangement for dual temperature and strain calibration of Er^{3+} doped fibre sensors using a fibre-pigtailed laser diode and fibre-optic couplers.

by an OSA.

Co-propagating ${}^4\text{I}_{13/2}$ fluorescence was guided through a WDM 980/1550 nm fibre-optic coupler. This coupler exhibited a 0/100 split ratio at 800/1550 nm and no further filtering was required to remove the residual propagating pump.

5.5.1 Temperature and Strain Environment

The effects of applied temperature and strain on the fluorescence intensity ratio and Bragg wavelength were measured by centering the fibre sensor within the controlled zone of an electronically, temperature-stabilised tube furnace (Carbolite, type: MTF 12/38/400). The sensor was suspended within a 10 mm diameter Schott glass tube. A K-type thermocouple, fixed on the glass tube alongside the sensor in the tube oven, was used to monitor the temperature within the controlled zone. Thermocouple profiling of the tube furnace was performed at various temperatures up to 1000 °C. Temperature versus position along the tube oven is shown in Figure 5.9, in which the oven was set at 200 °C prior to measurements being recorded. The

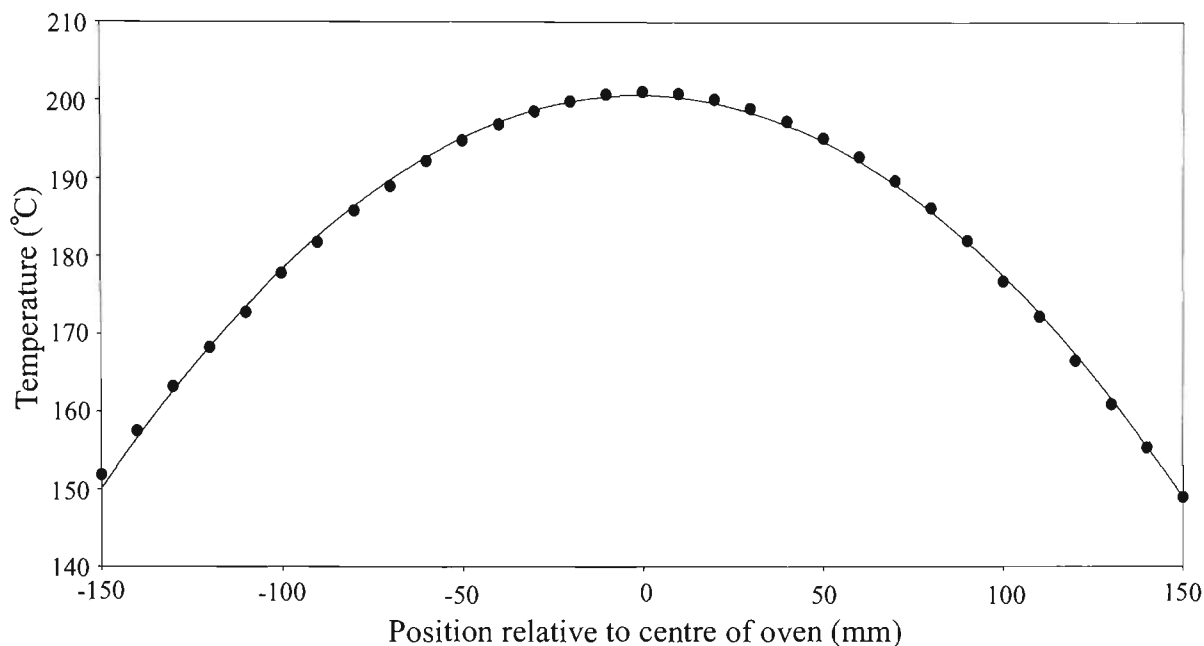


Figure 5.9: Temperature versus position within the Carbolite tube oven at a stabilised temperature of 200 °C.

reference position (0 mm) was set at the centre along the length of the oven. At the centre of the oven, the temperature only deviated by $\approx 4^\circ\text{C}$ over a region of 10 mm, representing a 2% variation. When the oven was set at 50 °C, the temperature deviation was only 1 °C over the same length.

Strain was applied to the sensor using a pulley and weight system. The test fibre containing the sensor was clamped at one end on a fibre spool. At the other end, a custom made clamp was fixed on the fibre hanging over the pulley to enable the attachment of known masses between 32 and 232 grams. Care was taken to prevent the test fibre from touching the Schott glass tube, and to lubricate the pulley in order to minimise friction, for better repeatability. These weights were progressively cycled in a controlled manner to exert reproducible strain on the sensor. The applied strain, ϵ , was calculated using:

$$\epsilon = \frac{mg}{AY} \quad (5.3)$$

where A is the cross-sectional area of the sensing fibre ($1.23 \times 10^{-8} \text{ m}^2$ for 125 μm diameter fibre used in this work), and Y is Young's modulus ($7.31 \times 10^{10} \text{ N/m}^2$ for

fused quartz) [33]. Therefore, the applied strain values used for this work ranged between 350 and 2534 $\mu\epsilon$. This is an effective and accurate method of determining the strain exerted on an optical fibre, with systematic error being attributed to variation in the cross-sectional area of the fibre.

5.6 Er1 Sensor Calibrations

Two sensors using Er1 fibre were calibrated for their temperature and strain responses and their performance compared. Sensor 1 used Sensor A configuration, while Sensor 2 used Sensor B configuration. The temperature and strain performance of Sensor 2 was compared to Sensor 1. The important parameters for Sensors 1 and 2 are summarised in Table 5.2.

Table 5.2: Summary of important parameters for Er1 sensors.

Sensor	Sensor	Doped fibre	Sensor	Calibration Range	
	Config.	length (cm)	Length (cm)	Temp. ($^{\circ}\text{C}$)	Strain ($\mu\epsilon$)
1	A	6	12	18 - 200	350 - 2534
2	B	10	10	18 - 200	350 - 2534

5.6.1 Sensor 1 Results

The experimental arrangement shown in Figure 5.7 was used to measure the dependence of the FIR and Bragg wavelength shift to temperature and strain. The excitation source produced 575 mW at 803 nm. The FBG spectra were captured on the OSA with the resolution set to 0.2 nm. Five strain cycles at eight particular strain values were performed at each of the eight temperatures tested.

Fluorescence spectra from the $^2\text{H}_{11/2}$ and $^4\text{S}_{3/2}$ thermally coupled energy levels at three different temperatures are shown in Figure 5.10. As expected, it can be seen that the fluorescence from the $^2\text{H}_{11/2}$ energy level increases with increasing temper-

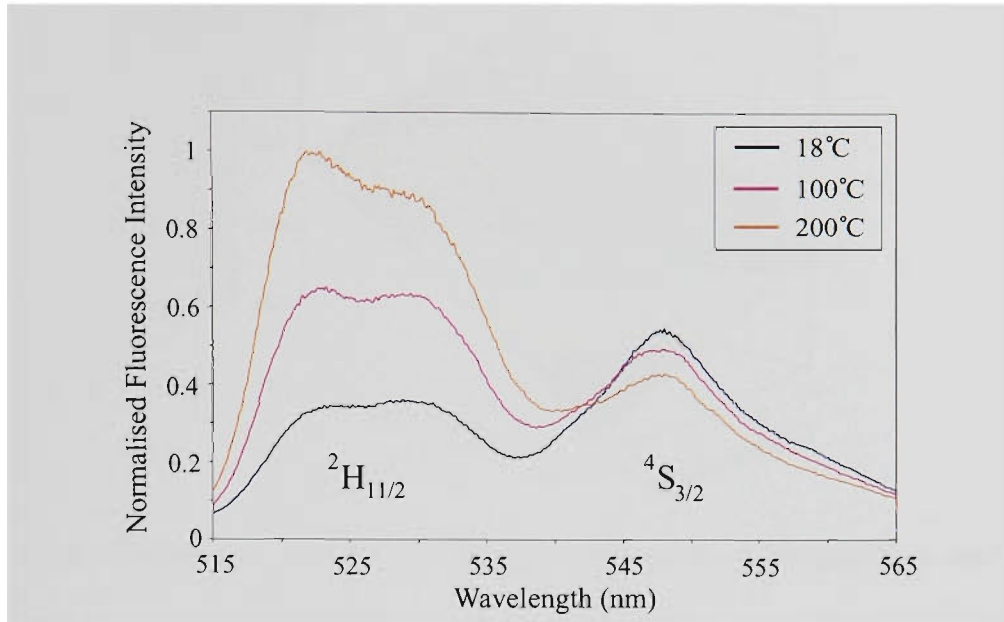


Figure 5.10: Counter-propagating fluorescence spectra from Sensor 1 at various temperatures. Note: OSA resolution set to 5 nm.

ature while the fluorescence from the $^4S_{3/2}$ energy level decreases. The FIR was calculated by integrating the intensities of these spectra over the wavelength ranges indicated in Equations 5.1 and 5.2. To verify the Boltzmann distribution theory, a fit of Equation 3.2 was made to the data for the FIR as a function of temperature and gave an energy gap between the $^2H_{11/2}$ and $^4S_{3/2}$ levels of $794 \pm 41 \text{ cm}^{-1}$. This value is in good agreement with the expected energy difference documented in previous work [49].

Figure 5.11 shows the Bragg wavelength shift as a function of temperature and strain, while Figure 5.12 shows $FIR1$ and $FIR2$ as a function of temperature and strain for Sensor 1. The temperature and strain cross-sensitivity of the FBG is clearly evident in Figure 5.11. As anticipated, the strain independent temperature response of the FIR is clearly evident. It can be seen from Figure 5.12 that $FIR2$ exhibits a greater temperature sensitivity by approximately twofold compared to $FIR1$. Also, $FIR2$ exhibits a greater, non-linear temperature dependence compared to $FIR1$.

Initially, Method A was used to de-convolve the temperature and strain information

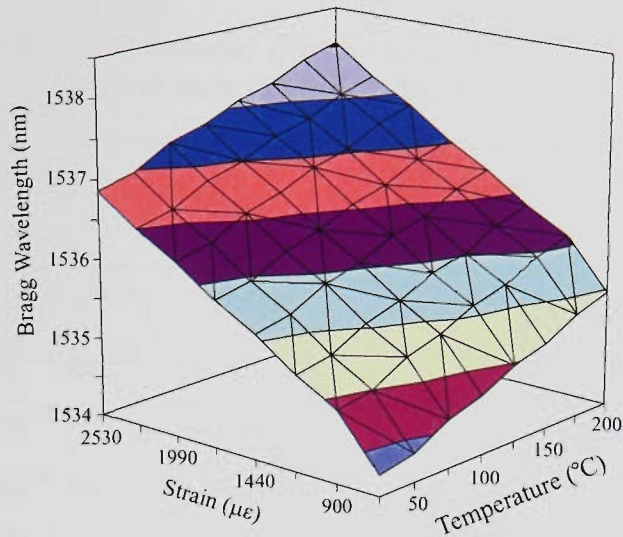


Figure 5.11: Calibration map of the Bragg wavelength vs temperature and strain for Sensor 1.

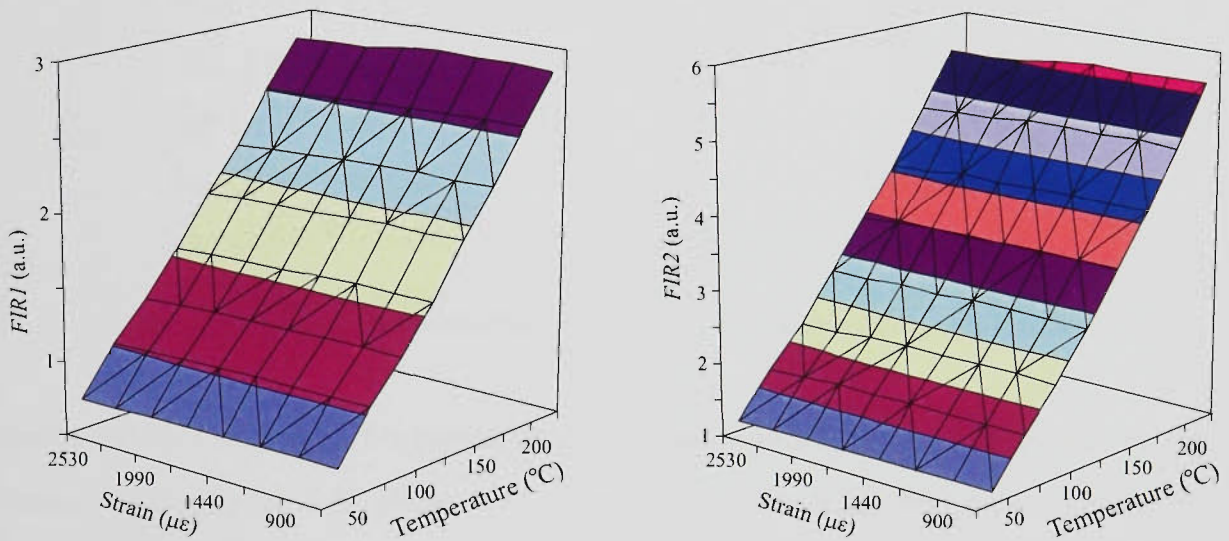


Figure 5.12: Calibration maps of the two FIR ranges (*FIR1* and *FIR2*) used to calibrate against temperature for Sensor 1.

from the FIR and Bragg wavelength shift. As previously explained in Section 4.1, for this method to be valid, linear approximations need to be made for the dependence of the FIR and Bragg wavelength to temperature and strain. Table 5.3 shows the FIR and Bragg wavelength temperature and strain coefficients with their associated errors, for Sensor 1.

By using Equations 4.10 and 4.11, calibration formulae for determining the absolute temperature ($^{\circ}\text{C}$) and strain ($\mu\epsilon$) over the two temperature ranges considered were formulated for Sensor 1. The data produced by the calibration formulae were then

Table 5.3: Linear coefficients deduced from calibration data with associated errors for Sensor 1. The coefficient symbols were defined in Section 4.1

Matrix Element	Sensor	Temperature Range (°C)	Coefficient
$K_{1T} (\times 10^{-2} \text{ }^\circ\text{C}^{-1})$	<i>FIR1</i>	18-200	1.18 ± 0.01
$K_{1\epsilon} (\times 10^{-5} \text{ } \mu\epsilon^{-1})$			-2.0 ± 0.8
$K_{1T} (\times 10^{-2} \text{ }^\circ\text{C}^{-1})$	<i>FIR2</i>		2.44 ± 0.02
$K_{1\epsilon} (\times 10^{-5} \text{ } \mu\epsilon^{-1})$			-3.0 ± 2.0
$K_{1T} (\times 10^{-2} \text{ }^\circ\text{C}^{-1})$	<i>FIR1</i>	18-150	1.121 ± 0.009
$K_{1\epsilon} (\times 10^{-5} \text{ } \mu\epsilon^{-1})$			-1.6 ± 0.5
$K_{1T} (\times 10^{-2} \text{ }^\circ\text{C}^{-1})$	<i>FIR2</i>		2.24 ± 0.01
$K_{1\epsilon} (\times 10^{-5} \text{ } \mu\epsilon^{-1})$			-2 ± 1
$K_{2T} (\times 10^{-3} \text{ nm}/^\circ\text{C})$	FBG	18-200	8.6 ± 0.1
$K_{2\epsilon} (\times 10^{-3} \text{ nm}/\mu\epsilon)$			1.185 ± 0.001
$K_{2T} (\times 10^{-3} \text{ nm}/^\circ\text{C})$	FBG	18-150	8.3 ± 0.1
$K_{2\epsilon} (\times 10^{-3} \text{ nm}/\mu\epsilon)$			1.187 ± 0.001

compared to the known temperature and strain conditions applied during the calibration test. Figure 5.13 shows the temperature and strain differences between the known conditions and those deduced for *FIR1* and *FIR2* from Sensor 1 using the analysis techniques denoted Method A and Half-Maximum. The non-linear temperature dependence of the FIR from Sensor 1 is clearly evident in Figure 5.13. It can also be seen from Figure 5.13 how different FIR wavelength ranges, namely *FIR1* and *FIR2*, affect the difference between the known strain and that determined by the calibration formulae. The greater non-linear temperature dependence of *FIR2* results in larger temperature errors, particularly at the limits of the temperature ranges used here, which is clearly evident in Figure 5.13. These larger temperature errors contribute inevitably to larger strain errors.

The strain independent, non-linear temperature dependence of the FIR was also used to de-convolve the temperature and strain information, as described in detail

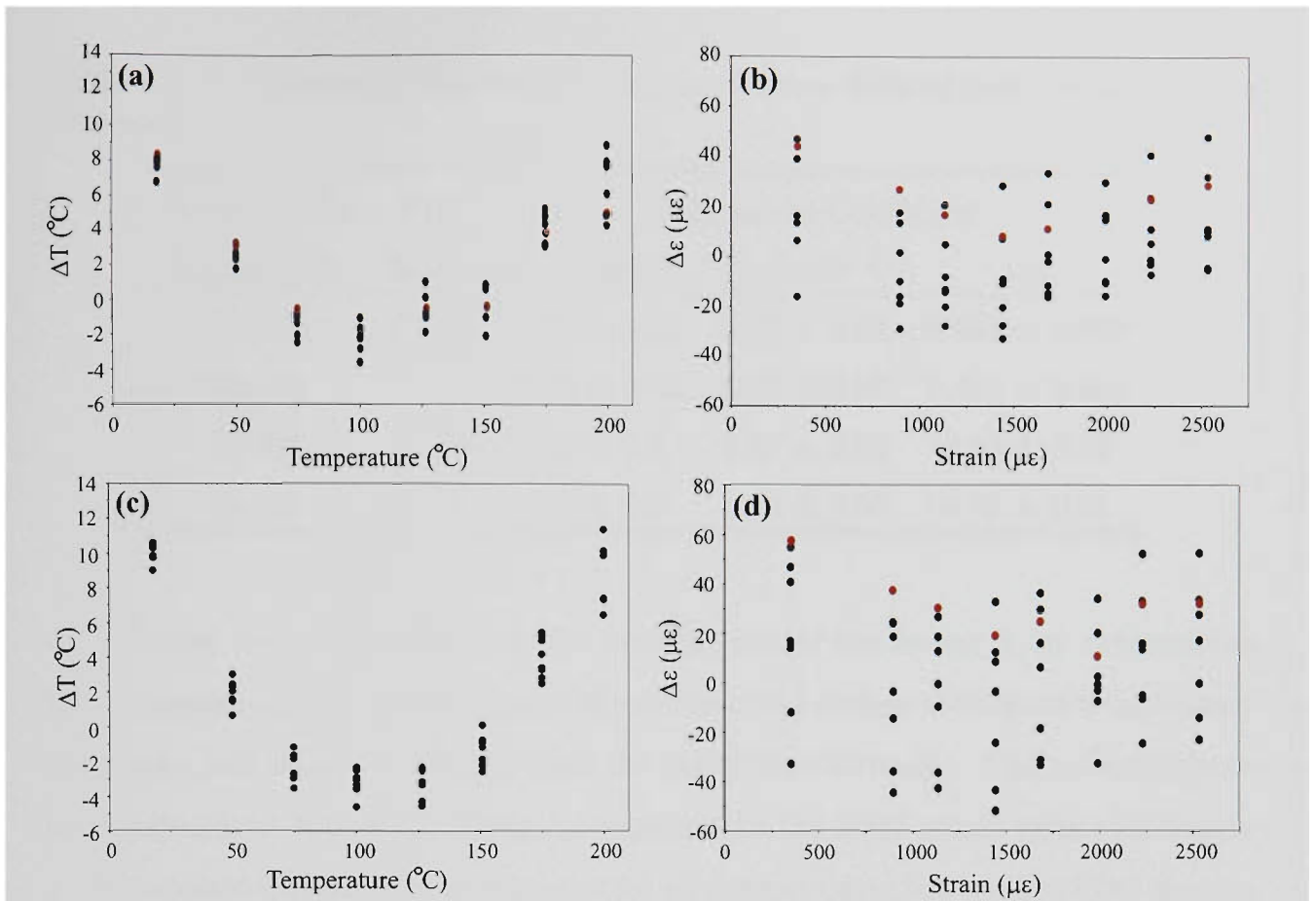


Figure 5.13: Comparison of temperature and strain deviations from known conditions for Sensor 1 when using Method A, Half-Maximum technique, and (a)-(b) *FIR1* and (c)-(d) *FIR2*.

in Section 4.2. Table 5.4 shows the the second order polynomial coefficients with their associated errors for Sensor 1. By using Equation 4.20, calibration formulae for determining temperature only from the FIR calibration data were formulated. Once the temperature was determined using the FIR, the strain information was deduced by using the temperature information to offset the FBG temperature dependence.

Figure 5.14 illustrates the temperature and strain differences between the known conditions and those deduced from the calibration formulae for Sensor 1. When comparing the data in Figure 5.13 to Figure 5.14 it can be seen clearly that adopting a non-linear function to the temperature dependent FIR data, results in reduced deviations from the known conditions. The data illustrated in these figures were analysed using Method C, which also assumed a non-linear temperature dependence of the Bragg wavelength.

Table 5.4: Polynomial coefficients with associated errors deduced from calibration data for Sensor 1.

Temperature Range (°C)	FIR Range	Polynomial Coefficient		
		$A_R (\times 10^{-5})$	$B_R (\times 10^{-2})$	C_R
18-200	<i>FIR1</i>	1.34 ± 0.08	0.89 ± 0.02	0.549 ± 0.009
18-150		1.44 ± 0.09	0.88 ± 0.01	0.555 ± 0.008
18-200	<i>FIR2</i>	4.0 ± 0.3	1.57 ± 0.04	0.86 ± 0.02
18-150		3.9 ± 0.2	1.58 ± 0.03	0.86 ± 0.01

An effective method of assessing the performance of the sensor is by determining the root-mean-square (RMS) error of the differences between the known temperature and strain and those determined from the calibration formulae. This technique was used throughout this work. Table 5.5 summarises the RMS strain errors for Sensor 1. The analysis methods were repeated for all sensors using the various FBG spectra

Table 5.5: Summary of RMS strain errors for Sensor 1.

Temperature Range (°C)	FBG Analysis by Method:	RMS Strain Error ($\mu\epsilon$) by:					
		Method A		Method B		Method C	
		<i>FIR1</i>	<i>FIR2</i>	<i>FIR1</i>	<i>FIR2</i>	<i>FIR1</i>	<i>FIR2</i>
18-200	Minima	22.5	28.8	25.9	24.2	24.8	23.6
	Half-Maximum	20.0	27.8	22.1	20.4	21.5	19.8
	Weighted Ave.	19.9	27.5	22.1	20.5	21.4	19.9
18-150	Minima	21.8	23.0	23.6	21.7	22.0	19.8
	Half-Maximum	18.2	21.0	18.6	16.7	18.5	15.9
	Weighted Ave.	18.1	20.9	18.5	16.7	18.5	16.0

analysis techniques. Results from the various techniques used for Sensor 1 showed that both the Half-Maximum and Weighted Average methods gave RMS strain error improvements of up to 15% relative to the Minima method. No improvement in the RMS temperature error was observed for either sensor when comparing the FBG

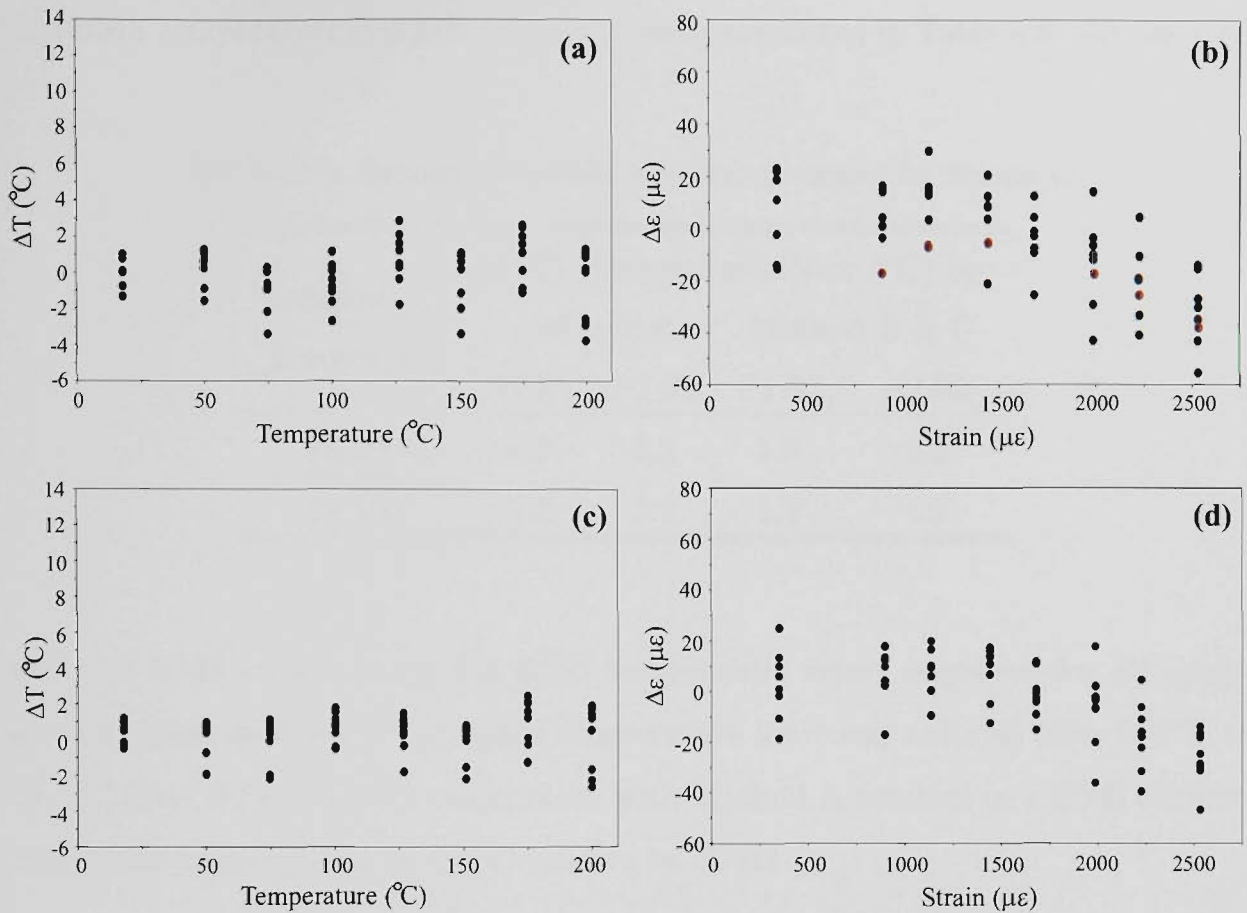


Figure 5.14: Temperature and strain deviations from the known conditions for Sensor 1 using the strain independent, non-linear temperature dependence (Method C) of (a)-(b) *FIR1* and (c)-(d) *FIR2*.

spectra analysis methods.

As anticipated, an improvement is evident in the RMS strain error for all analysis methods when the upper, pre-determined temperature limit is reduced from 200 to 150 °C. When comparing the two FIR wavelength ranges for Sensor 1, *FIR1* exhibited improved RMS strain errors when Method A was used. This was due to the greater non-linear temperature dependence of *FIR2* compared to *FIR1*. In contrast, *FIR2* showed better strain performance when Method B was used. This may be due to the increased temperature sensitivity of *FIR2*. A small improvement was also observed when a quadratic temperature dependence of the Bragg wavelength was assumed (Method C). Overall, *FIR2* used in conjunction with Method C and the Half-Maximum method resulted in the best strain performance.

The RMS temperature errors for Sensor 1 are summarised in Table 5.6. As observed

Table 5.6: Summary of RMS temperature errors for Sensor 1.

Temperature Range (°C)	RMS Temperature Error (°C) by:			
	Method A		Method B & C	
	<i>FIR1</i>	<i>FIR2</i>	<i>FIR1</i>	<i>FIR2</i>
18-200	3.7	5.2	1.5	1.3
18-150	2.5	3.2	1.2	1.0

with the RMS strain errors, the RMS temperature errors improved for all analysis techniques used when the upper temperature limit was reduced from 200 °C to 150 °C. Also, *FIR1* used in conjunction with Method A resulted in a RMS temperature error improvement of 1.5 °C relative to *FIR2*.

Another technique of analysing the performance of the sensor is to examine the fits to the calibration data. The regression square (r^2) is a measure of the quality of the fit, where the value of 1 represents a perfect fit. Table 5.7 summarises the r^2 values for fits to the FIR data from Sensor 1.

As expected, an improvement was observed when a non-linear fit was performed on the FIR for Sensor 1. The best r^2 of 0.99992 resulted from using Methods B and C in conjunction with *FIR2*. These improvements in the r^2 values of the fits is consistent with the improvement of the RMS temperature and strain errors shown in Tables 5.5 and 5.6.

5.6.2 Sensor 2 Results

As described in Section 5.4, Sensor 2 was configured as a co-located sensor in which the FBG was inscribed within the doped fibre region. The performance of Sensor 2 was compared to that of Sensor 1. This was done to determine which sensor configuration would give improved temperature and strain measurements.

Table 5.7: r^2 values for function fits to FIR temperature calibration data for Sensor 1.

FIR Range	Analysis Method	Temperature Range (°C)	r^2 Value
<i>FIR1</i>	Method A	18-200	0.9963 ± 0.0004
	Method A	18-150	0.9972 ± 0.0004
	Method B & C	18-200	0.99981 ± 0.00008
	Method B & C	18-150	0.99979 ± 0.00009
<i>FIR2</i>	Method A	18-200	0.9925 ± 0.0009
	Method A	18-150	0.9951 ± 0.0004
	Method B & C	18-200	0.99991 ± 0.00006
	Method B & C	18-150	0.99992 ± 0.00009

The experimental and analysis procedures that were performed on Sensor 1 were repeated for Sensor 2. As shown in Table 5.2, the temperature and strain calibration ranges used for Sensor 2 were the same as those for Sensor 1. The calibrations performed on Sensor 2 were performed using a high (765 mW) and low (140 mW) pump power from a Ti:Sapphire laser. Acceptable sensor performance at low pump powers would lead to the practical use of a low-powered, fibre-pigtailed laser diode as the pump source.

Table 5.8 shows a comparison of the linear matrix coefficients for the two different pump powers. It is evident that, apart from K_{1T} , all coefficients are consistent at different pump powers. The variation in K_{1T} to pump power was expected, as previously detailed in Section 5.2. The results show a reduction in the temperature sensitivities by $\approx 15\%$ in both FIR ranges when the power is reduced from 765 to 140 mW. When variations of doped fibre length are taken into consideration, the temperature sensitivity of *FIR1* for Sensor 2 is comparable to that of Sensor 1 at high pump powers. Again, as with Sensor 1, the strain dependence of the FIR is consistent with zero. Also, the linear coefficients of Sensor 2 exhibit smaller errors

Table 5.8: Linear coefficients with associated errors deduced from calibration data for Sensor 2 over a temperature range of 25 to 200 °C.

Matrix Coefficient	FIR Range	Pump Power (mW)	
		765	140
K_{1T} ($\times 10^{-2}$ °C $^{-1}$)	<i>FIR1</i>	1.003 ± 0.009	0.853 ± 0.004
$K_{1\epsilon}$ ($\times 10^{-5}$ $\mu\epsilon^{-1}$)	<i>FIR1</i>	0.5 ± 0.5	0.4 ± 0.2
K_{1T} ($\times 10^{-2}$ °C $^{-1}$)	<i>FIR2</i>	1.96 ± 0.01	1.53 ± 0.01
$K_{1\epsilon}$ ($\times 10^{-5}$ $\mu\epsilon^{-1}$)	<i>FIR2</i>	1.2 ± 0.5	1.1 ± 0.5
K_{2T} ($\times 10^{-3}$ nm/°C)		10.18 ± 0.05	10.22 ± 0.06
$K_{2\epsilon}$ ($\times 10^{-3}$ nm/ $\mu\epsilon$)		1.143 ± 0.004	1.147 ± 0.004

compared to Sensor 1.

The strain sensitivity of the FBG written in Er1 fibre (Sensor 2) appears to be consistent with that of the FBG inscribed in standard telecommunications fibre (Sensor 1). However, the temperature sensitivity, K_{2T} , is shown to increase by approximately 15% for the FBG inscribed within the Er1 fibre. This may be caused by a change in the thermal expansion coefficient of the fibre, due to the different glass composition.

Tables 5.9 and 5.10 summarise the RMS strain errors for Sensor 2 when pumped with 765 and 140 mW, respectively. As previously shown in the results for Sensor 1, significant improvements in the RMS strain errors were observed for the Half-Maximum and Weighted Average methods compared to the Minima method. The results show a consistent, small improvement in RMS strain error when a pump power of 765 mW was used. This observed improvement would not justify the cost of using a laser source producing an extra 500 mW. Using the co-located configuration adopted for Sensor 2, the results show improved strain performance compared to Sensor 1 using all analysis methods. RMS strain errors as low as $5.04 \mu\epsilon$ and $7.42 \mu\epsilon$ for pump powers of 765 mW and 140 mW, respectively were demonstrated.

Table 5.9: Summary of RMS strain errors for Sensor 2 using a pump power of 765 mW.

Temperature Range (°C)	FBG Analysis by Method:	RMS Strain Error ($\mu\epsilon$) by:					
		Method A		Method B		Method C	
		<i>FIR1</i>	<i>FIR2</i>	<i>FIR1</i>	<i>FIR2</i>	<i>FIR1</i>	<i>FIR2</i>
25-200	Minima	17.9	20.7	16.8	17.4	16.6	16.9
	Half-Maximum	12.2	15.7	10.7	9.48	6.95	7.09
	Weighted Ave.	12.6	16.1	12.0	9.58	6.90	7.45
25-150	Minima	14.6	16.5	15.2	15.4	14.6	14.7
	Half-Maximum	8.92	9.66	8.61	8.67	5.86	5.04
	Weighted Ave.	9.41	10.6	9.20	9.22	5.96	5.36

Table 5.11 summarises the RMS temperature errors for Sensor 2. As was observed with the RMS strain errors, an improvement was demonstrated when the high pump power was used, but showed comparable performance when a non-linear temperature dependence was used for the FIR. Again, *FIR2* exhibited greater temperature sensitivity but this did not translate into improved performance when Method B and C were adopted, as was observed with Sensor 1.

Sensor 2 exhibited better temperature performance compared to Sensor 1 using all analysis methods. Results showed RMS temperature errors as low as $\approx 0.6^\circ\text{C}$ and $\approx 0.8^\circ\text{C}$ for pump powers of 765 mW and 140 mW, respectively. These results indicate that Sensor B configuration, which consists of an FBG inscribed within the rare earth doped fibre, would be preferred for the measurement of temperature and strain simultaneously.

Table 5.10: RMS strain errors for Sensor 2 using a pump power of 140 mW.

Temperature Range (°C)	FBG Analysis by Method:	RMS Strain Error ($\mu\epsilon$) by:					
		Method A		Method B		Method C	
		<i>FIR1</i>	<i>FIR2</i>	<i>FIR1</i>	<i>FIR2</i>	<i>FIR1</i>	<i>FIR2</i>
25-200	Minima	14.9	20.0	21.6	22.0	10.6	11.0
	Half-Maximum	12.8	18.8	19.6	19.7	8.87	9.73
	Weighted Ave.	11.8	18.7	19.6	20.3	8.95	9.12
25-150	Minima	13.3	18.3	15.5	16.2	9.61	10.3
	Half-Maximum	12.0	17.6	14.3	15.5	8.23	9.18
	Weighted Ave.	11.0	17.2	14.1	15.8	7.42	8.44

Table 5.11: Summary of RMS temperature errors for Sensor 2.

Pump Power (mW)	Temperature Range (°C)	RMS Temp. Error (°C) by:			
		Method A		Method B & C	
		<i>FIR1</i>	<i>FIR2</i>	<i>FIR1</i>	<i>FIR2</i>
765	18-200	1.4	2.1	0.8	0.9
	18-150	1.3	1.9	0.6	0.6
140	18-200	3.3	4.9	1.0	1.1
	18-150	2.6	3.6	0.8	0.9

5.7 Er3 Sensor Calibrations

Er3 fibre had a higher erbium concentration than Er1. This enabled shorter fibre samples to be used which could be pumped with lower powers to produce sufficient fluorescence for this sensing scheme. In this Section, Sensors 3 and 4 are compared to Sensor 2, as all these sensors adopted the Sensor B configuration. A further comparison of performance was made between Sensors 3 and 4. Table 5.12 summarises the important parameters for Sensors 3 and 4. Sensor 4 was the only erbium based

Table 5.12: Summary of important parameters for Er3 sensors.

Sensor	Sensor	Doped fibre	Pump	Calibration Range	
	Config.	length (cm)	Source	Temp. ($^{\circ}\text{C}$)	Strain ($\mu\epsilon$)
3	B	6	Ti:Sapphire	27 - 200	350 - 1988
4	B	9	Laser Diode	25 - 100	350 - 1460

sensor to be tested using a complete fibre system and laser diode, as illustrated in Figure 5.8. Er3 was chosen as the preferred doped fibre for Sensor 4 as it generated the highest levels of fluorescence. A longer length of Er3 was used to generate higher levels of fluorescence intensity to compensate for the lower powered laser diode (50 mW in fibre). The complete fibre system would potentially reduce spectral noise and, therefore, improve the RMS temperature and strain errors of the sensor.

5.7.1 Sensors 3 and 4 Results

As described in Table 5.1, Sensor 3 was configured like Sensor 2, but utilised a shorter length of doped fibre (6 cm). The temperature and strain calibrations performed on Sensor 3 used the experimental arrangement illustrated in Figure 5.7 with a pump power of 400 mW. A reduced strain range was used on Sensor 3 due to the mechanical strength of the fusion splice between the standard Corning SMF28 and the Er3 fibre being unable to withstand higher strain. This problem was not experienced with Er1. Five strain cycles at six particular strain values were performed at each

of the eight temperatures tested. The excitation wavelength was 803 nm.

The experimental arrangement used for Sensor 4 is shown in Figure 5.8. Five strain cycles at eight particular strain values were performed at each of the six temperatures tested.

Figure 5.15 illustrates the green fluorescence from Er3 fibre at three different temperatures. The spectral profile from the $^2H_{11/2}$ level from highly doped Er3

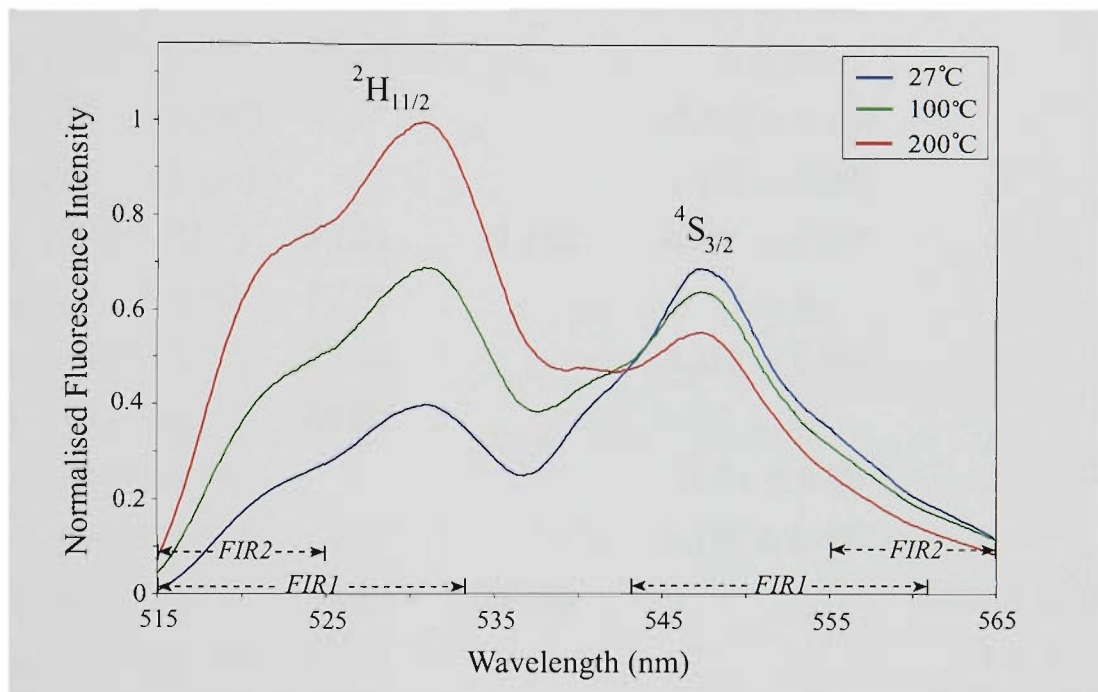


Figure 5.15: Counter-propagating fluorescence spectra from Sensor 3 at various temperatures. Note: OSA resolution set to 5 nm.

fibre differs significantly compared with that from the Er1 fibre sample. This may be due to the increased erbium concentration and the lack of phosphorous in Er3 relative to Er1 fibre. Less spectral noise is evident from the spectra shown in Figure 5.15 compared to that from Er1 in Figure 5.10. This may be due to the higher levels of fluorescence intensity generated from the more highly doped Er3 fibre.

Table 5.13 shows a comparison of the linear matrix coefficients for Sensors 3 and 4. Comparing the FIR temperature sensitivities for Sensors 3 and 4, which are based on Er3, to those on Er1, it is evident that the sensitivity has decreased with the

higher erbium doped Er3. As determined with Er1, the use of *FIR2* resulted in the

Table 5.13: Linear coefficients with associated errors deduced from calibration data for Sensors 3 and 4.

Matrix Coefficient	FIR Range	Temperature Range (°C)	Sensor 3	Sensor 4
$K_{1T} (\times 10^{-2} \text{ }^\circ\text{C}^{-1})$	<i>FIR1</i>	27-200	0.796 ± 0.006	
$K_{1\epsilon} (\times 10^{-6} \text{ } \mu\epsilon^{-1})$	<i>FIR1</i>		-0.01 ± 0.05	
$K_{1T} (\times 10^{-2} \text{ }^\circ\text{C}^{-1})$	<i>FIR2</i>		1.478 ± 0.001	
$K_{1\epsilon} (\times 10^{-6} \text{ } \mu\epsilon^{-1})$	<i>FIR2</i>		4 ± 15	
$K_{2T} (\times 10^{-3} \text{ nm}/^\circ\text{C})$			11.580 ± 0.007	
$K_{2\epsilon} (\times 10^{-3} \text{ nm}/\mu\epsilon)$			1.152 ± 0.007	
$K_{1T} (\times 10^{-2} \text{ }^\circ\text{C}^{-1})$	<i>FIR1</i>	27-150	0.757 ± 0.007	
$K_{1\epsilon} (\times 10^{-6} \text{ } \mu\epsilon^{-1})$	<i>FIR1</i>		-1 ± 5	
$K_{1T} (\times 10^{-2} \text{ }^\circ\text{C}^{-1})$	<i>FIR2</i>		1.312 ± 0.001	
$K_{1\epsilon} (\times 10^{-6} \text{ } \mu\epsilon^{-1})$	<i>FIR2</i>		1 ± 15	
$K_{2T} (\times 10^{-3} \text{ nm}/^\circ\text{C})$			11.03 ± 0.09	
$K_{2\epsilon} (\times 10^{-3} \text{ nm}/\mu\epsilon)$			1.154 ± 0.007	
$K_{1T} (\times 10^{-2} \text{ }^\circ\text{C}^{-1})$	<i>FIR1</i>	25-100		0.464 ± 0.003
$K_{1\epsilon} (\times 10^{-6} \text{ } \mu\epsilon^{-1})$	<i>FIR1</i>			-1 ± 1
$K_{1T} (\times 10^{-2} \text{ }^\circ\text{C}^{-1})$	<i>FIR2</i>			0.58 ± 0.01
$K_{1\epsilon} (\times 10^{-6} \text{ } \mu\epsilon^{-1})$	<i>FIR2</i>			1 ± 7
$K_{2T} (\times 10^{-3} \text{ nm}/^\circ\text{C})$				11.03 ± 0.03
$K_{2\epsilon} (\times 10^{-3} \text{ nm}/\mu\epsilon)$				1.223 ± 0.003

temperature sensitivity increasing by approximately twofold and 20% for Sensors 3 and 4, respectively, compared to *FIR1*. The *FIR* temperature coefficients for Sensor 4 exhibited the lowest sensitivity relative to the sensors previously calibrated. This was expected due to the pump power used being lower than that used for Sensors 1-3. This was also demonstrated by Sensor 2, where the temperature sensitivity of the *FIR* decreased when the pump power was reduced from 765 to 140 mW. Another

contributing factor was the reduction of the temperature range to 100 °C. The strain sensitivity of the FIR was found to be approximately zero, which is consistent with that found from the sensors investigated previously.

It is evident that the temperature dependencies of the FBGs inscribed in Er3 (Sensors 3 and 4) have increased, compared to those of Sensor 2. The temperature sensitivity, K_{2T} , of the FBG in Er3 has shown to have increased by $\approx 10\%$. This may be due to the different core compositions between Er1 and Er3, which would affect their thermal properties. The FBG strain dependencies of Sensors 3 and 4 were found to be comparable to those of Sensor 2.

The RMS strain errors for Sensor 3 are shown in Table 5.14. As with the previously calibrated sensors, an improvement in the RMS strain error for all analysis methods is observed when the upper, pre-determined temperature limit is reduced from 200 °C to 150 °C. No improvement in performance was observed when *FIR2*, was used and in most cases resulted in larger RMS strain errors. As expected, su-

Table 5.14: Summary of RMS strain errors for Sensor 3 using a pump power of 400 mW.

Temperature Range (°C)	FBG Analysis by Method:	RMS Strain Error ($\mu\epsilon$) by:					
		Method A		Method B		Method C	
		<i>FIR1</i>	<i>FIR2</i>	<i>FIR1</i>	<i>FIR2</i>	<i>FIR1</i>	<i>FIR2</i>
27-200	Minima	14.8	35.0	32.6	35.0	14.5	17.8
	Half-Maximum	14.9	33.8	33.5	33.8	14.2	17.4
	Weighted Ave.	14.8	33.9	33.8	33.9	14.7	17.8
27-150	Minima	14.5	14.1	27.3	27.7	12.6	12.7
	Half-Maximum	14.3	13.2	27.9	28.2	12.1	12.2
	Weighted Ave.	14.5	13.6	28.4	28.7	12.8	12.7

perior performance was observed when the temperature sensitivities of the FIR and Bragg wavelength were assumed non-linear, with RMS strain errors as low as 12.1 $\mu\epsilon$.

The RMS strain errors for Sensor 4 are shown in Table 5.15. A significant improvement in the RMS strain error is observed when the Half-Maximum and Weighted

Table 5.15: Summary of RMS strain errors for Sensor 4 using a 50 mW fibre pigtailed laser diode over a temperature range of 25 - 100 °C.

FBG Analysis by Method:	RMS Strain Error ($\mu\epsilon$) by Method:					
	Method A		Method B		Method C	
	<i>FIR1</i>	<i>FIR2</i>	<i>FIR1</i>	<i>FIR2</i>	<i>FIR1</i>	<i>FIR2</i>
Minima	19.0	23.5	18.0	20.2	17.9	20.2
Half-Maximum	8.16	14.6	4.83	7.88	4.83	7.88
Weighted Ave.	7.60	13.9	4.86	7.59	4.80	7.55

Average methods are used, compared to the Minima method. This may be due to the increased noise in the FBG spectra, to which the Minima method is highly susceptible. This increased noise is due to the lower fluorescence intensity levels from the $^4I_{13/2}$ level. *FIR1* showed superior strain performance using all methods (A-C) compared to *FIR2*. Minimal improvement in the RMS strain error was observed when assuming a non-linear temperature dependence of the Bragg wavelength. This is due to the non-linear effect being almost negligible over narrow temperature ranges. Overall, when *FIR1* was used in conjunction with Method C and the FBG spectra was analysed using the Weighted Average method, superior strain performance was observed, in the order of $4.80 \mu\epsilon$.

Comparing the RMS strain errors for Sensors 3 and 4 to Sensor 2, it was found that over similar temperature ranges Sensor 2 demonstrated improved RMS strain errors to Sensor 3. In contrast, although calibrated over a narrower temperature range, Sensor 4 demonstrated strain performance better than both Sensors 2 and 3. This may be due to less noise being present in the fluorescence spectra as it was an 'all in-fibre' arrangement.

Table 5.16 summarises the RMS temperature errors for Sensors 3 and 4. Sensor 3 showed very good temperature performance with a RMS temperature error as low as 0.8°C. This was comparable to that achieved with the sensors using Er1.

Table 5.16: Summary of RMS temperature errors for Sensors 3 and 4.

Sensor	Temperature Range (°C)	RMS Temperature Error (°C) by:			
		Method A		Method B & C	
		<i>FIR1</i>	<i>FIR2</i>	<i>FIR1</i>	<i>FIR2</i>
3	27-200	3.0	6.0	0.8	0.8
	27-150	1.9	3.3	0.8	0.8
4	25-100	0.8	1.6	0.3	0.7

For both Sensors 3 and 4, *FIR1* exhibited superior temperature performance using all analysis methods compared to *FIR2*. Comparable temperature performance was demonstrated between Sensors 2 and 3 indicating that the increase in Er³⁺ concentration does not affect this parameter. Sensor 4 demonstrated an RMS temperature error as low as 0.3°C. This RMS temperature error is superior to the results of all the previously calibrated sensors (Sensors 1-3). This may be due to reduced noise in the green fluorescence from the ‘all in-fibre’ sensor system and the reduced temperature range. This system also provides the lowest pump power, potentially reducing cost of this fibre-optic sensing scheme.

5.8 Er4 Sensor High Temperature Calibration

The problems associated with FBG sustainability at high temperatures have been well documented in Chapters 2 and 3. The Er4 fibre used in this thesis was fabricated with tin doped within its core region. As described in Chapter 3, FBGs inscribed in tin doped fibre have shown to be more resilient to high temperature exposure. The Er4 fibre used here has been shown to exhibit excellent FBG sustainability [164] and is used for simultaneous high temperature and strain sensing.

5.8.1 Sensor 5 Results

Sensor 5 was the only erbium based sensor to be tested at high temperatures ($>200^{\circ}\text{C}$). Due to the low erbium concentration, Sensor 5 was tested using the configuration illustrated by Figure 5.7, enabling the doped fibre to be pumped with high powers from the Ti:Sapphire laser. As shown in Figure 5.4, longer lengths of Er4 are required to achieve comparable fluorescence levels to the other, higher doped fibres (e.g. Er1 and Er3) and, therefore, Sensor 5 consisted of a relatively long length (16 cm) of Er4.

The temperature and strain calibrations for Sensor 5 were performed with a pump power of 500 mW and excitation wavelength of 803 nm. The temperature and strain ranges used were 25 to 600°C and 350 to $1988\mu\epsilon$, respectively. Although a reduced strain range was also used on this sensor, it did fracture when strained at temperatures above 600°C . The mechanical strength of the fibre was reduced at high temperatures due to its silicone jacketing material completely burning off. Five strain cycles at six particular strain values were performed at each of the seven temperatures tested.

Figure 5.16 shows reflected FBG spectra at three temperatures used for calibrating Sensor 5. It is clear that the FBG exhibits minimal reduction in its reflectance at temperatures of $\sim 300^{\circ}\text{C}$, but experiences decay at higher temperatures. Although the FBG did experience significant decay, sufficient reflectance was main-

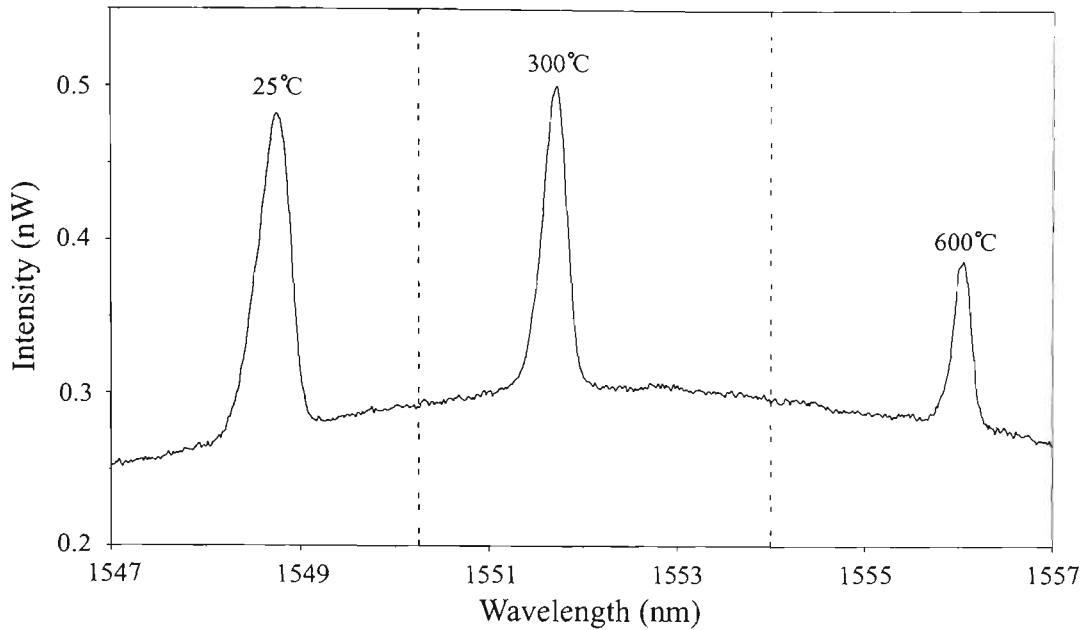


Figure 5.16: FBG reflection spectra from Sensor 5 at three different temperatures. Note: All spectra recorded with an applied $350 \mu\epsilon$ strain.

tained for the Bragg wavelength to be determined at 600°C using the OSA and a custom LabViewTM program. More detailed analysis of the sustainability of FBGs inscribed in Er4 and the other fibres used in this work is provided in Chapter 7.

Method A was not used to deconvolve the temperature and strain values. This was due to the increased non-linearity of the temperature dependence of the Bragg wavelength and the FIR over wide temperature ranges producing undesirably large errors. Only Method C was used to calibrate the Bragg wavelength to temperature. Figure 5.17 shows the temperature and strain dependence of the Bragg wavelength with its corresponding temperature sensitivity. It can be seen that the temperature sensitivity of the Bragg wavelength increases linearly with temperature at $0.014 \text{ pm}/^\circ\text{C}$. An increase in the rate of thermal expansion to temperature is predicted by the thermo-optic effect [8, 160, 161, 165], and as described in Section 4.2.2. It was assumed that this temperature sensitivity was independent of strain.

Figure 5.18 shows the temperature and strain dependence of the FIR (*FIR1*) together with its corresponding temperature sensitivity. The strain independence of the FIR is clearly evident in Figure 5.18(a). A third and sixth order polynomial

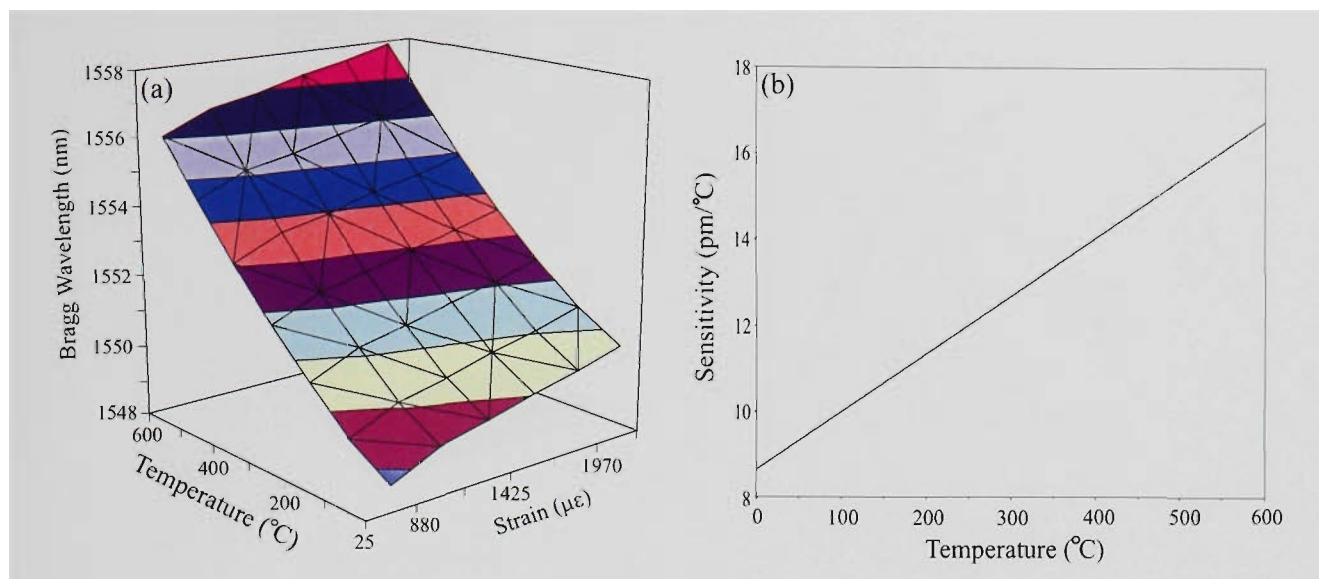


Figure 5.17: Plots of (a) Bragg wavelength temperature and strain calibration map and (b) Bragg wavelength sensitivity vs temperature for Sensor 5. Note: Solid lines shown in the plot of Bragg wavelength vs temperature are 2^{nd} order polynomial fits.

were used to calibrate *FIR1*. The temperature sensitivity shown in Figure 5.18(b) corresponds to the third order polynomial fit to *FIR1*. It is evident that *FIR1* exhibits maximum sensitivity at $\sim 300^\circ\text{C}$, and approaches zero at extremely high and low temperatures, as predicted by the Boltzmann distribution. *FIR2* exhibited a higher peak sensitivity, but suffered from zero sensitivity within the temperature range investigated here, and therefore was not considered any further.

Table 5.17 summarises the RMS temperature and strain errors deduced from using a modified version of Method C. The variation in Method C involves the use

Table 5.17: RMS temperature and strain errors for Sensor 5.

Fit to FIR	RMS Temp. Error ($^\circ\text{C}$)	RMS Strain Error ($\mu\epsilon$) by Method:		
		Minima	Half-Maximum	Weighted Ave.
3^{rd} Order Polynomial	5.8	58.2	56.7	56.9
6^{th} Order Polynomial	1.7	30.1	27.8	27.0

of higher order polynomials to describe the temperature dependence of the FIR. A second order polynomial was not used to calibrate the FIR due to the poor fit

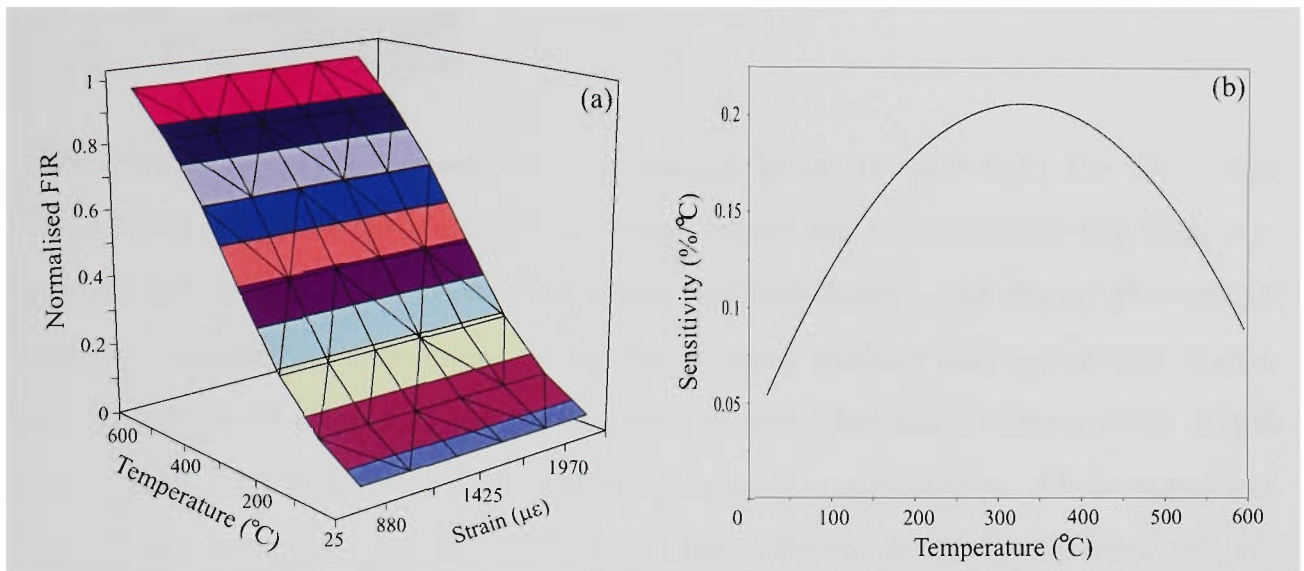


Figure 5.18: Plots of (a) FIR temperature and strain calibration map and (b) FIR sensitivity vs temperature for Sensor 5 (*FIR1*). Note: Solid line in (a) represents a 3rd order polynomial.

it would have for the data shown in Figure 5.18(a). Using the third polynomial resulted in a relatively poor RMS temperature error. Even though the FBG calibration gave comparable fits (in terms of their corresponding r^2 values) to the previous sensors, the poor temperature performance resulted in degraded RMS strain errors. Therefore, a sixth order polynomial was used to improve the RMS temperature error. This fit resulted in an acceptable RMS temperature error of 1.7°C , which is equal to 0.3% error over the measured temperature range. This improved temperature performance also resulted in an improved RMS strain error of $27.0\ \mu\epsilon$, which is equal to 1.7% error over the measured strain range. As shown with the previous sensors, the Weighted Average and Half-Maximum methods showed improved strain performance relative to the Minima Method.

5.9 Conclusions

The combination of FBGs and the fluorescence intensity ratio from the ${}^2\text{H}_{11/2}$ and ${}^4\text{S}_{3/2}$ levels in erbium for simultaneous temperature and strain sensing has been presented. Initially, the effects of pump power and wavelength, and doped fibre length were investigated to determine the optimum pump settings and doped fibre length for these type of sensors. Five sensors were investigated using three erbium doped fibres (Er1, Er3 and Er4), each with varying core compositions. Their important parameters are summarised in Table 5.18. Two different wavelength ranges, namely *FIR1* and *FIR2*, were used to analyse the FIR. The FIR temperature and strain

Table 5.18: Summary of important parameters for Sensors 1-5.

Parameter	Sensor				
	1 ^a	2 ^b	3	4	5
Er ³⁺ Doped Fibre	Er1	Er1	Er3	Er3	Er4
Er ³⁺ Conc. (ppm)	1430	1430	2680	2680	90
Core Diameter (μm)	8.0	8.0	3.9	3.9	4.9
Sensor Length (cm)	12	10	6	9	16
Sensor Configuration	A	B	B	B	C
Pump Source	Ti:Sapp	Ti:Sapp	Ti:Sapp	Laser Diode	Ti:Sapp
Pump Wavelength (nm)	803	803	803	808	803
Pump Power (mW)	574	765	400	50	500
		140			

^a Er³⁺ doped fibre length was 6 cm.

^b Sensor investigated using two different pump powers.

coefficients for Sensors 1-4 are summarised in Figure 5.19. As can be seen from Figure 5.19(a), *FIR1* was found to exhibit a smaller temperature sensitivity compared to *FIR2*. Also, Figure 5.19(b) shows that the FIR was found to exhibit a strain sensitivity that is approaching zero at one standard deviation. Figure 5.20 summarises the RMS temperature and strain errors deduced using the various analysis

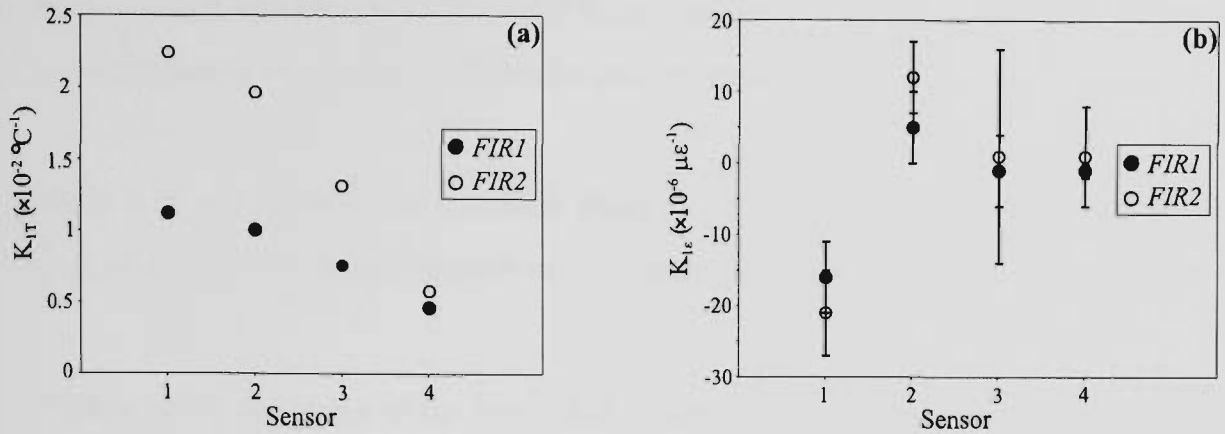


Figure 5.19: Summary of linear (a) temperature and (b) strain FIR coefficients evaluated using Method A for Sensors 1-4.

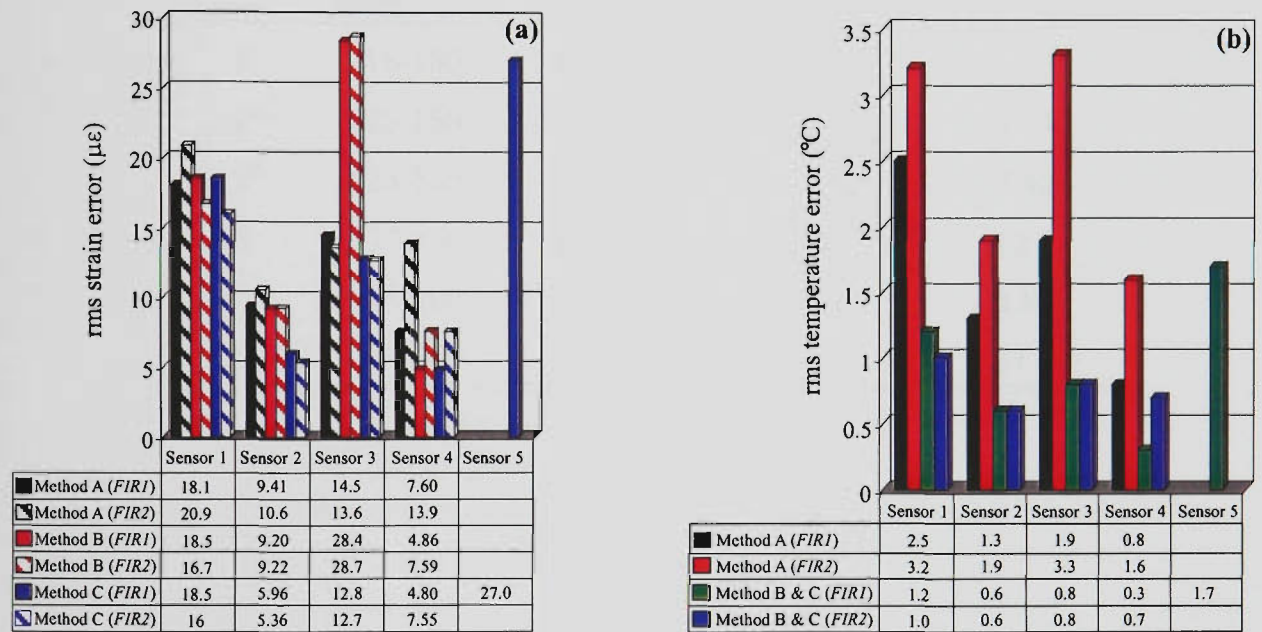


Figure 5.20: Summary of some of the best RMS (a) strain and (b) temperature errors for Sensors 1-5. Note: errors shown are those deduced using the Weighted Average technique.

techniques. It can be seen that Method C produced significantly smaller RMS errors compared to Methods A and B. Also, the less temperature sensitive *FIR1* produced consistently smaller RMS temperature and strain errors compared to *FIR2*.

Type I FBGs were used for all sensors demonstrated here. FBGs were fabricated within the doped fibre of Sensors 2-5, while the FBG for Sensor 1 was fabricated in standard telecommunications fibre. Sensors with FBGs fabricated within the doped fibre showed consistently superior performance in determining temperature and strain simultaneously. The Half-Maximum and Weighted Average methods used

to determine the Bragg wavelength from the spectra showed superior performance in determining the strain, relative to the Minima method.

Table 5.19 summarises the optimum RMS strain and temperature errors achieved by each of the erbium based sensors investigated. All sensors showed reasonable perfor-

Table 5.19: Summary of the best RMS temperature and strain errors for Sensors 1-5.

Sensor	Measurement Range		RMS Errors	
	Temp. ($^{\circ}\text{C}$)	Strain ($\mu\epsilon$)	Temp. ($^{\circ}\text{C}$)	Strain ($\mu\epsilon$)
1	18-150	350-2534	1.0	15.9
2 ^a	25-150	350-2534	0.6	5.04
2 ^b	25-150	350-2534	0.8	7.42
3	27-150	350-1988	0.8	12.1
4	25-100	350-1460	0.3	4.80
5 ^c	25-600	350-1988	1.7	27.0

^a 765 mW pump power.

^b 140 mW pump power.

^c 6th order polynomial fitted to FIR data.

mance, with Sensors 2 and 4 showing RMS temperature errors below 1°C and RMS strain errors in the order of $5\mu\epsilon$. Although tested over relatively narrow temperature and strain ranges, Sensor 4 showed the most promise in being further developed as a practical sensor. The sensor system exhibited the smallest RMS temperature and strain errors and apart from the interrogation system, is an ‘all in-fibre’ system. The high FBG sustainable fibre, Er4 (Sensor 5), demonstrated reasonable performance across a wide range of operating temperatures. This scheme demonstrated better temperature and strain results compared to a similar technique, referred to as the fluorescence peak power ratio (FPPR), which was recently reported [93]. This technique is based on a combination of the FPPR from the $^4\text{I}_{13/2}$ level in erbium and a FBG. The superior results shown in this thesis may be due to the lower susceptibility of the FIR to pump power fluctuations compared to the FPPR. Also, the

FIR technique integrates the fluorescence spectra over specific wavelength bands, whereas the FPPR takes a ratio of two intensity readings (off an OSA). This would make the temperature and strain measurements of FPPR technique more susceptible to spectral noise. Also, Sensor 5 could potential exhibit improved performance if developed into an all 'in-fibre' sensing scheme.

Chapter 6

ERBIUM:YTTERBIUM BASED SENSORS

This chapter details investigations made into erbium:ytterbium doped fibre combined with FBGs for potential use for simultaneous temperature and strain measurement. The performance of these sensors will be compared to those investigated in Chapter 5 to determine whether the FIR from Yb^{3+} and the ytterbium sensitised $^4\text{I}_{13/2}$ fluorescence from Er^{3+} provide advantages when applied to simultaneous temperature and strain sensing. The intrinsic advantages of ytterbium sensitised erbium have previously been highlighted in Section 3.1.3. Also, variations in excitation power and wavelength, and rare earth doped fibre length are investigated to determine their effects on the fluorescence properties of these fibres.

Calibrations were performed on five sensors fabricated from ErYb1, ErYb2 and ErYb3 fibre. Due to ErYb3 generating the highest levels of fluorescence from short fibre lengths compared to ErYb1 and ErYb2, three of the five sensors were fabricated using this fibre. All FBGs were inscribed within the rare earth doped fibre, as detailed in Chapter 3.

6.1 FIR Wavelength Ranges

The wavelength ranges over which the fluorescence intensities were summed were chosen to select fluorescence from the thermalising Stark split levels from the $^2\text{F}_{5/2}$ level in Yb^{3+} . The FIR range, denoted here as *FIR3*, has previously been shown to

exhibit the highest temperature sensitivity for Yb^{3+} [59] and is given by

$$FIR3 = \frac{\sum_{900}^{910} I}{\sum_{1051.5}^{1070} I}, \quad (6.1)$$

where I represents the intensity at each wavelength and the wavelength limits of the sum are given in nanometres. These wavelength bands also correspond to some commercially available notch filters.

An alternate, much broader range of wavelengths was also chosen as a comparison to $FIR3$ and is denoted here as $FIR4$. It is given as

$$FIR4 = \frac{\sum_{880}^{970} I}{\sum_{1040}^{1070} I}. \quad (6.2)$$

6.2 Pump Power and Wavelength Effects

The dependence of the pump power on the fluorescence properties of $\text{Er}^{3+}:\text{Yb}^{3+}$ doped fibre was investigated to quantify its effect on sensor performance. There are two fluorescence bands of interest. The ${}^2F_{5/2}$ level of ytterbium is utilised for the FIR technique to measure temperature, while the ytterbium sensitised ${}^4I_{13/2}$ level of erbium is utilised as a broadband source to interrogate the Bragg wavelength. The FIR from the ${}^2F_{5/2}$ level of ytterbium has been investigated previously [59].

The sample used for this investigation was ErYb3 (see Table 3.1). Fluorescence from ErYb3 was measured for launched pump powers between 50 mW and 510 mW using 808 nm emission from a Ti:Sapphire laser. This wavelength was chosen to correspond with the wavelength of the laser diode used in this thesis and for reasons that are explained later in this Section.

Figure 6.1 shows the normalised FIR versus pump power. The wavelength band

chosen to investigate the dependence of the FIR to pump power was *FIR4*. The

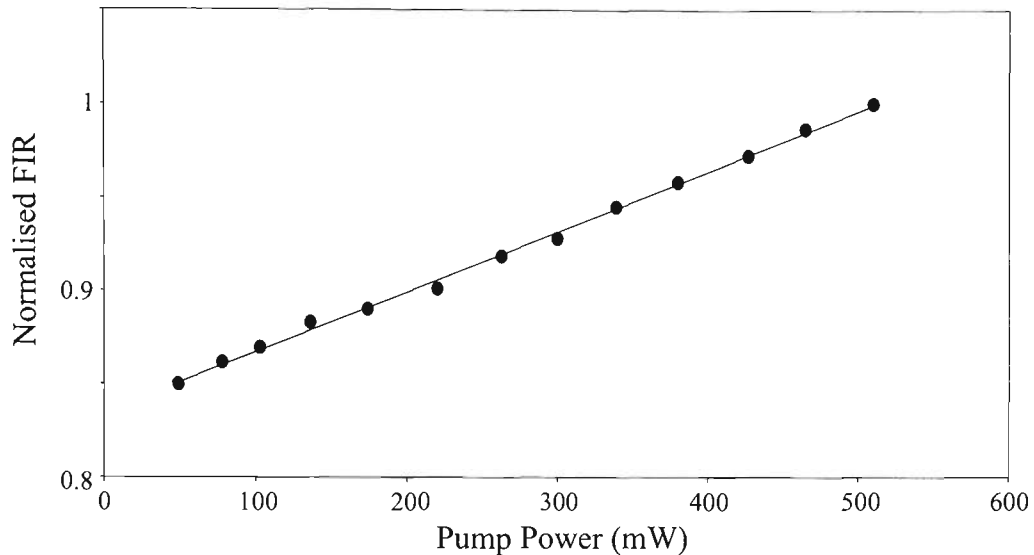


Figure 6.1: Normalised fluorescence intensity ratio (*FIR4*) versus pump power for ErYb3 fibre. The solid line represents a regression fit to the data.

solid line shown represents a simple regression fit to the data. The dependence of the FIR to pump power was found to be $3.215 \times 10^{-4} \text{ mW}^{-1}$. When considering the FIR temperature coefficient for Sensor 8, a temperature fluctuation of $0.02 \text{ }^\circ\text{C/mW}$ would be present.

The pump power levels and the laser source used in acquiring these results aren't practical for the development of a prototype sensor, although it does give a good approximation of the pump power effects on the fluorescence originating from the $^2\text{F}_{5/2}$ level of ytterbium.

As in Chapter 5, fluorescence from the $^4\text{I}_{13/2}$ level in erbium was used as a broadband light source for the purpose of interrogating the Bragg wavelength. Figure 6.2 shows the normalised fluorescence intensity from the $^4\text{I}_{13/2}$ level versus pump power. As expected, it can be seen that the fluorescence begins to saturate at higher pump powers. Practical powers for sensors developed in this work would be in the order of 10s of milliwatts, and so the available laser diode (50 mW) would result in ap-

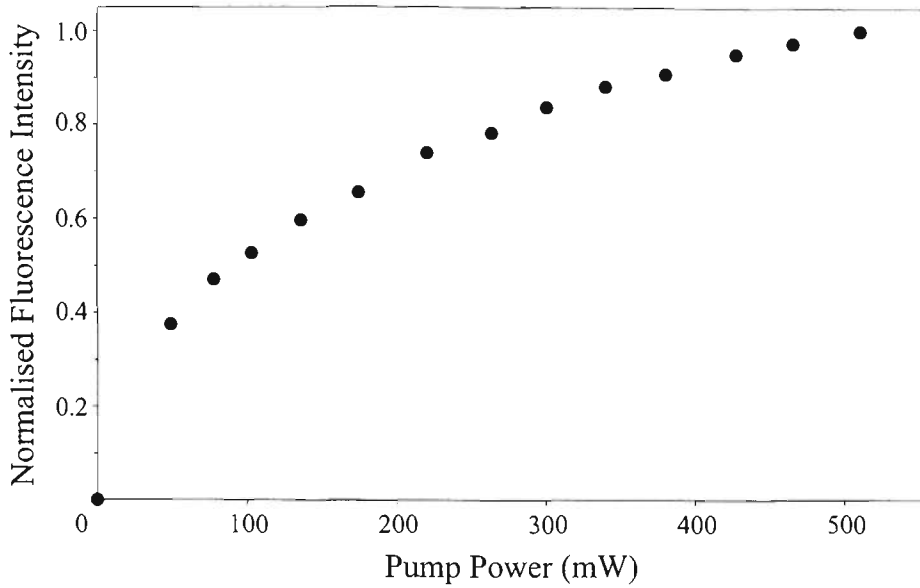


Figure 6.2: Normalised fluorescence intensity versus pump power from the erbium $^4I_{13/2}$ level in ErYb3.

proximately 40% of the total fluorescence generated from the $^4I_{13/2}$ level in ErYb3. Also, there is no evidence of saturation at pump powers near 50 mW.

The normalised fluorescence intensities from the $^4I_{13/2}$ and $^2F_{5/2}$ levels versus pump wavelength are shown in Figure 6.3. For this sensing scheme, it was important to select the pump wavelength in a region of the spectrum that would have no interference

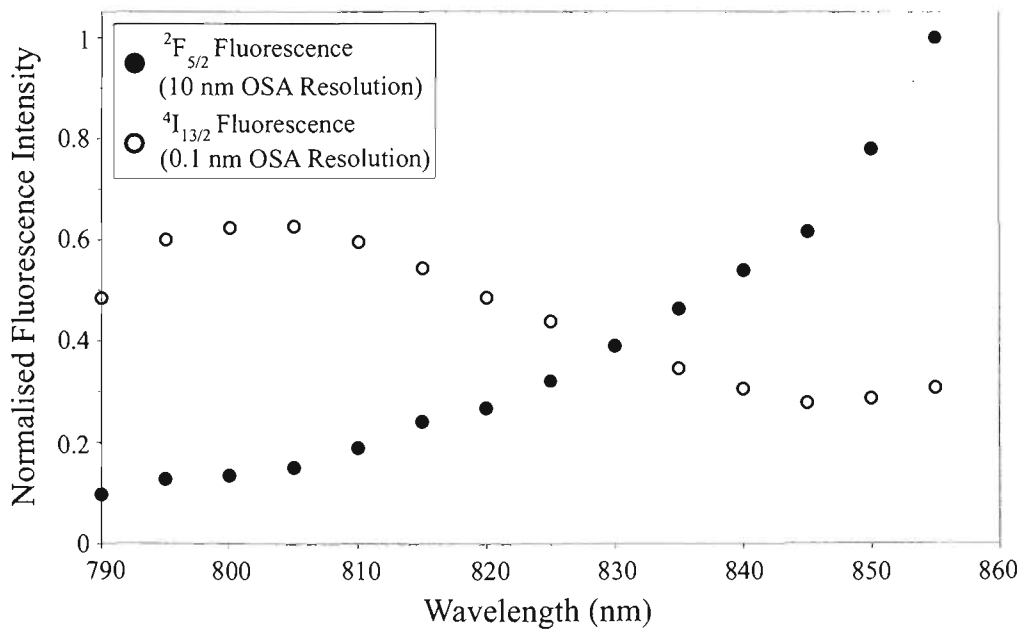


Figure 6.3: $^4I_{13/2}$ and $^2F_{5/2}$ fluorescence intensity versus pump wavelength. Intensities normalised relative to each other.

on the wavelength bands chosen for the FIR. This is necessary to avoid any overlap between the upper Stark split bands in the ${}^2F_{5/2}$ level and the residual pump tails of the source. Also, due to resolution requirements, a high level of fluorescence was required from the ${}^4I_{13/2}$ level in erbium to interrogate the FBG spectrum. Therefore, it is evident from Figure 6.3 that the preferred pump wavelength is approximately 808 nm. This wavelength enables maximum and reasonable fluorescence intensities from the ${}^4I_{13/2}$ and ${}^2F_{5/2}$ levels without affecting the preferred FIR wavelength bands. It must be also noted that laser diodes at this wavelength are commonly available.

6.3 Doped Fibre Length

The effect of doped fibre length on the ${}^2F_{5/2}$ fluorescence from ytterbium and the ${}^4I_{13/2}$ level in erbium was investigated. Fluorescence intensity measurements were made for doped fibre lengths up to 0.5 m. Fluorescence spectra were recorded from ErYb1 and ErYb3 doped fibre, which was pumped by 50 mW at 808 nm from a fibre pigtailed laser diode. Co-propagating ${}^2F_{5/2}$ and ${}^4I_{13/2}$ fluorescence was captured by the OSA set to 10 nm and 0.1 nm resolution, respectively.

The normalised fluorescence intensity versus doped fibre length from both fluorescing levels, and fluorescence spectra for various lengths of ErYb1 and ErYb3 are illustrated in Figure 6.4. As expected, Figure 6.4(a) shows that the ${}^2F_{5/2}$ fluorescence from the fibre with the higher $\text{Er}^{3+}:\text{Yb}^{3+}$ concentration, ErYb3, begins to saturate at shorter lengths compared to ErYb1. This is particularly evident with the ${}^4I_{13/2}$ fluorescence intensity (Figure 6.4 (b)) where ErYb3 begins to saturate, whereas ErYb1 exhibits no signs of saturation. As with the work in Chapter 5 involving erbium based sensors, the region of interest is in lengths < 20 cm. It can be seen that the ${}^2F_{5/2}$ fluorescence from both fibres demonstrated a small amount of excited state absorption at these fibre lengths, whereas, only the ${}^4I_{13/2}$ fluorescence from ErYb3 suffered from excited state absorption. Also, as expected, the fibre with the higher $\text{Er}^{3+}:\text{Yb}^{3+}$ concentration demonstrated higher levels of fluorescence for short lengths of fibre. Figure 6.4(c) shows the ${}^2F_{5/2}$ fluorescence spectrum at various

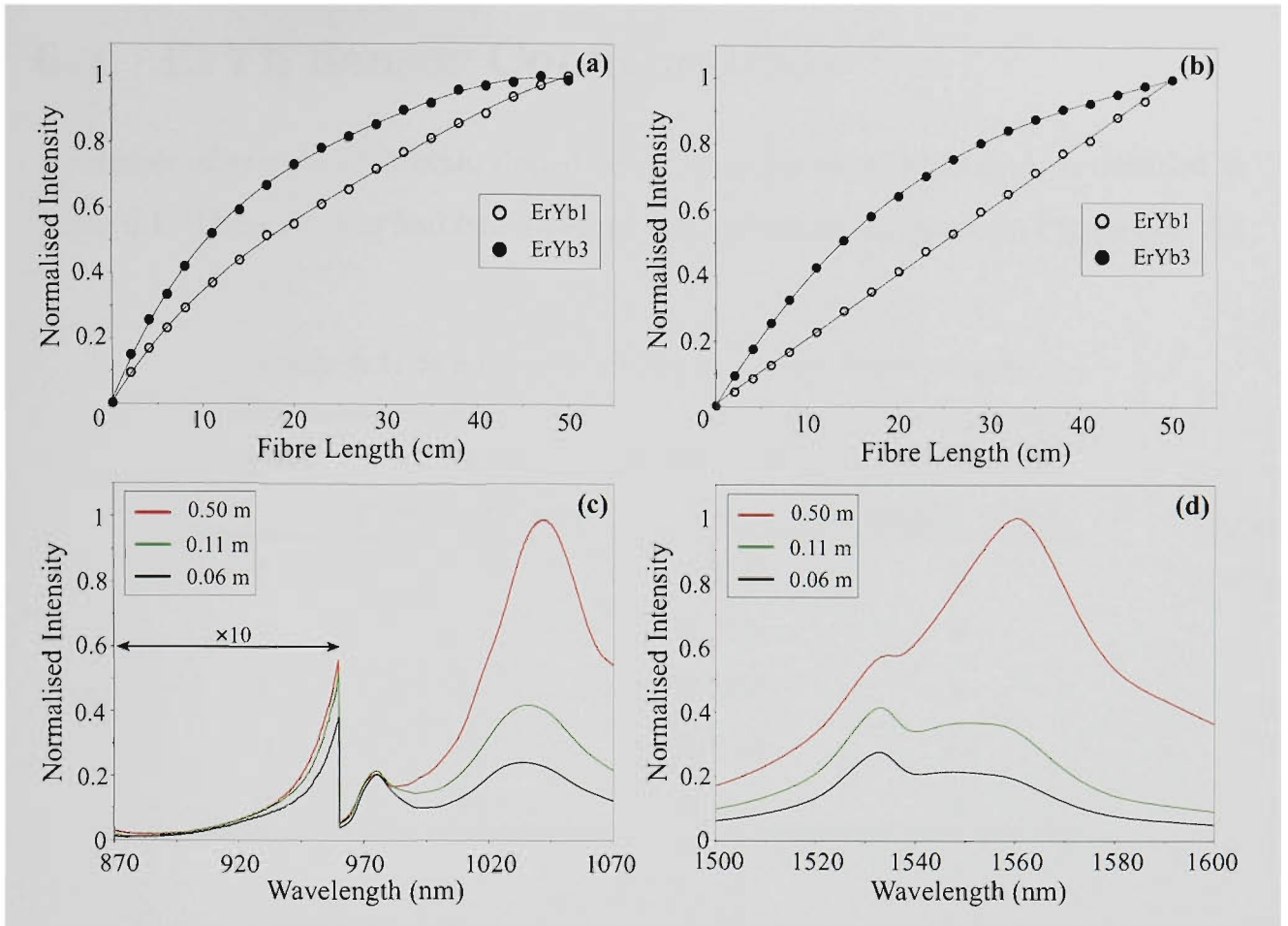


Figure 6.4: Independently normalised (a) ${}^2F_{5/2}$ and (b) ${}^4I_{13/2}$ fluorescence intensity versus doped fibre length for ErYb1 and ErYb3 (note: solid lines provided as a guide for the eye only). Normalised (c) ${}^2F_{5/2}$ and (d) ${}^4I_{13/2}$ fluorescence spectra at various ErYb3 fibre lengths.

ErYb3 fibre lengths. It can be seen that at the fibre lengths of interest here (e.g. 11 cm), the fluorescence intensity generated is 40% of that generated using a 50 cm fibre length.

It must also be noted that the peak intensity from the ${}^4I_{13/2}$ level in erbium shifts to a longer wavelength band with increasing fibre length, as can be seen in Figure 6.4(d). This is an important factor when determining the bandwidth for the interrogation of the Bragg wavelength. The Bragg wavelength should be chosen to lie within the maximum intensity region of the ${}^4I_{13/2}$ fluorescence.

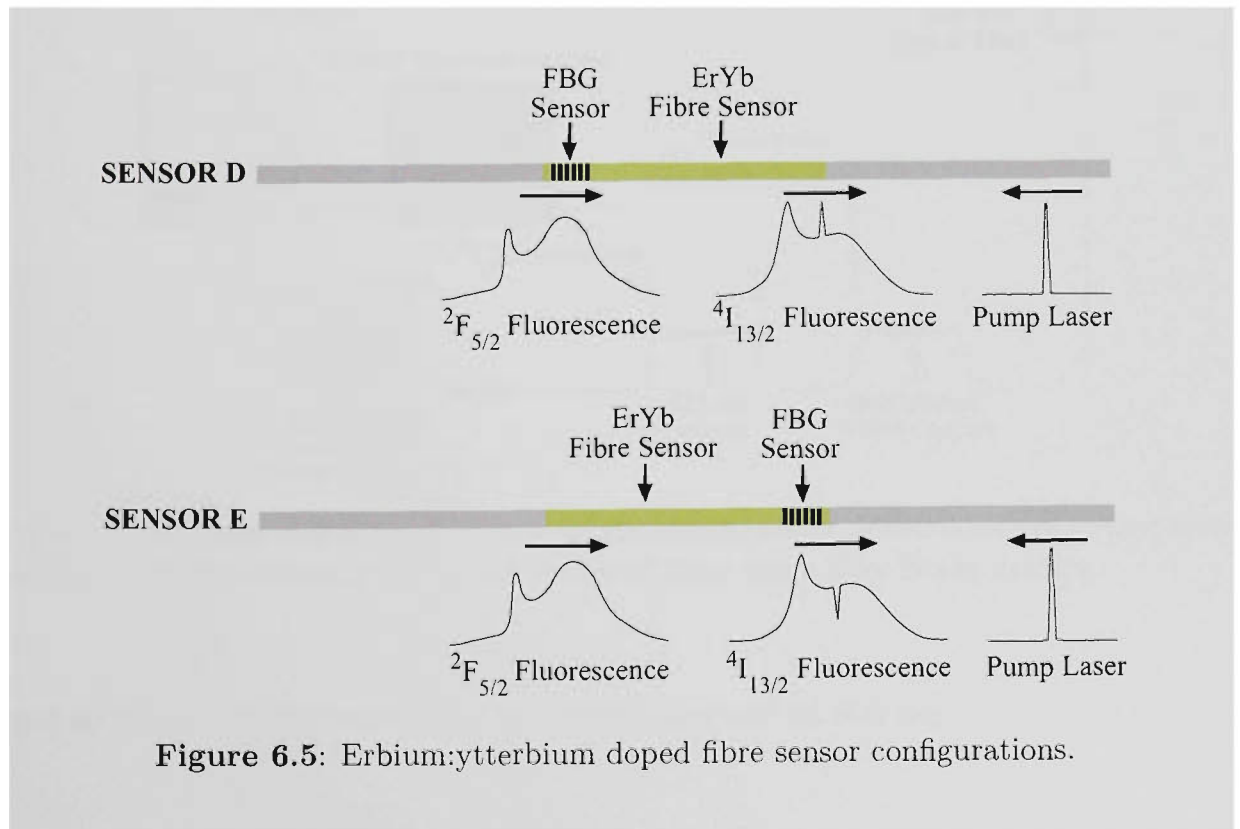
6.4 ErYb Sensor Configurations

A number of erbium:ytterbium doped sensor samples were fabricated, as detailed in Table 6.1. These sensors had two different configurations, as shown in Figure 6.5. All

Table 6.1: Summary of erbium:ytterbium based sensors.

Sensor	Sensor Configuration	ErYb doped fibre	Total Sensor length (cm)
6	D	ErYb1	9
7	D	ErYb2	9
8	E	ErYb3	5
9	E	ErYb3	12
10	E	ErYb3	9

sensors were configured so that all fluorescence was captured counter-propagating.



For sensors adopting Sensor D configuration, the FBG was inscribed near the doped fibre end furthest from the detection system. This resulted in a reflected FBG

spectrum to be observed. Sensor E configuration had the FBG inscribed near the doped fibre end closest to the monitoring system, which resulted in a transmitted FBG spectrum being detected.

6.5 Experimental Arrangement

The experimental arrangement used for measuring the FIR and Bragg wavelength shift to temperature and strain for the ErYb sensors is illustrated in Figure 6.6. Depending on the ErYb fibre used, either a laser diode or Ti:Sapphire laser was

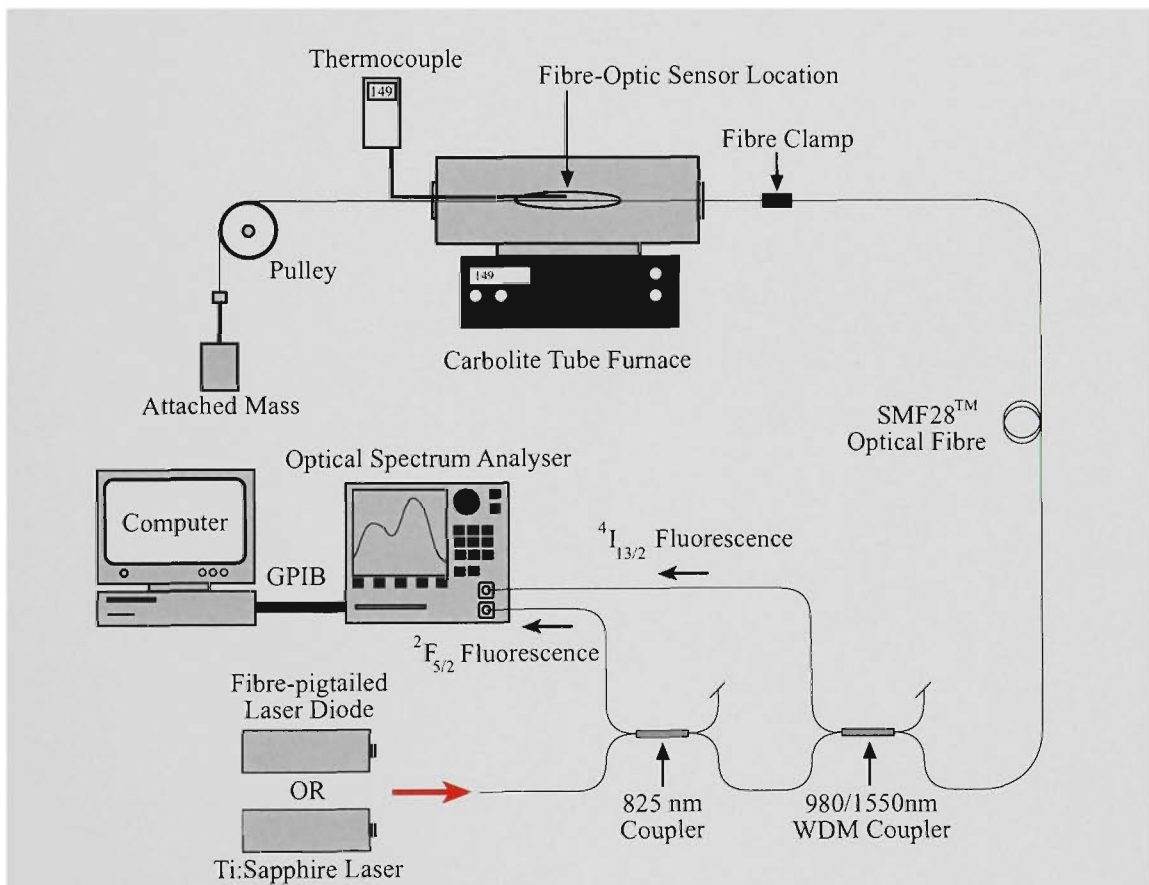


Figure 6.6: Experimental arrangement for the simultaneous measurement of temperature and strain using a combination of Er:Yb doped fibre and a fibre Bragg grating.

used as the excitation source, both of which emitted at 808 nm.

The arrangement of the fibre-optic couplers differed from that shown in Figure 5.8. The couplers were arranged so that all fluorescence was captured counter-propagating, which allows the sensor to be used as a probe. This was possible due

to the 980/1550 nm WDM coupler propagating both the 808 nm pump and the ${}^2F_{5/2}$ fluorescence through one port. The detection system and data acquisition used was the same as that described in Section 5.5. Also, the temperature and strain environments that the sensors were calibrated to were the same as that used for the erbium based sensors, as described in Section 5.5.1.

6.6 ErYb1 and ErYb2 Sensor Calibrations

One sensor using ErYb1 and another using ErYb2 fibre were calibrated against temperature and strain. ErYb1 contained the lowest concentration of $\text{Er}^{3+}:\text{Yb}^{3+}$, while ErYb2 had a $\text{Er}^{3+}:\text{Yb}^{3+}$ concentration between ErYb1 and ErYb3. Due to both ErYb1 and ErYb2 generating lower levels of fluorescence intensity compared to ErYb3, the Bragg grating and rare earth doped fibre were oriented to follow Sensor Configuration D. This allowed a higher peak power to be reflected by the FBG as compared with a transmitted FBG spectrum. The pump sources for Sensors 6 and 7 were the fibre pigtailed laser diode and 500 mW from a Ti:Sapphire laser, respectively.

6.7 Sensors 6 and 7 Results

The temperature and strain calibrations for Sensor 6 were performed over temperatures and strains ranging from 20-100 °C and 350-1460 $\mu\epsilon$, respectively, while the temperature and strain ranges for Sensor 7 were 20-150 °C and 350-2534 $\mu\epsilon$, respectively. The experimental arrangement shown in Figure 6.6 was used to measure the dependence of the FIR and Bragg wavelength shift on temperature and strain. Five strain cycles at eight particular strain values were performed at each of the six and eight temperatures tested for Sensors 6 and 7, respectively.

Figure 6.7 illustrates fluorescence from the ${}^2\text{F}_{5/2}$ energy level from ErYb2 fibre at three different temperatures. As observed with the FIR from erbium in Chapter 5, the upper level fluorescence intensity increases with temperature while the lower level intensity decreases.

Table 6.2 summarises the linear matrix coefficients for both FIR ranges and the Bragg wavelength. As expected, the temperature and strain coefficients of the Bragg wavelength were consistent with those for the FBGs inscribed in erbium doped fibre. Due to the non-linear temperature dependence of the Bragg wavelength, the

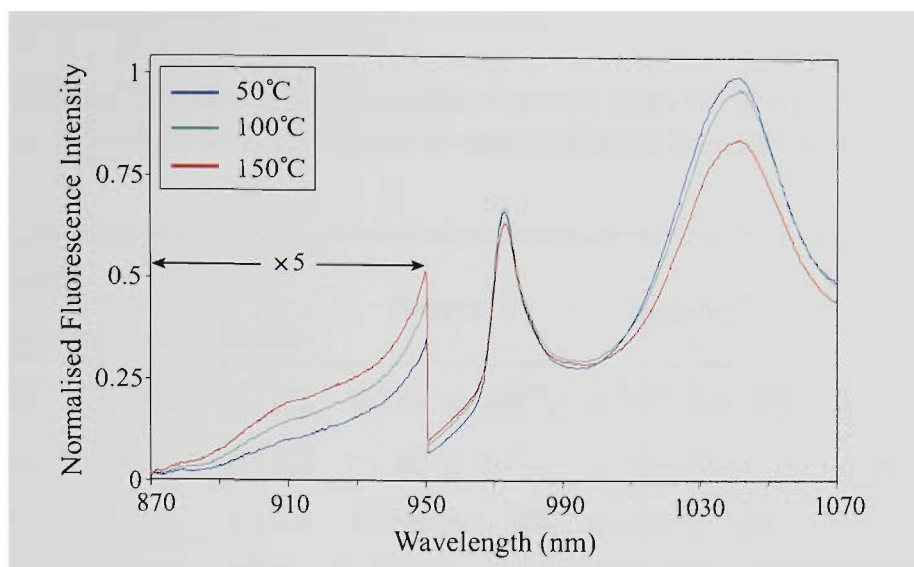


Figure 6.7: Counter-propagating fluorescence spectra from Sensor 7 at various temperatures. Note: OSA resolution set to 5 nm.

small variation in the temperature and strain coefficients is evident when Sensor 7 is calibrated over an extended temperature range. A small decrease in the strain coefficient can be seen for Sensor 7 relative to Sensor 6. This may indicate that the Bragg wavelength strain sensitivity may have a small dependence on the glass composition.

A comparison of the FIR ranges showed that *FIR4* exhibited an increased temperature sensitivity of approximately 5-fold relative to *FIR3* for both Sensors 6 and 7. As expected, when the temperature range was increased from 100 °C to 150 °C, the FIR temperature sensitivity increased. ErYb1 fibre exhibited greater temperature sensitivity compared to ErYb2. This may be due to the lower $\text{Er}^{3+}:\text{Yb}^{3+}$ concentration of ErYb1 compared to ErYb2. As with the FIR strain coefficient in the erbium based sensors, when taking into consideration the errors, the strain dependence of both *FIR3* and *FIR4* for both Sensors 6 and 7 can be assumed to be consistent with zero.

The temperature and strain de-convolution procedure was the same as that used for the erbium based sensors. Calibration formulae were generated for Methods A, B and C, which also incorporated the various FBG analysis techniques (Minima, Half-Maximum and Weighted Average). Figure 6.8 shows the temperature and strain differences versus the actual temperature and strain, respectively. The

Table 6.2: Linear coefficients with associated errors deduced from calibration data for Sensors 6 and 7. Temperature and strain ranges used were 20 - 100 °C and 350 - 1460 $\mu\epsilon$, respectively.

Matrix Coefficient	FIR Range	Sensor 6	Sensor 7	Sensor 7 ^a
K_{1T} ($\times 10^{-3}$ °C ⁻¹)	<i>FIR3</i>	0.189 ± 0.001	0.137 ± 0.001	0.147 ± 0.001
$K_{1\epsilon}$ ($\times 10^{-9}$ $\mu\epsilon^{-1}$)	<i>FIR3</i>	60 ± 80	52 ± 54	0.3 ± 2
K_{1T} ($\times 10^{-3}$ °C ⁻¹)	<i>FIR4</i>	1.079 ± 0.006	0.744 ± 0.001	0.772 ± 0.002
$K_{1\epsilon}$ ($\times 10^{-9}$ $\mu\epsilon^{-1}$)	<i>FIR4</i>	-4 ± 25	-6 ± 24	-2 ± 17
K_{2T} ($\times 10^{-3}$ nm/°C)		9.73 ± 0.05	9.70 ± 0.09	10.1 ± 0.1
$K_{2\epsilon}$ ($\times 10^{-3}$ nm/ $\mu\epsilon$)		1.179 ± 0.004	1.135 ± 0.005	1.144 ± 0.009

^a Extended temperature and strain ranges used (20 - 150 °C and 350 - 2534 $\mu\epsilon$).

temperature and strain differences shown were deduced from calibration formulae results, which used Method C and the Weighted Average technique, being compared to the known temperature and strain conditions. Similar plots were generated for all other calibration formulae used but are not shown here. It is evident from Figure 6.8 that larger temperature and strain errors are present for Sensor 7 when the extended temperature and strain ranges were used compared to Sensor 6. This observation was consistent with the other results not shown here.

Table 6.3 shows a summary of the RMS temperature errors deduced from the temperature differences, such as those shown in Figure 6.8(a)(c). As expected, Method B generated improvements in the RMS temperature errors compared to Method A. This was due to a non-linear factor being included in the calibration formulae. The higher temperature sensitive *FIR4* resulted in significant improvements compared to *FIR3*, particularly when using Method A. Overall, Sensor 6 exhibited better RMS temperature errors compared to Sensor 7.

Table 6.4 shows a summary of the RMS strain errors for Sensors 6 and 7. As was observed with the erbium based sensors, the Weighted Average technique of

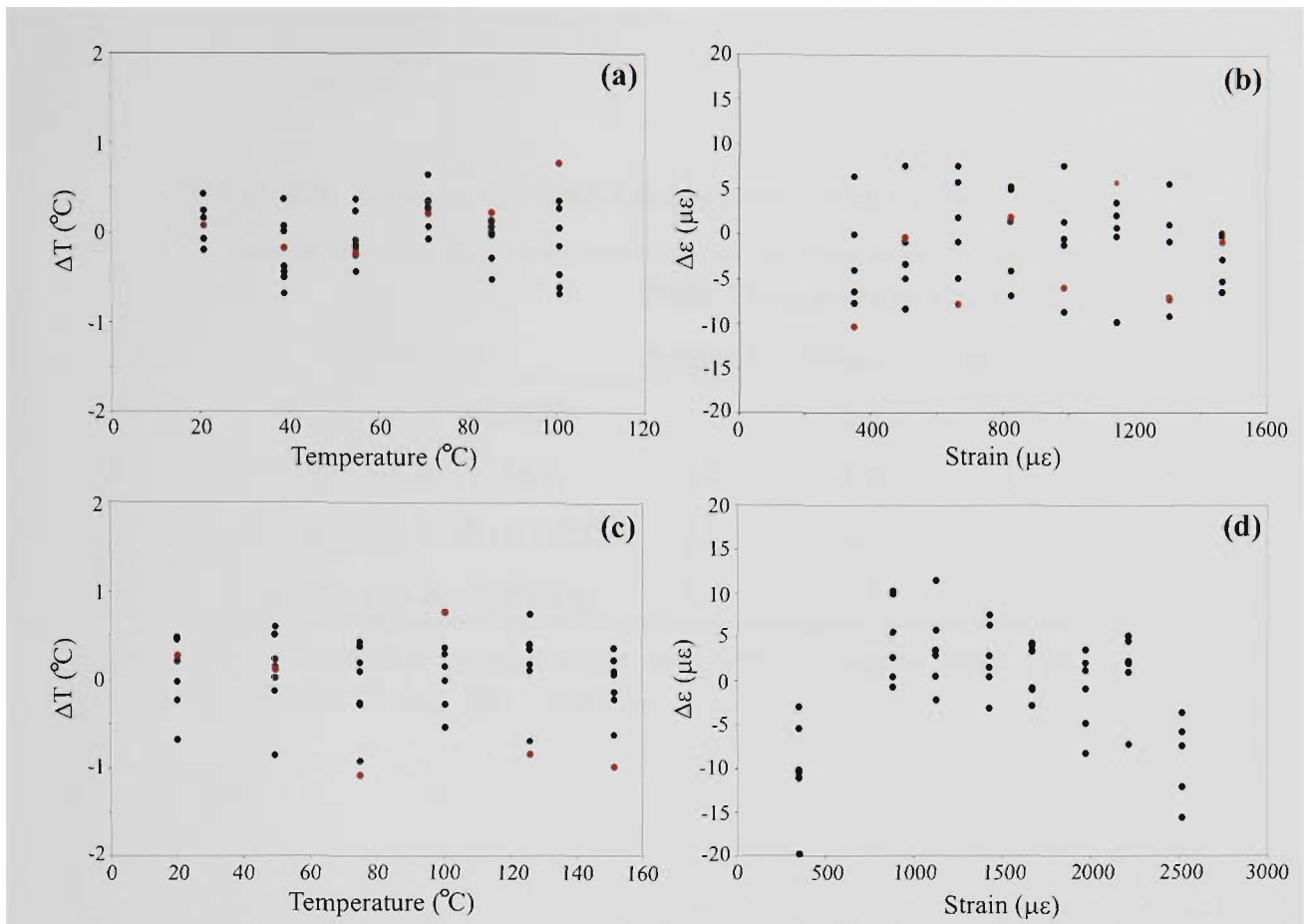


Figure 6.8: Comparison of temperature and strain deviations from known conditions for Sensors 6 ((a) and (b)) and 7 ((c) and (d)).

analysing the FBG spectra produced the smallest errors, while the Minima method generated the worst. Generally, better RMS strain errors were demonstrated when *FIR4* was used. This may be due to the improved RMS temperature errors translating also to an improvement in the RMS strain errors. Although Method B produced superior temperature results compared with Method A, it produced the worst RMS strain errors for both Sensors 6 and 7. Method C, which includes non-linear factors for both the temperature dependence of the FIR and the Bragg wavelength produced the best results, with RMS strain errors as small as 4.94 and $3.63 \mu\epsilon$ for Sensors 6 and 7, respectively. When the temperature and strain ranges were increased for Sensor 7, the RMS errors increased but still exhibited good performance with errors of 0.5°C and $6.57 \mu\epsilon$.

Table 6.3: Summary of RMS temperature errors for Sensors 6 and 7.

Analysis Method	RMS Temperature Error ($^{\circ}\text{C}$)		
	Sensor 6	Sensor 7	Sensor 7 ^a
Method A (<i>FIR3</i>)	1.2	1.9	2.5
Method A (<i>FIR4</i>)	0.7	1.0	1.5
Method B & C (<i>FIR3</i>)	0.5	0.5	0.8
Method B & C(<i>FIR4</i>)	0.3	0.4	0.5

^a Extended temperature and strain ranges used (20 - 150 $^{\circ}\text{C}$ and 350 - 2534 $\mu\epsilon$).

Table 6.4: Summary of RMS strain errors for Sensors 6 and 7.

Sensor	RMS Strain Error ($\mu\epsilon$) by Method:	Analysis Method					
		Method A		Method B		Method C	
		<i>FIR3</i>	<i>FIR4</i>	<i>FIR3</i>	<i>FIR4</i>	<i>FIR3</i>	<i>FIR4</i>
6	Minima	9.68	9.27	12.2	11.5	6.52	5.64
	Half-Maximum	6.37	5.47	10.5	10.1	5.54	5.18
	Weighted Ave.	6.14	5.33	10.3	9.90	5.40	4.94
7	Minima	10.9	4.95	8.63	8.01	5.97	4.82
	Half-Maximum	8.69	3.75	4.77	4.07	4.41	3.63
	Weighted Ave.	8.60	3.70	4.79	4.09	4.40	3.65
7 ^a	Minima	11.9	11.5	20.8	20.3	11.5	9.57
	Half-Maximum	9.34	8.51	19.3	18.7	8.79	6.57
	Weighted Ave.	9.29	8.57	19.2	18.7	8.75	6.63

^a Extended temperature and strain ranges used (20 - 150 $^{\circ}\text{C}$ and 350 - 2534 $\mu\epsilon$).

6.8 ErYb3 Sensor Calibrations

Three sensors using ErYb3 were calibrated against temperature and strain. Each sensor utilised a different length of doped fibre. One was equal to that used for the sensors fabricated from ErYb1 and ErYb2, another was longer and the other was shorter than that length. A comparison of sensor performance was made to determine the optimum doped fibre length required. ErYb3 produced the most fluorescence compared to the other two ErYb fibres investigated here, and so the Bragg grating was oriented in the rare earth fibre in the Sensor E configuration. This allowed the interrogation system to capture a transmitted FBG spectrum directly.

6.9 Sensors 8, 9 and 10 Results

The temperature and strain calibrations for Sensors 8, 9 and 10 were performed over temperature and strain ranges of 20-100 °C and 350-1460 $\mu\epsilon$, respectively. Five strain cycles at eight particular strain values were performed at each of the six temperatures tested for Sensors 8, 9 and 10.

The experimental arrangement shown in Figure 6.6 was used to measure the dependence of the FIR and Bragg wavelength shift upon temperature and strain. Sensor 8 was pumped with a Ti:Sapphire laser producing 480 mW, while the fibre-pigtailed laser diode was used for Sensors 9 and 10.

Figure 6.9(a) illustrates reflected FBG spectra from Sensor 7, while (b) shows transmitted FBG spectra from Sensor 8 at various strain levels and at a constant 100 °C. During fabrication, the FBGs inscribed in the ErYb3 fibres had reflectivities of 90%, but from Figure 6.9(b) it is clearly evident that the reflectance appears to be approximately 60%. This reduction is not due to annealing effects at this temperature, but is due to the fluorescence generated from the doped fibre between the FBG and the detection system partially 'washing out' the FBG reflectivity. This is advantageous as it does not produce a noisy spectra in the region of the Bragg

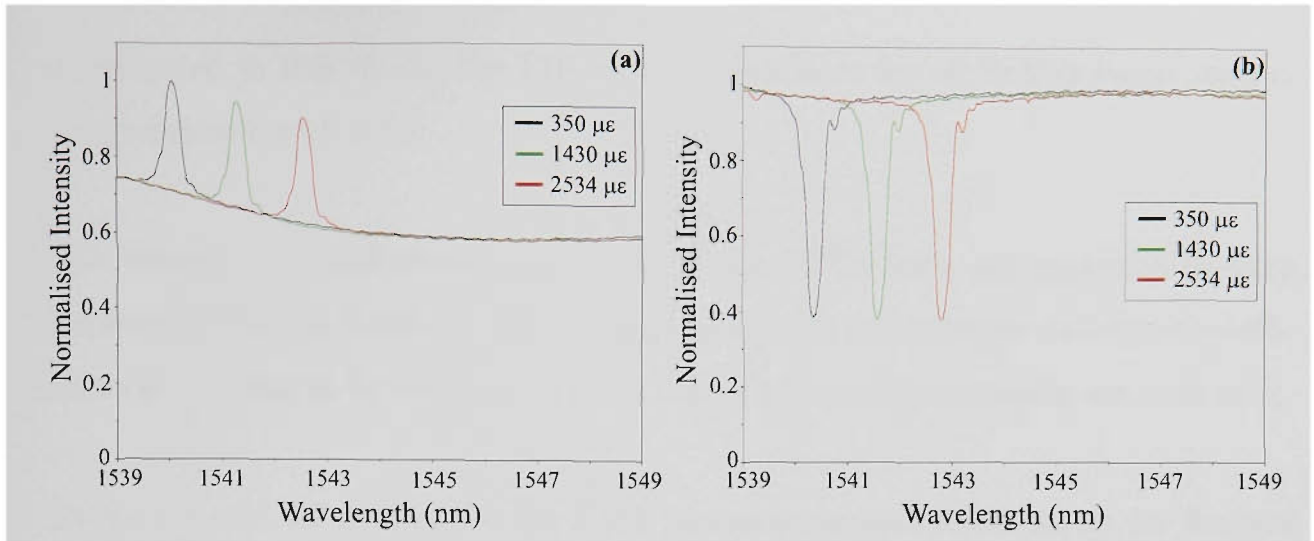


Figure 6.9: (a) Reflected and (b) transmitted FBG spectra at various strain levels and at 100 °C. The transmitted and reflected spectra are from Sensors 7 and 8, respectively.

wavelength since the intensity level is well above the noise floor. A similar effect is observed with the reflected FBG spectrum, as shown in Figure 6.9(a).

Table 6.5 shows a comparison of the linear matrix coefficients for Sensors 8, 9 and 10. The FIR temperature sensitivity, for both *FIR3* and *FIR4*, appeared to increase as the length of the doped fibre was decreased. This illustrates that there is an expected ‘trade off’ between fluorescence intensity being generated by the ErYb3 fibre length and the sensitivity of the FIR. Again, as observed with all previous sensors

Table 6.5: Linear coefficients with associated errors deduced from calibration data for Sensors 8, 9 and 10.

Matrix Coefficient	FIR Range	Sensor		
		8	9	10
$K_{1T} (\times 10^{-3} \text{ } ^\circ\text{C}^{-1})$	<i>FIR3</i>	0.1800 ± 0.0004	0.102 ± 0.003	0.12 ± 0.01
$K_{1\epsilon} (\times 10^{-9} \text{ } \mu\epsilon^{-1})$	<i>FIR3</i>	82 ± 89	79 ± 80	115 ± 285
$K_{1T} (\times 10^{-3} \text{ } ^\circ\text{C}^{-1})$	<i>FIR4</i>	1.105 ± 0.006	0.655 ± 0.006	0.81 ± 0.03
$K_{1\epsilon} (\times 10^{-9} \text{ } \mu\epsilon^{-1})$	<i>FIR4</i>	29 ± 62	160 ± 517	-31 ± 104
$K_{2T} (\times 10^{-3} \text{ nm}/^\circ\text{C})$		9.93 ± 0.04	9.45 ± 0.05	9.1 ± 0.3
$K_{2\epsilon} (\times 10^{-3} \text{ nm}/\mu\epsilon)$		1.130 ± 0.005	1.134 ± 0.005	1.13 ± 0.02

investigated in this thesis, the FIR strain dependence for all ErYb₃ based sensors was consistent with zero.

The temperature and strain coefficients of the FBGs were not expected to vary between Sensors 8, 9 and 10. The Bragg wavelength temperature and strain coefficients were found to be comparable when taking into consideration the errors present.

Tables 6.6 and 6.7 summarise the RMS temperature and strain errors for Sensors 8, 9 and 10, respectively. The results show consistently that Method C, used in conjunction with *FIR4*, produced the best RMS temperature errors. As exhibited

Table 6.6: Summary of RMS temperature errors for Sensors 8, 9 and 10.

Analysis Method	RMS Temperature Error (°C)			
	Sensor 8 ^a	Sensor 8	Sensor 9	Sensor 10
Method A (<i>FIR3</i>)	4.4	1.5	2.0	3.3
Method A (<i>FIR4</i>)	1.9	0.7	1.6	1.3
Method B & C (<i>FIR3</i>)	1.0	0.4	1.4	3.2
Method B & C (<i>FIR4</i>)	0.5	0.4	0.8	1.2

^a Extended temperature and strain ranges used (20 - 150 °C and 350 - 2534 $\mu\epsilon$).

by Sensors 6 and 7, *FIR4* showed superior performance compared to *FIR3*. Sensor 8 demonstrated the best RMS temperature error, while Sensor 10 the worst. Also, Sensor 8 exhibited smaller temperature errors compared to Sensors 9 and 10 when calibrated over extended temperature and strain ranges. This is further supported by Figure 6.10(a),(c) and (e), which shows the temperature difference versus temperature for Sensors 8, 9 and 10, respectively. The spread of residual temperature errors can be seen to be greatest for Sensor 10 and smallest for Sensor 8. The calibration formulae used for the results shown in Figure 6.10(a),(c) and (e) included the non-linear temperature coefficients for both the FIR and Bragg wavelength. Therefore, no non-linear effects of the residual temperature errors are present, such as those

Table 6.7: Summary of RMS strain errors for Sensors 8, 9 and 10.

Sensor	RMS Strain	Analysis Method					
	Error ($\mu\epsilon$)	Method A		Method B		Method C	
	by Method:	<i>FIR3</i>	<i>FIR4</i>	<i>FIR3</i>	<i>FIR4</i>	<i>FIR3</i>	<i>FIR4</i>
8 ^a	Minima	23.5	10.3	24.6	22.6	12.6	10.2
	Half-Maximum	23.2	8.15	23.5	21.1	11.1	7.59
	Weighted Ave.	23.0	7.86	23.3	21.0	10.8	7.28
8	Minima	16.7	9.97	21.2	19.8	10.6	9.78
	Half-Maximum	8.18	4.51	8.30	7.71	5.32	4.49
	Weighted Ave.	8.25	4.52	8.35	7.80	5.38	4.48
9	Minima	15.9	10.6	13.4	9.23	12.6	7.91
	Half-Maximum	13.2	7.48	13.0	9.11	11.8	7.27
	Weighted Ave.	11.9	7.56	12.9	9.08	11.5	7.16
10	Minima	27.8	15.7	28.1	14.5	27.2	13.4
	Half-Maximum	25.8	12.8	26.5	13.1	26.2	12.7
	Weighted Ave.	25.9	12.9	26.8	13.2	26.3	12.7

^a Extended temperature and strain ranges used (20 - 150 °C and 350 - 2534 $\mu\epsilon$).

observed when Method A is used (e.g. Figure 5.13(a) and (c)).

The improved RMS temperature errors using *FIR4* compared to *FIR3* also contributed to better RMS strain errors. As observed with all the other sensors investigated in this thesis, the Half-Maximum and Weighted Average techniques showed comparable results, but exhibited a distinct improvement over the Minima method. As demonstrated by the RMS temperature errors, Sensor 8 exhibited the smallest strain errors, while Sensor 10 the largest. This is consistent with the residual strain error spreads shown in Figure 6.10(b), (d) and (f), for Sensors 8, 9 and 10, respectively. Also, Sensor 8 exhibited comparable strain errors compared to Sensor 9 when calibrated over extended temperature and strain ranges.

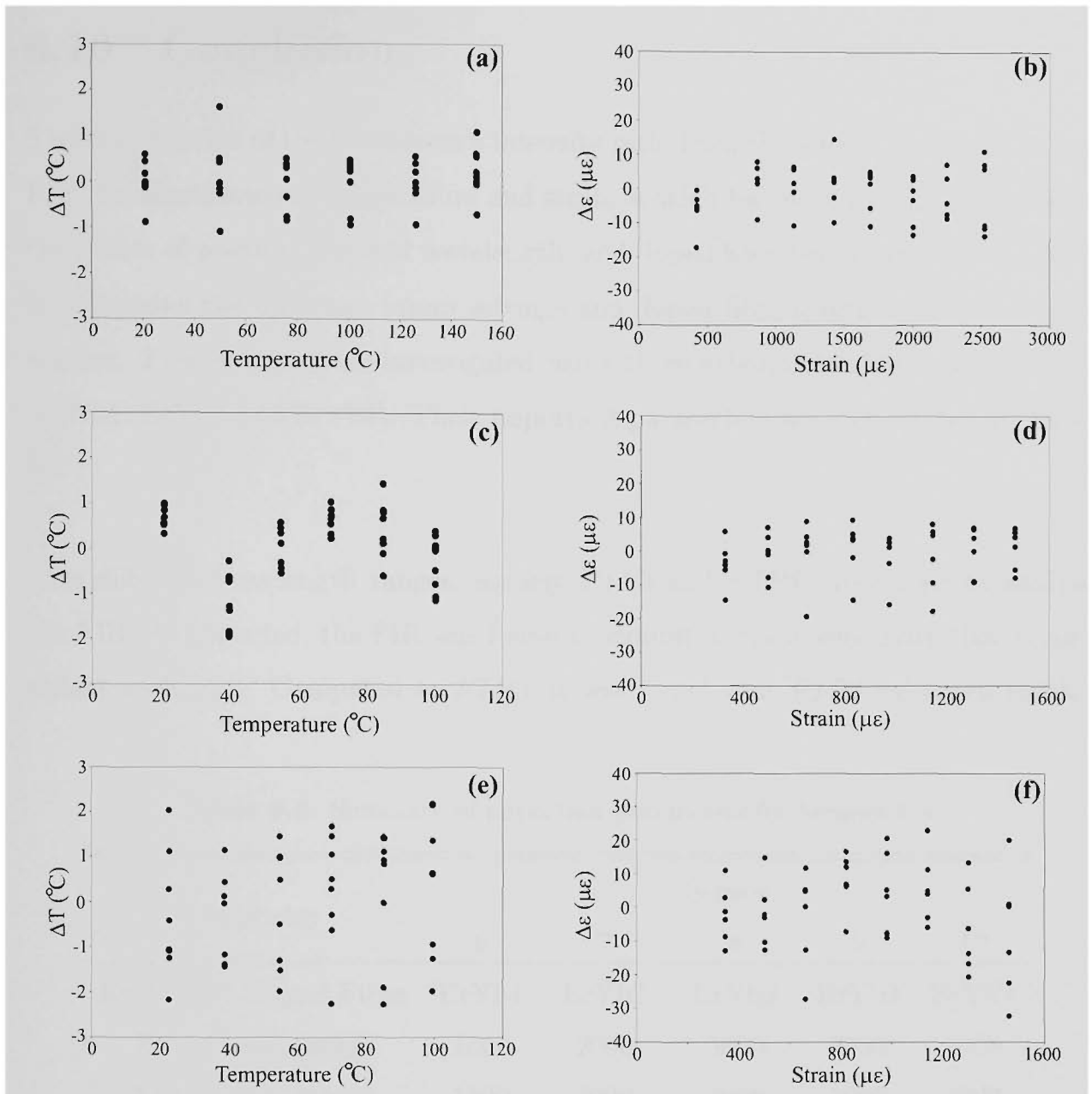


Figure 6.10: Comparison of temperature and strain deviations from known conditions for Sensors 8 ((a),(b)), 9 ((c),(d)) and 10 ((e),(f)) using *FIR4* and the Weighted Average technique together with Method C.

Sensor 8 also consisted of the shortest doped fibre length compared to the other ErYb3 sensors investigated, possibly indicating that longer lengths of highly doped fibre have a detrimental effect on the RMS temperature and strain errors of the sensor. The disadvantage of Sensor 8 was that the pump source used was 480 mW from a Ti:Sapphire laser, which would not be a practical or viable source for a commercialised sensing system.

6.10 Conclusions

The combination of the fluorescence intensity ratio from ${}^2F_{5/2}$ level in ytterbium and FBG for simultaneous temperature and strain sensing has been presented. Initially, the effects of pump power and wavelength, and doped fibre length were investigated to determine the optimum pump settings and doped fibre length for these type of sensors. Five sensors were investigated using three erbium:ytterbium doped fibres (ErYb1, ErYb2 and ErYb3). Their important parameters are summarised in Table 6.8.

Two different wavelength ranges, namely *FIR3* and *FIR4*, were used to analyse the FIR. As expected, the FIR was found to exhibit a strain sensitivity that is consistent with zero. Compared to *FIR3*, it was found that *FIR4* exhibited greater

Table 6.8: Summary of important parameters for Sensors 1-5.

Parameter	Sensor				
	6	7	8	9	10
Er ³⁺ :Yb ³⁺ Doped Fibre	ErYb1	ErYb2	ErYb3	ErYb3	ErYb3
Er ³⁺ Conc. (ppm)	1500	2000	3000	3000	3000
Yb ³⁺ Conc. (ppm)	1500	2000	3000	3000	3000
Core Diameter (μm)	3.8	5.5	4.4	4.4	4.4
Sensor Length (cm)	9	9	5	12	9
Sensor Configuration	D	D	E	E	E
Pump Source	LD	Ti:Sapp	Ti:Sapp	LD	LD
Pump Wavelength (nm)	808	808	808	808	808
Pump Power (mW)	50	500	480	50	50

temperature sensitivity and superior performance when applied to simultaneous temperature and strain sensing. Comparison of the RMS temperature errors of the three different ErYb fibres used shows that the RMS error improved as the rare earth concentration in the doped fibre decreased (e.g. ErYb1 exhibited the best performance

while ErYb3 the worst). Although the temperature sensitivities from the ErYb fibres were approximately an order of magnitude lower than those from the Er fibres in Chapter 5, they had comparable RMS temperature errors. This indicates that the low temperature sensitivity of Yb³⁺ doesn't have any influence on the resultant RMS temperature errors.

Type I FBGs were fabricated within the ErYb fibre for all sensors investigated in this Chapter. The Bragg wavelength strain sensitivity was found to increase with decreasing Er³⁺:Yb³⁺ concentration, while the temperature sensitivity increased with increasing Er³⁺:Yb³⁺ concentration. This indicates that the Bragg wavelength temperature and strain sensitivities may have a small dependence on the glass composition of the ErYb fibre.

Figure 6.11 shows the RMS temperature and strain errors deduced using the various analysis techniques, while Table 6.9 summarises the best RMS strain and temper-

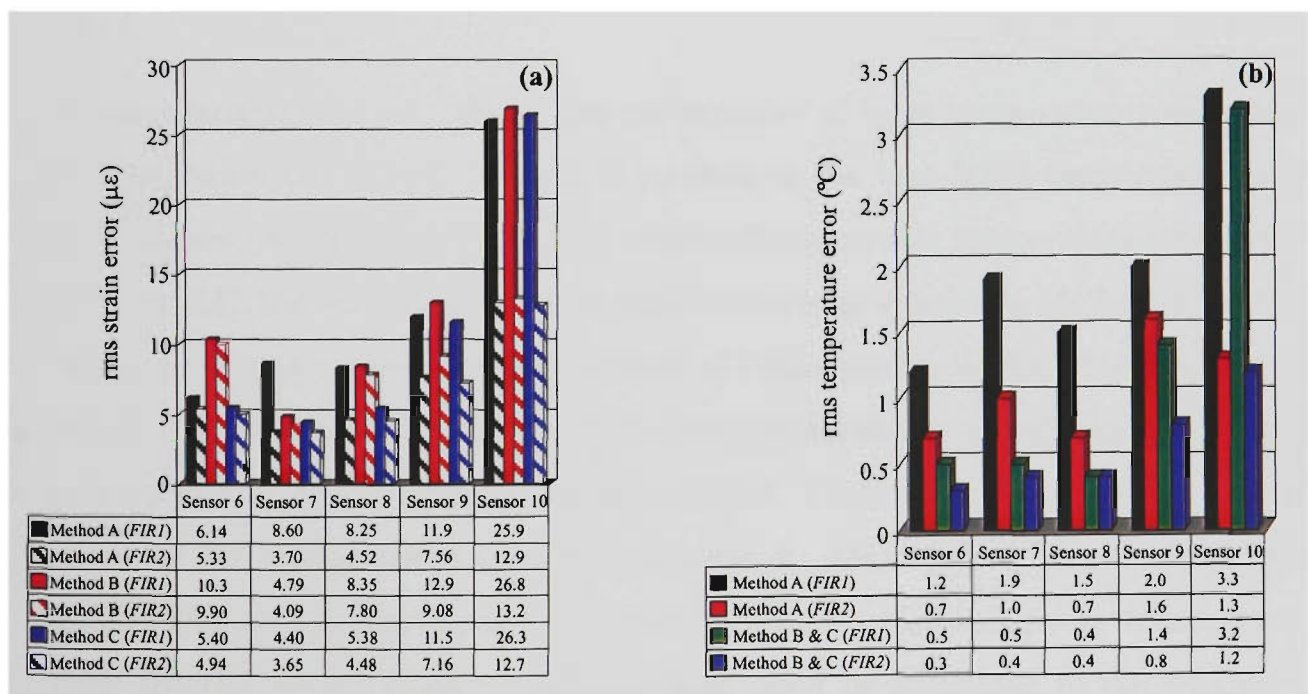


Figure 6.11: Summary of some of the RMS (a) strain and (b) temperature errors for Sensors 6-10. Note: errors shown are those deduced using the Weighted Average technique.

ature errors achieved by each of the erbium:ytterbium based sensors. All sensors showed very good performance, with only Sensor 10 showing an RMS tempera-

ture and strain error above 1°C and $8\mu\epsilon$, respectively. The lower concentration $\text{Er}^{3+}:\text{Yb}^{3+}$, ErYb1 and ErYb2, doped fibres (Sensors 7 and 8) demonstrated better performance compared to the higher doped ErYb3 sensors.

Table 6.9: Summary of RMS temperature and strain errors for Sensors 6-10.

Sensor	Measurement Range		RMS Errors	
	Temp. ($^{\circ}\text{C}$)	Strain ($\mu\epsilon$)	Temp. ($^{\circ}\text{C}$)	Strain ($\mu\epsilon$)
6	20-100	350-1460	0.3	4.94
7	20-100	350-1460	0.4	3.63
7	20-150	350-2534	0.5	6.57
8	20-100	350-1460	0.4	4.48
8	20-150	350-2534	0.5	7.28
9	20-100	350-1460	0.8	7.16
10	20-100	350-1460	1.2	12.7

When comparisons were made of the performance of three temperature and strain de-convolution techniques, Method C resulted in the best RMS temperature and strain errors. As expected, Method B exhibited comparable temperature accuracies to Method C, but exhibited the worst RMS strain error relative to Method A and C. When comparing varying analysis methods of FBG spectra, the Half-Maximum and Weighted Average methods demonstrated comparable results and were a distinct improvement over the conventional Minima method. These findings are consistent with those for the erbium based sensors in Chapter 5. Also, analysis of reflected FBG spectra (Sensor Configuration D) showed improved performance over transmitted FBG spectra (Sensor Configuration E). This could be attributed to the relatively small signal-to-noise ratio in the region of the Bragg wavelength, which was particularly evident when using the Minima method.

Overall, compared to the other sensors investigated in this chapter, Sensor 6 demon-

strated the best RMS temperature error (0.3°C) and a strain error below $5\mu\epsilon$. Although Sensor 7 exhibited a slightly larger temperature error (0.4°C), compared to Sensor 6, it did demonstrate the best RMS strain error ($3.63\mu\epsilon$). A practical limitation of Sensor 7 was that a Ti:Sapphire laser emitting 500 mW was used as the pump source. These results are comparable to the best performing erbium based sensor (Sensor 5), as detailed in Chapter 5.

Chapter 7

FBG CHARACTERISTICS AT ELEVATED TEMPERATURES

7.1 Thermal Stability of FBGs

A significant limitation of FBGs, particularly Type I FBGs, as temperature sensors, has been their self-erasure over prolonged periods of operation at elevated temperatures (Section 2.3.1). The high temperature characteristics of FBGs inscribed in various erbium doped fibres will be investigated in this Chapter. The results will be compared with chemical composition gratings (discussed in Section 3.2), a promising type of grating for high temperature applications due to its survivability at elevated temperatures. The characteristics of these gratings formed in erbium doped fibres, for the first time, will be presented in this Chapter.

7.2 Experimental Arrangement

Figure 7.1 shows the experimental arrangement used for the thermal treatment and interrogation of all FBGs investigated in Chapter 3. The transmitted spectral profile

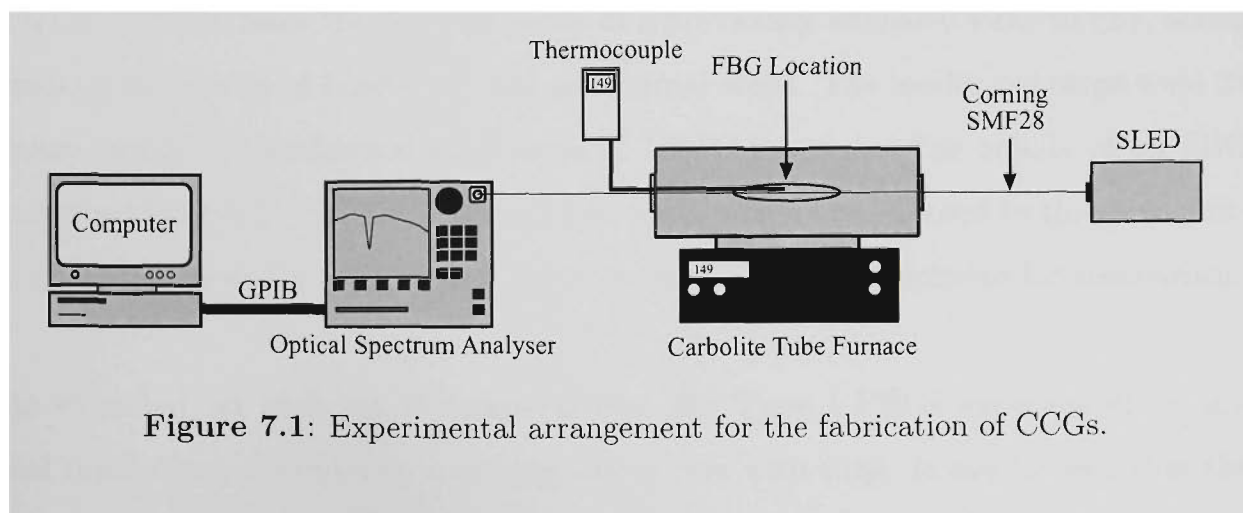


Figure 7.1: Experimental arrangement for the fabrication of CCGs.

of the Bragg grating was monitored using an OSA with a resolution set at 0.05 nm. Illumination of the FBG was provided by a broadband 1550 nm super-luminescent light emitting diode (SLED). The fibre containing the FBG was passed through a tube oven and a K-type thermocouple was placed in close proximity to the FBG to measure the temperature during the tests. The fibre was clamped at both ends, allowing it to be suspended in the tube oven. This was done to prevent the FBG from touching any other surface during the annealing process. A customised Lab-View program recorded FBG spectra at set intervals during each test.

The test samples were fabricated by splicing a short length (≈ 10 cm) of the particular Er^{3+} doped fibre, in which FBGs were inscribed, between longer lengths of Corning SMF28 fibre. This was done to allow 'real-time' monitoring of the FBG transmission spectra during the thermal treatment process.

7.3 Type I FBGs in Erbium Doped Fibre

The characteristics of Type I FBGs at elevated temperatures have been well documented [61,69,138]. Here, investigations are made into the thermal sustainability of FBGs inscribed in Er1 fibre. These investigations were not performed on Er4 fibre, as it has been extensively examined recently [96,153,164]. As all FBGs used here were inscribed in hydrogen loaded fibre, use of the Power Law model detailed in Section 3.2.3.1 would not be valid.

Figure 7.2 illustrates the thermal decay of a previously annealed FBG in Er1, which undergoes a series of isochronal and isothermal steps. The isochronal steps were 24 hours, while the isothermal steps were at 100 °C intervals. The results of an FBG inscribed in OptixTM telecommunications fibre, which was exposed to the same writing conditions and annealing procedure as the Er1 fibre, is included for comparison.

As expected, at each set of temperatures, the Type I FBGs experienced an initial rapid decay followed by a slowing decay rate with time. It can be seen that the

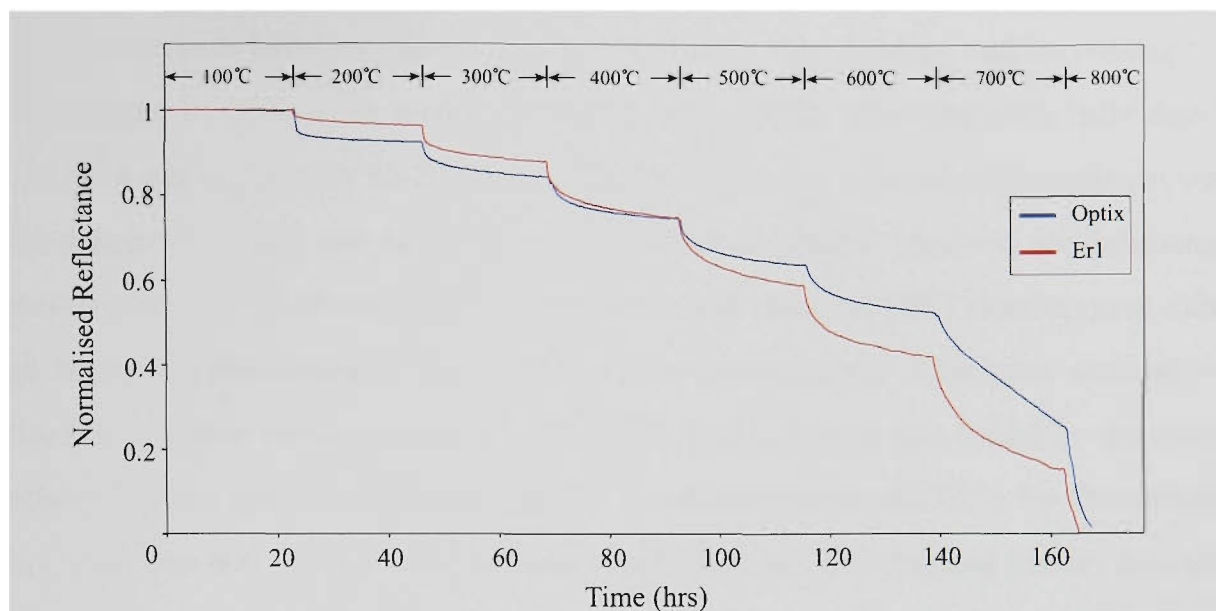


Figure 7.2: Normalised reflectance vs time for Type I FBGs in Er1 and Optix fibre when exposed to various isothermal temperatures. Temperatures shown on the top section of the plot indicate each isothermal step taken over the corresponding time.

reflectance from each FBG decreases at an increased rate with increasing temperature. The FBG in Er1 retained a higher reflectance at temperatures up to 300 °C compared to the FBG in standard communications fibre, but exhibited increased decay above these temperatures. It is also evident that both these FBGs experience complete erasure at 800 °C, which makes them unsuitable as temperature sensors at temperatures at ≥ 800 °C.

7.4 Chemical Composition Gratings

A promising technology for high-temperature sensing applications that has been recently reported is the fabrication of CCGs [131, 133, 134]. In CCGs the underlying mechanism of the refractive index modulation is a periodic change in the concentration of one or several dopants in the core of the fibre. A change in composition will cause a change in refractive index, as described in Section 3.2. Due to this different process, the thermal decay of these gratings cannot be explained by the models previously detailed in Section 3.2.3.

The thermal treatment procedure is crucial in the formation of CCGs [131]. Their

initial occurrence involved inserting a grating into a tube furnace and increasing the temperature to 1000 °C at a rate of ~ 25 °C/min. CCGs were generally fully developed after approximately 15-20 mins at 1000 °C, with the whole development process taking approximately one hour. Later, an improved process involved instantaneous exposure to 1000 °C which resulted in significantly reduced CCG development time and increased mechanical strength of the heat treated fibre. This later method resulted in a higher refractive index modulation [131]. It was also found by the same author that the optimum temperature for the development of CCGs for the specific fibre used was 600 - 700 °C. It has been concluded that the thermal history and the thermal ramping procedure are important parameters to be considered for the final value of the CCG refractive index modulation [131].

The following section discusses the fabrication, heat treatment and characterisation of CCGs in various erbium doped fibres.

7.4.1 Fabrication of CCGs

Gratings resembling CCGs were fabricated using various annealing procedures during the erasure of the Type I FBGs. Four different Er^{3+} doped fibres were used to investigate the fabrication of CCGs (denoted as Er1-Er4 in this work). Type I FBGs were inscribed in all of these erbium doped fibres and their details are documented in Table 3.3. The growth of gratings resembling CCGs was observed in three of the four erbium doped fibres investigated. Table 7.1 documents the annealing procedures for each FBG sample investigated. It has been found that an optimum annealing temperature for the fabrication of CCGs in germanosilicate fibres was 600-700 °C [134]. Therefore, the annealing procedure of most erbium doped fibres consisted of two annealing steps at 600 and 700 °C.

7.4.1.1 CCGs in Er1 Fibre

The first sample treated was a FBG in Er1 fibre (shown as Er1-a in Figure 7.2). As expected, during the 800 °C step the Type I grating experienced complete erasure.

Table 7.1: Annealing procedure of Type I FBGs for the formation of CCGs. A tick (✓) indicates that the fibre was maintained at the corresponding temperature. Isochronal steps of 24 hrs were used for each temperature step except where indicated.

Er ³⁺ Fibre Sample	Initial Type I FBG Reflectivity (%)	Isothermal Step (°C)							
		100	200	300	400	500	600	700	800 ^a
Er1-a	98	✓	✓	✓	✓	✓	✓	✓	19
Er1-b	95	✓	✓	✓	✓	✓	✓	✓	33
Er1-c	90	✗	✗	✗	✗	✗	✗	✗	33
Er1-d	95	✗	✗	✗	✗	✗	✗	✓	20
Er1-e	95	✗	✗	✗	✗	✗	✓	✓	34
Er1-f	87	✗	✗	✗	✗	✗	✓	✓	32
Er2	50	✗	✗	✗	✗	✗	✓	✓	34
Er3	90	✗	✗	✗	✗	✗	✓	✓	48
Er4	95	✗	✗	✗	✗	✗	✓	✓	21

^a Time interval at this isothermal step given in hours.

Subsequently, a new grating began to develop in a fashion that resembled the growth characteristic of a CCG [131]. Unfortunately, observation of the growth process of the newly formed grating was interrupted when it had reached a reflectance of $\approx 19\%$ due to a sudden, unexplained, total loss of signal. Thus it was necessary to repeat the same annealing process on another FBG in Er1 (Er1-b). The growth characteristics of the CCG in Er1-a and Er1-b is shown in Figure 7.3. Er1-b experienced a reduced growth rate compared to Er1-a and appeared to have reached a maximum reflectance of $\approx 18\%$. This possibly may be attributed to the initial lower reflectance of the type I FBG in Er1-b (95%) compared to that of Er1-a (98%).

To discover whether the final strength of the CCG is not only dependent on the initial strength of the Type I FBG, but also on the annealing process this grating is exposed to, the Type I grating in Er1-c was annealed directly at 800°C. After a short period of time of being exposed to this temperature, the Type I grating experienced complete erasure. As observed with the previous Er1 samples, a CCG

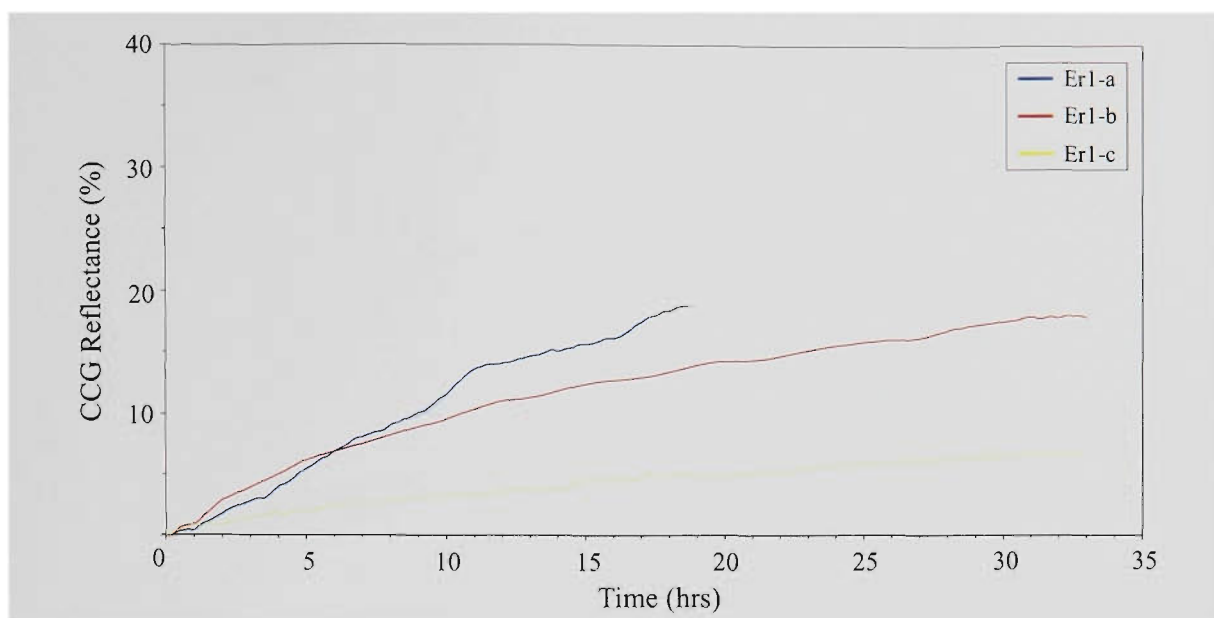


Figure 7.3: Reflectance versus time during fabrication of CCGs in Er1 fibre. Initial Type I FBGs inscribed using the Victoria University facility.

began to develop, as shown in Figure 7.3. The CCG in Er1-c produced the lowest reflectance compared with Er1-a and Er1-b. These results indicate that the final reflectance of the CCG may be dependent on the initial reflectance and the annealing process performed on the Type I grating.

Further tests were carried out on Type I gratings fabricated in Er1 using the fibre Bragg grating fabrication facility at Swinburne University. As can be seen from Table 3.3, these Type I gratings were formed with different hydrogen loading and writing conditions. Figure 7.4 illustrates the growth characteristics of CCGs in samples Er1-d, Er1-e and Er1-f. The annealing procedures for all three Type I gratings are documented in Table 7.1. Er1-d demonstrated the strongest reflecting CCG (26%). This CCG has the highest reflectance of all CCGs fabricated in Er1. Both Er1-e and Er1-f were exposed to an additional annealing step compared to Er1-d. Although the initial strength of the Type I FBG in Er1-e was similar to Er1-d, it achieved a significantly lower reflectance compared to Er1-d. These results indicate that the best annealing process and writing condition for Type I FBGs in Er1 fibre that result in the highest CCG reflectance is that used for Er1-d.

The results from Er1-e and Er1-f further indicate the correlation between the initial

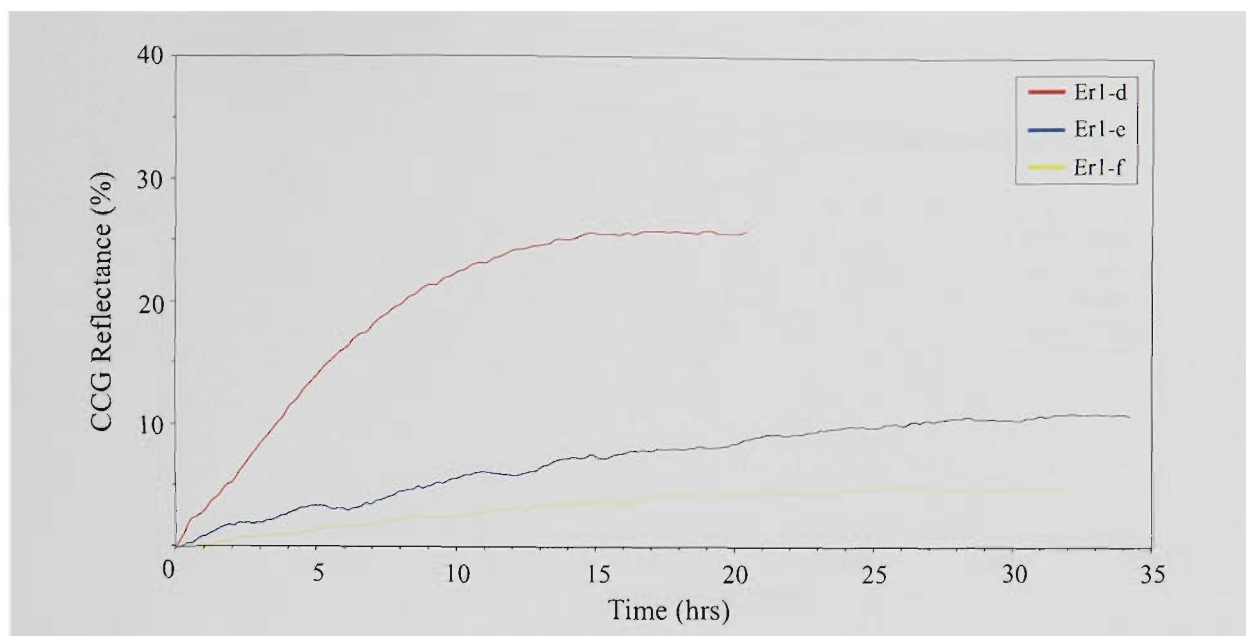


Figure 7.4: Reflectance versus time during fabrication of CCGs in Er1 fibre. Initial Type I FBGs were inscribed using the Swinburne University facility.

strength of the Type I grating and that of the final CCG. Both these gratings were exposed to the same annealing procedure. The Type I grating in Er1-e exhibited a larger initial reflectance relative to Er1-f. Therefore, as expected, the resultant reflectance of the CCG in Er1-e was greater.

It was also noted that the newly formed CCGs exhibited a decrease of their Bragg wavelength during fabrication. Figure 7.5 illustrates the reflectance spectra of the CCG in Er1-d at different times during heat treatment. The original transmission spectrum of the Type I grating was shown previously in Section 3.2.4.3. It is clear that with an increase of reflectance the Bragg wavelength decreases. This is in contrast to standard Type I FBGs, and suggests that the average refractive index modulation experiences a decrease rather than the usual increase. This is in agreement with previously reported work on the fabrication of CCGs in germanosilicate fibres [133].

7.4.1.2 CCGs in Other Erbium Doped Fibres

Three other tests were performed on the other erbium doped fibres used in this thesis, namely, Er2, Er3 and Er4. The Type I FBGs in Er2 and Er4 were inscribed using the Victoria University facility, while the FBG in Er3 was fabricated using the

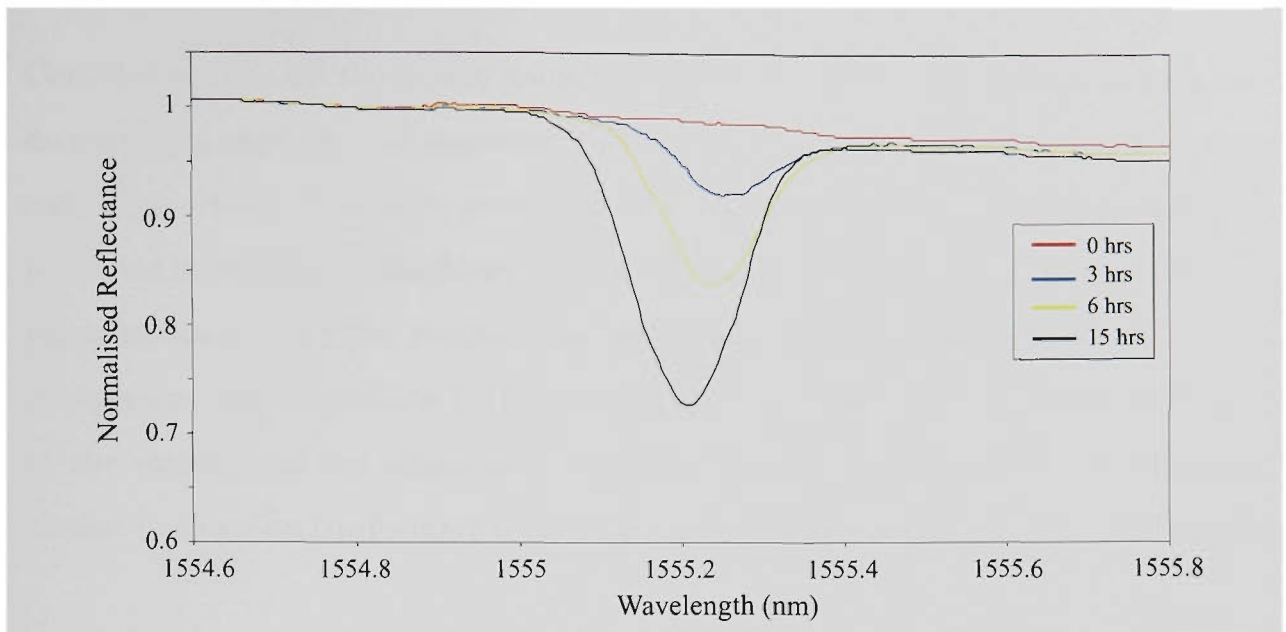


Figure 7.5: Normalised reflectance versus wavelength at four different time periods during the fabrication of the CCG in Er1-d at 20 °C.

Swinburne University facility. As shown in Table 7.1, the same annealing procedure was used for all the Type I FBGs in these fibres. The decay of the Type I FBGs in Er1-e, Er2 and Er4, using the annealing procedure mentioned above, is illustrated in Figure 7.6. As can be seen, all Type I FBGs in these fibres experienced total

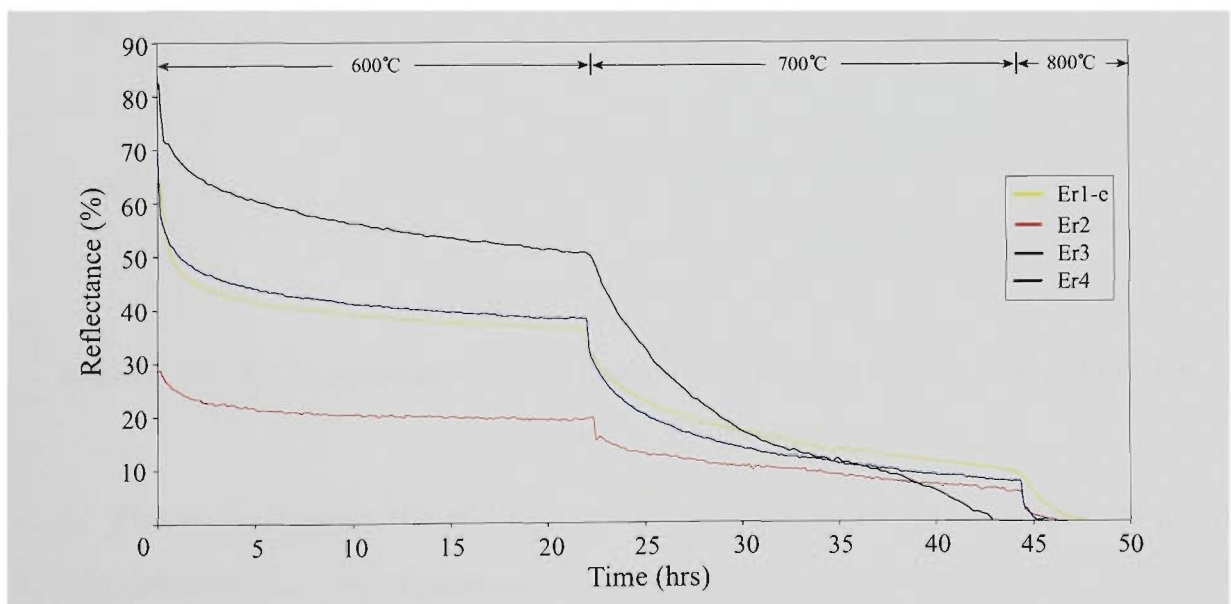


Figure 7.6: Reflectance versus time during annealing process of Type I FBGs prior to growth of CCGs in Er1-e, Er2, Er3 and Er4.

erasure during either the 700 °C or 800 °C annealing step.

Considering that all the fibres, namely Er2, Er3 and Er4, were erbium doped, germanosilicate type, it was expected that CCGs would be formed in samples from each fibre. Apart from Er3, growth of CCGs was observed in all erbium doped fibres used in this thesis. As shown in Table 3.1, only the Er3 fibre did not contain any phosphorous or tin. The results show that other processes, that involve tin and/or phosphorus, may contribute in the creation of CCGs. These elements may contribute to the variation of the refractive index modulation during the diffusion processes, similar to those for the formation of oxygen and fluorine -modulated CCGs [131,133].

Figure 7.7 shows the growth characteristics of CCGs in Er2 and Er4 fibre. The CCG formed in Er4 exhibited the largest reflectance of all CCGs fabricated in this

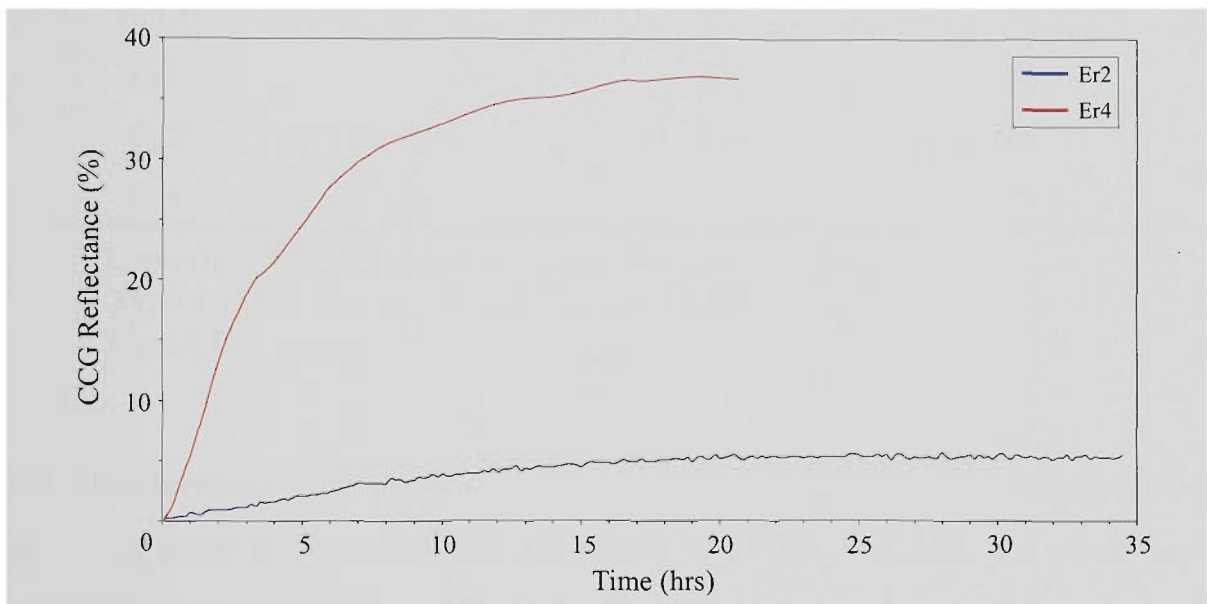


Figure 7.7: CCG reflectance versus time during fabrication in Er2 and Er4 fibre.

work. This suggests that the addition of tin may have an increased contribution during the diffusion process to generate a larger refractive index modulation. The CCG formed in Er2 exhibited a relatively small reflectance. As this fibre was of a similar composition to Er1, with the difference being a reduced erbium concentration, the low CCG reflectance could be attributed primarily to the initial low reflectivity of the Type I FBG ($\approx 50\%$).

Table 7.2 summarises all the fibre samples in which CCG fabrication was attempted. The results show a correlation between the final CCG reflectance and the initial Type

Table 7.2: Characteristics summary of all CCGs formed in Er^{3+} doped fibre.

Er^{3+} Fibre	Initial Type I FBG	Final CCG	CCG Fabrication
Sample	Reflectivity (%)	Reflectivity (%)	Time at 800 °C (hrs)
Er1-a ^a	98	19	19
Er1-b	95	18	33
Er1-c	90	7	33
Er1-d ^b	95	26	20
Er1-e ^b	95	11	34
Er1-f ^b	87	5	32
Er2	50	5	34
Er3 ^c	90	0	48
Er4	95	37	21

^a Growth of CCG stopped at this reflectance.

^b Type I FBG written using Swinburne facility.

^c No CCG formed.

I FBG reflectance of Er1-e and Er1-f. Although it has been shown that additional annealing steps increase the final reflectance of CCGs [131, 132], the results shown here indicate further work is required before any conclusions can be drawn as to the optimum annealing steps required for each particular fibre type. It can be seen that removing the 600 °C annealing step for Er1-d resulted in a reflectance of 26% compared to Er1-e, which had a reflectance of 11%. Both these samples were exposed to the same writing condition and exhibited the same strength of the initial type I FBG. The results also show that the final reflectivity of the CCG is dependent on the composition of the fibre. CCGs formed in Er4 exhibited the largest reflectivity, even though the writing and annealing procedures for the type I FBGs were consistent with some of the other Er1 samples. Other variables that may affect the final CCG strength are the different laser source, fabrication method (e.g. scanning beam) and

hydrogen loading conditions.

7.4.2 Temperature Dependence of CCGs

The temperature dependence, repeatability and stability of the Bragg wavelength of the newly formed CCGs were investigated from room temperature to 800 °C. Table 7.3 summarises the linear temperature dependencies, over a narrow range, of the

Table 7.3: Linear temperature coefficients of CCGs over relatively narrow temperature ranges.

Er Fibre Sample	Temperature Range (°C)	Temperature Coefficient ($\times 10^{-3}$ nm/°C)
Er1-c	26-100	10.132
Er1-d	30-100	10.143
Er4	25-100	10.328

Bragg wavelength for CCGs formed in Er1 (Er1-c and Er1-d) and Er4 fibre. As expected, the temperature coefficients of the CCG Bragg wavelength appear to be consistent with those exhibited by the Type I FBGs for these fibres, as shown in Chapter 5, over comparable temperature ranges. An increase in temperature sensitivity can be seen with the CCG in Er4 compared to those in Er1. The different fibre composition of Er4 compared to Er1 may have caused its thermal expansion properties to vary.

Over an extended temperature range (e.g. 20-800 °C) the temperature dependence is more accurately described by a non-linear relationship. Figure 7.8 shows the typical temperature dependence of the Bragg wavelength of a CCG (Er1-c) over this temperature range. Also demonstrated in this Figure is the repeatability of the CCG in a high temperature environment. The solid line represents a second order polynomial fitted to the data for one cycle of heating and cooling of the CCG. No evidence of hysteresis or an irreversible wavelength shift is evident.

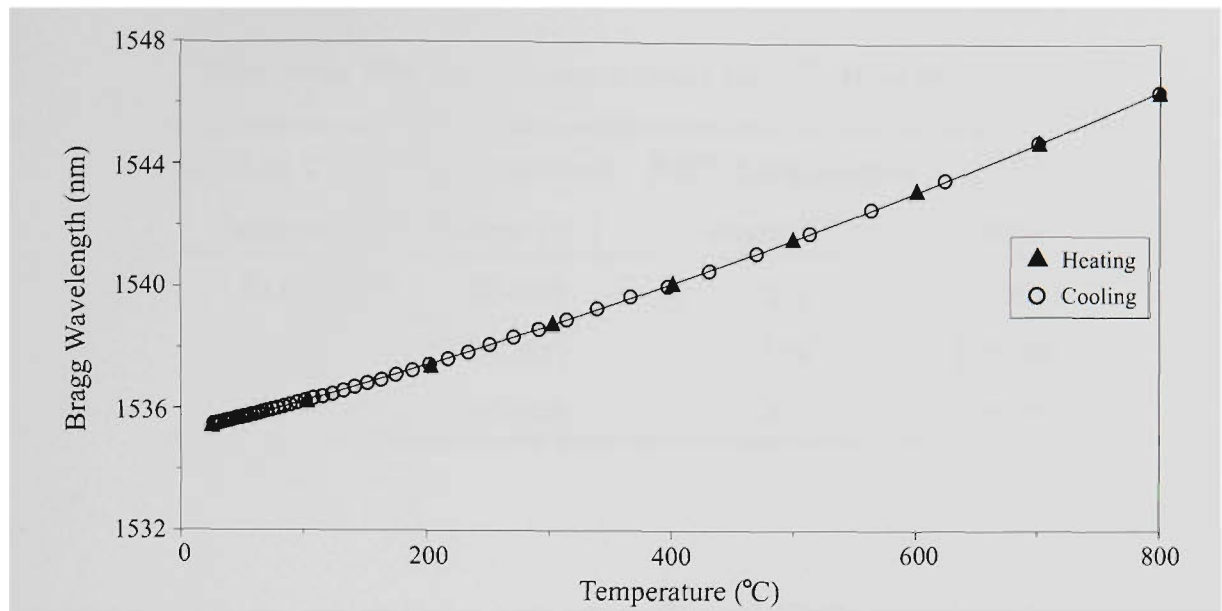


Figure 7.8: Bragg wavelength versus temperature over a heating/cooling cycle for a CCG in Er1-c.

Temperature calibrations were performed on a number of CCGs fabricated in this thesis. Table 7.4 summarises the r^2 values and RMS temperature errors for CCGs in Er1 and Er4 fibre. The best RMS temperature error was demonstrated by the CCG in Er1-d. It was found to be 1.9°C , which may be interpreted as a temperature accuracy of 0.2% over the temperature range used. Figure 7.9 illustrates the

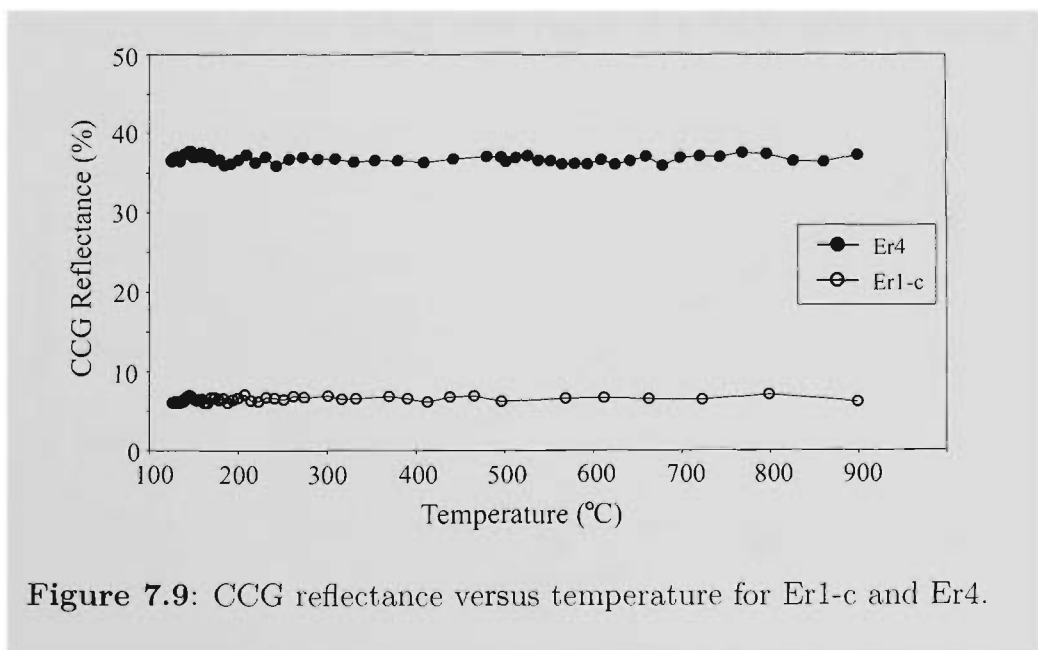


Figure 7.9: CCG reflectance versus temperature for Er1-c and Er4.

stability of the CCGs from 20-800°C. It is evident that the CCG doesn't suffer from any decrease in reflectance over this

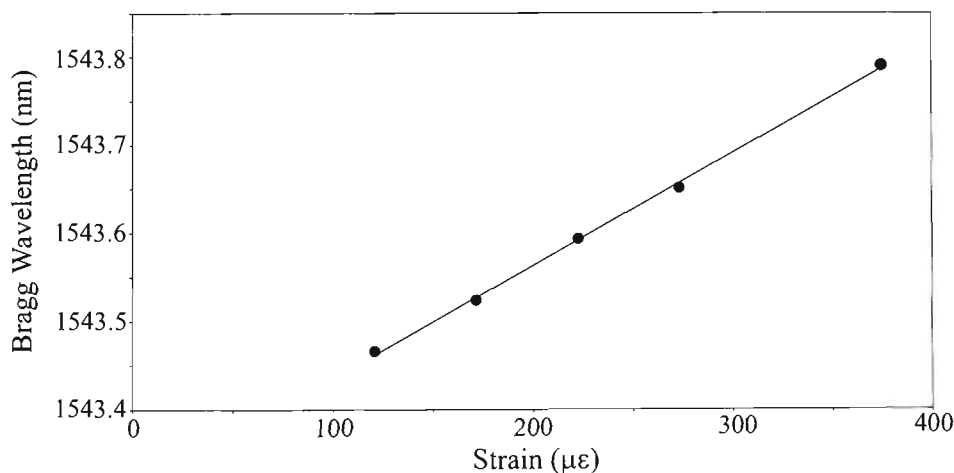
Table 7.4: RMS temperature errors and r^2 values for CCGs.

CCG in Fibre	Temperature	RMS temperature	r^2
Sample:	Range ($^{\circ}\text{C}$)	error ($^{\circ}\text{C}$)	value
Er1-c	25-800	3.4	0.99983
Er1-d	28-800	1.9	0.99995
Er4	20-800	3.6	0.99978

temperature range, which is in contrast to Type I FBGs, which suffer from a progressive decay of reflectance and irreversible shift of the Bragg wavelength over this temperature range as shown in Figure 7.2. These results indicate that these CCGs would be suitable for temperature measurement over extended time periods for these temperature ranges with no reduction in reflectivity.

7.4.3 Strain Dependence of CCGs

Due to the effect of high temperature on the mechanical strength of uncoated optical fibre, accurate strain calibrations of the CCGs could not be performed. Figure 7.10 shows a plot of the Bragg wavelength of a CCG (Er1-c) versus strain,

**Figure 7.10:** Bragg wavelength versus strain for CCG in Er1-c at room temperature.

which was performed at room temperature. The strain coefficient was found to

be $(1.30 \pm 0.02) \times 10^{-3}$ nm/ $\mu\epsilon$. Taking into consideration the larger errors present, the strain coefficient of the CCG is comparable to that of standard Type I FBGs. The solid line shown in Figure 7.10 exhibited an r^2 value of 0.99875. For accurate strain calibrations, the optical fibre would need to be mechanically strengthened with a jacketing material that is capable of withstanding an applied strain at high temperatures.

7.5 Conclusions

FBGs resembling CCGs, having reflectivities of up to 37%, have been fabricated in Er³⁺ doped germanosilicate optical fibre. Er:Sn doped fibre (Er4) produced CCGs with the highest reflectivities, while Er³⁺ doped germanosilicate fibre that did not contain tin or phosphorus (Er3) resulted in no fabrication of CCGs. To date, it has been demonstrated that the elements, oxygen and/or fluorine, are responsible for the formation of CCGs in germanosilicate fibre [131, 133]. The null result demonstrated in germanosilicate fibre from this work indicates that there may be other contributing processes involved in the formation of CCGs. The results also indicate that there is a strong correlation between the initial strength of the Type I FBG and the final CCG reflectivity produced after annealing.

The CCGs fabricated in this work demonstrated excellent thermal stability and repeatability to temperatures up to 800 °C, with no sign of a reduction in reflectance or irreversible shift of the Bragg wavelength, which is inherent in standard Type I, II and IIA FBGs. This suggests that these CCGs could be useful for high temperature applications. These gratings could potentially be used in sensor schemes, like those described in Chapters 5 and 6 for simultaneous temperature and strain sensing over extended temperature ranges.

Chapter 8

CONCLUSIONS

8.1 Summary of Key Outcomes

An in-depth investigation of a novel sensing scheme, which utilises rare earth doped fibre combined with an FBG for simultaneous and co-located measurement of temperature and strain has been performed.

Initially, a detailed literature and commercial review of fibre-optic temperature and strain sensors was presented, together with their current applications. Current optoelectronic interrogation techniques of the fluorescence intensity ratio and Bragg wavelength were also summarised.

A description of the fabrication techniques of rare earth doped fibres and FBGs were made in Chapter 3. The various effects that particular dopants have on FBG characteristics were also summarised. To further this, the fabrication methodologies of FBGs in various erbium and erbium:ytterbium doped fibres used in this thesis, together with their corresponding characteristics were presented. Type I FBGs were successfully inscribed in all erbium and erbium:ytterbium doped fibres. Also explained, was the fluorescence scheme used for the FIR and ASE for the interrogation of the Bragg wavelength. The sensing scheme investigated in this thesis required only a single pump source to ‘illuminate’ two independent sensors, namely, the FIR and FBG.

The mathematical de-convolution techniques used for determining temperature and strain simultaneously from the measurement techniques used in this thesis were presented. Three techniques were used. The matrix method, which assumes lin-

ear temperature and strain dependencies, was limited to applications over narrow temperature ranges, where the non-linear temperature dependencies of the FIR and Bragg wavelength were considered small. When the strain insensitive, non-linear temperature dependence of the FIR was considered, significant improvements in the temperature errors were demonstrated, but with a consequential increase in the strain errors. In this case, the inability to account for the non-linear temperature dependence of the Bragg wavelength reduced the quality of the strain fits. However, when the non-linear temperature dependencies of both the FIR and Bragg wavelength were included, both temperature and strain errors reduced. Due to this method producing the best calibration curve fits to the measurement data from both the FIR and Bragg wavelength, it exhibited consistently the smallest RMS temperature and strain errors compared to the two previously mentioned techniques for all sensors investigated in this thesis.

Three analysis techniques were developed to analyse the FBG spectra. The two techniques that did not determine the Bragg wavelength from the FBG spectrum by using just a single intensity and wavelength exhibited the smallest strain errors. Although these techniques produced better results, they require additional computational processing compared to the method that determined the Bragg wavelength from the FBG spectrum by recording a single intensity and wavelength.

Five erbium based sensors were investigated. As expected, the FIR was found to exhibit a strain sensitivity that was consistent with zero. The FIR that demonstrated a smaller temperature sensitivity showed superior temperature performance when applied to simultaneous temperature and strain measurement. Sensors with FBGs fabricated within the doped fibre showed consistently superior performance in determining temperature and strain simultaneously compared to those that were spliced outside of the doped fibre region. This was due to the co-location of the two independent sensors, which effectively reduced any measurement errors induced by a fluctuations in measurand, particular temperature, along the length of the optical fibre sensor.

All erbium based sensors showed reasonable performance, with only the sensor that had the FBG spliced outside the doped fibre region demonstrating RMS temperature and strain errors above 1°C and $15\ \mu\epsilon$, respectively. The doped fibre with an erbium concentration of 2680 ppm showed the most promise in being developed further as a practical sensor. One of the sensors utilising this fibre exhibited the smallest RMS temperature and strain errors and, apart from the interrogation system, is an 'all in-fibre' system. The Sn:Er doped fibre demonstrated reasonable performance over wide operating temperatures ($25 - 600^{\circ}\text{C}$), with RMS temperature and strain errors of 1.7°C and $27\ \mu\epsilon$, respectively.

Five erbium:ytterbium based sensors were investigated. As with the FIR from erbium, the ytterbium FIR was found to exhibit a strain sensitivity that was consistent with zero. The FIR that exhibited the best temperature sensitivity produced superior temperature performance when applied to simultaneous temperature and strain measurement. This is in contrast to the FIR from erbium. Also, although the FIR temperature sensitivities from ytterbium were approximately an order of magnitude lower than those from the erbium, they exhibited comparable RMS temperature errors. This indicates that there may be an optimum FIR temperature sensitivity for erbium and ytterbium when applied to simultaneous temperature and strain measurement. The magnitude of the non-linear factor of the FIR also influences the sensor's performance; this is determined by the fluorescence lineshape and the two wavelength ranges chosen. There may be a 'trade-off' between the temperature sensitivity and the non-linearity of the FIR that will produce the best performance for simultaneous temperature and strain measurement. The fit quality of the calibration formulae, which is proportional to the RMS errors, is dependent on these parameters.

When using the same pump power, the erbium:ytterbium fibre generated higher fluorescence intensities for interrogation of the Bragg wavelength compared to erbium fibre. This produced larger signal-to-noise ratios, which translated into smaller RMS errors. The Bragg wavelength strain sensitivity was found to increase with de-

creasing $\text{Er}^{3+}:\text{Yb}^{3+}$ concentration, while the temperature sensitivity increased with increasing $\text{Er}^{3+}:\text{Yb}^{3+}$ concentration. This indicates that the Bragg wavelength temperature and strain sensitivities may have a small dependence on the glass composition of the ErYb fibre.

All erbium:ytterbium based sensors showed similar performance to those based on erbium doped fibre. Generally, the lower concentration $\text{Er}^{3+}:\text{Yb}^{3+}$ doped fibres demonstrated better performance compared to the the higher concentration fibres. Comparable performance from the higher concentration fibre (3000:3000 ppm of erbium:ytterbium) was achieved when the fibre length was reduced to 5 cm. This is due to the increase of the FIR stability at lower fluorescence intensities, which produces smaller temperature errors.

Table 8.1 provides a summary of the most promising Er and Er:Yb based sensors investigated. All the best performing sensors shown in this table were co-located and had sensor lengths less than 10 cm, which would be considered acceptable as a point sensor for many applications. Only the Er:Sn based sensor consisted of a

Table 8.1: Summary of most promising sensors investigated in this work. All sensors were characterised using the same analysis techniques (Method C and the Weighted Average technique).

Sensor	Sensor Length (cm)	Doped Fibre Conc. (ppm)		Measurement Range		RMS Errors	
		Er^{3+}	Yb^{3+}	Temp. ($^{\circ}\text{C}$)	Strain ($\mu\epsilon$)	Temp. ($^{\circ}\text{C}$)	Strain ($\mu\epsilon$)
2	10	1430	-	25-150	350-2534	0.6	5.04
4	9	2680	-	25-100	350-1460	0.3	4.80
5	16	90	-	25-600	350-1988	1.7	27.0
6	9	1500	1500	20-100	350-1460	0.3	4.94
7	9	2000	2000	20-100	350-1460	0.4	3.63
8	5	3000	3000	20-100	350-1460	0.4	4.48

longer fibre length. This was due to the very low concentration of erbium generating lower fluorescence intensity levels compared to the other erbium doped fibres of the same length. Prior to commercialisation, sensor specifications such as, doped fibre length and rare earth concentration, need to be defined for particular applications (e.g. higher fluorescence intensities are required if the sensor is to be implemented in applications which place it at large distances from the interrogation equipment).

Figure 8.1 compares the results from this thesis to those of other authors (also shown in tabular form in Chapter 2). It is clear that the performance of a combination of the FIR and FBG is better than all those reported to date. Although the technique based on a dual polarisation DFB fibre laser [106] produced smaller RMS

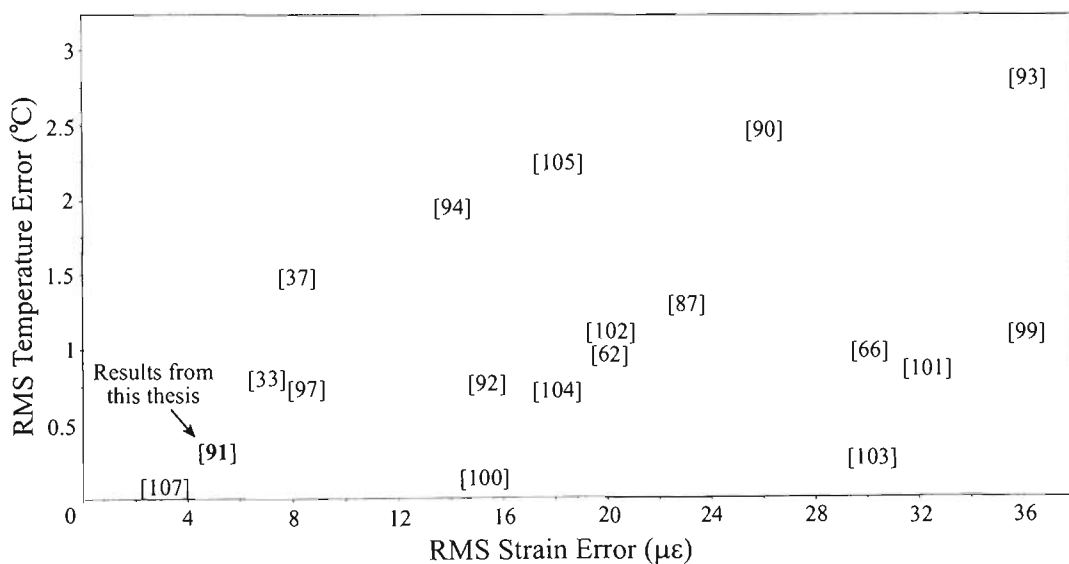


Figure 8.1: RMS temperature and strain error comparison of the results from this work to that of other authors (reference numbers are shown).

temperature and strain errors, it must be noted that this sensor was calibrated over a much narrower temperature range. The main reason why it is believed the sensor scheme investigated in this thesis is superior to previously reported schemes is that the FIR is insensitive to strain. Therefore, less parameters, and their associated errors, are present in the deconvolution process. Overall, sensors based on both types of rare earth doped fibres investigated in this thesis demonstrated excellent RMS temperature and strain errors, in the order of 0.3°C and $3.63\mu\epsilon$, respectively and

they exhibit advantages such as:

- Co-located simultaneous temperature and strain sensing
- Short sensor lengths for point sensing
- Strain insensitive temperature measurement by FIR sensor
- Single light source required to illuminate two independent sensors
- Simple 'all-in-fibre' intrinsic sensor design
- Potential for high temperature application

Previous to this work, fluorine and oxygen modulated CCGs had been fabricated. The investigations performed in this thesis have found that oxygen modulated CCGs can be fabricated in germanosilicate fibres that include of other types of dopants as well. FBGs resembling oxygen modulated CCGs, having reflectivities of up to 37%, have been fabricated in Er^{3+} doped germanosilicate optical fibre. $\text{Er}^{3+}:\text{Sn}$ doped germanosilicate fibre produced CCGs with the highest reflectivities, while Er^{3+} doped germanosilicate fibre that did not contain tin or phosphorus did not result in a CCG. This indicates that there may be other unknown contributing effects in the formation of CCGs. The CCG reflectivities from this work are comparable to those previously reported in germanosilicate fibres. These results build upon the current knowledge of the processes involved in the formation of CCGs, which is relatively limited. Results from this thesis also indicate that there is a strong correlation between the initial strength of the Type I FBG and the final CCG reflectivity.

The CCGs fabricated in this work demonstrated excellent thermal stability and repeatability to temperatures up to 800°C , with no sign of a reduction in reflectance or irreversible shift of the Bragg wavelength, which is inherent in standard Type I, II and IIA FBGs. CCGs fabricated in erbium doped fibre have produced RMS temperature errors in the order of 1.9°C over a temperature range of $28\text{-}800^\circ\text{C}$.

8.2 Future Work

In the future, various efforts can be undertaken to bring the FIR and FBG based, simultaneous temperature and strain sensing scheme closer to a commercialisation stage. A number of issues would need to be addressed and are mentioned below.

To date, FBG based strain sensors, together with their interrogation equipment are very expensive compared to conventional electrical based strain sensors. To an extent, the excellent multiplexing ability of FBG sensors has been able to bridge the cost gap between these two technologies, which has resulted in some inroads being made into commercial markets. The FIR technique combined with FBGs is limited, in terms of the low multiplexing capability of rare earth fluorescence compared to FBGs. This sensing scheme is limited to two sensing probes per optical fibre, which essentially removes the multiplexing advantage of FBG sensors. For this sensor system to be commercially feasible, extensive investigations need to be performed in the optoelectronic detection schemes of the two measurement techniques used, namely the FBG and FIR from Er and Yb, with cost being the most sensitive parameter.

Specialised optoelectronic interrogation devices need to be developed, which would be capable of measuring the different wavelength bands of the FIR and Bragg wavelength, such as those investigated in this thesis. Resolution requirements are not critical with the FIR but need consideration when determining the Bragg wavelength. Generally, as the cost of photonic equipment decreases, devices such as, diffraction gratings, polychromatic mirrors and CCD arrays, that could be used to measure different wavelength bands simultaneously, could be investigated as potential means of reducing the cost of such interrogation systems.

Prior to commercialisation, further investigations are required into the effects that fibre host composition has on the FIR characteristics, such as fluorescence line-shape and temperature sensitivity. The long-term stability and repeatability of the FIR and Bragg wavelength need to be further investigated, particularly at elevated

temperatures. Also, investigations of optical fibre protective materials for harsh environments such as, high strain and temperature environments need to be conducted.

The results from this thesis and those of other authors clearly indicate that there is a requirement to develop a better understanding of the photosensitivity and refractive index properties of optical fibres with particular doping elements, which are responsible for the formation of CCGs. This also includes the effects of hydrogen loading on these dopants.

Further investigations are required into the annealing effect on Type I FBGs and its relationship to the physical and optical properties of CCGs. These investigations would also include the effects the initial fabrication methods for Type I FBGs have on the characteristics of CCGs.

An improved understanding of all these effects would potentially improve the efficiency of the CCG fabrication processes and could result in higher quality CCGs for sensing applications. To further this, investigations could be made into the combination of CCGs and the FIR for application in simultaneous and co-located, temperature and strain measurement over extended high temperature ranges.

BIBLIOGRAPHY

- [1] B. Culshaw. Optical fiber sensor technologies: opportunities and-perhaps-pitfalls. *J. Lightwave Technol.*, **22**(1):39–50, 2004.
- [2] K. T. V. Grattan and T. Sun. Optical-fiber sensors: Temperature and pressure sensors. *MRS BULLETIN*, **27**(5):389–395, 2002.
- [3] Z. Y. Zhang, K. T. V. Grattan, and B. T. Meggitt. Thulium-doped fiber optic decay-time temperature sensors: Characterization of high temperature performance. *Rev. Sci. Instrum.*, **71**(4):1614–1620, 2000.
- [4] E. Maurice, S. A. Wade, S.F. Collins, G. Monnom, and G. W. Baxter. A self-referenced point temperature sensor based on a fluorescence intensity ratio in Yb³⁺-doped silica fibre. *Appl. Opt.*, **36**(31):8264–8269, 1997.
- [5] T. Sun, Z. Y. Zhang, and K. T. V. Grattan. Erbium/ytterbium fluorescence based fiber optic temperature sensor system. *Rev. Sci. Instrum.*, **71**(11):4017–4022, 2000.
- [6] S. A. Wade, S. F. Collins, and G. W. Baxter. Fluorescence intensity ratio technique for optical fiber point temperature sensing. *J. Appl. Phys.*, **94**(8):4743–4756, 2003.
- [7] Y. J. Rao. In-fiber Bragg grating sensors. *Meas. Sci. Technol.*, **8**:355–375, 1997.
- [8] A. D. Kersey, M. A. Davis, H. J. Patrick, M. LeBlanc, K. P. Koo, C. G. Askins, M. A. Putnam, and E. J. Friebele. Fiber grating sensors. *J. Lightwave Technol.*, **15**(8):1442–1463, 1997.
- [9] J. Jung, H. Nam, B. Lee, J. O. Byun, and N. S. Kim. Fiber Bragg grating temperature sensor with controllable sensitivity. *Appl. Opt.*, **38**(13):2752–2754, 1999.

- [10] F. Farahi, D. J. Webb, J. D. C. Jones, and D. A. Jackson. Simultaneous measurement of temperature and strain: cross-sensitivity considerations. *J. Lightwave Technol.*, **8**(2):138–142, 1990.
- [11] T. R. Parker, M. Farhadiroushan, V. A. Handerek, and A. J. Rogers. A fully distributed simultaneous strain and temperature sensor using spontaneous Brillouin backscatter. *IEEE Photonics Technol. Lett.*, **9**(7):979–981, 1997.
- [12] K. Kyuma, S. Tai, K. Hamanaka, and M. Nunoshita. Laser doppler velocimeter with a novel optical fiber probe. *Appl. Opt.*, **20**(14):2424–2429, 1981.
- [13] W. C. Michie, I. McKenzie, B. Culshaw, and P. Gardiner. A fiber optic/hydrogel probe for distributed chemical measurements. *Proc. SPIE*, **2360**:130–133, 1994.
- [14] R. A. Atkins, J. H. Gardner, W. N. Gibler, C. E. Lee, M. O. Oakland, M. D. Spears, V. P. Swensen, H. F. Taylor, J. McCoy, and G. Beshouri. Fiber-optic pressure sensors for internal combustion engines. *Appl. Opt.*, **33**(7):1315–1319, 1994.
- [15] Y. Lin, T. Swatari, and C. J. Hartley. Fiber optic pressure catheter for cardiovascular applications. *Proc. SPIE*, **3245**:51–59, 1998.
- [16] C. C. Lee, P. W. Chiang, and S. Chi. Utilization of a dispersion-shifted fiber for simultaneous measurement of distributed strain and temperature through Brillouin frequency shift. *IEEE Photonics Technol. Lett.*, **13**(10):1094–1096, 2001.
- [17] D. Inaudi, A. Elamari, N. Pflug, L. Gisin, and S. Breguet, J. Vurpillot. Low coherence deformation sensors for the monitoring of civil structures. *Sensors and Actuators A*, **44**:125–130, 1994.
- [18] R. A. Badcock and G. F. Fernando. Fatigue damage detection in carbon-fiber-reinforced composites using an intensity based optical fiber sensor. *J. Smart Mater. Struct.*, **4**:223–232, 1995.

- [19] E. Udd, W. L. Schulz, and J. M. Seim. Measurement of multidimensional strain fields using fiber grating sensors for structural monitoring. In *Proc. SPIE 3860*, pages 24–34, 1999.
- [20] S. R. Waite, R. P. Tatam, and A. Jackson. Use of optical fiber for damage and strain detection in composite materials. *Composites*, **19**(6):435–442, 1988.
- [21] K. Weir, W. J. O. Boyle, B. T. Meggit, K. T. V. Grattan, and A. W. Palmer. A novel adaptation of the Michelson Interferometer for the measurement of vibration. *J. Lightwave Technol.*, **10**(8):700–703, 1992.
- [22] W. B. Spillman Jr. and R. O. Claus. Optical-fiber sensors for the detection of acoustic emission. *MRS BULLETIN*, **27**(5):396–399, 2002.
- [23] A. Koch and R. Ulrich. Fiber-optic displacement sensor with $0.02\ \mu\text{m}$ resolution by white-light interferometry. *Sensors and Actuators A*, **25-27**:201–207, 1991.
- [24] K. T. V. Grattan and B. G. Meggitt. *Optical Fiber Sensor Technology; Vol.2: Devices and Technology*. Chapman & Hall, London, 1997.
- [25] H. H. Kee, G. P. Lees, and T. P. Newson. $1.65\ \mu\text{m}$ Raman-based distributed temperature sensor. *Electron. Lett.*, **35**(21):1869–1871, 1999.
- [26] K. De Souza, P. C. Wait, and T. P. Newson. Characterisation of strain dependence of the Landau-Placzek ratio for distributed sensing. *Electron. Lett.*, **33**(7):615–616, 1997.
- [27] H. H. Kee, G. P. Lees, and T. P. Newson. All-fiber system for simultaneous interrogation of distributed strain and temperature sensing by spontaneous Brillouin scattering. *Opt. Lett.*, **25**(10):695–697, 2000.
- [28] S. M. Maughan, H. H. Kee, and T. P. Newson. Simultaneous distributed fibre temperature and strain sensor using microwave coherent detection of spontaneous Brillouin backscatter. *Meas. Sci. Technol.*, **12**:834–842, 2001.
- [29] E. D. J. Smith, B. A. Patterson, R. J. Webster, P. A. Krug, S. K. Jones, and D. D. Sampson. Engineering a portable quasi-distributed fibre-Bragg-grating

- temperature sensing system for clinical hyperthermia. In *Technical Digest 15th International Conference on Optical Fiber Sensors*, pages 269–272, Portland, USA, (IEEE, Piscataway NJ USA), 2002.
- [30] K. T. V. Grattan and B. G. Meggitt. *Optical Fiber Sensor Technology*. Chapman & Hall, London, 1994.
- [31] K. T. V. Grattan and B. G. Meggitt. *Optical Fiber Sensor Technology; Vol 3: Applications and Systems*. Kluwer Academic Publishing, Dordrecht, 1998.
- [32] K. T. V. Grattan and B. G. Meggitt. *Optical Fiber Sensor Technology; Vol 4: Chemical and Environmental Sensing*. Kluwer Academic Publishing, Dordrecht, 1999.
- [33] D. I. Forsyth, S. A. Wade, T. Sun, X. Chen, and K. T. V. Grattan. Dual temperature and strain measurement with the combined fluorescence lifetime and Bragg wavelength shift approach in doped optical fiber. *Appl. Opt.*, **41**(31):6585–6592, 2002.
- [34] S. A. Wade, D. I. Forsyth, Grattan K. T. V., and Q. Guofu. Fiber optic sensor for dual measurement of temperature and strain using a combined fluorescence lifetime decay and fiber Bragg grating technique. *Rev. Sci. Instrum.*, **72**(6):3186–3190, 2001.
- [35] S. F. Collins, G. W. Baxter, S. A. Wade, T. Sun, K. T. V. Grattan, Z. Y. Zhang, and A. W. Palmer. Comparison of fluorescence-based temperature sensor schemes: Theoretical analysis and experimental validation. *J. Appl. Phys.*, **84**(9):4649–4654, 1998.
- [36] S. Pal, T. Sun, K. T. V. Grattan, S. A. Wade, S. F. Collins, G. W. Baxter, B. Dussardier, and G. Monnom. Strain-independent temperature measurement using type-I and type-IIA optical fiber Bragg grating combination. *Rev. Sci. Instrum.*, **75**(5):1327–1331, 2004.

- [37] O. Frazao, M. J. N. Lima, and J. L. Santos. Simultaneous measurement of strain and temperature using type I and type IIA fibre Bragg gratings. *J. Opt. A: Pure Appl. Opt.*, **5**:183–185, 2003.
- [38] X. Shu, Y. Liu, D. Zhao, B. Gwandu, F. Floreani, L. Zhang, and I. Bennion. Dependence of temperature and strain coefficients on fiber grating type and its application to simultaneous temperature and strain measurement. *Opt. Lett.*, **27**(9):701–703, 2002.
- [39] Frost and Sullivan Market Intelligence. World fiber optic sensor markets. In *Report No. 5*, pages 319–32, 1997.
- [40] S. R. Mordon, B. Buys, and Y. Moschetto. Zirconium fluoride glass fiber radiometer for low temperature measurements. *J. Lightwave Technol.*, **7**(7):1097–1100, 1989.
- [41] R. R. Dils. High-temperature optical fiber thermometer. *J. Appl. Phys.*, **54**(3):1198–1201, 1983.
- [42] D. A. Christensen and J. T. Ives. Fiberoptic temperature probe using a semiconductor sensor. In *Proc. NATO Advanced Studies Institute*, pages 361–368, Dordrecht, Netherlands, 1987.
- [43] T. Sun, Z. Y. Zhang, K. T. V. Grattan, and A. W. Palmer. Ytterbium-based fluorescence decay time fiber optic temperature sensor systems. *Rev. Sci. Instrum.*, **69**(12):4179–4185, 1998.
- [44] Z. Y. Zhang, K. T. V. Grattan, A. W. Palmer, B. T. Meggitt, and T. Sun. Characterization of erbium-doped intrinsic optical fiber sensor probes at high temperatures. *Rev. Sci. Instrum.*, **69**(8):2924–2929, 1998.
- [45] A. Arnaud, D. I. Forsyth, T. Sun, Z. Y. Zhang, and K. T. V. Grattan. Strain and temperature effects on erbium -doped fiber for decay-time based sensing. *Rev. Sci. Instrum.*, **71**(1):104–108, 2000.

- [46] B. G. Koziol, S. F. Collins, S. A. Wade, and G. W. Baxter. Temperature and strain dependence of fluorescence lifetime in Pr-doped fibres. In *ACOFT2004: 29th Australian Conference on Optical Fibre Technology*, (CD-ROM: ISBN 0-7315-5222-9), 2004.
- [47] H. Kusama, O. J. Sovers, and T. Yoshioka. Line shift method for phosphor temperature measurements. *Jap. J. Appl. Phys.*, **15**:2349–2358, 1976.
- [48] H. Berthou and C. K. Jorgensen. Optical-fiber temperature sensor based on upconversion-excited fluorescence. *Opt. Lett.*, **15**:1100–1102, 1990.
- [49] E. Maurice, G. Monnom, B. Dussadier, A. Saïssy, D. B. Ostrowsky, and G. W. Baxter. Erbium-doped silica fibers: for intrinsic fiber-optic temperature sensors. *Appl. Opt.*, **34**(34):8019–8025, 1995.
- [50] P. V. dos Santos, M. T. de Araujo, A. S. Gouveia-Neto, J. A. Medeiros Neto, and A. S. E. Sombra. Optical thermometry through infrared excited upconversion fluorescence emission in Er^{3+} - and Er^{3+} - Yb^{3+} -doped chalcogenide glasses. *IEEE J. Quantum Electron.*, **35**(2):395–399, 1999.
- [51] G. Paez and M. Strojnik. Erbium-doped optical fiber fluorescence temperature sensor with enhanced sensitivity, a high signal-to-noise ratio, and a power ratio in the 520-530- and 550-560-nm bands. *Appl. Opt.*, **42**(16):3251–3258, 2003.
- [52] E. Maurice, G. Monnom, G.W. Baxter, S.A. Wade, B.P. Petreski, and S.F. Collins. Blue LED-pumped point temperature sensor based on the fluorescence intensity ratio in Pr^{3+} :ZBLAN glass. *Optical Review*, **4**(1A):89, 1997.
- [53] G. S. Maciel, De. S. Menezes, A. S. L. Gomes, C. B. De. Araugio, Y. Messaddeq, A. Florez, and M. A. Aegerter. Temperature sensor based on frequency upconversion in Er^{3+} -doped fluorindate glass. *IEEE Photonics Technol. Lett.*, **7**(12):1474–1476, 1995.
- [54] D. N. Messias, M. V. D. Vermelho, A. S. Gouveia-Neto, and J. S. Aitchison. All optical integrated upconversion fluorescence-based point temperature sens-

- ing system using Er^{3+} -doped silica-on-silicon waveguides. *Rev. Sci. Instrum.*, **73**(2):476–479, 2002.
- [55] E. Maurice, G. Monnom, D. B. Ostrowsky, and Baxter G. W. High dynamic range temperature point sensor using green fluorescence intensity ratio in erbium-doped silica fiber. *J. Lightwave Technol.*, **13**(7):1349–1353, 1995.
- [56] F. Sidiroglou, S. A. Wade, N. M. Dragomir, G. W. Baxter, and S. F. Collins. Effects of high-temperature heat treatment on Nd^{3+} -doped optical fibers for use in fluorescence intensity ratio based temperature sensing. *Rev. Sci. Instrum.*, **74**(7):3524–3530, 2003.
- [57] S. F. Collins, G. W. Baxter, S. A. Wade, and P. M. Farrell. Strain dependence of fluorescence from rare-earth-doped optical fibres: application to the simultaneous, co-located, measurement of strain and temperature. *Compos. Struct.*, **58**:373–379, 2002.
- [58] S. A. Wade, J. C. Muscat, S. F. Collins, and G. W. Baxter. Optical fiber temperature sensor using the fluorescence intensity ratio in Nd^{3+} -doped silica fiber. *Rev. Sci. Instrum.*, **70**(11):4279–4282, 1999.
- [59] S. A. Wade. *Temperature measurement using rare earth doped fibre fluorescence*. Ph.D. Thesis, Victoria University, Australia, 1999.
- [60] K. O. Hill, Y. Fuji, D. C. Johnson, and B. S. Kawasaki. Photosensitivity in optical fiber waveguides: Application to reflection filter fabrication. *Appl. Phys. Lett.*, **32**(10):647–649, 1978.
- [61] R. Kashyap. *Fiber Bragg Gratings*. Academic Press, San Diego, 1999.
- [62] Y. J. Rao, S. F. Yuan, X. K. Zeng, Y. Lian, D. K. Zhu, Y. P. Wang, S. L. Huang, T. Y. Liu, G. F. Fernando, L. Zhang, and I. Bennion. Simultaneous strain and temperature measurement of advanced 3-D braided composite materials using an improved EFPI/FBG system. *Opt. and Lasers Eng.*, **38**:557–566, 2002.

- [63] Y. J. Rao, D. J. Webb, D. A. Jackson, Z. Lin, and I. Bennion. In-fiber Bragg-grating temperature sensor system for medical applications. *J. Lightwave Technol.*, **15**(5):779–785, 1997.
- [64] Micron Optics. si425 optical sensing interrogation. Micron Optics. <http://www.micronoptics.com/si425.htm>, March 2005.
- [65] Y. L. Lo. Using in-fiber Bragg-grating sensors for measuring axial strain and temperature simultaneously on surfaces and structures. *Opt. Eng.*, **37**(8):2272–2276, 1998.
- [66] H. K. Kang, D. H. Kang, C. S. Hong, and C. G. Kim. Simultaneous monitoring of strain and temperature during and after cure of unsymmetric composite laminate using fibre-optic sensors. *Smart Mater. Struct.*, **12**:29–35, 2003.
- [67] Y. H. Shen, J. Xia, T. Sun, and K. T. V. Grattan. Photosensitive indium-doped germano-silica fiber for strong FBGs with high temperature sustainability. *IEEE Photonics Technol. Lett.*, **16**(5):1319–1321, 2004.
- [68] Y. H. Shen, J. He, T. Sun, and K. T. V. Grattan. High-temperature sustainability of strong fiber Bragg gratings written into Sb-Ge-codoped photosensitive fiber: decay mechanisms involved during annealing. *Opt. Lett.*, **29**(6):554–556, 2004.
- [69] S. Pal, J. Mandal, T. Sun, K. T. V. Grattan, M. Fokine, F. Carlsson, P. Y. Fongjallaz, S. A. Wade, and S. F. Collins. Characteristics of potential fibre Bragg grating sensor-based devices at elevated temperatures. *Meas. Sci. Technol.*, **14**(7):1131–1136, 2003.
- [70] O. V. Butov, K. M. Golant, and I. V. Nikolin. Ultra-thermo-resistant Bragg gratings written in nitrogen-doped silica fibres. *Electron. Lett.*, **38**(11):523–525, 2002.
- [71] G. Brambilla. High-temperature fibre Bragg grating thermometer. *Electron. Lett.*, **38**(17):954–956, 2002.

- [72] B. Culshaw and J. Dakin. *Optical Fiber Sensors: Components and Subsystems, Vol 3*. Artech House, Norwood MA, 1996.
- [73] A. Cusano, G. Breglio, M. Giordano, L. Nicolais, and A. Cutolo. Multifunction fiber optic sensing system for smart applications. *IEEE/ASME Trans. Mechatronics*, **9**(1):40–49, 2004.
- [74] P. Niewczas, A. J. Willshire, L. Dziuda, and J. R. McDonald. Performance analysis of the fiber Bragg grating interrogation system based on an arrayed waveguide grating. *Trans. Instrum. Meas.*, **53**(4):1192–1196, 2004.
- [75] K. Zhou, A. G. Simpson, X. Chen, L. Zhang, and I. Bennion. Fiber Bragg grating sensor interrogation system using CCD side detection method with superimposed blazed gratings. *IEEE Photonics Technol. Lett.*, **16**(6):1549–1551, 2004.
- [76] Y. Sano and T. Yoshino. Fast optical wavelength interrogator employing arrayed waveguide grating for distributed fiber Bragg grating sensors. *IEEE Photonics Technol. Lett.*, **21**(1):132–139, 2003.
- [77] J. M. Gong, J. M. K. MacAlpine, C. C. Chan, W. Jin, M. Zhang, and Y. B. Liao. A novel wavelength detection technique for fiber Bragg grating sensors. *IEEE Photonics Technol. Lett.*, **14**(5):678–680, 2002.
- [78] C. Boulet, D. J. Webb, M. Douay, and P. Niay. Simultaneous interrogation of fiber Bragg grating sensors using an acousto-optic tunable filter. *IEEE Photonics Technol. Lett.*, **13**(11):1215–1217, 2001.
- [79] EXFO Burleigh Products Group. *Fiber Bragg Grating Sensors*. White Paper no. 3, United States of America, 2003.
- [80] T. Amarel and W. Gornall. Michelson interferometry interrogates fiber Bragg grating sensors. *Photonics Spectra*, **37**(10):67–69, 2003.
- [81] C. J. Myatt and N. G. Traggis. Tunable laser wavelength calibration for fiber sensing. *Photonics Spectra.*, **37**(10):72–74, 2003.

- [82] R. Nabiev and W. Yuen. Tunable lasers for multichannel fiber-optic sensors. Bandwidth9. <http://www.sensorsmag.com/articles/0803/28/main.shtml>, August 2003.
- [83] R. Posey, S. T. Vohra, and A. B. Tveten. Simultaneous measurements of temperature and strain using stimulated Brillouin scattering in GeO₂-doped core and dispersion shifted fiber. *IEICE Trans. Electron.*, **E83-C(3)**:413–417, 2000.
- [84] R. Posey and S. T. Vohra. An eight-channel fiber-optic Bragg grating and stimulated Brillouin sensor system for simultaneous temperature and strain measurements. *IEEE Photonics Technol. Lett.*, **11(12)**:1641–1643, 1999.
- [85] T. R. Parker, M. Farhadiroushan, V. A. Faced, V. A. Handerek, and A. J. Rogers. Simultaneous distributed measurement of strain and temperature from noise-initiated Brillouin scattering in optical fibers. *IEEE J. Quantum Electron.*, **34(4)**:645–659, 1998.
- [86] J. Jung, N. Park, and B. Lee. Simultaneous measurement of strain and temperature by use of a single fiber Bragg grating written in an erbium:ytterbium-doped fiber. *Appl. Opt.*, **39(7)**:1118–1120, 2000.
- [87] Y. Han, C. S. Kim, U. C. Paek, and Y. Chung. Performance enhancement of long period fiber gratings for strain and temperature sensing. *IEICE Trans. Electron.*, **E83-C(3)**:282–286, 2000.
- [88] M. G. Xu, J. L. Archambault, L. Reekie, and J. P. Dakin. Discrimination between strain and temperature effects using dual-wavelength fiber grating sensors. *Electron. Lett.*, **30(13)**:1085–1087, 1994.
- [89] J. Echevarria, A. Quintela, C. Jauregui, and J. M. Lopez-Higuera. Uniform fiber Bragg grating first- and second-order diffraction wavelength experimental characterization for strain-temperature discrimination. *IEEE Photonics Technol. Lett.*, **13(7)**:696–698, 2001.

- [90] L. A. Ferreira, F. M. Arujo, J. L. Santos, and F. Farahi. Simultaneous measurement of strain and temperature using interferometrically interrogated fiber Bragg grating sensors. *Opt. Eng.*, **39**(8):2226–2233, 2000.
- [91] S. Trpkovski, S. A. Wade, S. F. Collins, and G. W. Baxter. Er³⁺:Yb³⁺ doped fiber with embedded FBG for simultaneous measurement of temperature and longitudinal strain. *Meas. Sci. Technol.*, **16**:488–496, 2005.
- [92] K. J. Han, Y. W. Lee, J. Kwon, S. Roh, J. Jung, and B. Lee. Simultaneous measurement of strain and temperature incorporating a long-period fiber grating inscribed on a polarization-maintaining fiber. *IEEE Photonics Technol. Lett.*, **16**(9):2114–2116, 2004.
- [93] S. Pal, Y. Shen, J. Mandel, T. Sun, and K. T. V. Grattan. Combined fluorescence and grating-based technique for wider range strain-temperature simultaneous measurement using Sb-Er-doped fibre. *Proc. SPIE*, **5502**(1):160–163, 2004.
- [94] G. Chen, L. Liu, H. Jia, J. Yu, L. Xu, and W. Wang. Simultaneous strain and temperature measurements with fiber Bragg grating written in novel Hi-Bi optical fiber. *IEEE Photonics Technol. Lett.*, **16**(1):221–223, 2004.
- [95] S. Trpkovski, S. A. Wade, G. W. Baxter, and S. F. Collins. Dual temperature and strain sensor using a combined fiber Bragg grating and fluorescence intensity ratio technique in Er³⁺-doped fiber. *Rev. Sci. Instrum.*, **74**(5):2880–2885, 2003.
- [96] S. Pal, T. Sun, K. T. V. Grattan, S. A. Wade, S. F. Collins, G. W. Baxter, B. Dussardier, and G. Monnom. Bragg grating performance in Er-Sn-doped germanosilicate fiber for simultaneous measurement of wide range temperature (to 500 °C) and strain. *Rev. Sci. Instrum.*, **74**(11):4858–4862, 2003.
- [97] Y. G. Han, S. B. Lee, C. S. Kim, J. U. Kang, U. C. Paek, and Y. Chung. Simultaneous measurement of temperature and strain using dual long-period fiber

- gratings with controlled temperature and strain sensitivities. *Opt. Express*, **11**(5):476–481, 2003.
- [98] C. Fernandez-Valdivielso, I. R. Matias, and F. J. Arregui. Simultaneous measurement of strain and temperature using a fiber Bragg grating and a thermochromic material. *Sensors and Actuators A*, **1001**:107–116, 2002.
- [99] H. K. Kang, C. Y. Ryu, C. S. Hong, and C. G. Kim. Simultaneous measurement of strain and temperature of structures using fiber optic sensor. *J. Intelligent Material Systems Struct.*, **12**:277–281, 2001.
- [100] O. Hadeler, M. Ibsen, and M. N. Zervas. Distributed-feedback fiber laser sensor for simultaneous strain and temperature measurements operating in the radio-frequency domain. *Appl. Opt.*, **40**(19):3169–3175, 2001.
- [101] T. Liu, G. F. Fernando, Z. Y. Zhang, and K. T. V. Grattan. Simultaneous strain and temperature measurements in composites using extrinsic Fabry-Perot interferometric and intrinsic rare-earth doped fiber sensors. *Sensors and Actuators*, **80**:208–215, 2000.
- [102] B. G. Guan, H. Y. Tam, X. M. Tao, and X. Y. Dong. Simultaneous strain and temperature measurement using a superstructure fiber Bragg grating. *IEEE Photonics Technol. Lett.*, **12**(6):675–677, 2000.
- [103] W. C. Du, X. M. Tao, and H. Y. Tam. Fiber Bragg grating cavity sensor for simultaneous measurement of strain and temperature. *IEEE Photonics Technol. Lett.*, **11**(1):105–107, 1999.
- [104] J. Jung, H. Nam, J. H. Lee, N. Park, and B. Lee. Simultaneous measurement of strain and temperature by use of a single-fiber Bragg grating and an erbium-doped fiber amplifier. *Appl. Opt.*, **38**(13):2749–2751, 1999.
- [105] P. M. Cavaleiro, L. A. Araujo, L. A. Ferreira, J. L. Santos, and F. Farahi. Simultaneous measurement of strain and temperature using Bragg gratings written in germanosilicate and boron-codoped germanosilicate fibers. *IEEE Photonics Technol. Lett.*, **11**(12):1635–1637, 1999.

- [106] O. Hadeler, E. Ronnekleiv, M. Ibsen, and R. I. Laming. Polarimetric distributed feedback fiber laser sensor for simultaneous strain and temperature measurements. *Appl. Opt.*, **38**(10):1953–1958, 1999.
- [107] P. G. Sinha and T. Yoshino. Acoustically scanned low-coherence interrogated simultaneous measurement of absolute strain and temperature using highly birefringent fibers. *J. Lightwave Technol.*, **16**(11):2010–2015, 1998.
- [108] G. P. Brady, K. Kalli, D. J. Webb, D. A. Jackson, L. Reekie, and J. L. Archambault. Simultaneous measurement of strain and temperature using the first- and second-order diffraction wavelengths of Bragg gratings. *IEE Proc.-Optoelectron.*, **144**(3):156–161, 1997.
- [109] V. Bhatia, D. Campbell, and R. O. Claus. Simultaneous strain and temperature measurement with long-period gratings. *Opt. Lett.*, **22**(9):648–650, 1997.
- [110] S. W. James, M. L. Dockney, and R. P. Tatam. Simultaneous independent temperature and strain measurement using in-fibre Bragg grating sensors. *Electron. Lett.*, **32**(12):1133–1134, 1996.
- [111] Y. J. Rao. Recent progress in applications of in-fibre Bragg grating sensors. *Opt. and Lasers Eng.*, **31**:297–324, 1999.
- [112] E. J. Friebele, C. G. Askins, A. B. Bosse, A. D. Kersey, H. J. Patrick, W. R. Pogue, M. A. Putnam, W. R. Simon, W. S. Tasker, F. A. Vincent, and S. T. Vohra. Optical fiber sensors for spacecraft applications. *Smart Mater. Struct.*, **8**:813–838, 1999.
- [113] R. Jones and S. Galea. Health monitoring of composite repairs and joints using optical fibres. *Compos. Struct.*, **58**(3):397–403, 2002.
- [114] K. Pran, G. B. Havsgard, G. Sagvolden, O. Farsund, and G. Wang. Wavelength multiplexed fibre Bragg grating system for high-strain health monitoring applications. *Meas. Sci. Technol.*, **13**:471–476, 2002.

- [115] Smart Fibres. Project: Jacqualina mast. Smart Fibres. <http://www.smartfibres.com/Project-Jacqualina.htm>, January 2005.
- [116] E. Udd, K. Corona-Bittick, K. T. Slattery, D. J. Dorr, C. R. Crowe, T. L. Vandiver, and R. N. Evans. Fiber grating systems used to measure strain in cylindrical structures. *Opt. Eng.*, **36**(7):1893–1900, 1997.
- [117] R. C. Tennyson, A. A. Mufti, S. Rizkalla, G. Tadros, and B. Benmokrane. Structural health monitoring of innovative bridges in Canada with fiber optic sensors. *Smart Mater. Struct.*, **10**(3):560–573, 2001.
- [118] M. de Vries, M. Nasta, V. Bhatia, T. Tran, J. Greene, R. O. Claus, and S. Masri. Performance of embedded short-gage-length optical fiber sensors in a fatigue-loaded reinforced concrete specimen. *Smart Mater. Struct.*, **4**:107–113, 1995.
- [119] X. C. Li, F. Prinz, and J. Seim. Thermal behavior of a metal embedded fiber Bragg grating sensor. *Smart Mater. Struct.*, **10**(4):575–579, 2001.
- [120] C. I. Merzbacher, A. D. Kersey, and E. J. Friebele. Fiber optic sensors in concrete structures: a review. *Smart Mater. Struct.*, **5**:196–208, 1996.
- [121] T. Bowker and M. Shaw. Beyond telecom: FBGs find use in oil and gas industries. *Laser Focus World*, **39**(5):123–126, 2003.
- [122] P. M. Nellen, P. Mauron, A. Frank, U. Sennhauser, K. Bohnert, P. Pequignot, P. Bodor, and H. Brandle. Reliability of fiber Bragg grating based sensors for downhole applications. *Sensors and Actuators A*, **103**(3):364–376, 2003.
- [123] C. Helmig and D. Peier. Optical measurement system for power cable monitoring. *Proc. SPIE*, **3746**:228–231, 1999.
- [124] W. J. Miniscalco. Optical and electronic properties of rare earth ions in glasses. In M. J. F. Digonnet, editor, *Rare Earth Doped Fiber Lasers and Amplifiers*, 2nd Ed. Marcel Dekker Inc., New York, 1993.

- [125] S. Sudo. Outline of optical fibre amplifiers. In S. Sudo, editor, *Optical Fibre Amplifiers: Materials, devices and Applications*. Artech House Inc., 1997.
- [126] S. B. Poole, D. N. Payne, and M. E. Fermann. Fabrication of low-loss optical fibres containing rare-earth ions. *Electron. Lett.*, **21**(17):737–738, 1985.
- [127] M. J. F. Digonnet. Broadband fiber sources. In M. J. Digonnet, editor, *Rare Earth Doped Fiber Amplifiers, 2nd Ed.* Marcel Dekker Inc., New York, 2001.
- [128] T. B. Nguyen. *Determining rare earth dopant concentrations in optical fibres and waveguides*. Ph.D. Thesis, Victoria University Australia, 2004.
- [129] E. Desurvire. *Erbium-Doped Fiber Amplifiers: Principles and Applications*. John Wiley & Sons Inc., 1994.
- [130] S. J. Mihailov, C. W. Smelser, P. Lu, R. B. Walker, D. Grobnic, H. Ding, and G. Henderson. Fiber Bragg gratings made with a phase mask and 800 nm femtosecond radiation. *Opt. Lett.*, **28**(12):995–997, 2003.
- [131] M. Fokine. Growth dynamics of chemical composition gratings in fluorine-doped silica optical fibers. *Opt. Lett.*, **27**(22):1974–1976, 2002.
- [132] M. Fokine. Thermal stability of chemical composition gratings in fluorine-germanium-doped silica fibers. *Opt. Lett.*, **27**(12):1016–1018, 2002.
- [133] V. Grubsky, D. Starodubov, and W. W. Morey. High-temperature Bragg gratings in germanosilicate fibers. In *Bragg gratings photosensitivity and poling in glass waveguides*, pages 33–35, (OSA, Washington DC USA), 2003.
- [134] M. Fokine. Thermal stability of oxygen-modulated chemical-composition gratings in standard telecommunication fiber. *Opt. Lett.*, **29**(11):1185–1187, 2004.
- [135] S. Trpkovski, D. Kitcher, G. W. Baxter, S. F. Collins, and S. A. Wade. High temperature-resistant chemical composition Bragg gratings in Er^{3+} doped optical fiber. *Opt. Lett.*, **30**(6):607–609, 2005.

- [136] H. Hosono, Y. Abe, D. L. Kinser, R. A. Weeks, K. Muta, and H. Kawazoe. Nature and origin of the 5-eV band in $\text{GeO}_2\text{:SiO}_2$ glasses. *Phys. Rev. B*, **46**:11445–11451, 1992.
- [137] L. Dong, J. L. Archambault, L. Reekie, P. St. J. Russel, and D. N. Payne. Photoinduced absorption change in germanosilicate preforms: evidence for the color-center model of photosensitivity. *Appl. Opt.*, **34**(18):3436–3440, 1995.
- [138] A. Othonos and K. Kalli. *Fiber Bragg Gratings: Fundamentals and Applications in Telecommunications and Sensing*. Artech House, Boston, 1999.
- [139] M. G. Sceats, G. R. Atkins, and S. B. Poole. Photolytic index changes in optical fibers. *Annual Rev. Material Sci.*, **23**:381–410, 1993.
- [140] M. G. Sceats and P. A. Krug. Photoviscous annealing - dynamics and stability of photorefractivity in optical fibres. *Proc. SPIE*, **2044**:113–120, 1993.
- [141] M. Douay, W. X. Xie, T. Taunay, P. Bernage, P. Niay, P. Cordier, L. Poumellec, B. Dong, J. F. Bayon, H. Poignant, and E. Delevaque. Densification involved in the UV based photosensitivity of silica glasses and optical fibres. *J. Lightwave Technol.*, **15**(8):1329–1342, 1997.
- [142] P. Y. Fonjallaz, H. G. Limberger, R. P. Salathe, F. Cochet, and B. Leuenberger. Tension increase correlated to refractive index change in fibers containing UV written Bragg gratings. *Opt. Lett.*, **20**(11):1346–1348, 1995.
- [143] P. J. Lemaire. Reliability of optical fibers exposed to hydrogen: prediction of long-term loss increases. *Opt. Eng.*, **30**(6):780–781, 1991.
- [144] G. Meltz and W. W. Morey. Bragg grating formation and germanosilicate fiber photosensitivity. *Proc. SPIE*, **1516**:185–199, 1991.
- [145] P. J. Lemaire, R. M. Atkins, V. Mizrahi, and A. W. A. Reed. High pressure H_2 loading as a technique for achieving ultrahigh UV photosensitivity and thermal stability in GeO_2 doped optical fibres. *Electron. Lett.*, **29**(13):1191–1193, 1993.

- [146] G. A. Ball, W. W. Morey, and J. P. Waters. Nd³⁺ fiber laser utilising intracore Bragg reflectors. *Electron. Lett.*, **26**(21):1829, 1990.
- [147] D. L. Williams, B. J. Ainslie, J. R. Armitage, R. Kashyap, and R. Campbell. Enhanced UV photosensitivity in boron codoped germanosilicate fibres. *Electron. Lett.*, **29**:45–47, 1993.
- [148] S. R. Baker, H. N. Rourke, V. Baker, and D. Goodchild. Thermal decay of fiber Bragg gratings written in boron and germanium codoped silica fiber. *J. Lightwave Technol.*, **15**(8):1470–1477, 1997.
- [149] T. A. Strasser, A. E. White, M. F. Yan, P. J. Lemaire, and T. Erdogan. Strong Bragg phase gratings in phosphorus-doped fiber induced by ArF excimer radiation. In *Technical Digest: OFC95 Optical Fiber Conference*, page 159, San Jose, CA, (OSA, Washington DC USA), 1995.
- [150] J. Canning and P. F. Hu. Low-temperature hypersensitization of phosphosilicate waveguides in hydrogen. *Opt. Lett.*, **26**:1230–1232, 2001.
- [151] L. Dong, J. L. Cruz, L. Reekie, M. G. Xu, and D. N. Payne. Enhanced photosensitivity in tin-codoped germanosilicate optical fibers. *IEEE Photonics Technol. Lett.*, **7**:1048–1050, 1995.
- [152] L. Dong, J. L. Cruz, J. A. Tucknott, L. Reekie, and D. N. Payne. Strong photosensitive gratings in tin-doped phosphosilicate optical fibers. *Opt. Lett.*, **20**:1982–1984, 1995.
- [153] Y. H. Shen, S. Pal, J. Mandal, T. Sun, K. T. V. Grattan, S. A. Wade, S. F. Collins, G. W. Baxter, B. Dussardier, and G Monnom. Investigation of the photosensitivity, temperature sustainability and fluorescence characteristics of several Er-doped photosensitive fibers. *Opt. Commun.*, **237**:301–308, 2004.
- [154] E. M. Dianov, K. M. Golant, V. M. Mashinsky, O. I. Medvedkov, I. V. Nikolin, O. D. Sazhin, and S. A. Vasiliev. Highly photosensitive nitrogen-doped germanosilicate fibre for index grating writing. *Electron. Lett.*, **33**:1334–1336, 1997.

- [155] E. M. Dianov, K. M. Golant, R. R. Khrapko, A. S. Kurkov, B. Leconte, M. Douay, P. Bernage, and P. Niay. Grating formation in a germanium free silicon oxynitride fibre. *Electron. Lett.*, **33**:236–238, 1997.
- [156] T. Erdogan, V. Mizrahi, P. J. Lemaire, and D. Monroe. Decay of ultraviolet-induced fiber Bragg gratings. *J. Appl. Phys.*, **76**(1):73–80, 1994.
- [157] H. Patrick, S. L. Gilbert, A. Lidgard, and M. D. Gallagher. Annealing of Bragg gratings in hydrogen-loaded optical fiber. *J. Appl. Phys.*, **78**(5):2941–2945, 1995.
- [158] W. Jin, W. C. Michie, G. Thursby, M. Konstantaki, and B. Culshaw. Simultaneous measurement of strain and temperature: error analysis. *Opt. Eng.*, **36**(2):598–609, 1997.
- [159] S. Pal, T. Sun, K. T. V. Grattan, S. A. Wade, S. F. Collins, G. W. Baxter, B. Dussardier, and G. Monnom. Non-linear temperature dependence of Bragg gratings written in different fibres, optimised for sensor applications over a wide range of temperatures. *Sensors and Actuators A*, **112**:211–219, 2004.
- [160] G. M. H. Flockhart, W. N. MacPherson, J. S. Barton, J. D. C. Jones, L. Zhang, and I. Bennion. Departure from linearity of fiber Bragg grating temperature coefficients. In *Technical Digest: 15th International Conference on Optical Fiber Sensors*, pages 75–78, Oregon, USA, (IEEE, Piscataway NJ USA), 2002.
- [161] M. B. Reid and M. Ozcan. Temperature dependence of fiber optic Bragg gratings at low temperatures. *Opt. Eng.*, **37**:237–240, 1998.
- [162] G. Paez and M. Strojnik. Experimental results of ratio-based erbium-doped-silica temperature sensor. *Opt. Eng.*, **42**(6):1805–1811, 2003.
- [163] E. Maurice. *Phénomènes multiphotoniques dans les fibres optiques de silice dopée terres rares application à un capteur de température*. Ph.D. Thesis, University of Nice, France, 1994.

- [164] Y. H. Shen, S. Pal, J. Mandal, T. Sun, K. T. V. Grattan, S. A. Wade, S. F. Collins, G. W. Baxter, B. Dussardier, and G. Monnom. Investigation of the photosensitivity, temperature sustainability and fluorescence characteristics of several Er-doped photosensitive fibers. *Opt. Commun.*, **237**:301–308, 2004.
- [165] Y. Zhou, S. Ping, and L. Chao. Temperature insensitive measurements of static displacements using a fiber Bragg grating. *Opt. Express*, **11**(16):1918–1924, 2003.

Appendix A

LIST OF PUBLICATIONS

Throughout the duration of this thesis, numerous publications were generated. Work was presented in oral and poster form at both international and national conferences. Other publications that the author contributed in are also shown. Journal articles and conference proceedings are listed chronologically, with the most recent first.

A.1 Journal Articles

1. **S. Trpkovski**, D. J. Kitcher, G. W. Baxter, S. F. Collins and S. A. Wade. High-temperature-resistant chemical composition Bragg gratings in Er^{3+} doped optical fiber. *Opt. Lett.*, **30**(6):607–609, 2005.
2. **S. Trpkovski**, S. A. Wade, S. F. Collins and G. W. Baxter. $\text{Er}^{3+}:\text{Yb}^{3+}$ doped fibre with embedded FBG for simultaneous measurement of temperature and longitudinal strain. *Meas. Sci. Technol.*, **16**:488–496, 2005.
3. **S. Trpkovski**, S. A. Wade, G. W. Baxter and S. F. Collins. Dual temperature and strain sensor using a combined fibre Bragg grating and fluorescence intensity ratio in Er^{3+} -doped fibre. *Rev. Sci. Instrum.*, **74**(5):2880–2885, 2003.
4. T. B. Nguyen, **S. Trpkovski**, P. M. Farrell, G. W. Baxter and S. F. Collins. Dependence of the fluorescence lifetime on dopant concentration and temperature in praseodymium doped fluoride glass. *Opt. Comm.*, **186**:277–281, 2000.

A.2 International Conference Proceedings

1. C. M. Rollinson, **S. Trpkovski**, S. A. Wade, N. M. Dragomir, G. W. Baxter and S.F. Collins. Three parameter measurement using a single fiber Bragg grating inscribed in $\text{Er}^{3+}:\text{Yb}^{3+}$ -codoped fiber. In *17th International Conference on Optical Fiber Sensors*, Bruges, Belgium, 23-27 May 2005.
2. **S. Trpkovski**, D. J. Kitcher, G. W. Baxter, S. F. Collins, S. A. Wade, B. Dussardier and G. Monnom. Fiber Bragg gratings suitable for very high temperature measurement. In *Proc. of International Symposium on Advances and Trends in Fiber Optics and Applications*, Chongqing, China, Chongqing University Press (ISBN 7-5624-3279-1), pp. 322-326, 2004.
3. **S. Trpkovski**, S. A. Wade, S. F. Collins and G. W. Baxter. Er:Yb doped fiber with embedded FBG for simultaneous point measurement of temperature and strain. In *2nd European Workshop on Optical Fiber Sensors*, Proc. SPIE 5502, pp. 64-67, Santander, Spain, 2004.
4. **S. Trpkovski**, S. A. Wade, G. W. Baxter and S.F. Collins. Comparison of two simultaneous temperature and strain sensors utilizing a combined fiber Bragg grating/fluorescence intensity ratio technique. In *Technical Digest 16th International Optical Fiber Sensors Conference*, Nara, Japan (IEICE, Japan), pp. 108-111, 2003.
5. **S. Trpkovski**, S. A. Wade, G. W. Baxter and S.F. Collins. Simultaneous and co-located measurement of strain and temperature in optical fibre using a Bragg grating and strain-independent erbium fluorescence. In *12th Conference on Sensors and their Applications*, Limerick, Ireland, (IOP, Bristol UK), pp. 21-27, 2003.
6. **S. Trpkovski**, S. A. Wade, S. F. Collins, G. W. Baxter and P. M. Farrell. Temperature and strain measurement using a combined fiber Bragg grating and fluorescence intensity ratio technique in Er^{3+} -doped fiber". In *Technical Digest 15th International Conference on Optical Fiber Sensors*, Portland,

- Oregon USA, (IEEE Cat. No. 02EX533, Piscataway NJ USA), pp. 107-110, 2002.
7. T. B. Nguyen, **S. Trpkovski**, P. M. Farrell, G. W. Baxter and S. F. Collins. The concentration dependence in Pr^{3+} :ZBLAN optical fibre temperature sensors. In *Technical Digest 14th International Conference on Optical Fiber Sensors*, Venice, Italy, (Proc. SPIE 4185, Bellingham, WA), pp. 688-691, 2000.
 8. **S. Trpkovski**, T. B. Nguyen, P. M. Farrell, G. W. Baxter and S. F. Collins. Temperature and concentration dependence of the lifetime of a praseodymium excited state in fluorozirconate glass. In *Conference on Lasers and Electro-Optics Europe*, Nice, France, (IEEE Cat. No. 00TH8505, Piscataway NJ USA), 2000.

A.3 National Conference Proceedings

1. D. J. Kitcher, **S. Trpkovski**, M. Dagher, G. W. Baxter and S. F. Collins. Annealing dynamics of erbium doped fibre Bragg gratings. In *16th Biennial Congress of the Australian Institute of Physics incorporating the Conference of the Australian Optical Society*, Canberra, Abstracts p. 105, 2005.
2. M. Dagher, **S. Trpkovski**, S. A. Wade, G. W. Baxter, S. F. Collins, B. Dussardier and G. Monnom. Stability of fibre Bragg gratings written in Er^{3+} -doped fibre. In *Proc. 29th Australian Conference on Optical Fibre Technology*, Canberra, CD-ROM: ACOFT/AOS 04 ISBN 0-7315-5222-9 (ANU, ACT Australia), PO8, 2004.
3. **S. Trpkovski**, S. A. Wade, D. J. Kitcher, G. W. Baxter, S. F. Collins, B. Dussardier and G. Monnom. Ultra stable fibre Bragg gratings at very high temperatures. In *Proc. 29th Australian Conference on Optical Fibre Technology*, Canberra, CD-ROM: ACOFT/AOS 04 ISBN 0-7315-5222-9 (ANU, ACT Australia), PO9, 2004.

4. **S. Trpkovski**, S. A. Wade, S. F. Collins and G. W. Baxter. Utilisation of a FBG and fluorescence from Er:Yb doped fibre for simultaneous point measurement of temperature and strain. In *Proc. Australasian Conference on Optics, Lasers and Spectroscopy*, Melbourne, Abstracts p. 122, 2003.
5. **S. Trpkovski**, J. MacDonald, S. A. Wade and S. F. Collins. Fibre optic strain and temperature sensors for very high temperatures using Er³⁺:Sn co-doped fibre. In *Proc. Australasian Conference on Optics, Lasers and Spectroscopy*, Melbourne, Australia, Abstracts p. 279, 2003.
6. **S. Trpkovski**, S. A. Wade, S. F. Collins and G. W. Baxter. Dual strain and temperature sensor using a fluorescence intensity ratio in Er³⁺-doped fibre combined with a fibre Bragg grating. In *Proc. 27th Australian Conference on Optical Fibre Technology, co-located with 15th National Congress of the Australian Institute of Physics*, Sydney, (ISBN 0-9581182-0-5), pp. 122-124, 2002.
7. T. B. Nguyen, **S. Trpkovski**, P. Corbett and G. W. Baxter. Determination of erbium dopant concentration in erbium-ytterbium co-doped fibres. In *Proc. Australasian Conference on Optics, Lasers and Spectroscopy*, Brisbane, (ISBN 0-9580000-0-X), p. 125, 2001.
8. **S. Trpkovski**, T. B. Nguyen, S. F. Collins, P. M. Farrell, G. W. Baxter and S. A. Wade. Strain and temperature measurement using a combined fluorescence intensity ratio and fibre Bragg grating technique. In *Proc. Australasian Conference on Optics, Lasers and Spectroscopy*, Brisbane, (ISBN 0-9580000-0-X), p. 106, 2001.
9. T. B. Nguyen, **S. Trpkovski**, P. M. Farrell, G. W. Baxter and S. F. Collins. Concentration and temperature dependence of the fluorescence lifetime of Pr³⁺:ZBLAN. In *Proc. 25th Australian Conference on Optical Fibre Technology*, Canberra, Australia, 2000.
10. C. M. Sullivan, C. J. Vale, **S. Trpkovski**, P. M. Farrell and R. E. Scholten.

External cavity laser diodes at 767 nm, 1323 nm and 1529 nm. In *Proc. Australian Optical Society*, Sydney, Australia, 1999.